Influence of a forward-facing step on crossflow instability and transition
An experimental study in a swept wing boundary-layer

Rius Vidales, A.F.

DOI
10.4233/uuid:6fd8a152-ab7a-4ecd-a817-61945d431bef

Publication date
2022

Document Version
Final published version

Citation (APA)
Rius Vidales, A. F. (2022). *Influence of a forward-facing step on crossflow instability and transition: An experimental study in a swept wing boundary-layer*. [Dissertation (TU Delft), Delft University of Technology]. https://doi.org/10.4233/uuid:6fd8a152-ab7a-4ecd-a817-61945d431bef

Influence of a Forward-Facing Step on Crossflow Instability and Transition

An Experimental Study in a Swept Wing Boundary-Layer

Alberto Felipe Rius Vidales

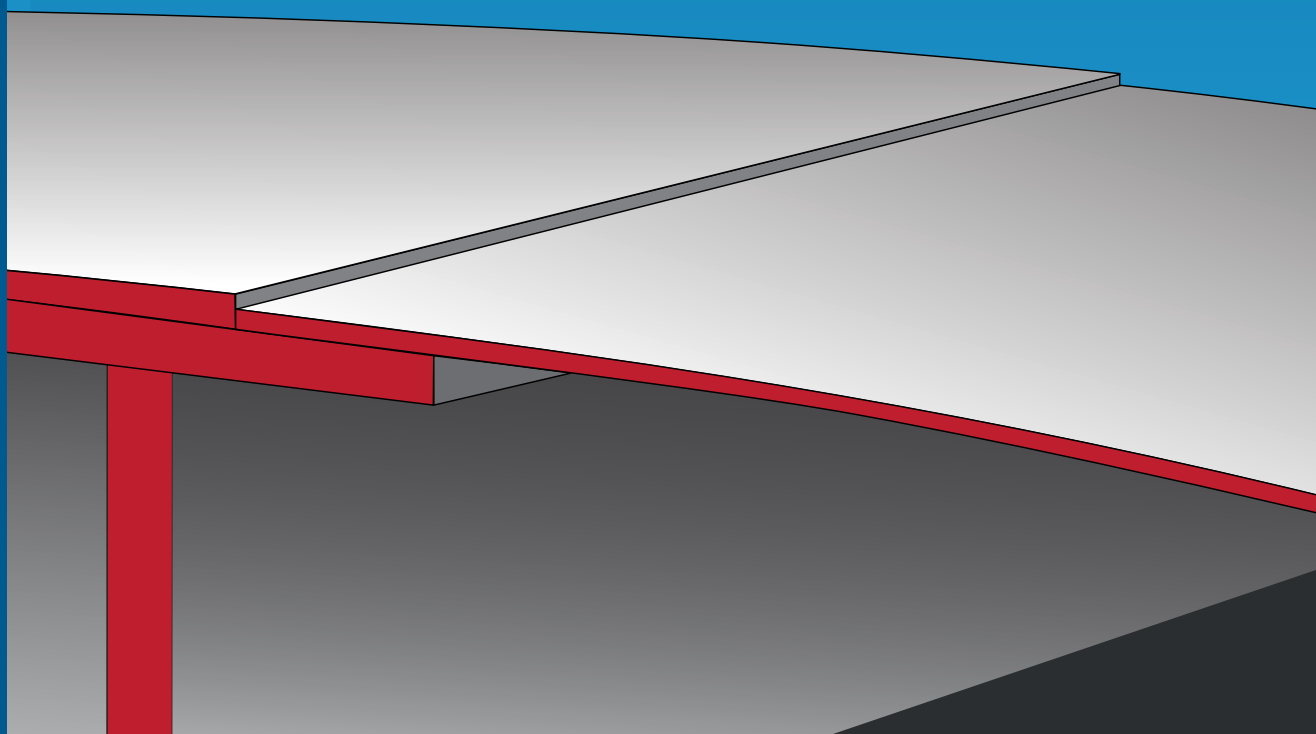

Influence of a Forward-Facing Step on Crossflow Instability and Transition

An Experimental Study in a Swept Wing Boundary-Layer

Dissertation

for the purpose of obtaining the degree of doctor
at Delft University of Technology
by the authority of the Rector Magnificus prof. dr. ir. T.H.J.J. van der Hagen,
Chair of the Board of Doctorates,
to be defended publicly on
Tuesday 31 May 2022 at 15:00 hours

by

Alberto Felipe Rius Vidales

Master of Science in Aerospace Engineering,
Delft University of Technology, the Netherlands,
born in Mexico City, Mexico.

This dissertation has been approved by

promotor: Dr. M. Kotsonis
promotor: Prof. dr. F. Scarano

Composition of the doctoral committee:

Rector Magnificus,	chairperson
Dr. M. Kotsonis,	Delft University of Technology, promotor
Prof. dr. F. Scarano,	Delft University of Technology, promotor

Independent members:

Dr. A.P Antunes,	Heart Aerospace, Sweden
Dr. J.L. Eppink,	NASA Langley, United States of America
Prof. Dr.-Ing U. Rist,	Universität Stuttgart, Germany
Prof. dr. ir. L.L.M. Veldhuis,	Delft University of Technology
Prof. dr. E.B White,	Texas A&M University, United States of America

Reserve member:

Prof. Dr.-Ing.habil. S. Hickel	Delft University of Technology, reserve member

Parts of this dissertation are published in:

Rius-Vidales, A.F. & Kotsonis, M. 2020 Influence of a forward facing step surface irregularity on swept wing transition. AIAA Journal **58(12)**, 5243-5253.

Rius-Vidales, A.F. & Kotsonis, M. 2021 Impact of a forward-facing step on the development of crossflow instability. Journal of Fluid Mechanics **924**, A34.

Rius-Vidales, A.F. & Kotsonis, M. 2022 Unsteady interaction of crossflow instability with a forward-facing step. Journal of fluid Mechanics, **939**, A19.

Keywords: Swept wings, Boundary-layer transition, Crossflow Instability, Forward-Facing Step, Surface Irregularities

Printed by: Uitgeverij U2pi – Den Haag, Nederland

Front & Back: design by P. Rius Vidales and A.F. Rius Vidales..

ISBN 978-94-6366-544-5

An electronic version of this dissertation is available at
`http://repository.tudelft.nl/`.

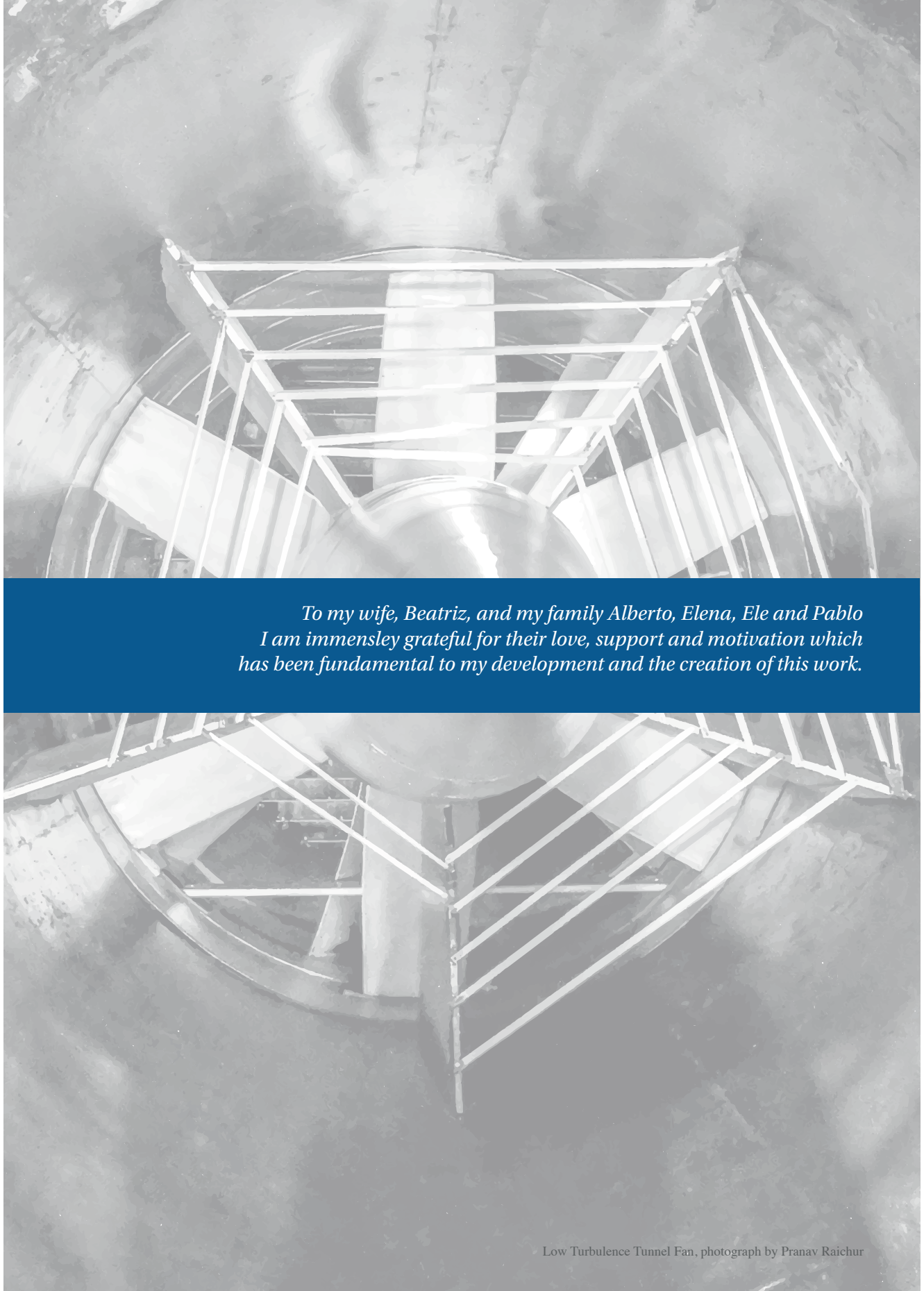

To my wife, Beatriz, and my family Alberto, Elena, Ele and Pablo
I am immensley grateful for their love, support and motivation which has been fundamental to my development and the creation of this work.

Low Turbulence Tunnel Fan, photograph by Pranav Raichur

ACKNOWLEDGEMENTS

After several years of persistent work aiming to earn a doctoral degree, the writing of this section signals the end of this journey and the start of a new one. As I reflect on the years that passed by, I cannot help but think of what a unique experience it has been. The PhD resulted in an invaluable personal and professional growth, which would have not been posible without the continuous support and motivation of my family, friends, and colleagues. I owe my deepest gratitude to them for making this period in my life one which I will always cherish.

My profound appreciation goes to Marios. He has given me a great example of what kind of daily supervisor and academic I would like to become. His supervision has been an invaluable source of knowledge, motivation and support. After following his first advice -"Before you decide to begin ask my students about their experience with me as supervisor"- I decided to start my doctoral education under his supervision. To my surprise, only after a couple of months of starting my new job, he left for Japan on a sabbatical to conduct research. Even though I was worried at first, it didn't take me long to realize that, despite the distance, he would be following closely my progress. I will always be thankful to him and Anke for the extra effort they made to compensate for Marios' physical absence during that period and for the friendship that followed. Marios is a great leader and scientist. Most importantly he is a greater person who constantly seeks to bring out the best in others. For this reason, I am looking forward to continuing working and learning from him in the years to come.

My time in Delft has shown me how contagious Fulvio's passion and enthusiasm towards experimental aerodynamics are. He started as my supervisor during my master studies and continued as my promotor during the PhD. I am very grateful for his encouragement and approachability and for providing me with valuable and honest feedback on my research and my development as a researcher.

It has been a great honour to share the last phase of my doctoral journey with the doctoral committee members Dr. Alexandre Antunes, Dr. Jenna Eppink, Prof. Ulrich Rist, Prof. Leo Veldhuis, Prof. Edward White, Prof. Stefan Hickel and Prof. Chris Kleijn. I would like to especially thank Alexandre for his advice and involvement on my research during the collaboration project between Embraer S.A. and TU Delft. Similarly, I express my gratitude to Jenna for following closely the progress of my research, and providing me with insightful comments and suggestions on different occasions. In addition, I acknowledge the anonymous reviewers whose feedback in the journal papers indirectly contributed to this dissertation.

During the last years, I had the opportunity to meet great researchers from KTH and DLR. I want to thank Francesco Tocci, Stefan Hein, Ardeshir Hanifi, Guillaume Chauvat, Juan Alberto Franco and Marco Costantini for our fruitful discussions and ongoing collaborations.

Throughout the years, I came to realize that although pursuing a doctoral degree is a personal journey, one must not travel it alone. I am thankful to all my PhD colleagues for

accompanying me on this journey. Starting from the older generation, I thank Jacopo, Beppe, Theo, Mustafa and Henry for their friendship. I am deeply grateful to Jacopo not only for his advice but also for the beautiful swept wing model (i.e. M3J) that I inherited from him. He paved the way for me with his important and carefully conducted research.

As the old guard of PhDs left, new recruits arrived, with whom I had the opportunity to share many special moments in the Netherlands and abroad. I express my gratitude to Ale, Alex, Constantin, Christoph, Edo, Giulia, Gabriel, Haohua, Haris, Jordi, John, Kaisheng, Kushal, Luis, Martin, Mohamad, Rodrigo, Sven, Srikar, Sagard, Tiago, Varun, Weibo, Xiaodong, Yi and Zeno. They all contributed in one way or the other in making my time in the Netherlands a fun and memorable one. The friendship that I built with many of them has been an essential ingredient in the recipe for the healthy completion of my doctoral education, especially during the pandemic. To my newest colleagues Giulio, Jane, Ata, Babak, Thomas, Ilda, Yu and Wencan, I wish you the best in this period of your life. I look forward to know each other better in the following years.

I would like to take the opportunity to especially thank Kaisheng, Giulia, Jordi, Sven and Theo. It has been a privilege to be part of such a committed team. I will certainly miss our time together and our frequent discussions starting with food, switching to boundary-layer instabilities, and ending in politics. All of them contributed to this dissertation by accompanying and helping me during lengthy experimental campaigns at the low turbulence wind tunnel on our beloved swept wing model.

My doctoral experience was enriched by supervising three master's students: Patrick, Niveditha and Marina. I appreciate the time we spent together in the wind tunnel experiments and the conversations we had. Thanks for helping me to become a better supervisor. In addition, I express my gratitude to my colleagues Reynard, Nando, Dani, Biaggio, Tomas, and Olaf, who have given me important advice on experimental aerodynamics and many other topics during their frequent visits to the Low-Speed Laboratory and at mojito parties. In particular, I thank Reynard and Nando for the very useful tips on the final printing process and for the Dutch translations for this dissertation.

A big thanks goes to Colette for her administrative support. She has been an essential guide and ally in the procedures within the university and has been key in organizing the different academic and social events within our research section. In addition, I am grateful to Denis, Ruud, Frits, Henk-Jan, Nando and Ferry for their administrative and maintenance work which indirectly supported my research. This research would have not been possible without the direct technical support provided by Stefan, Emiel, Pieter, Leo and Nico at different stages. For this and our interesting coffee conversations, which were a pleasant break from the daily routine, I am very thankful.

My time in Europe wouldn't have been the same without the friendship of Ankur, Krishti, Reynard, Ale, Marc, Steff, Edo, Ale, Pamela, Tobias, Michel, Asier, Cristina and Pedro. I am thankful to all of them for making me feel at home in the Netherlands. A special mention goes to my European-Mexican family Jaime, Donata and Mia who have always been a constant support during my studies. Jaime, many thanks for encouraging me to pursue my graduate studies abroad and for your guidance in my first years in the Netherlands. In addition, I thank my good friends, Rodrigo, Alfredo, Rafael and Mauricio for their motivation throughout the years.

I am in debt to Angel Abbud-Madrid for his mentorship and friendship. He has been

a true “Sensei" during my aerospace engineering studies. I am deeply grateful for our frequent conversations and advice on my personal and academic life.

I have been very fortunate to always be able to count on the people that I care and love the most: my wife Beatriz, my parents Alberto and Elena, and my siblings Ele and Pablo. Throughout my life, I had many teachers and friends but the most important ones, without doubt, are my parents. They gave me a great education and the necessary tools and space to develop my creativity in many aspects of my life. I am deeply grateful to them because without their love and encouragement, it would have not been possible to follow my aspirations and I would certainly be a very different person. In addition, they gave me two essential life-long allies, confidants and friends, my siblings. Ele and Pablo have been a pillar in my life. I am very proud of them and feel lucky to be their oldest brother. I would also like to acknowledge my extended family: Beatriz, Humberto, Beto, Itzel, and Tony. I appreciate their continuous support throughout the years.

Finally, the person to whom I am most grateful to for supporting me in these years is my wife, Beatriz. She is my best friend and companion. Without her love, this journey would have never begun. Her motivation, understanding and advice have been essential to becoming a better person and professional. I am deeply thankful to her for supporting my aspirations to become an aerospace engineer and for starting together a new life adventure, even though it meant being far away from our families and friends. I will always be grateful to her for believing in me and taking care of us since the beginning of our relationship.

Alberto Felipe Rius Vidales
The Hague, April 2022

SUMMARY

The market growth expected for commercial aviation in the coming decades and the increasing social awareness regarding the effects of global warming are driving significant technological developments necessary for emission reduction in future transport aircraft. From the aerodynamics perspective, a significant increase in aircraft efficiency can be obtained by applying Laminar Flow Control (LFC) techniques.

The objective of LFC techniques is to reduce the skin-friction drag component by delaying the laminar-turbulent transition through the stabilisation of boundary-layer instabilities. Relevant to high-subsonic transport aircraft is the development of Crossflow (CF) instability, which manifests as a series of co-rotating vortices inside the boundary-layer flow on swept aerodynamic surfaces.

Of particular importance in the practical applications of LFC is the smoothness of the aerodynamic surface, since two-dimensional (i.e. panel joints, seals and seams) and three-dimensional (i.e. rivets, debris, insect contamination) irregularities can perturb the boundary-layer flow and promote a premature laminar-turbulent boundary-layer transition which reduces the effectiveness of an LFC technique.

Therefore, the objective of the research contained in this dissertation is to experimentally characterise the influence that a two-dimensional surface irregularity in the form of a Forward-Facing Step (FFS) has on the development of the CF instability and laminar-turbulent boundary-layer transition. To this end, a series of experimental investigations have been conducted at the Low-Turbulence Tunnel (LTT) of the Delft University of Technology on a swept wing model.

The first chapter presents the research's context, relevance, and objectives by providing a comprehensive review of the development of CF instability and the laminar-turbulent boundary-layer transition influenced by step-like surface irregularities. The second chapter introduces first the wind tunnel facility, swept wing model and the manufacturing of FFS surface irregularities. In addition, an overview of the measurement techniques and numerical methods used in the acquisition, processing and interpretation of experimental data is given.

The third chapter considers the influence of the FFS on the laminar-turbulent transition behaviour under unforced (i.e. smooth leading edge) and forced (i.e. using discrete roughness elements) conditions. The results reveal the importance of considering multiple parameters when estimating the critical FFS height. The unforced cases indicate that one-parameter correlations (i.e. based on the crossflow vortex core height or boundary-layer displacement thickness) are not sufficient to universally capture the dynamics of these complex flows. Analysis of the forced cases shows that in addition to local parameters (i.e. step height and vortex core height), the FFS influence on transition depends on the stability characteristics of the incoming instability mode.

The fourth chapter presents a detailed quantification of the development of crossflow instability under the influence of a forward-facing step. The results reveal that the

forced monochromatic stationary CF vortices experience an abrupt change in their trajectory as they interact with the step geometry. As the boundary-layer intercepts the step, an increase in the vertical velocity component and an amplification of the cross-flow vortices are observed. Near the step, the vortices reach maximum amplification, while dampening downstream. The smaller FFS cases show a local stabilising effect on the primary stationary mode and its harmonics, while in the higher step cases, transition occurs. The analysis of the temporal velocity fluctuations shows that the velocity fluctuations in the region associated with type I secondary instabilities increase past the FFS edge. Nonetheless, in the shortest FFS cases, these velocity fluctuations eventually decay below the levels of the clean configuration (i.e. without an FFS). This behaviour is linked to a novel transition delay effect for the shortest step height investigated.

The fifth chapter presents a detailed analysis of the step-induced unsteady disturbances and ensuing laminar-turbulent transition. The results reveal that the presence of the FFS at the conditions under study leads to either a critical (i.e. moderate transition advancement) or a supercritical (i.e. transition advancing abruptly to the FFS location) transition behaviour. Analysis of unsteady flow features for the critical cases indicates temporal velocity fluctuations following closely the development of the baseline configuration (i.e. agreeing with the development of secondary instabilities). Consequently, laminar flow breakdown originates from the outer side of the upwelling region of the CF vortices. In contrast, for the supercritical FFS, the laminar breakdown unexpectedly originates from the inner side of the upwelling region. Evidence points to the existence of an unsteady mechanism possibly supported by locally enhanced spanwise-modulated shears and the recirculation region downstream of the FFS edge. This mechanism appears to govern the abrupt tripping of the flow in supercritical step cases.

Finally, the sixth and last chapter presents the conclusions and recommendations of this dissertation. In addition, an outlook section is included which describes a dedicated Swept Transition Experimental Platform (STEP) for the continuation of detailed investigations on surface irregularities at the TU Delft.

SAMENVATTING

De verwachte groei van de commercile luchtvaart in de komende decennia en het maatschappelijke bewustzijn over het verminderen van de effecten van de opwarming van de aarde zorgen voor belangrijke technologische ontwikkelingen die nodig zijn voor emissiereductie in toekomstige transportvliegtuigen. Vanuit het oogpunt van aerodynamica kan een significante verhoging van de vliegtuigefficintie worden bereikt door Laminar Flow Control (LFC) technieken toe te passen.

Het doel van LFC-technieken is om de wrijvingscomponent van de weerstand te verminderen door de laminair-turbulente omslag te vertragen door de stabilisatie van grenslaaginstabiliteiten. Relevant voor hoog-subsonische transportvliegtuigen is de ontwikkeling van Crossflow (CF) instabiliteit, die zich manifesteert als een reeks co-roterende wervels in de grenslaagstroom op gepijlde aerodynamische vlakken.

Van bijzonder belang bij de praktische toepassingen van LFC is de gladheid van het aerodynamische oppervlak. Aangezien tweedimensionale (d.w.z. paneelverbindingen, afdichtingen en naden) en driedimensionale (d.w.z. klinknagels, puin, insectenverontreiniging) onregelmatigheden de grenslaagstroom kunnen verstoren en een voortijdige laminair-turbulente grenslaagomslag kunnen bevorderen, verlagen deze verstoringen de effectiviteit van een LFC-techniek.

Het doel van het onderzoek in dit proefschrift is daarom om experimenteel de invloed te karakteriseren die een tweedimensionale oppervlakte-onregelmatigheid in de vorm van een Forward-Facing Step (FFS) heeft op de ontwikkeling van de CF-instabiliteit en laminair-turbulente grens- laag omslag. Hiertoe is een serie experimentele onderzoeken uitgevoerd in de Lage Turbulentie Tunnel (LTT) van de TU Delft op een vleugel model met een pijlhoek.

Het eerste hoofdstuk presenteert de context, relevantie en doelstellingen van het onderzoek door een uitgebreid overzicht te geven van de ontwikkeling van CF-instabiliteit en de laminair-turbulente grenslaagomslag die wordt benvloed door oppervlakte -onregelmatigheden in de vorm van een stap. Het tweede hoofdstuk introduceert eerst de windtunnelfaciliteit, het gepijlde vleugelmodel en de productie van FFS-oppervlakteonregelmatigheden. Daarnaast wordt een overzicht gegeven van de meettechnieken en numerieke methoden die gebruikt zijn bij het verwerven, verwerken en interpreteren van de experimenten.

Het derde hoofdstuk behandelt de invloed van de FFS op het laminair-turbulente omslagsgedrag onder ongeforceerde (d.w.z. gladde voorrand) en geforceerde omstandigheden (d.w.z. met behulp van discrete ruwheidselementen). De resultaten laten zien hoe belangrijk het is om meerdere parameters in overweging te nemen bij het schatten van de kritische FFS-hoogte. De niet-geforceerde gevallen geven aan dat correlaties met n parameter (d.w.z. gebaseerd op de hoogte van de kern van de dwarsstroom wervel of de dikte van de grenslaagverplaatsing) niet voldoende zijn om de dynamiek van deze complexe stromen universeel vast te leggen. Analyse van de geforceerde gevallen laat zien

dat naast lokale parameters (d.w.z. staphoogte en kern van de dwarsstroom wervel), de FFS-invloed op de omslag afhangt van de stabiliteitskenmerken van de inkomende instabiliteitsmodus.

Het vierde hoofdstuk presenteert een gedetailleerde kwantificering van de ontwikkeling van crossflow-instabiliteit onder invloed van een voorwaarts gerichte stap. De resultaten laten zien dat de geforceerde monochromatische stationaire CF-wervels een abrupte verandering in hun traject ervaren als ze interageren met de stapgeometrie. Wanneer de grenslaag de stap nadert, wordt een toename van de verticale snelheidscomponent en een versterking van de dwarsstroomwervels waargenomen. In de buurt van de stap bereiken de wervels maximale versterking, terwijl ze stroomafwaarts worden gedempt. De kleinere FFS-gevallen vertonen een lokaal stabiliserend effect op de primaire stationaire modus en zijn harmonischen, terwijl in de gevallen van een grotere staphoogte omslag optreedt. De analyse van de tijdsafhankelijke snelheidsfluctuaties laat zien dat de snelheidsfluctuaties in het gebied geassocieerd met type I secundaire instabiliteiten, toenemen voorbij de FFS-rand. Desalniettemin, in de laagste FFS-gevallen, vervallen deze snelheidsfluctuaties uiteindelijk onder de onverstoorde configuratie (d.w.z. zonder een FFS) niveaus. Dit gedrag is gekoppeld aan een nieuw vertragingseffect voor omslag voor de laagste onderzochte staphoogte.

Het vijfde hoofdstuk presenteert een gedetailleerde analyse van de stap-genduceerde onstabiele verstoringen en de daaruit voortvloeiende laminair-turbulente omslag. De resultaten laten zien dat de aanwezigheid van de FFS onder de onderzochte omstandigheden leidt tot ofwel een kritisch (d.w.z. geleidelijke omslag) of een superkritisch omslagsgedrag (d.w.z. een omslag die abrupt plaatsvindt richting de FFS-locatie). Analyse van de onstabiele stromingskenmerken voor de kritieke gevallen laten tijdsafhankelijke snelheidsfluctuaties zien die sterk lijken op het verloop van de basisconfiguratie (d.w.z. in lijn liggen met de ontwikkeling van secundaire instabiliteiten). Derhalve vindt de afbraak van de laminaire stroming zijn oorsprong aan de buitenzijde van het oplopende gebied van de CF-wervels. Daarentegen is voor de superkritische FFS de laminaire afbraak afkomstig van de binnenkant van het oplopende gebied, wat een onverwachte uitkomst is. Bewijs wijst op het bestaan van een onstabiel mechanisme dat mogelijk wordt ondersteund door lokaal verbeterde spanwijdte-gemoduleerde schuiving en het recirculatiegebied stroomafwaarts van de FFS-rand. Dit mechanisme lijkt de abrupte omslag van de stroom in superkritische stapgevallen te regelen.

Het zesde en laatste hoofdstuk presenteert de conclusies, aanbevelingen en een vooruitzicht die specifiek een Swept Transition Experimental Platform (STEP) beschrijft voor de voortzetting van gedetailleerd onderzoek naar oppervlakte-onregelmatigheden aan de TU Delft.

Part I

Background

1

Introduction

"But nature did not deem her business to make the discovery of her laws easy for us."

– In letter from Albert Einstein to Erwin Freundlich, September 1911‡–

This chapter sets the context, relevance and objectives of the research encompassed in this doctoral dissertation by providing a comprehensive review on the development of crossflow instability and the laminar–turbulent boundary-layer transition influenced by surface irregularities.

Parts of this chapter are published in:

- Rius-Vidales, A.F. & Kotsonis, M. 2020 Influence of a forward facing step surface irregularity on swept wing transition. AIAA Journal **58(12)**, 5243-5253.
- Rius-Vidales, A.F. & Kotsonis, M. 2021 Impact of a forward-facing step on the development of crossflow instability. Journal of Fluid Mechanics **924**, A34.
- Rius-Vidales, A.F. & Kotsonis, 2022 M. Unsteady interaction of crossflow instability with a forward-facing step. Journal of fluid Mechanics, **939**, A19.

‡Beck, A., & Howard, D. (1995). The collected papers of Albert Einstein: The Swiss years correspondence 1902-1914 Volume 5 (English Translation), Princeton University Press, pp. 201-202.

1

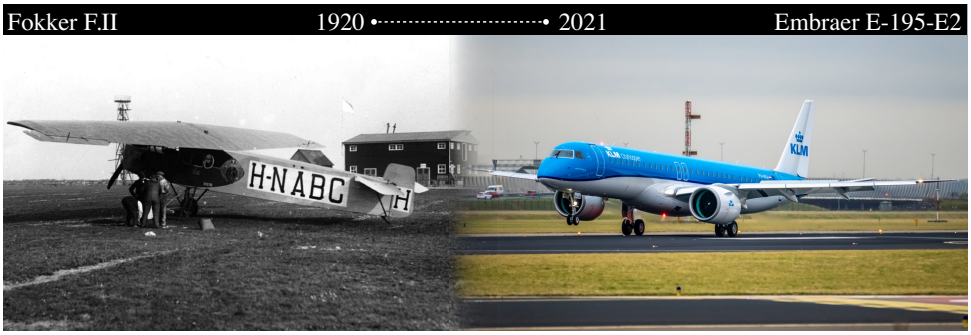

Figure 1.1: Evolution of KLM Royal Dutch Airlines over a century at Schiphol Airport. Left: First KLM passenger aircraft a 4-seater Fokker F.II (image obtained from [5]), Right: Latest aircraft in the KLM fleet, a 132-seater Embraer E-195-E2 (image obtained from [6]).

1.1. MOTIVATION

In over a century, civil aviation has evolved to become an important contributor of the world economy[1]. The foundations of commercial aviation date back to 1919 when single or twin-engine First World War (WWI) bombers were re-purposed for civilian transportation [2].

On the 7 of October 1919 a group of intrepid investors founded an airline under the name *Koninlijke Luchtvaart Maatschappij voor Nederland en Kolonien* [see 3], later to become the renowned KLM (*Koninklijke Luchtvaart Maatschappij*) airline. KLM commercial operations began officially on the 17^{th} of May 1920 with a flight from London to Amsterdam using a leased De Havilland DH-16 WWI bomber [4]. At the same time, KLM presented its first dedicated passenger aircraft, a 4-seater Fokker F.II [5], a picture of which is shown on the left of figure 1.1. During its first year of operations, KLM completed 584 flights transporting around 345 passengers and 22 tons of freight using four aircraft [5].

Nowadays, the latest model in KLM's fleet (Embraer E195-E2 shown on the right of figure 1.1) is capable of transporting 132 passengers per flight. One hundred years after its foundation, KLM transported over 35 million passengers and 599,320 tons of freight with a fleet of 229 aircraft [7]. Technological developments in the aviation industry transformed this extraordinary method of transportation into an ordinary one. To illustrate this, figure 1.2(a) shows the exponential growth of the historic passenger traffic measured in Revenue Passenger Kilometer (RPK)[2] between 1960-2017 [8]. Forecasts by Airbus in 2019 [see 9] and Boeing in 2021[see 10] indicate that the worldwide commercial aircraft fleet would need to nearly double in the following decades to cope with this upward trend in demand.

The unfolding COVID-19 pandemic has been particularly challenging for the commercial aviation industry. In 2020 only 1.8 billion passengers travelled by air around the

[1] In 2019, the commercial aviation direct economic activity accounted for 1.1% of the global GDP [1].
[2] The RPK is an industry metric of the volume of passenger traffic.

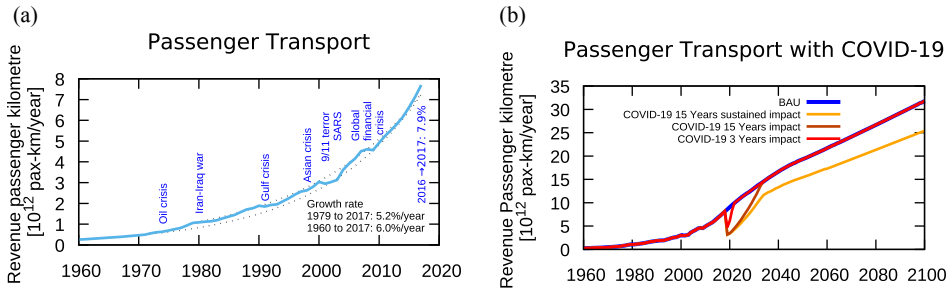

Figure 1.2: Volume of passenger traffic measured in industry metric Revenue Passenger Kilometer RPK. (a) Historical trends through major economic crisis (figure reproduced from [8]) (b) Estimated impact of COVID-19 pandemic based on different recovery scenarios (figure reproduced from [8]).

world. This figure contrasts heavily with the 4.5 billion passenger a year earlier in 2019 [11, 12]. This pandemic qualifies as the most severe crisis for the aviation industry since the end of the Second World War (WWII) in 1945 [11]. Nonetheless, its effect is not expected to influence the long-term demand considerably since estimates of the annual RPK show only a temporary decay as shown by Grewe *et al.* [8] and reproduced in figure 1.2(b).

The projected market growth of the commercial aviation industry clashes with the reduction of emissions required to limit the effects of global warming in the near future. The emission of carbon dioxide (CO2), nitrous oxide (NOX) and contrail cirrus formation are the main contributions of the aviation industry to the ongoing climate change [13]. Although the aviation industry has considerably increased its efficiency (i.e. reduced gCO2/RPK), the expansion of the market in the last forty years has resulted in a nearly monotonic increase in CO2 emissions [13]. In 2018, the civil aviation industry accounted for 2.4% of the total anthropogenic CO2 emissions [13]. Environmental concerns regarding the industry footprint on climate change led recently to the development of the carbon offsetting and reduction scheme (CORSIA) by the International Civil Aviation Organization [14]. With the enforcement of this resolution by 2027, and the rising social awareness on global warming, the aviation industry needs more energy-efficient aircraft.

Increasing the performance of high-subsonic transport aircraft by reducing the total drag is an active area of investigation. Figure 1.3 shows a typical breakdown of the total drag of a Boeing 737 commercial airliner in cruise conditions. A detailed description of each component contributing to the total drag can be found in the classical textbook by Torenbeek [15, Ch.4].

Figure 1.3 shows that of special consideration to the aerodynamic performance of the aircraft is the skin-friction drag component since it accounts for over half of the total drag budget [see 16–19]. Exploiting the fact that at comparable Reynolds numbers a laminar boundary-layer will produce significantly less skin-friction drag than a turbulent boundary-layer, an attractive solution to reduce this drag component is to apply Laminar Flow Control (LFC) techniques to stabilise the boundary-layer flow and extend

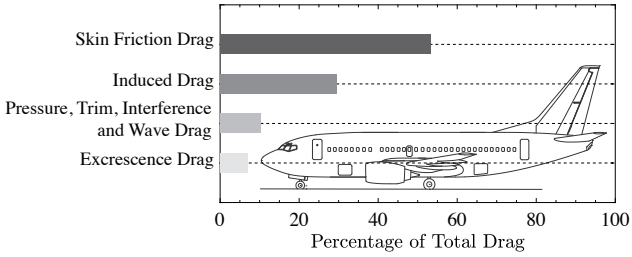

Figure 1.3: Drag component breakdown typical of a Boeing 737 during cruise (M = 0.785 at 12km), showing that the major contribution to the total drag is provided by the skin-friction. The data has been obtained from [20]. The background illustration from a 737-500 has been re-adapted from [21]

the regions of laminar flow on the outer surface of the aircraft. Estimates by Schrauf [17] indicate that a typical transport aircraft could benefit from a 16% total drag reduction if the boundary-layer flow on the wing, horizontal tail, fin, and nacelles remains laminar for over 40% of their surface. For an in-depth historical review of LFC techniques, the reader is referred to Joslin [16], while more recent updates can be found in Arnal and Archambaud [18] and Saric *et al.* [19].

The idea of Laminar Flow Control pivots on the stabilisation of the boundary-layer flow against the growth of various instabilities such as Tollmien-Schlichting (TS) waves, Attachment-line instability and contamination, Görtler vortices and Crossflow (CF) vortices. The growth of any of these instabilities leads to an anticipation of the laminar–turbulent transition. A comprehensive review of available control strategies for each of these instabilities is provided by Saric *et al.* [19].

Despite the promising technological advancements in LFC techniques, their performance is highly dependent on the smoothness of the aerodynamic surface, which in practical applications is far from ideal. Manufacturing requirements and operational conditions result in two-dimensional (i.e. panel joints, seals and seams) and three-dimensional (i.e. rivets, fowl and insect strikes) surface irregularities. These irregularities can reduce the effectiveness of LFC techniques by perturbing the boundary-layer flow and promoting a premature laminar–turbulent boundary-layer transition. Consequently, understanding the impact of these surface features on boundary-layer transition is of paramount importance for the practical application of LFC techniques and the accuracy of transition prediction models required for the reliable design and optimization of laminar flow components.

1.2. FUNDAMENTALS OF SWEPT WING TRANSITION

Technological developments during WWII revolutionized the aviation industry during the post-war period. One of the most significant inventions of this era is the jet engine. The additional power offered by this engine resulted in faster aircrafts capable of reaching Mach numbers closer to unity ($M = U_\infty / a_\infty$). As the aircraft speed approaches

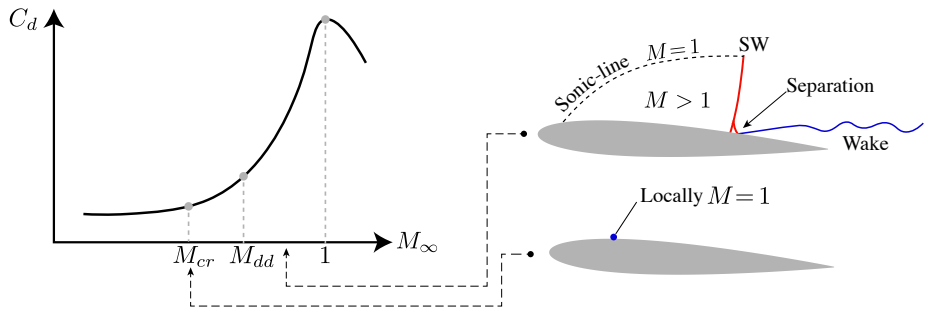

Figure 1.4: Notional schematic illustrating the change in drag coefficient (C_d) with increasing Mach number and expected changes in the flowfield, based on [22].

the one of sound[3] (a_∞), a strong increase in wave drag occurs. Consequently, early attempts to fly at speeds within the transonic regime (i.e. $0.8 < M_\infty < 1.2$) failed. Figure 1.4 schematically illustrates the flow conditions and the associated increase in wave drag (i.e. drag-divergence) as M_∞ approaches unity. The boundary-layer flow in high-subsonic aircraft can locally achieve supersonic conditions ($M > 1$). The free-stream Mach number (M_∞) at which this first occurs is defined as the critical Mach number (M_{cr}, see figure 1.4). Beyond M_{cr}, the regions of supersonic flow lead to the onset of shockwaves (SW), which induce flow separation increasing the wave drag strongly. The Mach number at which this behaviour occurs is known as the Mach Divergence Drag number (M_{dd}).

Henceforth, to enhance the aerodynamic performance of high-subsonic transport aircraft, it is desirable to increase the M_{cr} to postpone the drag-divergence. Common wing design techniques to increase M_{cr} involve reducing the airfoil thickness, using supercritical airfoils[4], applying area ruling[5] and using swept wings.

The potential of swept wings to increase the critical Mach number was described by Busemann in the Volta Conference in 1935 [22]. During the WWII period, several investigations into the development of swept wings were conducted in Germany. A comprehensive review of these first efforts is compiled by Hamel [24].

Anderson [22] and Vos and Farokhi [25] explain that the swept wing advantage over a non-swept one lies on the fact that by applying sweep, the thickness to chord ratio of the airfoil shape in the streamwise direction is virtually reduced, given that the airfoil thickness remains constant but the streamwise chord increases ($c_X = c_x / \cos\Lambda$). This, in turn, leads to a milder pressure coefficient and an increase in the critical Mach number with respect to the non-swept wing. Nevertheless, the application of this simple and revolutionary idea leads to a complicated three-dimensional boundary-layer. This boundary-layer flow is the object of study in this doctoral dissertation and is of particular importance to modern high-subsonic transport aircraft, as their wings, horizontal tails, and fins are swept.

[3] The speed of sound is calculated as: $a_\infty = \sqrt{\gamma R T_K}$, at sea-level and 15°C is 340.6m sec^{-1}

[4] Airfoil shape designed to avoid a strong shockwave formation, see Bertin and Cummings [23, Sec.9.3.2].

[5] Aircraft design strategy to reduce transonic drag, see Bertin and Cummings [23, Sec.9.4.1].

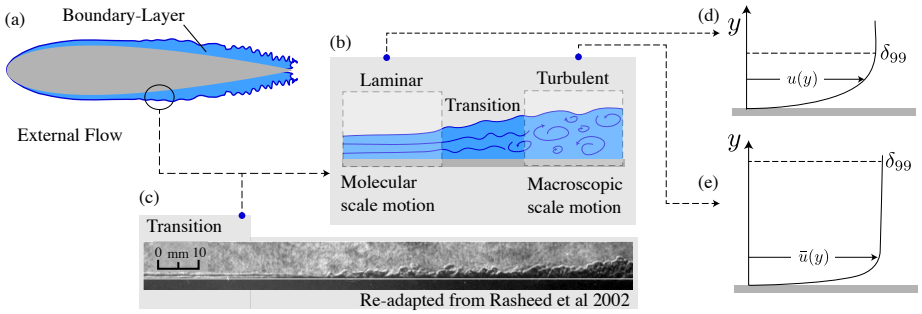

Figure 1.5: General schematic of laminar–turbulent boundary-layer transition: (a) Boundary-layer concept. (b) Notional depiction of transition process. (c) Schlieren shadowgraphy visualization of the transition process re-adapted from [26]. (d,e) Notional laminar and turbulent boundary-layer velocity profiles.

1.2.1. BOUNDARY-LAYER THEORY

The boundary-layer concept is a cornerstone in modern fluid mechanics analysis. Since its formal introduction by Prandtl [27][6], the study of the flow dynamics and stability in this thin fluid region has been of particular interest. Henceforth, a vast number of numerical and experimental investigations dedicated to this topic have been conducted as historically described by Tani [29] and found in the classical textbook by Schlichting and Gersten [30].

The brilliance behind Prandtl's concept of a "frictional layer" is to consider that for practical applications in low viscosity fluids (e.g. air and water), the role of the viscous forces in the fluid dynamics is restricted to a thin region termed the boundary-layer. Hence, the viscous forces can be neglected outside this region (i.e. external flow) and the flow is considered inviscid. To illustrate these regions, figure 1.5(a) depicts a conceptual diagram of the two-dimensional flow around an airfoil. In this case, to satisfy the no-slip boundary condition, a velocity deficit occurs in the fluid region near the airfoil's surface. The interface between the boundary-layer and the external flow region is determined at each streamwise position as the wall-normal height (δ_{99}) at which $u(y) = 0.99u_e$, with u_e being the flow velocity away from the surface. Even though the spatial extent of the boundary-layer region is somewhat limited, its flow dynamics strongly impact the airfoil's aerodynamic performance (e.g. skin-friction drag and flow separation).

Typically, on an airfoil, the boundary-layer originates in a laminar flow state from the stagnation point. In the laminar portion of the boundary-layer, the transfer of momentum occurs at a molecular scale driven by the viscous shear-stress of adjacent fluid layers [23], as depicted in figure 1.5(b). As the boundary-layer flow develops along the surface of the airfoil, environmental conditions (e.g. freestream turbulence, acoustic forcing and surface roughness) develop disturbances that can amplify inside the boundary-layer region. A detailed review of this process, known as receptivity, is provided by Saric *et al.* [31]. The unstable growth of these disturbances can lead to the transition of the boundary-layer from a laminar to a turbulent flow state following different paths (i.e. A-E) as described on the "roadmap" by Morkovin [32] presented in figure 1.6(a). A detailed

[6] A commented English translation of this work is presented in Ackroyd *et al.* [28]

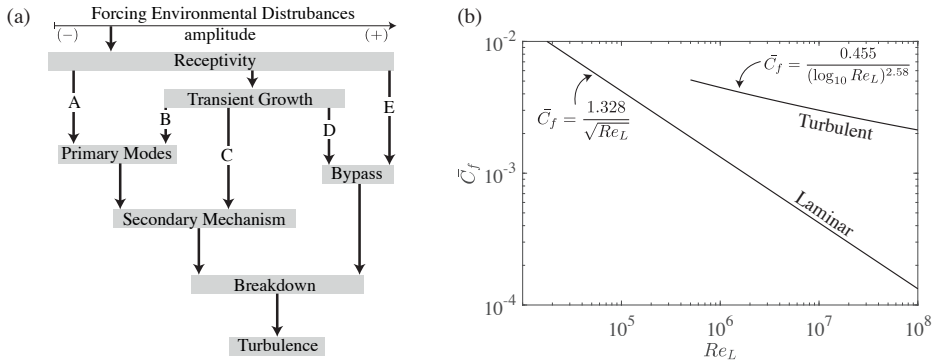

Figure 1.6: (a) Roadmap to turbulence through several path A to E, figure based on [31, 32] (b) Comparison of the estimated total skin-friction drag coefficient for a laminar and turbulent boundary-layer on a flat-plate with zero-pressure gradient, figure based on [23]

description of this diagram can be found in Saric *et al.* [31] and Reed and Saric [33].

Once the boundary-layer becomes turbulent, the transfer of momentum occurs at a macroscopic scale through eddies of different sizes [23], as depicted in figure 1.5(b). The laminar–turbulent boundary-layer transition occurs over a finite extent as captured on the schlieren shadowgraphy visualizations by Rasheed *et al.* [26], shown in figure 1.5(c).

Figure 1.5(d,e) depicts notional laminar and turbulent boundary-layer velocity profiles. The macroscopic momentum transfer in the turbulent boundary-layer increases the fluid velocity near the wall. This results in higher wall-shear stress ($\tau = \mu(\partial u/\partial y|_{y=0})$) and an increase in the local skin-friction drag coefficient ($C_f = \tau/(0.5\rho u_e^2)$) with respect to the laminar one.

Figure 1.6(b) shows a comparison of the total skin friction drag coefficient (i.e. integrated local skin friction) in a laminar and turbulent boundary-layer on a flat plate at zero-pressure gradient. The results illustrate that a considerable increase in skin-friction drag occurs when the boundary-layer becomes turbulent. Consequentially, the development of control techniques to maintain and extend the laminar flow region is critical to decrease future aircraft power consumption.

1.2.2. BOUNDARY-LAYER DEVELOPMENT AND INSTABILITIES

The boundary-layer flow in a swept wing develops in a three-dimensional manner. The free-stream velocity (U_∞) is decomposed into a streamwise (u_∞, i.e. normal to the leading edge) and spanwise (w_∞, i.e. parallel to the leading edge) velocity component, as shown on the infinite swept wing schematic in figure 1.7(a). The infinite swept wing assumption implies that the wing has no taper or twist and the airfoil shape is constant along an "infinite" span (i.e. tip and root effects neglected). Henceforth, in configurations on which this assumption is applicable, the boundary-layer analysis is simplified by considering that the spanwise velocity (w_e) external to the boundary-layer is constant and equal to the freestream spanwise velocity (w_∞). The simplified formulation of the boundary-layer equations is known as 2.5D and will be discussed in more detail in §2.3.

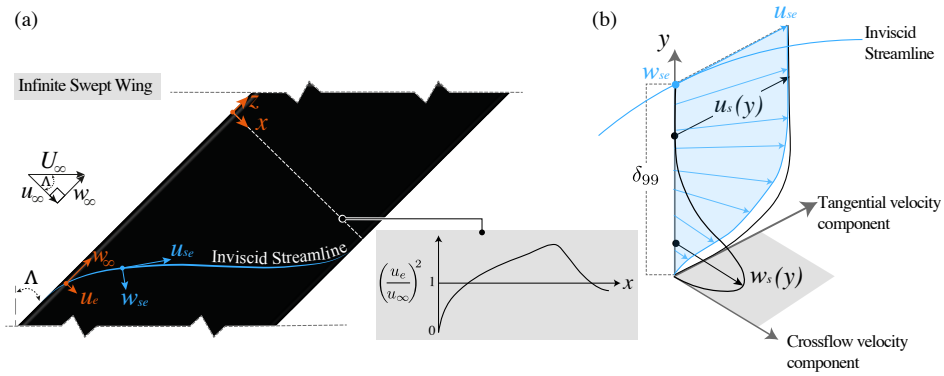

Figure 1.7: Schematic of the boundary-layer in an infinite swept wing: (a) Development of inviscid streamline on an infinite swept wing. (b) Three-dimensional boundary-layer velocity profile. Figure based on [34] and [35]

In the limiting case of a non-swept wing (i.e. $\Lambda = 0°$), the flow stagnates near the leading edge (i.e. $u_e = 0$ and $w_e = 0$). For a swept wing (i.e. $\Lambda > 0°$), in contrast, the flow near the leading edge forms an attachment line due to the spanwise velocity component being $w_e = w_\infty$. In an infinite swept wing the spanwise velocity component w_∞ is constant and has the direction as shown in the schematic on figure 1.7(a). Considering the velocity distribution shown on the inset on figure 1.7(a), the streamwise external velocity (u_e) will progressively increase until reaching a maximum at the point of minimum pressure ($Cp_{\min}$) curving the inviscid streamline, as schematically depicted. In the external flow region, the centripetal force due to the inviscid streamline curvature is balanced by the pressure forces across the streamline [see 34, 35]. Nevertheless, the momentum deficit inside the boundary-layer breaks this balance of forces and leads to a secondary flow known as crossflow [see 34, 35].

A direct consequence of this secondary flow is the generation of a three-dimensional boundary-layer velocity profile (depicted in figure 1.7b), where an inflectional instability, known as crossflow (CF) instability originates [34–36]. Figure 1.7(b) shows the decomposition of this three-dimensional velocity profile into a velocity component tangent (u_s) and normal (w_s) to the inviscid streamline. The latter is the well known crossflow component.

This three-dimensional boundary-layer flow is susceptible to four different types of instabilities, depicted in figure 1.8 [see 34–37]: (a) Attachment line instability or contamination; (b) A centrifugal instability driven by concave surface curvature and manifesting as counter-rotating vortices (i.e. Görtler vortices); (c) A streamwise instability driven by streamwise adverse pressure gradients and manifesting as Tollmien-Schlichting waves; (d) Crossflow instability, which manifests as co-rotating vortices (i.e. CF vortices). For completeness, a summary of each instability is presented next.

ATTACHMENT LINE

As discussed previously, in the limiting case of a non-swept wing (i.e. $\Lambda = 0°$) a stagnation line divides the flow between the pressure and suction side of the wing. Instead,

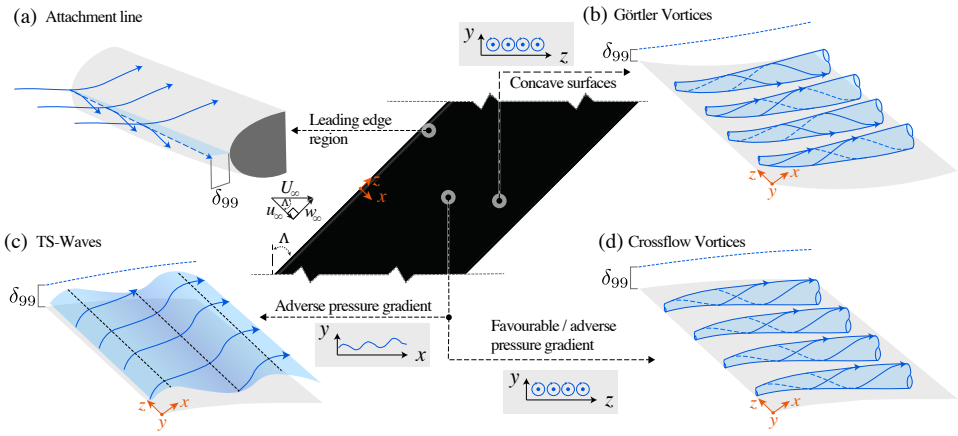

Figure 1.8: Schematic of different boundary-layer instabilities which can develop in a swept wing: (a) Attachment line instability or contamination. (b) Görtler instability. (c) Tollmien-Schlichting waves instability. (d) Crossflow instability

in swept wings, an attachment line driven by the spanwise velocity component (w_∞) separates the flow on each side of the wing, as depicted in the notional schematic in figure 1.8(a). Early experiments on swept wings and cylinders showed that under certain conditions, premature laminar–turbulent boundary-layer transition can originate from the attachment line [e.g. 38–40]. Based on the flow conditions at the root of the wing, two different regimes have been observed and referred to as leading-edge contamination and attachment-line instability [see 41, 42].

A leading-edge contamination occurs when disturbances from a turbulent boundary-layer (i.e. wing-body junction, pylons etc...) propagate along the attachment-line and trip the boundary-layer on the swept surface [18, 37, 41, 42]. This phenomenon was observed and analyzed in more detail during the flight program of the X-21 LFC demonstration aircraft [38]. Subsequent experimental studies showed that the leading edge geometry (i.e. its radius of curvature) plays a major role in determining the stability of the attachment-line boundary-layer [e.g. 39, 40, 43]. Henceforth, a simple criterion ($\bar{R} = \sqrt{(U_\infty R \sin\Lambda \tan\Lambda)/(\nu_\infty + e\nu_\infty)} \leq 247$) based on experimental observations is commonly used to determine the conditions at which leading-edge contamination can be expected. As indicated by Reed and Saric [41] the calculation of $\bar{R}$ involves calculating the surface radius (R) normal to the leading-edge and replacing the airfoil geometry by an equivalent ellipse[7] to calculate its thickness to chord ratio (e).

In practical applications on a commercial transport aircraft, large values of $\bar{R}$ often occur [42]. Gaster [44] presented the well-known "Gaster Bump" device to mitigate this effect. The idea behind this device is to produce a stagnation point using a bump-like fairing at the wing root, to avoid the propagation of the wing-body junction boundary-layer towards the swept wing leading edge [41, 42]. By employing this device, an increase in $\bar{R}$ to values between 350 to 400 has been reported [e.g. 42, 45]. More recently, Fiore *et*

[7] Following Vos and Farokhi [25, Ch.8] the equivalent ellipse thickness to chord ratio is: $e = (2r/c_x)/(t_{\max}/c_x)$.

al. [42] studied the use of higher-efficiency chevron-shaped anti-contamination devices to extend further this limit for application in high-subsonic transport aircraft.

If contamination is avoided, then a laminar boundary-layer will propagate along the leading edge of the swept wing. In the backward swept configuration (i.e. $\Lambda > 0°$), the direction of propagation will be from root towards the tip, as shown in figure 1.8(a). As this laminar boundary-layer propagates along the span, it can destabilize, and the laminar–turbulent transition can occur near the leading-edge of the swept wing [41, 42]. Henceforth, the development of instabilities in this boundary-layer is an ongoing area of investigation. Based on the current knowledge, an acceptable design criterion at which the boundary-layer has been observed to remain laminar at the leading-edge is given when $\bar{R} \leq 583$ [see 41].

GÖRTLER VORTICES

Early experiments by Liepmann [46] on the boundary-layer flow over a concave surface revealed an upstream shift of the transition front when compared to a flat surface case (i.e. no curvature). Liepmann [46] attributed the reduction in the critical Reynolds number to the theoretical work by Görtler [47]. Görtler suggested that a boundary-layer developing over a concave surface can experience a centrifugal instability in the form of counter-rotating streamwise vortices (i.e. Görtler vortices). Subsequent experimental investigations [e.g. 48, 49] captured the development of these vortices under different conditions in boundary-layer flows.

The origin of the Görtler instability is traced to the imbalance of pressure and centrifugal forces in the boundary-layer flow [50]. This centrifugal instability has been observed in boundary-layers developing over concave surfaces or at locations where there is a considerable streamline curvature [50, 51]. Floryan [49] and Saric [52] provide a detailed review of the principal research efforts in the study of this instability.

As depicted in figure 1.8(b), the Görtler vortices are streamwise oriented spanwise periodic structures [52]. The counter-rotating nature (inset in figure 1.8b) of the vortices results in a strong mean-flow distortion due to transfer of high momentum fluid towards the wall (i.e. downwelling) and low-momentum fluid away from it (i.e. upwelling)[49, 52]. This momentum exchange leads to the formation of a characteristic mushroom-shaped pattern in the downwelling region.

The boundary-layer transition to turbulence is dictated by the amplitude saturation of the Görtler vortices and the development of secondary instabilities driven by the spanwise and wall-normal velocity gradients [52]. Two main types of secondary instability modes have been reported in different numerical and experimental investigations [e.g. 53–56]. The first type, known as "sinuous mode" (i.e. meandering), is an oscillation driven by the spanwise velocity gradients. The second type, known as "varicose mode", has been related to the development of horse-shoe vortices driven by the wall-normal gradients [49, 52]. Detailed numerical studies by Li and Malik [54] have shown that the spanwise wavelength of the vortices plays an important role in determining the dominance of one mode over the other (i.e. short-wavelength vortices lead to stronger spanwise gradients and dominance of the sinuous mode).

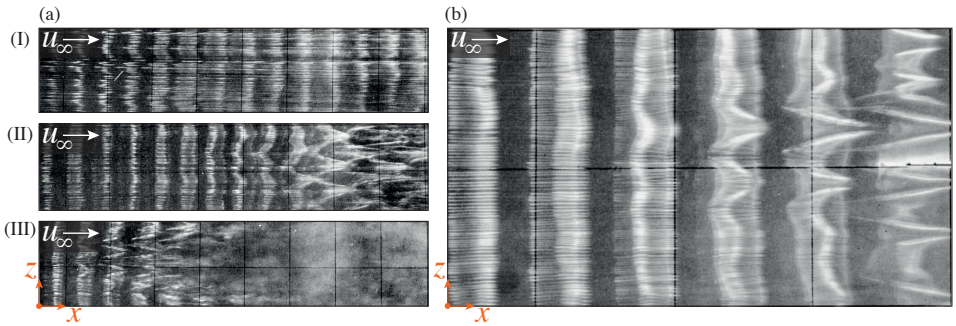

Figure 1.9: Flow visualizations (flow from left to right) re-adapted from Saric [57] of the boundary-layer flow showing the development of Tollmien-Schlichting Waves using a smoke wire technique. The experiments are conducted at $u_\infty = 6.6\,\mathrm{m\,s^{-1}}$ and the TS-waves are forced at a frequency of 39Hz using a vibrating ribbon the reference amplitude is taken at branch II: (Ia) TS-waves at an amplitude $u' = 0.2\%u_\infty$. (IIa) H-type breakdown of TS-waves at an amplitude $u' = 0.4\%u_\infty$. (IIIa) K-type breakdown of TS-waves at an amplitude $u' = 1\%u_\infty$ (b) Close-up view of the K-type non-staggered peak-valley pattern

TOLLMIEN-SCHLICHTING WAVES

The Tollmien-Schlichting (TS) waves are a well-known viscous instability. Its name has been attributed after Tollmien [58] and Schlichting [59], whose pioneering efforts led to the successful determination of the stability of the Blasius boundary-layer flow (i.e. two-dimensional, zero-pressure gradient flow). The TS instability manifests as a travelling wave that propagates in the boundary-layer flow towards the trailing edge, as depicted schematically in figure 1.8(c) and observed in the flow visualization by Saric [57] re-produced in figure 1.9(Ia). Herbert [60] and Kachanov [61] provide detailed reviews on the study of this instability.

Schubauer and Skramstad [62] experimentally proved the existence of the instability and showed its characteristic double-lobed disturbance profile. More recently, Ross *et al.* [63] revised and extended these experiments to different free-stream conditions. At small amplitudes (i.e. $\approx 0.1\%u_\infty$), the behaviour of the TS-Waves follows closely the one predicted by linear stability theory [64]. Henceforth, the amplitude of the TS-Waves decays upstream of branch-I (i.e. stability diagram neutral curve), amplifies from branch-I until branch-II and decays again after branch-II [50, 64]. In contrast, at higher amplitudes, the TS-Waves nonlinearly saturate downstream of branch-I [50].

Detailed experiments by Klebanoff *et al.* [65] showed that the TS-Waves undergo a spanwise modulation when reaching large amplitudes [64], as shown in figure 1.9(b). Moreover, this amplitude saturation signals the development of secondary instabilities, which rapidly amplify and lead to the breakdown of the laminar flow and transition to turbulence as depicted in figure 1.9(IIIa). Different numerical and experimental studies on the development of TS-waves secondary instabilities have categorized the breakdown of the boundary-layer flow into a K-type or H-type (also known as N-type) [see 50, 64].

In either K or H type breakdown, the spanwise modulation of the TS-waves creates strong shear layers from which a series of Λ vortices originate [50, 64]. The difference between the types of breakdown lies in the topological arrangement of the Λ vortices, and their dominance is dependent on the TS-Waves' initial amplitude [50]. In the K-type

(high initial amplitude), the Λ vortices are aligned, while in the H-type (lower initial amplitude), they are staggered along the span direction [50, 64]. Both types of breakdown are shown in figure 1.9.

Research into Laminar Flow Control has shown the dominance of TS-waves in transition on swept wings, featuring a moderate sweep angle between $0° \leq \Lambda \leq 25°$ [see 16]. Henceforth, control techniques in these cases entail tailoring the pressure distribution to reduce the adverse pressure gradient regions, which enhance the growth of TS-waves [16]. Unfortunately, strong adverse pressure gradient regions occur in swept wings beyond the pressure minima point as the pressure recovers. The effect of pressure changeover on the TS-waves amplification and their interaction with CF instability has been studied by Wassermann and Kloker [66].

CROSSFLOW INSTABILITY

As described previously, the amplification of the attachment-line, streamwise and centrifugal instabilities are suppressed by avoiding a large leading-edge radius, strong regions of adverse pressure gradient and concave surfaces [19]. Henceforth, the development and breakdown of CF vortices has been a long-standing topic of interest as it remains the dominant instability in the laminar–turbulent transition in swept wings.

The origin of the inflectional CF instability is related to the development of a three-dimensional boundary-layer (see notional velocity profile in figure 1.7b). In contrast to TS-waves cases, a favourable pressure gradient, such as the one prescribed by a natural laminar flow (NLF) airfoil, leads to a destabilizing effect. The instability manifests in the boundary-layer flow as a series of co-rotating vortices, which develop in a direction closely aligned with the inviscid streamline direction as depicted in figure. 1.8(d) [see 34, 35, 37].

Early experiments revealed the development of the CF instability and its implication on the laminar–turbulent boundary-layer transition in swept configurations [see 67, 68]. In particular, Anscombe and Illingsworth [68] observed a considerable reduction in the extension of laminar flow with increasing sweep angle and the formation of streaky surface patterns on transition measurement using sublimation techniques. Since then, a considerable number of investigations have been conducted to understand and control the CF instability. Detailed reviews of these efforts are provided in [34, 35, 37, 69–71]. Both experimental and numerical studies reveal that the CF vortices can remain stationary or travel along the span. The dominance of either stationary or travelling CF modes in the laminar–turbulent transition is dependent on receptivity mechanisms related to the surface roughness of the wing and disturbances outside the boundary-layer flow.

In experiments, valuable information on the dominance of either type of primary CF instability mode in the transition process can be retrieved using flow visualization techniques. The appearance of a "jagged" or "sawtooth" laminar–turbulent transition front pattern (figure 1.10Ia,IIa-IIb) has been traced to the breakdown process typical of stationary CF vortices [see 34, 35, 72, 73]. As the stationary CF vortices saturate, a rapidly growing secondary instability leads to their local breakdown characterized by contiguous turbulent wedges forming along the span. In contrast, when the transition is dominated by travelling CF vortices, a more smooth (i.e. non wedged) time-averaged transition front is observed due to the movement of CF vortices along the span.

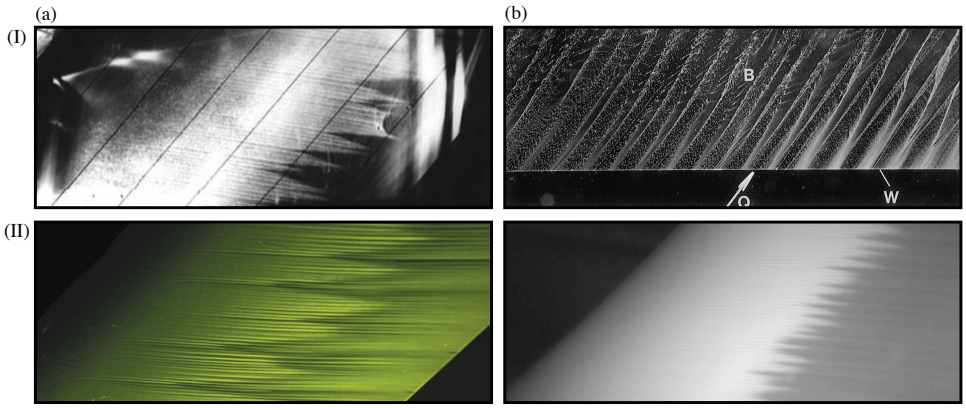

Figure 1.10: Experimental visualization of jagged transition fronts (Ia,IIa-IIb, flow from left to right) and stationary CF vortices (Ib, flow from bottom to top) : (Ia) Naphthalene identification of jagged transition front and surface streaky pattern, re-adapted from [74]. (Ib) Hydrogen bubble visualization in water tank, re-adapted from [34]. (IIa) Oil flow visualization of jagged transition front and surface streaky pattern, re-adapted from [75]. (IIb) Infrared thermography visualization of jagged transition front and surface streaky pattern, re-adapted from [76]

Receptivity Considerable numerical and experimental efforts have been devoted to study the receptivity mechanisms in swept wings [e.g. 34, 73, 77–82]. When considering the study of environmental disturbances, a distinction is made between acoustic (i.e. long wavelength) and vortical (i.e. short wavelength) disturbances [34]. Detailed experiments conducted by Deyhle and Bippes [77] showed that the receptivity of CF instability to acoustic disturbances is of minor importance when compared to the vortical ones (i.e. free-stream turbulence).

Bippes [34] reported the dominance of the travelling modes over the stationary ones in the laminar–turbulent transition at high turbulence levels (i.e. $Tu > 0.15\%$). Nevertheless, White *et al.* [83] found that the surface roughness of the model plays an equally important role in the receptivity process. The results indicate that the turbulence intensity level is not sufficient to determine the dominance of travelling modes over stationary ones. Instead, it is the interaction of the free-stream fluctuations with surface roughness which leads to the growth of the travelling modes at high levels of free-stream turbulence.

Relevant to the low-turbulence level in-flight environment [84] is the study of stationary CF vortices conditioned by the wing surface roughness. Müller and Bippes [85] [see also 34] verified that the initial conditions of the stationary CF modes are related to the surface roughness of the model. Subsequently, Deyhle and Bippes [77] and Reibert *et al.* [86] reported the use of discrete roughness elements (DREs) to force monochromatic CF vortices for the experimental study of stationary CF instability. Since then, the use of DREs to condition the stationary CF vortices spanwise wavelength and their initial amplitude has been widely adopted in experimental studies.

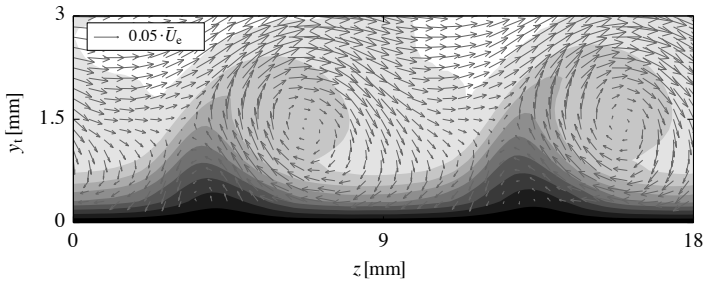

Figure 1.11: Contours of time-averaged streamwise velocity along a constant plane in the span direction (i.e. along z), 10 levels $\bar{u}/\bar{u}_e$ from 0 to 1 and vectors $\sqrt{\bar{v}^2 + \bar{w}^2}/\bar{u}_e$, showing the structure of the CF vortices developing on the boundary layer flow on a 45 degree swept wing model, reproduced from [71]

Primary Instability The stationary CF vortices distort the boundary-layer flow by transferring high-momentum fluid from the boundary-layer edge towards the wall (downwelling) and low-momentum fluid from the wall towards the boundary-layer edge (upwelling), as depicted in figure 1.11. Consequently, alternating low and high shear regions form near the wall and give rise to the spanwise periodic streaky surface sublimation patterns, reported by Anscombe and Illingsworth [68] and commonly observed in experimental studies as shown in figure 1.10.

As the stationary CF vortices develop in the boundary-layer, the transfer of momentum leads to a nonlinear (i.e. interaction between disturbance and baseflow) distortion of the boundary-layer flow and amplitude saturation [34]. Interestingly, Bippes [34] and Lerche [87] report that the interaction of travelling CF modes can nonlinearly reduce the growth of stationary ones. The extended streamwise distance between the location of amplitude saturation of the stationary CF vortices and the onset of the laminar–turbulent transition poses a challenge to the application of traditional transition prediction methods based on linear stability (i.e. OS, LPSE)[see 34–36].

Secondary Instability The nonlinear amplitude saturation of the stationary CF vortices is characterized by a highly modulated boundary-layer flow with strong wall-normal and spanwise velocity gradients and inflectional velocity profiles. From this distorted flowfield, secondary high-frequency instabilities originate [34–36]. The overall consensus is that the secondary CF instability rapidly amplifies leading to the breakdown of the CF vortices and the laminar–turbulent transition.

One of the first indications on the development of the secondary CF instability is traced to experiments conducted by Poll [40], which showed the development of high-frequency disturbances prior to the laminar–turbulent transition on a swept cylinder model. Since then, numerous experimental [e.g. 77, 88–90] and numerical [e.g. 91–97] investigations have provided important knowledge on the development of secondary instability within the highly distorted boundary-layer subject to primary stationary CF instability.

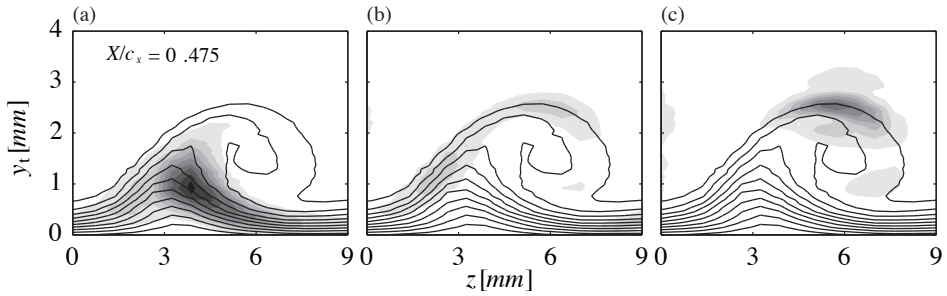

Figure 1.12: Contours of bandpass filtered velocity fluctuations and time-average fields (10 levels from 0 to U_∞, solid lines) from hot-wire measurements on a 45-degree swept wing model re-adapted from [71]. The frequency bands correspond to the secondary instability modes: (a)type-III (350Hz≤ f ≤ 550Hz) 10 levels from 0 to 0.24 U_∞, (b) type-I (5kHz≤ f ≤6kHz) 10 levels from 0 to 0.6 U_∞ and (c) type-II (7kHz≤ f ≤8kHz) 10 levels from 0 to 0.6 U_∞.

Several coherent fluctuations have been identified, typically corresponding to either primary travelling modes or a secondary high-frequency instability of the Kelvin-Helmholtz type. The first region of fluctuations has been classified as a type-I mode [94, 98, 99] or z-mode [93]. This region coincides with the local minimum of the spanwise gradient located at the outer side of the upwelling region of the CF vortices, as illustrated on the hot-wire measurements by Serpieri and Kotsonis [71] presented in figure 1.12(b). The second region of fluctuations has been classified as type-II mode [94, 98, 99] or y-mode [93]. This region coincides with higher levels of the wall-normal gradient and manifests near the top of the CF vortices (figure 1.12c). Finally, the third region of fluctuations known as Type-III mode [94, 95] has been observed near the wall on the inner side of the upwelling region and coincides with the local maxima of the spanwise gradient (figure 1.12a).

The origin of the velocity fluctuations in the region pertaining to type III has been traced to the interaction between travelling and stationary CF instability modes [71, 89, 94, 99]. The type III instability can be considered as a primary CF instability with non-zero frequency. Nevertheless, in environments of enhanced stationary CF instability modes, type III instability is identified through the "footprint" of the nonlinear interaction between stationary and travelling modes.

Conversely, the velocity fluctuations in the regions pertaining to type I and II differ entirely in nature from the type III, as they have been associated to secondary instabilities of Kelvin-Helmholtz type [see 95], which emerge on the strong velocity shears of the saturated stationary CF vortices. These high frequency rapidly amplifying instabilities, are extremely sensitive to small changes in the developing shears and lead to the breakdown of the CF vortices and transition to turbulent flow [71, 89, 94]. Previous studies on the mechanisms of these instabilities have shown the appearance of a secondary set of structures that develop in the shear layer on the outer side of the upwelling region [see 71, 94].

Control A considerable advance in understanding and controlling the CF instability has been achieved in the last two decades. A summary of different LFC techniques for cases dominated by CF instability can be found in the work of Messing and Kloker [100] and Serpieri *et al.* [101] and Saric *et al.* [102].

Based on the experimental study by Reibert *et al.* [86], Saric *et al.* [36] proposed a passive strategy to control the development of stationary CF vortices by using DREs near the leading edge of a swept wing. In the DRE control strategy, a selected sub-critical stationary CF instability mode is forced to inhibit the growth of the critical mode (i.e. naturally dominant) and delay the laminar–turbulent boundary-layer transition. The initial success of this technique in wind tunnel conditions inspired subsequent numerical investigations, which confirmed its transition delay capabilities [94, 96]. The detailed direct numerical simulations (DNS) by Wassermann and Kloker [94] revealed that the success of the control strategy lies in the mean-flow distortion caused by forcing a sub-critical stationary CF instability mode. The mean-flow distortion delays the growth of the critical mode and postpones the onset of the secondary instability responsible for the laminar breakdown of the boundary-layer flow. An up to date review of the current limitations (i.e. flight environment validation) and experimental/numerical research efforts towards enabling the DRE flow control strategy is given by Saric *et al.* [102].

A general term (i.e. not necessarily restricted to passive control using DRE) for the control strategy mentioned earlier was presented by Wassermann and Kloker [94] as upstream flow deformation (UFD). Since the introduction of the DRE or UFD technique, pneumatic actuators [103], wall suction/blowing [e.g. 100, 104], and plasma actuators [e.g. 101, 105, 106] have been used to control stationary CF vortices.

Alternatively, numerical studies by Dörr and Kloker [107], showed that the CF instabilities could also be controlled by modifying the base-flow, which result in a reduction of the CF component inside the boundary-layer. Recently, the transition delay potential of this strategy using plasma actuators has been experimentally confirmed by Yadala *et al.* [108] for low Reynolds number conditions.

Despite the technological advancements in LFC mentioned above, their performance is limited by non-ideal surfaces with two-dimensional irregularities, which are commonly present in practical applications, as described in detail in the following section.

1.3. TWO-DIMENSIONAL SURFACE IRREGULARITIES

Two-dimensional (i.e. spanwise invariant) surface irregularities in the form of backward- and forward-facing steps and gaps have been a longstanding topic of interest for the design of laminar flow components. These types of surface irregularities result from manufacturing requirements and operational conditions (i.e. panel joints, seals and seams) as schematically depicted in figure 1.13. Henceforth, the need for a universal method to determine the critical (i.e. transition advancement) step height or gap geometry has driven numerous research efforts to study the laminar–turbulent transition influenced by these surface irregularities.

TOLLMIEN-SCHLICHTING INSTABILITY WAVES DOMINATED CASES

In cases where TS waves dominate, early low-speed wind tunnel experiments on a flat plate model with steps and gaps were conducted as part of the X-21A demonstration

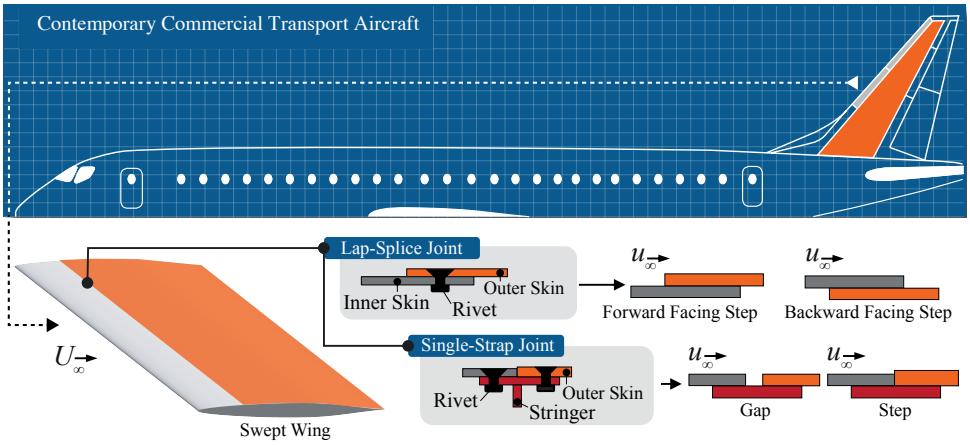

Figure 1.13: Surface irregularities on aircraft surface panels, showing schematics of commonly used panel joints and conceptualized types of surface irregularities resulting from these panel joints.

program [109]. The results indicate that the geometrical limits of surface irregularities compatible with laminar flow could be determined through a critical Reynolds number[8] (Re_h) based on the step height or gap width. Subsequent investigations conducted by Holmes *et al.* [110] on a T34-C aircraft extended the Re_h criterion to consider different step-edge shapes (i.e. rounded edge or chamfered edge) for forward-facing (FFS) and backward-facing (BFS) steps. The results indicate that an increase in the critical Re_h can be obtained by modifying the step-edge geometry. Additional flight tests by Zuniga *et al.* [111] and Drake *et al.* [112] studied the effect of step-gap configurations on the laminar–turbulent boundary-layer transition of a non-swept natural laminar flow (NLF) leading edge fixture mounted beneath an F104G aircraft. More recently, Drake *et al.* [113, 114] systematically studied the pressure gradient effect on the Re_h criterion by using different non-swept models in a low-speed wind tunnel and a novel towing facility. The results highlight the dependence of the Re_h criterion on the pressure gradient and show the stabilising effect of a favourable pressure gradient on the boundary-layer flow in cases with steps.

An alternative criterion for determining manufacturing tolerances for laminar flow components is the use of ΔN-factor models. These models incorporate the surface irregularities' influence in the widely used e^N transition prediction method. Wang and Gaster [115] conducted wind tunnel experiments on FFS and BFS on the surface of a non-swept flat plate model with zero pressure gradient at low turbulence conditions. The results indicate a correlation between the reduction in the transition N-Factor and the relative step height (h/δ^*). Moreover, a distinct laminar–turbulent boundary-layer transition behaviour was observed between FFS and BFS. In these experiments, FFS showed a less detrimental effect on the boundary-layer flow than BFS for the same step height and

[8] In cases of steps, the critical Reynolds number is given by $Re_h = (uh)/\nu$. Note that the velocity u used in literature is not always consistent since the free-stream velocity, the external velocity at the step location (Re_{he}) and the velocity in the boundary-layer at the step height (Re_{hh}) have been used.

wind tunnel conditions. Furthermore, Costantini *et al.* [116, 117] experimentally investigated the effect of pressure gradient, surface temperature and Mach number on the transition behaviour of FFS on a non-swept wing model in a cryogenic Ludwieg-tube wind tunnel.

A number of investigations have been conducted at the French Aerospace Laboratory (ONERA) to develop ΔN-factor models based on numerical simulations and experimental validation. The main results regarding step configurations are presented in [18, 118, 119]. A comprehensive review and extension of the work dedicated exclusively to gaps is provided by Beguet *et al.* [120]. The results presented by Perraud *et al.* [119] indicate that the influence of an FFS on the stability of the boundary-layer flow strongly differs from the one of a BFS of comparable height. Therefore, to account for these differences, the ΔN-factor in FFS cases is not modelled with a constant shift of the stability curve, but instead a more complex ΔN model is proposed.

In a different strategy, Crouch *et al.* [121] experimentally determined ΔN- factor models based on the change in the laminar–turbulent boundary-layer transition location induced by steps on the surface of a non-swept flat plate model under favourable and adverse pressure gradients. Crouch and Kosorygin [122] extended these empirical models to consider variations in the step location, two-dimensional strips (i.e. FFS followed by BFS), and shallow gaps. In addition, Crouch *et al.* [123] studied the effects of gaps in the laminar–turbulent boundary-layer transition on TS-dominated cases.

Recent numerical studies by Edelmann and Rist [124] and Zahn and Rist [125] have provided important insight into the boundary-layer stability modifications induced by two-dimensional surface irregularities for the further development of ΔN-factor models for non-swept geometries. Furthermore, numerical simulations by Rizzetta and Visbal [126] on a non-swept flat plate geometry with FFS and BFS elucidated important aspects of the step-induced transition mechanisms dominated by TS waves.

CROSSFLOW INSTABILITY DOMINATED CASES

The limited applicability of the aforementioned studies to swept wing cases dominated by CF instability led to parametric studies [e.g. 118, 127] and more detailed investigations [e.g. 128–132] on the interaction of CF vortices with steps configurations. The results from these studies highlight a complex interaction, occuring when surface irregularities in the form of steps interact with the CF instability. Furthermore, previous studies [e.g. 118, 129] on CF instability indicate that configuring a step as a forward-facing arrangement, instead of a backward-facing one, will result in a weaker destabilisation of the subsonic boundary-layer. Henceforth, the main efforts in studying this type of surface irregularity in swept geometries are discussed below to highlight the unresolved aspects that the present dissertation aims to clarify.

In the last decade, the research group at the Flight Research Laboratory and the Computational Stability and Transition Laboratory of the Texas A&M University investigated, numerically and experimentally (wind tunnel and flight tests) different aspects of swept wing transition under the influence of step surface irregularities. A summary of these efforts and their results is provided by Tufts *et al.* [129]. Duncan *et al.* [127] conducted experiments on a swept wing boundary-layer at low turbulence levels and demonstrated that the interaction between the FFS and the stationary CF instability lead to the amplification of the CF vortices downstream of the step position. More recently, Tufts *et al.*

[129], performed detailed numerical simulations complementary to the flight and wind tunnel experiments presented by Duncan *et al.* [127, 133] and Crawford *et al.* [134]. The numerical investigation confirmed the amplification of the incoming stationary CF vortices by the FFS for cases above a critical step height. Tufts *et al.* [129] suggested that due to the spanwise pressure gradients in aft swept wings, the localised recirculation regions upstream and downstream of the step form helical vortices, which travel along the span of the wing. The transition advancement and amplification of the stationary CF instability modes were attributed to a constructive interaction between the CF vortices and the downstream helical vortex (i.e. past the step edge) when the FFS height exceeds the core height of the CF vortices. Based on this interaction, Tufts *et al.* [129] proposed the use of the unperturbed (i.e. no FFS) CF vortices core height as a governing metric to determine a priori the criticality of a given FFS.

Although the idea of using the CF vortices core height as a metric provides a first-order approximation of the critical FFS height, further experimental investigations [e.g. 130, 135, 136], which confirmed the amplification of stationary CF instability modes by the FFS, found no evidence to support the constructive interaction proposed by Tufts *et al.* [129]. Moreover, these experiments revealed that the stationary CF vortices amplify at two distinct locations in the vicinity of the FFS.

Specifically, Eppink [130] studied the mechanisms involved in the FFS-CFI interaction and identified the amplification of the primary instability in two regions. The first region appears to be related to a destabilisation of the stationary CF instability by the strong inflectional velocity profiles generated by the adverse pressure gradient upstream of the FFS. The second amplification region was attributed to the growth of the primary mode harmonics by streamwise oriented vortices originating from the modulated recirculation region downstream of the FFS edge. Interestingly, Eppink [130, 137] reported the occurrence of high-frequency fluctuations which coincide with the location of the shear layer of this locally separated flow. Furthermore, a detailed stability analysis by Groot and Eppink [138] on these experiments revealed the convective nature of these unstable perturbations and identified their development on the top part of the local flow recirculation regions downstream of the supercritical FFS (i.e. tripping at the step position).

In addition, Eppink [130] showed that a subcritical FFS case could lead to a premature boundary-layer transition if the amplitude of the CF vortices was increased. This effect was attributed to a stronger spanwise modulation of the recirculation region downstream of the step edge for the cases with larger initial amplitude.

Numerical simulations by Casacuberta *et al.* [139] on the steady FFS-CFI interaction (i.e. simulating only stationary step-flow features) showed that, as the primary CF disturbance reaches the FFS, it does not directly impinge on the step edge but lifts off the surface and passes over it. This behaviour is in agreement with previous experimental observations by [e.g. 130, 140]. In addition, the numerical results of Casacuberta *et al.* [139] identified a series of near-wall perturbation streaks downstream of the FFS edge developing at the spanwise wavelength of the stationary CF vortices. Given that the wavelength of these secondary perturbations coincides with the primary CF disturbance, they manifest as a secondary peak near the wall superimposed on the disturbance profile as shown in Tufts *et al.* [129] and Eppink [130]. Under certain conditions (e.g. large FFS

at low-amplitude of the CF vortices) the identified near-wall peak can exceed the magnitude of the one corresponding to the primary CF disturbance. Thus, Casacuberta *et al.* [139] propose a set of metrics to adequately determine the growth of the primary CF disturbance in these conditions.

Finally, to mitigate the effect of an FFS on transition, Eppink and Casper [135] successfully applied onflat plate model dominated by stationary CFI the step-edge chamfering (i.e. slanted step face) strategy by Holmes *et al.* [110]. Eppink and Casper [135] showed that a variation in the angle of the FFS face reduced the recirculation region and CF reversal. This topological change leads to a weaker destabilisation of the primary CF instability mode and a transition postponement with respect to the straight FFS (i.e. vertical step face). More recently, Ivanov and Mischenko [141] used a series of two-dimensional strips (i.e. FFS followed by a BFS) along the span of a swept wing to stabilise the CFI following the theoretical analysis and concept presented by Ustinov and Ivanov [142]. The experiments by Ivanov and Mischenko [141] showed a postponement of the laminar–turbulent transition for strips oriented parallel to the leading edge and at 18 degrees with respect to the leading edge.

The aforementioned studies and the discrepancies between the mechanism proposed by Tufts *et al.* [129] and Eppink [130] highlight numerous unresolved aspects which require further study before the interaction between the FFS and CF vortices can be fully unveiled. Specifically, the dependence on the amplitude of the CF vortices, nonlinear interactions at the FFS, and laminar breakdown mechanisms are key features requiring experimental and numerical analysis within a range of governing parameters.

1.4. DISCUSSION & OUTLINE

The research encompassed within this doctoral dissertation entails studying the development and breakdown of the crossflow (CF) vortices when interacting with a surface irregularity in the form of a forward-facing step (FFS). As discussed in §1.1, understanding the impact of surface irregularities on the laminar–turbulent transition is critical for the application of cutting-edge laminar flow control technologies to reduce the fuel consumption of modern transport aircraft.

The literature review on the interaction between FFS and CF vortices presented in §1.3 indicates the limited studies concerning the experimental identification of CF vortices in the vicinity of the step and highlights unknown aspects regarding the parameters governing their interaction, and the step-induced development, amplification and breakdown of the CF vortices. Henceforth, to further the understanding of the FFS-CFI interaction, three main research objectives guided the work of this doctoral project:

> **Objective A** (Chapter 3): Investigate the applicability of current one-parameter critical FFS criteria (i.e. based on CF vortex core height or boundary-layer displacement thickness) and identify additional key parameters playing a role in the laminar–turbulent transition behaviour by systematically varying the Reynolds number and step height in both unforced (i.e. without DREs) and forced (i.e. with DREs) experimental conditions.
>
> **Objective B** (Chapter 4): Investigate the influence of the FFS on the development of the primary CF instability and its effects on the global transition location by characterising in detail the laminar–turbulent boundary-layer transition behaviour and quantifying the evolution of the CF vortices.
>
> **Objective C** (Chapter 5) Investigate the influence of the FFS on the CF vortices' breakdown by characterizing in detail the development of the secondary CF instability and step-induced unsteady disturbances.

The dissertation's outline is the following: Chapter 2 discusses the methodology used during the execution of the experiments and processing of the data. Chapters 3 to 5 present a complete description and analysis of the experiments conducted to address each of the main research objectives (A-C) in this dissertation. Finally, Chapter 6 presents a general discussion of the main findings and outlook of future research.

2

METHODOLOGY

This chapter first introduces the wind tunnel facility, swept wing model and the manufacturing of forward-facing step surface irregularities. This is followed by an overview of the measurement techniques and numerical methods used in the acquisition, processing and interpretation of the experiments.

Parts of this chapter are published in:

- Rius-Vidales, A.F. & Kotsonis, M. 2020 Influence of a forward facing step surface irregularity on swept wing transition. AIAA Journal **58(12)**, 5243-5253.
- Rius-Vidales, A.F. & Kotsonis, M. 2021 Impact of a forward-facing step on the development of crossflow instability. Journal of Fluid Mechanics **924**, A34.
- Rius-Vidales, A.F. & Kotsonis, M. 2022 Unsteady interaction of crossflow instability with a forward-facing step. Journal of fluid Mechanics, **939**, A19.

2.1. EXPERIMENTAL SETUP

In line with the research objectives presented at the end of Chapter 1, a series of experiments have been conducted on a 45 degree swept wing model (known as M3J) at the Low Turbulence Tunnel of the Delft University of Technology. This section provides an overview of the experimental setup by providing an in-depth description of the wind tunnel facility, the swept wing model, and the creation of the FFS on the model's surface.

2.1.1. LOW TURBULENCE WIND TUNNEL FACILITY LTT

A low turbulence environment ($Tu < 0.15\%$, [see 34]) is an essential element for the development of stationary CF vortices, as described in §1.2.2. Thereby, the use of the Low Turbulence Tunnel (LTT) located at the Delft University of Technology has been key to the research presented in Chapters 3 to 5.

A detailed description of the construction and characteristics of the LTT facility is presented by Dobbinga and Van Ghesel Grothe [143]. The plan to build a Low-Speed Laboratory (figure 2.1a) containing a high-quality wind tunnel facility for detailed aerodynamic research at TU Delft started in 1946 and was completed in the fall of 1953 [see 143]. The vertical arrangement of the LTT wind tunnel is quite peculiar since it is part of the construction of the TU Delft Low-Speed Laboratory (figure 2.1a) , as shown in the cut-out diagram of the building in figure 2.1(b). Therefore, except for the final part of the contraction, interchangeable test-section, and the initial part of the diffusor (shown in figure 2.2a) the wind tunnel is predominantly manufactured out of reinforced concrete.

The LTT facility is an atmospheric, low-turbulence, closed-return, and subsonic tunnel, which can reach a speed of 117 m/s (421 km/h) at the measurement site [143]. The main elements of this tunnel are indicated in figure 2.1(b) and described hereinafter. The airflow is driven by a six-blade propeller located on the ground floor (1). A shaft couples this propeller to a 525 kW DC electric engine installed on a room external to the wind tunnel circuit. The propellers' swirl on the airflow is minimized through a combination of guiding vanes and a spider-wave like grid. The divergent channel downstream of the propeller (2) decelerates the airflow before it is redirected vertically and then horizontally into the settling chamber by two rows of corner vanes (3a and 3b).

At the entrance to the settling chamber (4a), the airflow velocity is reduced even further through an increase in the tunnel's cross-sectional area and an expansion screen. Immediately downstream, the airflow passes through seven anti-turbulence screens (4b) built out of phosphor bronze (see table 2.1). Next, the airflow experiences a gradual velocity increase (ratio of 17.9:1, [143]) at the contraction (5) until it reaches the interchangeable octagonal test section (6) containing the in-house designed M3J swept wing model. The test-section features a height of 1.25 m, a width of 1.80 m, and a length of 2.60 m. The test section's vertical walls are slightly divergent to account for the solid blockage effect by the wind tunnel's boundary-layer at the measurement region. Although the overall pressure in the wind tunnel is higher than the atmospheric value, a gap at the end of the test-section ensures a pressure equilibrium at the measurement region [143].

Finally, downstream of the test-section and before it arrives back to the propeller, the airflow experiences a velocity reduction and a pressure increase in the diffusor (7) and a vertical and horizontal re-direction by a set of corner vanes (3c and 3d). In addition,

(a) Low-Speed Laboratory Building (b) Low Turbulence Tunnel cutout A-A

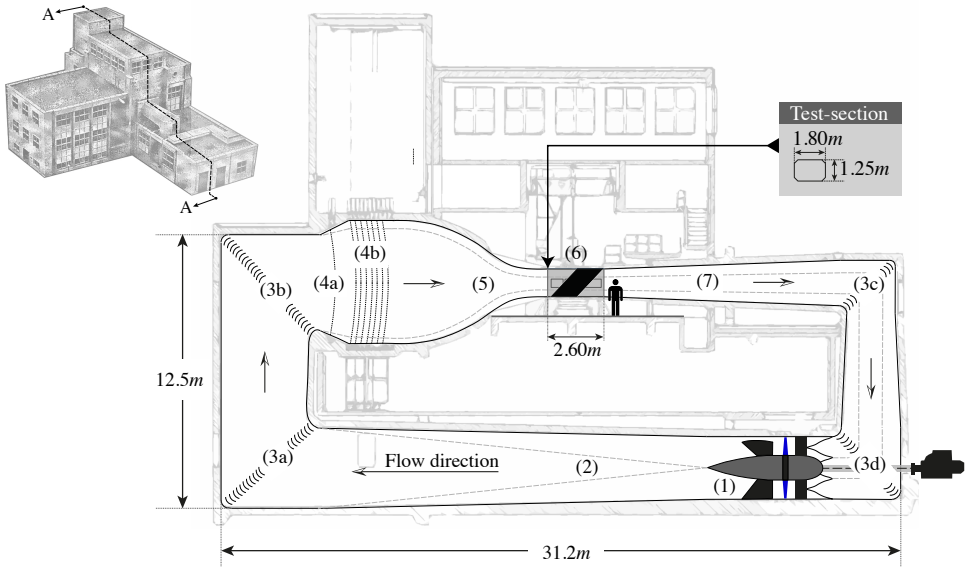

Figure 2.1: Schematic of the Low Turbulence Tunnel (LTT) at the TU Delft Low Speed Laboratory: (a) Diagram of the Low-speed Laboratory Building showing the LTT cut-out A-A, re-adapted from [143]. (b) Cut-out diagram A-A showing the different sections of the wind tunnel system re-adapted from report LSW91-1.

Table 2.1: Geometrical details of the LTT anti-turbulence grids, Dobbinga and Van Ghesel Grothe [see 143]

Anti-turbulence Grid No	1	2	3	4	5	6	7
Distance between wire centers [mm]	0.9	1.32	1.32	1.32	1.32	1.1	1.1
Wire Diameter [mm]	0.3	0.3	0.3	0.3	0.3	0.2	0.2

the corner vanes (3c and 3d) feature a cooling system to regulate the airflow temperature during long periods of operation. The temperature (T_C) of the flow is monitored at the wind tunnel's contraction using a Resistance Temperature Detector (RTD-Pt100)[1] and the atmospheric pressure (P_A) is measured outside the wind tunnel's test-section using a digital barometer[2]. From these measurements the fluid density[3] (ρ) and the reference kinematic viscosity[4] (ν) are calculated.

During operation, the pressure difference ($\Delta_{Pb} = P_{t,4} - P_{s,5}$) between the turbulence grids ($P_{t,4}$) and the end of the contraction ($P_{s,5}$) is measured using a digital pressure gauge[5]. Then, from this pressure difference, the reference dynamic pressure at the test-section ($P_{q,6}$) is determined based on an empty test-section calibration curve and the reference wind tunnel velocity obtained using: $U_\infty = \sqrt{2P_{q,6}/\rho}$.

[1] Platinum resistance temperature detector (Pt100), estimated accuracy (±0.4°C at 20°C)
[2] Digital Barometer by MENSOR (mensor.com), model: CPT6100, accuracy: 0.01% of reading
[3] Calculated as $\rho = P_A/(R(273.15 + T_C))$, [kg/m^3] using the specific gas constant $R = 287.05$, [N m/kg K]
[4] Calculated as $\nu = \mu/\rho$, [m^2/s] using Sutherlands' equation: $\mu = 1.458 \times 10^{-6}\{T_K^{1.5}/(T_K + 110.4)\}$, [kg/ms]
[5] Digital pressure gauge by MENSOR (mensor.com), model: DPG2101 (0-0.5 psi), accuracy: 0.010%FS

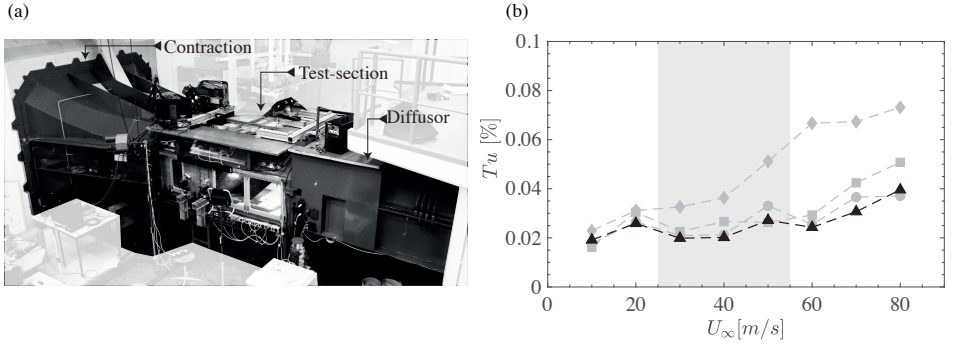

Figure 2.2: (a) Photograph of LTT wind tunnel at the measurement room. (b) Variation of turbulence intensity (Tu) with free-stream velocity (U_∞) and number of active anti-turbulence screens (7-▲ , 5-•, 2-■ and 0-⧫). Measurements obtained from [75] and conducted with M3J model installed (bandpass filtered between 2 and 5000 Hz).

As part of the turbulence intensity characterization of the LTT facility, Serpieri [75] conducted velocity measurements in the centre of the test section with the swept wing model installed using hot-wire anemometry. The turbulence intensity[6] (Tu) results reproduced from Serpieri [75] for different combinations of free-stream conditions and active anti-turbulence screens are presented in figure 2.2(b). Using all seven anti-turbulence screens at the free-stream conditions under which the wind tunnel was operated during the current work (i.e. 25 m/s $\leq U_\infty \leq$ 55 m/s, grey region in figure 2.2b), the turbulence intensity is $Tu \leq 0.03\%$. Henceforth, the combination of this experimental facility and swept wing model provides sufficient conditions for the investigation of stationary CF instability, as shown by Serpieri and Kotsonis [71].

2.1.2. M3J SWEPT WING MODEL

The wind tunnel model used in this work was designed in-house [see 75, pp.43-56] and manufactured by Glasfaser-Flugzeug-Service GmbH. The swept wing known as M3J, is built out of glass-fiber reinforced epoxy resin and sealed with a polyester gel coat dyed in black. The model features a streamwise chord of c_X = 1.27 m, a span of b = 1.25 m, and a sweep angle of 45 deg. This model has been extensively used at TU Delft for the detailed study of the primary and secondary CF instability and boundary-layer control [e.g. 71, 90, 101, 108].

Figure 2.3(a) presents a cross-sectional view of the wind tunnel test-section. The swept wing model is mounted vertically and spans the entire height of the test-section, as shown by the photograph in figure 2.4(a). This study uses two different spatial coordinate systems, and their origin coincides with the intersection between the leading edge and the wing mid-span. In the first coordinate system (X, Y, Z), the X-direction is aligned with the wind tunnel floor. In the second coordinate system (x, y, z) the x-direction is perpendicular to the leading edge.

[6] Turbulence intensity bandpass filtered between 2 and 5000 Hz and calculated as: $Tu{=}1/U_\infty\sqrt{(1/2)(\overline{U'^2}+\overline{V'^2})}$

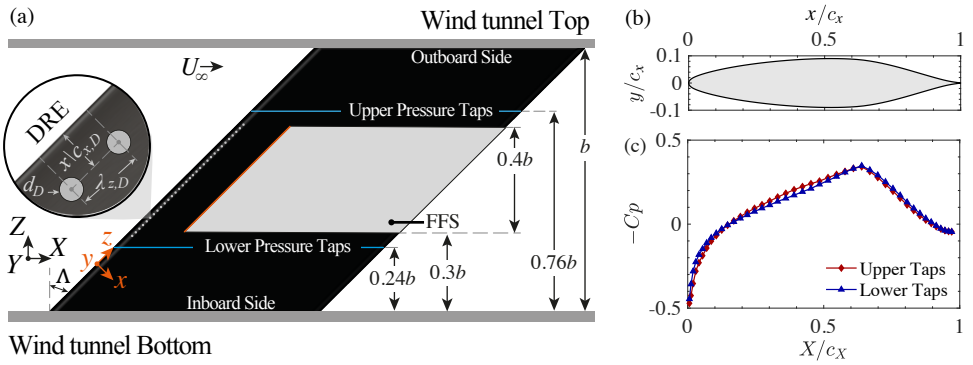

Figure 2.3: Experimental Setup: (a) Cross-sectional schematic of the swept wing model installed in the LTT test-section (flow direction left to right, c_X = 1.27m and b = 1.25m) showing the FFS (grey area) and DREs. (b) Airfoil geometry 66018M3J. (c) Streamwise (i.e. along the X coordinate) pressure coefficient distribution at $\alpha = 3°$ $Re_{c_X} = 3.7 \times 10^6$ on the pressure side of the model (max U_{Cp} = 0.001).

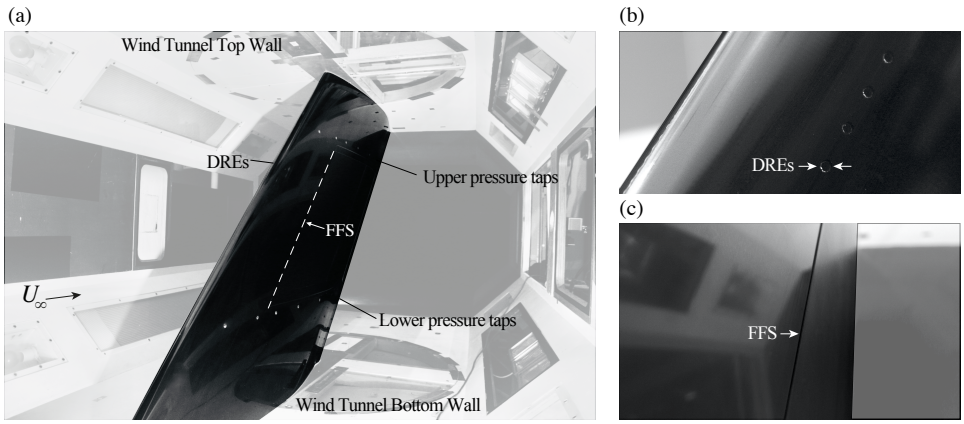

Figure 2.4: Photographs of experimental setup: (a) M3J swept wing model installed in LTT test-section. (b) Discrete roughness elements (DREs) installed on the M3J leading edge region. (c) Final installation of FFS surface add-on on swept wing model.

The model pressure distribution is measured using a total of 92 streamwise oriented (i.e. along X-coordinate) pressure taps equally divided on the upper (outboard) and lower (inboard) side of the model as depicted on the diagram in figure 2.3(a). Note that all the static pressure (P_s) measurements presented in this work are recorded on the "pressure side" of the model using a digital pressure scanner system[7]. The non-dimensional pressure coefficient (C_p, equation 2.1) is calculated with the reference dynamic ($P_{q,6}$) and static pressure ($P_{s,6}$). The reference static pressure ($P_{s,6} = P_t - P_{q,6}$) is

[7]Pressure scanner by TE Connectivity (te.com), model: DTC-Initium (1 psi channels), accuracy: 0.10%FS

calculated using the total pressure (P_t) obtained from a pitot-static tube located inside the test-section during the measurements.

$$C_p(X) = \frac{P_s(X) - P_{s,6}}{P_{q,6}} \tag{2.1}$$

The wing features a modified symmetric NACA 6-series (66018) airfoil, as shown in figure 2.3(b) and Appendix A [see also 75, Ch.3]. At a mild angle of attack ($\alpha = 3°$) the streamwise pressure distribution (pressure side of the wing) shows a favourable pressure gradient up to $X/c_X \approx 0.65$ (see figure 2.3c), prohibiting the amplification of TS-waves instability. Moreover, the lack of concave surfaces and a small leading edge radius (approximately 1% of the chord) lead respectively to the suppression of Görtler-type instabilities and attachment line contamination. These design features ensure an exclusive amplification of CF instability, as shown in Serpieri and Kotsonis [71].

To study fundamental features of CF dominated transition, the M3J is aerodynamically designed to achieve infinite swept wing conditions at the measurement region [144]. Although wall liners were initially designed and manufactured for this model, previous experimental results demonstrated that the aspect ratio is sufficient to achieve spanwise invariant conditions [71]. The small variation between the upper and lower pressure measurements at $\alpha = 3°$ and $Re_{c_X} = 3.7 \times 10^6$ presented in figure 2.3(c) confirms the validity of this approach.

Due to the extreme sensitivity of CF instability to surface roughness, great care was taken to ensure a consistent and polished surface, especially near the leading edge region. The surface roughness was monitored using a surface profilometer[8]. The resultant root mean square roughness of the wing surface is $R_q \approx 0.2$ µm [75].

In addition, to study the impact of an FFS on a particularly unstable stationary CF instability mode, Discrete Roughness Elements (DREs) are used in the vicinity of the leading edge (figure 2.4b) to force a single fundamental CF instability mode featuring a spanwise wavelength corresponding to the spacing of the elements ($\lambda_{z,D}$) in a strategy similar to Saric *et al.* [36], Serpieri and Kotsonis [71], and White and Saric [89].

The DREs were manufactured in-house from an adhesive transfer vinyl film using a custom laser cutting system. In the cases presented in Chapters 3-5 their nominal diameter is $d_D = 2$ mm and the nominal height is either $k_D = 100$ µm or 200 µm as indicated in Tables 3.1,4.1 and 5.1. A recent detailed characterization of the DREs geometry presented in Zoppini *et al.* [145], indicates that this nominal values would lead to an average final diameter of $\bar{d}_D = 1.772 \pm 0.017$ mm and respective heights of $\bar{k}_D = 114.7 \pm 2.3$ µm and 217.9 ± 3.1 µm after the manufacturing and application of the elements.

2.1.3. MANUFACTURING OF SURFACE IRREGULARITIES

In this work, FFS irregularities are created on the surface of the existing M3J swept wing model following a foil add-on strategy similar to the one presented by Holmes *et al.* [110] and Perraud and Seraudie [118]. Therefore, polyethylene terephthalate foils (Vivak® PETG) are cut to match a 45 degree rhomboid shape with a width of 500 mm a length of 1025 mm using a rolling blade on a computer numerical control Gerber ma-

[8] Profilometer manufactured by Mitutoyo (mitutoyo.com), model: SJ-301

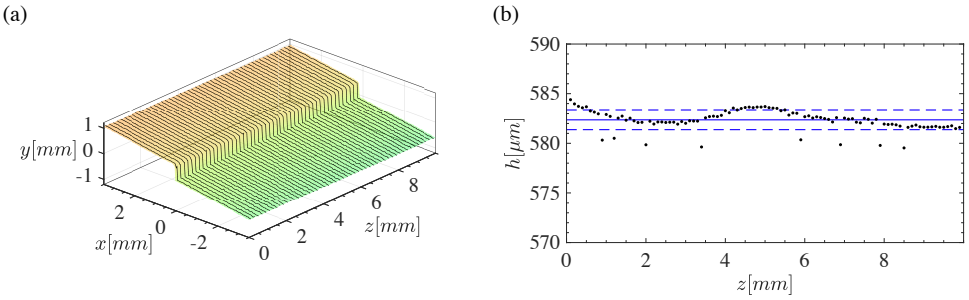

Figure 2.5: In-situ measurements of the step geometry using a Micro-Epsilon 2950-25 laser profilometer: (a) black lines show laser profilometer MicroEpsilon 2950-25 measurement, for visualization purposes a surface interpolation is presented. (b) Calculated step height from each measured profile along the span diection z, solid line indicated the average step height $\bar{h}$ and dashed lines indicate $\bar{h} \pm \sigma_h$

chine (model DCS 2500). The add-on spanwise extent is limited by the upper and lower row of pressure taps as shown in figure 2.3(a) to simplify its installation.

During the experiments, the custom-sized foils are installed on the surface of the M3J swept wing using a specialized repositionable tape[9]. In addition, the step height of the final installation (figure 2.4c) is characterised by traversing a laser profilometer[10] along the extent of the surface irregularity. The laser profilometer measures the individual location of 1280 laser points projected on a line on the model's surface. The result is a two-dimensional profile of the step geometry as shown by the solid black lines in figure 2.5(a). From this profile, the step height (h) is determined by projecting a linear fit based on the measurement upstream and downstream of its location. This procedure is followed for each profile to determine the spanwise variation of the step as shown in figure 2.5(b). Afterwards, the average step height ($\bar{h}$) and standard deviation (σ_h) are determined. These are the values reported in tables 3.1,4.1 and 5.1 for the different experiments presented in this dissertation.

2.2. MEASUREMENT TECHNIQUES

This section provides an overview of the flow measurement techniques employed during the experimental investigations in Chapters 3 to 5. First, a detailed description of the methodology to identify the laminar–turbulent transition location and spatial organization of the CF vortices using infrared thermography is presented. This is followed by a general overview of the particle image velocimetry and hot-wire anemometer measurement techniques to characterize the CF vortices' steady and unsteady interaction with forward-facing steps.

[9] Repositionable tape manufactured by 3M (3m.com), model: 9425HT
[10] Laser profilometer manufactured by Micro-Epsilon (micro-epsilon.com), model: 2950-25, resolution of 2 µm

2.2.1. INFRARED THERMOGRAPHY

Infrared (IR) Thermography has proven to be a valuable experimental method to determine the surface temperature distribution and near-wall heat transfer properties in many different fluid mechanics investigations. A comprehensive overview of fundamental aspects of heat radiation theory, technical features of IR cameras and applications in fluid mechanics is presented by Astarita and Carlomagno [146]. Moreover, a recent review of IR measurements for the laminar–turbulent boundary-layer transition identification, with particular emphasis on the development of Differential Infrared Thermography (DIT), is presented by Wolf *et al.* [147].

The idea to identify the location of the laminar–turbulent transition using IR measurements is based on the relation between the skin-friction coefficient and the convective heat transfer coefficient[11] at a given Prandtl number[12] dictated by the Reynolds analogy[13]. The analogy implies that an increase in wall shear stress resulting from a turbulent boundary layer increases the surface heat transfer. Therefore, when a model is actively heated (i.e. model surface temperature higher than the free-stream ambient temperature), a lower surface temperature is registered in the turbulent regions compared to the regions where the flow remains laminar. As discussed below, the difference in surface temperature between the laminar and turbulent portions of the boundary-layer is exploited to identify the transition location. In particular, the use of IR Thermography has proven to be a robust and efficient method for the analysis of swept wing transition [e.g. 148–150].

DETECTION OF LAMINAR–TURBULENT TRANSITION

In the experiments presented in Chapters 3 to 5, IR measurements are extensively used to determine the transition location on the M3J swept wing model. During the measurements, the M3J model is actively irradiated by six halogen lamps of 400 W and one of 1000 W located on different optical access ports on the test-section. The thermal equilibrium of the system ensures a minimal variation in the surface temperature of the model.

The destabilizing effect of uniform wall heating in TS-dominated boundary-layers is well-known [e.g. 30, 50, pp.460-462, pp.207-462]. Nevertheless, in cases dominated by crossflow instability a milder destabilizing effect is expected[see 74]. Eppink and Wlezien [151] observed that a change in wall temperature has its main influence on the travelling crossflow modes. More recently, Lemarechal *et al.* [152] used Temperature Sensitive Paint (TSP) to identify transition location on the boundary-layer of a swept wing model dominated by stationary crossflow modes. The results show that for a ratio $T_m/T_f \leq 1.04$ corresponding to the temperature on the model (T_m) to the one of the fluid (T_f), no change in transition location was observed. Therefore, a minimal influence of the wall heating on the transition location is expected during the IR measurements presented in Chapters 3 to 5.

Surface thermal maps are acquired on the pressure side of the model (surface emissivity 0.94) using an IR camera[14] with an uncooled focal plane array (FPA) sensor of

[11] Stanton number: $\mathrm{St} = \dot{q}/[\rho u_e c_p (T_e - T_w)]$, [see 23, p.185]

[12] Indicates the relation between the thermal and velocity boundary-layers (Air at 15°C, $\mathrm{Pr} = \mu c_p/k = 0.738$)

[13] The Reynold analogy for $\mathrm{Pr} \neq 1$ indicates: $\mathrm{St} = C_f/(2\mathrm{Pr}^{0.667})$, [see 23, pp.186-188]

[14] Infrared Camera manufactured by Optris GmbH (optris.global), model: PI640

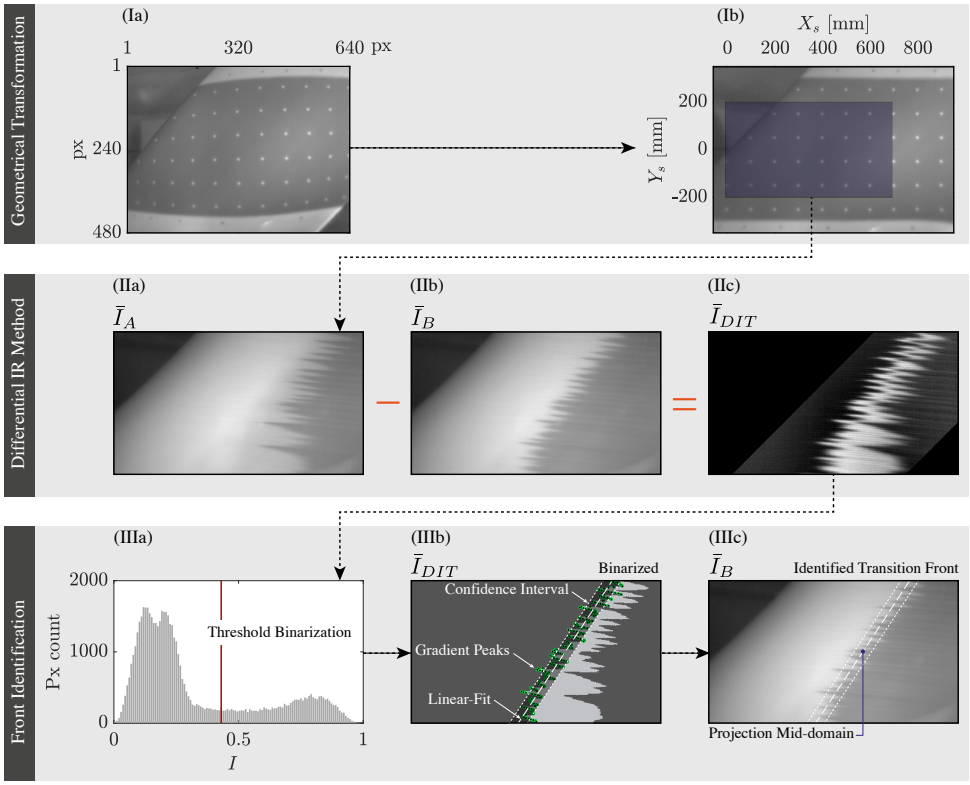

Figure 2.6: Schematic of transition location identification (flow from left to right), showing the IR source images $\bar{I}_A$ ($Re_{c_X} = 2\times10^6$) and $\bar{I}_B$ ($Re_{c_X} = 2.17\times10^6$) with lighter (higher temperature) and darker (lower temperature) regions.

640px × 480px with a 17 µm px pitch. The FPA sensor is sensitive to a spectral range of 7.5-13 µm and features a Noise Equivalent Temperature Difference (NETD) of 75 mK. The PI640 IR camera is calibrated by the manufacturer to operate using either a wide-angle, a mid-angle, or a narrow-angle lens with focal lengths of $f = 10.5, 18.7$ or 41.5 mm, respectively. Figure 2.6 shows a schematic of the methodology[15] followed for the determination of the transition location using the thermal maps acquired by the IR camera.

The process begins with a geometrical transformation, as shown in figure 2.6(Ia-Ib). During this procedure, the halogen lamps irradiate the model, and a reference IR image of an *ad hoc* calibration target on the model's surface is acquired, as shown in figure 2.6(Ia). The calibration target consists of a rectilinear grid[16] of black dots printed on a flexible white surface. Thereafter, a polynomial distortion correction [see 153, pp.100-107] is applied on these measurements to account for the airfoil curvature and camera position (the results are shown in figure 2.6Ib). The geometrical transformation obtained

[15] The building blocks of the custom algorithm are based on MATLAB image processing toolbox.
[16] The custom target consist of black dots of 10mm and spacing between dots of 100mm.

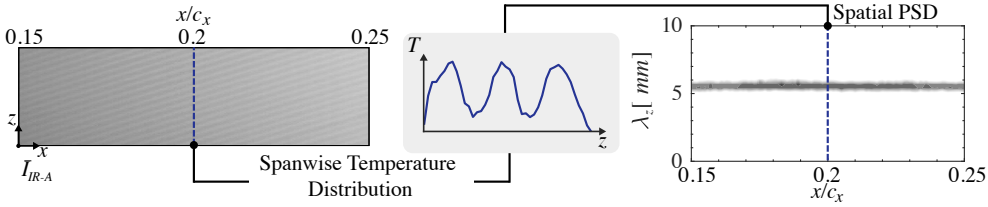

Figure 2.7: Schematic of the wavelength identification of the CF vortices (flow from left to right) forced ($\lambda_{z,D}$ = 5.5 mm) case without FFS ($\alpha = 3°, Re_{c_X} = 2.5 \times 10^6$): Left, IR source images $\bar{I}_{\text{IR-A}}$. Right, spatial power spectral density (PSD).

in this procedure is applied to all the measurements. Note that, although the coordinate system and origin coincides with the one indicated by figure 2.3(a), the subscript (s) denotes surface coordinates.

For the global transition location, the more suitable wide-angle lens (f = 10.5mm) is mounted on the IR camera. A typical measurement consisted of approximately 50 infrared images acquired at a sampling rate of $f \approx$3.5Hz. From these measurements, a distortion corrected time-average thermal map in the analysis region (blue area in figure 2.6Ib) is obtained, as shown in figure 2.6(IIa). Then, based on the concept presented by Raffel and Merz [154] and Raffel *et al.* [155] a differential infrared thermography (DIT) technique is applied on consecutive temperature fields with increasing Reynolds number. This technique minimises the background noise and decreases the possibility of a spurious identification of the transition front. Note that in the active heating modality, the lower temperature corresponds to the turbulent part of the boundary layer flow and the higher temperature to the laminar region, as shown in figure 2.6(IIa).

Figure 2.6(IIa-IIc) illustrates the DIT method by presenting the time-averaged IR images $\bar{I}_A$ ($\alpha = 3°, Re_{c_X} = 2 \times 10^6$) and $\bar{I}_B$ ($\alpha = 3°, Re_{c_X} = 2.17 \times 10^6$) and calculating the DIT as $\bar{I}_{DIT} = \bar{I}_A - \bar{I}_B$ as shown in figure 2.6(IIc). Subsequently, a suitable global threshold to binarize the $\bar{I}_{DIT}$ is obtained from the image histogram (figure. 2.6IIIa), following Otsu's method [see 153, 156, pp.747-751]. Subsequently, the local transition location is identified using the gradient of the binarized $\bar{I}_{DIT}$ and a linear-fit is performed along the span, as shown in figure 2.6(IIIb).

Finally, the reference transition location is extracted at the mid-domain height from the linear fit. Note that the confidence bands (dashed lines in figure 2.6IIIb-IIIc) of the fit indicate the uniformity of the transition front (i.e. jagged or smooth) and thus provide important insight into the dominant transition-inducing instability. More specifically, the stationary CF modes form a well-defined jagged pattern of localised wedges in the transition front, while travelling modes essentially "blur" the transition front, reducing the spanwise variance of the transition location.

DETECTION OF CROSSFLOW VORTICES FEATURES

In addition to the global transition location, the thermal maps from IR measurements can provide a qualitative representation of the CF vortices' thermal footprint. This can be further used to extract the spatial organization of coherent structures in the boundary layer as they interact with the FFS.

Therefore, a spatial power spectral density (PSD) analysis was performed on the distortion corrected time-average thermal map, as illustrated in figure 2.7. In this case, the field of view (FOV) of the IR camera is rotated 45° (i.e. the sensor height was oriented parallel to the LE direction). Thus, the spectral analysis is conducted on the thermal intensity profiles along the spanwise (z) component (i.e. the height of the IR images). For this type of measurements, the narrow-angle lens (f = 41.5mm) is preferred to obtain a resolution of around 2.5 px/mm on the thermal intensity profiles. This analysis makes it possible to determine the wavelength of the CF vortices based on their thermal footprint at the model surface and monitor changes as they interact with the flow near the FFS.

2.2.2. HOT-WIRE ANEMOMETRY

The Hot-wire Anemometry (HWA) is a reliable single-point measurement technique in which the fluid's velocity is determined by exploiting the convective heat transfer of a heated wire-sensor. An introduction to the HWA measurement technique and its application in different fluids (e.g. air, water, polymer solutions and mercury) is found in the textbook by Lomas [157]. In addition, Bruun [158] offers a complete overview of fundamental and practical aspects for the use of HWA.

The HWA is a well-established flow measurement technique, which has been a fundamental pillar in the development of experimental fluid mechanics. In Chapter 5, HWA measurements are extensively used to characterize the unsteady FFS-CFI interaction. A simplified schematic of the measurement system employed in this work is presented in figure 2.8. Three main components comprises the measurement system: (I) the HWA probe and wire-sensor; (II) the Wheatstone's bridge; (III) an analogue to digital acquisition equipment.

Depending on the experimental requirements, different types of HWA probes are available off-the-shelf from established manufacturers (e.g. Dantec Dynamics, TSI Incorporated). However, custom probes manufactured by a skill-full experimentalist are not uncommon. For the interested reader, a set of practical recommendations to manufacture and repair HWA probes are given by Lomas [157, pp.43-54]. In this work, a miniature ceramic body boundary-layer probe[17] is used, as shown in figure 2.8(I). A particular feature of this probe is the "fork-like" shape of the prongs to facilitate near-wall boundary-layer velocity measurements. The sensor on the probe consists of a tungsten wire with a nominal diameter (d_w) of 5 µm and a length (l_w) of 1.25 mm (nominal aspect ratio $l_w/d_w = 250$).

During operation of the HWA system, the probe is connected to a Constant Temperature Anemometer (CTA) Wheatstone's bridge[18]. A simplified schematic of a CTA mode Wheatstone's bridge is presented in figure 2.8(II). In its simplest form, the Wheatstone's bridge is an electric circuit containing four arms (a-d) with one resistor each. A particular feature of this electrical circuit is that when the ratio of the resistors is $R_b/R_a = R_d/R_c$, no current will flow between points (1) and (2), and the bridge is said to be "balanced". In HWA applications, one of the resistors is replaced by the HWA probe and a second one is replaced by a variable resistor, as shown in figure 2.8(II) for arm (c) and (d).

Before the bridge is initiated, the probe operating resistance must be determined

[17] Miniature boundary-layer probe manufactured by Dantec (dantec-dynamics.com), model: 55P15
[18] CTA bridge manufactured by TSI (tsi.com), model: IFA-300

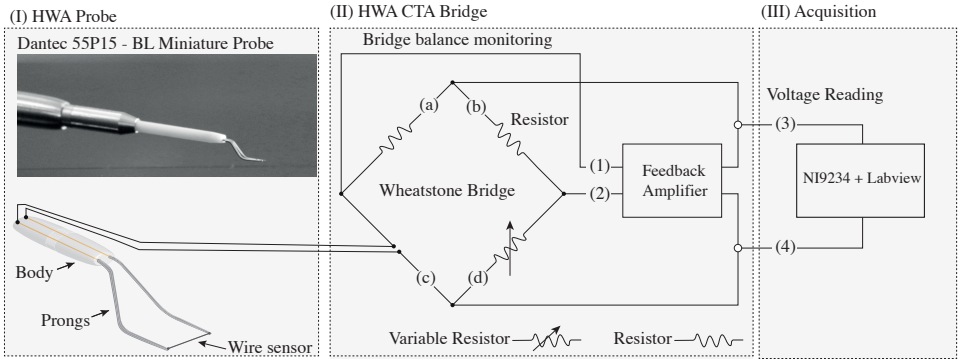

Figure 2.8: Schematic of Constant Temperature Anemometer (CTA) hot-wire system: (I) Hot-wire boundary-layer probe. (II) Constant temperature Wheatstone's bridge simplified electric diagram based on [157]. (III) Digital Acquisition system.

and the variable resistor adjusted so that the bridge starts in an unbalanced condition (i.e. electrical current between points 1 and 2). A feedback amplifier senses the unbalanced bridge and automatically changes the temperature-dependant resistance[19] of the tungsten wire sensor by increasing the current of the circuit until the operating conditions where the bridge is in balance [see 157, 158, pp.93-98, pp.45-48]. From this point onwards, any variation in the wire-sensor through convective heat transfer by the surrounding fluid will be compensated by the feedback amplifier to maintain a constant wire-sensor resistance and temperature (i.e. Constant Temperature Anemometer).

A digital acquisition system[20] (figure 2.8III) registers and converts the change in voltage across the bridge (i.e. point 3 and 4) into the corresponding flow velocity based on an in-situ calibration. The calibration procedure entails measuring simultaneously the HWA voltage and a reference flow velocity using a pitot-static probe. Then a relation between the output voltage and flow velocity is determined by fitting a fourth-order polynomial through the measurements at different reference velocities [see 158, pp.92-101]. When applying this calibration curve, a correction for variations in atmospheric pressure and flow temperature is applied [see 159].

The orientation of the probe's wire-sensor is essential to understand the measured velocity. A single-wire probe, such as the Dantec 55P15, offers a very compact design and simple operation at the expense of the inability to differentiate between velocity components and their direction, leading to a forward-reverse flow ambiguity [see 158, pp.234-264]. Jørgensen [160] proposes that the effective velocity measured by the wire-sensor is given by equation 2.2 [see 158, pp.71-73].

$$Q = \sqrt{q_n^2 + k^2 q_t^2 + h^2 q_b^2}. \tag{2.2}$$

As shown in figure 2.9, this is a combination of the velocity normal (q_n), tangential

[19] The sensor resistance is given by: $R_s = R_o(1 + \alpha(Ts - T_o))$, R_o and T_o is the reference sensor resistance and temperature and α is the material-dependent temperature coefficient of resistivity [157, pp.36-39]

[20] DAQ system manufactured by National Instruments (ni.com), chassis: NI cDaq-9174, modules: NI9234

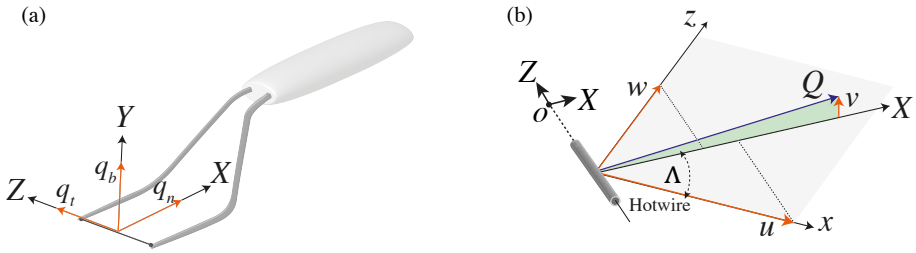

Figure 2.9: Schematic of HWA probe orientation: (a) Probe velocity decomposition into tangential (q_t), normal (q_n) and binormal (q_b) to the wire sensor. (b) Orientation of the wire-sensor effective velocity Q with respect to the swept wing leading edge aligned velocity components (u, v, w).

(q_t) and bi-normal (q_b) to the wire-sensor. The contribution of the q_t and q_b is determined by a yaw (k) and pitch (h) factors. Although these factors can vary between individual probes, an accepted value for a standard plated hot-wire probe is 0.2 and 1.05, respectively [158, pp.71-73].

In all the measurements, the wire-sensor of the HWA probe is mounted vertically (i.e. aligned to the Z axis) and orthogonal to the X-coordinate direction, as illustrated on the diagram in figure 2.9(b). Therefore, based on the relation proposed by equation 2.2, the effective velocity measured by the HWA is given by equation 2.3.

$$Q = \sqrt{(u\cos\Lambda + w\sin\Lambda)^2 + k^2(w\cos\Lambda - u\sin\Lambda)^2 + h^2 v^2} \tag{2.3}$$

Considering the higher sensitivity of the wire-sensor to the velocity component normal to the wire (q_n) and the nearly-parallel orientation of the prongs to the model's surface, the velocity conversion in this work is simplified as: $Q^2 = (u\cos\Lambda + w\sin\Lambda)^2 + v^2$.

The LTT wind tunnel facility is equipped with an automated traversing system capable of translating the HWA probe along the X, Y and Z directions with a resolution of 2.5 µm in each axis. The probe is mounted on a counterbalanced steel sting of approximately 2.5 meters long. Despite the heavy construction of the sting, inevitable mechanical vibrations affecting the measurements within the characteristic resonance frequencies are detected. Eppink and Wlezien [151] present an effective method to verify these vibrations by bandpass filtering the velocity fluctuations at the frequency of interest and qualitatively comparing the resulting flow-field with the time-average wall-normal velocity gradients.

Additionally, special care must be taken to avoid any electromagnetic interference (EMI) from the traversing system's stepper motors or the wind tunnel's engine. A practical strategy to minimize the EMI is to wrap the cable connecting the HWA probe to the Wheatstone's Bridge around several toroid magnets[21] to form a "coil-like" arrangement. Moreover, it is recommended to ground all the HWA electrical systems and connect them to a clean power supply.

A series of wall-normal boundary layer scans were conducted along the z-direction to form measurement planes at different streamwise locations to characterize the de-

[21] Toroid epoxy covered magnets manufactured by Ferroxcube (ferroxcube.com), model: TX36/23/15-3E5

velopment of the CF instability. At each X/c_X station, the measurement plane's starting position along the span has been adjusted using reference IR measurements to track the evolution of the CF vortices. Furthermore, when performing boundary-layer HWA measurements, is important to consider that the measurement points near the wall are affected by spurious heat transfer, leading to the so-called "tail". Hence, it is customary to commence the measurements at a given position away from the wall and later retrieve the wall location through extrapolation of the velocity profile [see 161]. In addition, the use of a micro alignment telescope[22] has been proven to be a valuable tool to monitor the position of the wire near the wall.

2.2.3. PARTICLE IMAGE VELOCIMETRY

Particle Image Velocimetry (PIV) is an optical flow measurement technique which indirectly determines a fluid's velocity through the displacement of tracing particles. A major advantage of PIV over single point-measurements (e.g. HWA, Laser Doppler Velocimetry and pressure measurements) is the spatial correlation of the velocity measurements. Thus, depending on the PIV variant used, two or three velocity components can be measured instantaneously in an entire plane (i.e. Planar PIV 2D2C and Stereo PIV 2D3C) or volume (i.e. Tomographic PIV 3D3C). A complete overview of fundamental and practical aspects for the use of PIV can be found in Adrian and Westerweel [162] and Raffel *et al.* [163].

In the experiments presented in Chapter 4, planar PIV (i.e. two velocity components measured in a plane 2D2C) is extensively used to characterize the impact of an FFS on the development of CF vortices. Figure 2.10(I) schematically presents the main elements of a planar PIV measurement system: (a) tracer particles; (b) illumination unit; (c) imaging unit. In addition, figure 2.10(II) shows a photograph of the planar PIV system on the top part of the LTT test-section during measurements on the M3J swept wing model. In the remainder of this section, a brief overview of each element used during the experiments is presented. More detailed information on each PIV subsystem can be found in Adrian and Westerweel [162] and Raffel *et al.* [163].

During the measurements, the wind tunnel's closed circuit is homogeneously seeded with water-glycol droplets[23] using a specialized fog machine[24] located in a vent on the diffusor (section 7 in figure 2.1) downstream of the test section.

The principal assumption in a PIV system is that the tracer particles faithfully follow the fluid's motion. The metric used to asses the tracing fidelity of the particles is given by the Stokes number (Stk = τ_p/τ_f), which indicates the ratio of the particle response time (τ_p)[25] to a characteristic time of the fluid fluctuations (τ_f)[26]. An adequate tracing fidelity for practical purposes is obtained when Stk < 0.1 [163, p.34]. For the experiments presented in Chapter 4, the tracing fidelity is Stk = 0.05 when considering twice the time period of the secondary CF instability of type-II (see figure 1.12) as the characteristic time of the fluid fluctuations (i.e. $\tau_f = 1/16000$).

[22] Micro alignment telescope manufactured by Taylor-Hobson (taylor-hobson.com), model: 112-2582

[23] Water-glycol average particle diameter and density: $\bar{d_p} \approx 1$ µm and $\rho_p \approx 1000$ kg/m^3

[24] Water-glycol fog machine manufactured by SAFEX GmbH (safex.de), model: Twin-Fog DP

[25] Particle's time delay to adapt to a fluid's velocity step change: $\tau_p = d_p^2(\rho_p/(18\mu))$ [163, p.34]

[26] According to Raffel *et al.* [163, p.34], in turbulent boundary layer cases τ_f can be: $\tau_f = \delta_{99}/u_e$.

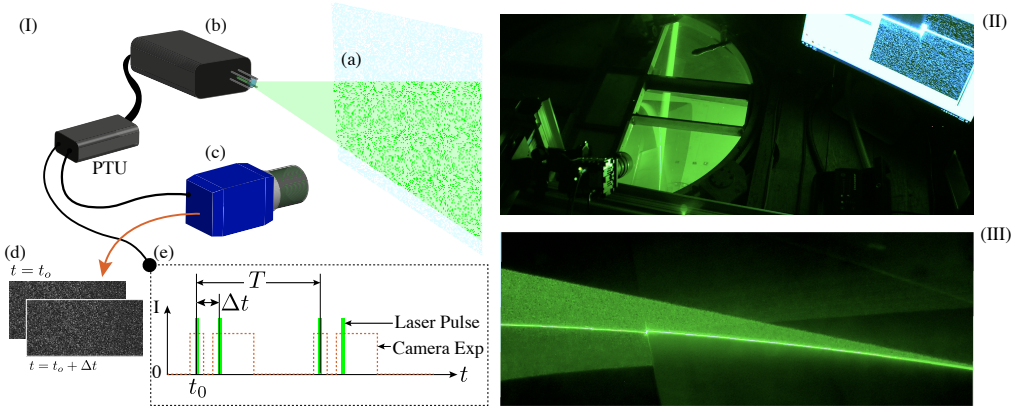

Figure 2.10: Planar PIV system: (I) Schematic of the system showing (a) Flow with tracer particles, (b) Laser unit , (c) Imaging system, (d) Resulting image pairs, and (e) Laser-image timing diagram for double-pulse operation. (II) Photograph of planar PIV system in operation at the LTT test-section. (III) Tracer particles in the laser-sheet across the FFS.

As the seeding recirculates in the closed circuit of the LTT wind tunnel, the seeding particles cross through the measurement region illuminated by a laser. This process is shown schematically in figure 2.10(Ia) and on actual PIV measurements on an FFS in the M3J swept wing in figure 2.10(III). The illumination unit consists of a low-repetition dual cavity 200 mJ Nd:YAG laser [27]. This dual-pulsed PIV laser operates in the green-light spectrum (i.e. $\lambda_L = 532$ nm) at a maximum repetition rate of 15 Hz. Through a set of carefully selected spherical and cylindrical optics [see 163, pp.77-80], the laser beam with a diameter of around 6.35 mm is shaped into a plane with a thickness of about one millimeter in the measurement region.

Images of the illuminated tracer particles at the measurement region are acquired by the imaging unit, as schematically shown in figure 2.10(Ic). The camera[28] features an sC-MOS sensor with a size of 2560 × 2160 pixels, a 6.5 µm pixel pitch (δ_{px}) and a digital output of 16-bit. The camera is located outside the wind tunnel as shown in figure 2.10(II). The selection of the most suitable camera objective (i.e. focal length) is dependent on the desired field of view (FOV) and the distance between the measurement plane and the camera. In particular, in the current experiments, the use of teleconverters[29] has proven to be a viable solution to increase the focal length of a given objective. In the experiments presented in Chapter 4, this optical configuration yields a magnification factor[30] of $M = 0.9$, necessary for the detailed measurement of the boundary layer flow near the FFS location.

The PIV system is operated in a double-frame/single exposure mode; a synchronization diagram between the illumination and imaging units is shown in figure 2.10(Ie). The

[27] Dual-pulsed PIV laser manufactured by Quantel (quantel-laser.com), model: Evergreen^2 EVG00200.
[28] PIV camera adapted by LaVision (lavision.de), model: Imager sCMOS CLHS
[29] Teleconverter manufactured by Kenko (kenkoglobal.com), model: Teleplus HD-2X-DGX
[30] The optical magnification is the ratio of the image (z_0) to the object (Z_0) distance: $M = z_0/Z_0 = l_{px}\delta_{px}/L_O$

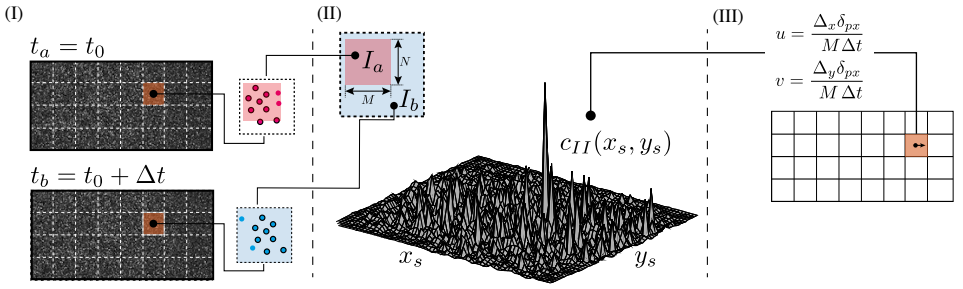

Figure 2.11: Schematic of PIV velocity evaluation: (I) Image pairs at time t_a and t_b. (II) Image cross-correlation map and interrogation window (I_a) and (I_b) discretization. (III) Velocity evaluation using particle displacement (Δ_x and Δ_y), pixel pitch (δ_{px}), optical magnification factor (M) and time interval between image pairs (Δ_t).

dashed orange lines indicate the exposure of the first and second frame while the green markers show the laser pulses. Starting at $t = t_0$, a pulse from the laser's first cavity is shot and the light scattered by the tracer particles is recorded in the image (i.e. first frame) as shown in figure 2.10(Id). Then, after a short time delay (Δt) the pulse from the laser's second cavity is shot and an image recorded on the second frame. The repetition rate of this process is given by the sampling frequency ($f_s = 1/T$).

For each measurement a set of image pairs at time $t_a = t_0$ and $t_b = t_0 + \Delta t$ are obtained, as shown in figure 2.11(I). Subsequently, each image at t_a and t_b is divided into interrogation windows (IW) where, the statistical particle shift on the images during the time delay Δt is obtained from a cross-correlation analysis. A description of the cross-correlation for general image analysis is found in Gonzalez and Woods [153, pp.915-917], while a detailed overview of its application to PIV measurements is found in Raffel *et al.* [163, pp.150-188].

In essence, the cross-correlation algorithm finds the horizontal (x_s) and vertical (y_s) shift resulting in the best match of similarity between two images. In the case of PIV, the shift required to match the particle intensity in the interrogation windows from the image pairs (figure 2.11II) determines the average displacement of the particles during the time delay Δt. The cross-correlation analysis involves moving around a template (I_a) from the interrogation window of the first frame (i.e. $t_a = t_0$) and comparing it to the corresponding region (I_b) extracted from the interrogation window of the second frame (i.e. $t_b = t_0 + \Delta_t$) by calculating the normalized correlation coefficient (c_{II}) given by equation 2.4. This process is repeated to form a map containing the values of the correlation coefficient (c_{II}) for all possible shifts (x_s and y_s), as schematically shown in figure 2.11(II). From the identification of the peaks, the average particle displacement in the horizontal (Δ_x) and vertical (Δ_y) direction is determined. Thereafter, using the cameras pixel pitch (δ_{px}) and the optical magnification factor[31] (M) (obtained from a physical-space transformation based on an optical calibration target with known markers) the average velocity is calculated using the time delay Δt as shown in figure 2.11(III).

[31] The optical magnification is the ratio of the image (z_0) to the object (Z_0) distance: $M = z_0/Z_0 = l_{px}\delta_{px}/L_O$

$$c_{II}(x_s, y_s) = \frac{\sum_{i=0}^{M}\sum_{j=0}^{N}\left[I_a(i,j) - \bar{I}_a\right]\left[I_b(x_s+i, y_s+j) - \bar{I}_{b,x_s y_s}\right]}{\left\{\sum_{i=0}^{M}\sum_{j=0}^{N}\left[I_a(i,j) - \bar{I}_a\right]^2 \sum_{i=0}^{M}\sum_{j=0}^{N}\left[I_b(i,j) - \bar{I}_{b,x_s y_s}\right]^2\right\}^{\frac{1}{2}}} \tag{2.4}$$

Therefore, the adjustment[32] of Δt during the experiment is of great importance. A short Δt will result in nearly no particle motion between image pairs, while with a large Δt the particle pattern will differ entirely. During the experiments presented in Chapter 4, an average particle displacement of 12 px was obtained in the free-stream. In this work, Davis 10 software by LaVision was used for the laser synchronization, image acquisition and evaluation using an advanced multi-stage cross-correlation [e.g. 163, pp.169-182].

In addition, an important consideration is the seeding density measured as particles per unit pixel area ($N_{ppp} = N_I / IW^2$). A low concentration would lead to a small number of image particles (N_I). Furthermore, the out-of-plane[33] (F_O) and in-plane[34] (F_O) loss of pairs could lead to an even lower number of effective particles ($N_p = N_I F_I F_O$) on which the cross-correlation is evaluated. A practical recommendation given by Raffel *et al.* [e.g. 163, p.224] is that $N_p > 5$ for an accurate estimation of the particle displacement.

2.2.4. MEASUREMENT ERRORS

The errors in a measurement technique can be categorized into systematic errors (i.e. also known as bias) and random errors. During a measurement, the magnitude and sign of the systematic errors (minimized with calibration) is fixed, while the ones of the random errors vary. A general overview of uncertainty analysis methods to estimate these errors can be found in Coleman and Steele [164].

A detailed description of the different measurement errors inherent to the use of HWA can be found in Bruun [158]. Error sources in HWA are related to: HWA probe disturbances, velocity calibration, signal interpretation in high-turbulence intensity, and reversed flow ambiguity. In the case of PIV, Sciacchitano [165] presents a detailed overview of the different error sources affecting the measurements. Error sources in PIV are related to: misalignment and synchronization of the system, particle tracing capability, imaging of the particles, laser-light illumination, flow topology, and image evaluation techniques.

Considering that the known systematic errors in the measurement techniques have been corrected, the uncertainty of the random errors in the velocity mean value ($U_{\bar{u}}$) and standard deviation (U_{σ_u}) of a measurement series can be estimated following the methodology described by Sciacchitano and Wieneke [166] using equations 2.5 and 2.6.

$$U_{\bar{u}} = \frac{\sigma_u}{\sqrt{N_{\text{eff}}}} \tag{2.5}$$

$$U_{\sigma_u} = \frac{\sigma_u}{\sqrt{2(N_{\text{eff}} - 1)}} \tag{2.6}$$

[32] A Δt which leads to a particle movement of 1/4 of the initial IW is often adequate Raffel *et al.* [163, p.156]
[33] Out-of-plane factor: $F_O = (1 - |\Delta z|/\Delta z_0)$ [163, p.207]
[34] In-plane factor: $F_I = (1 - |\Delta x|/D_I)(1 - |\Delta y|/D_I)$, with multipass $F_I \to 1$ [163, p.207]

Where σ_u is the sample standard deviation[35] of the measurement series and N_{eff} is the effective number of samples. When the samples are uncorrelated in time, the total number of measurements N_{T} can be used as $N_{\text{T}} = N_{\text{eff}}$. In this dissertation, this condition occurs for the PIV measurements due to the low sampling frequency (i.e. f_s = 15Hz). Instead, the high sampling frequency (i.e. f_s = 51.2 kHz) of the HWA leads to measurements correlated in time. In this case, the effective number of samples $N_{\text{eff}} = N_{\text{T}}/(2T_I/\Delta t)$ is based on the integral time scale T_I. Smith *et al.* [167] describe in detail the methodology to determine the integral time-scale T_I from the autocorrelation of the measurement series. An indication of the average random error for the time-average PIV and HWA results inside the boundary-layer can be obtained using equations 2.5 and 2.6. For the PIV measurements: $\overline{\text{U}}_{\bar{w}} = 0.11\,\%w_e$, $\overline{\text{U}}_{\sigma_w} = 0.10\,\%w_e$ and $\overline{\text{U}}_{\bar{v}} = 0.08\,\%w_e$, $\overline{\text{U}}_{\sigma_v} = 0.07\,\%w_e$. For the HWA measurements $\overline{\text{U}}_{\bar{Q}} = 0.18\,\%Q_e$ and $\overline{\text{U}}_{\sigma_Q} = 0.13\,\%Q_e$.

Finally, the spatial resolution is an important limitation of any measurement technique. Considering that the hot-wire sensor length is parallel to the surface, the maximum spatial resolution in the vertical direction is given by the diameter of the wire ($d_w \approx 5\mu$m), while in the case of the PIV, the maximum spatial resolution is given by the interrogation window and overlap considered. In the experiments presented in Chapter 4, the final interrogation window is 12×12 pixel (80 × 80 µm) at 75% overlap which results in a final vector spacing Δ_y of 20µm. An indication of the size of the smallest eddies in a turbulent flow are indicated by the Kolmogorov length $\eta \sim (\nu^3/\epsilon)^{1/4}$ and time $\tau_\eta \sim (\nu/\epsilon)^{1/2}$ microscales [see 168, p.20]. Approximating the kinetic energy dissipation rate as $\epsilon \sim u_e^3/\delta_{99}$, at conditions[36] representative of the experiment in this dissertation: $\eta \sim 4.8\mu$m, $\tau_\eta \sim 1.6\mu$s, and $f_\eta \sim 623$kHz. Comparing these values to the resolution and acquisition frequency of the measurement techniques, highlights the inherent limitations when conducting experiments.

However, of special importance to the experiments in this dissertation are two ratios. The first one is the ratio of the smallest step height (h) to the final spacing (Δ_y) of the velocity measurements. The second, the ratio of the maximum frequency of interest (f_I)(i.e. type-II secondary instability $f_I \approx 8000$ Hz) to the sampling frequency of the measurements (f_s). In Chapter 4, for the PIV measurement $h_{A_3}/\Delta_y \approx 18$ and $f_s/f_I \approx 0.002$, while in Chapter 5, using the HWA measurements $h_A/\Delta_y \approx 5$ and $f_s/f_I \approx 6$.

2.3. NUMERICAL METHODS

The approximate spanwise invariant conditions shown in the measured pressure distribution in figure 2.3(c), indicate the adequacy of the infinite swept wing assumption. Based on this assumption, and using the measured pressure distribution, laminar boundary layer solutions and their linear stability are calculated using an in-house numerical code. This in-house solver has been previously used in the study of swept wing flows [e.g. 71, 75, 108, 169]

An important consideration for this dissertation is that the numerical analysis of the boundary-layer is only conducted on cases without FFS and only used to determine ref-

[35] The sample standard deviation is given by: $\sigma_u = \sqrt{(1/(N_T-1))\sum_{i=1}^{N_T}(u_i-\bar{u})^2}$

[36] Estimation of Kolmogorov microscales based on: $u_e = 24.6\ [m/s]$, $\nu = 14.17\times10^{-6}\ [m^2/s]$ and $\delta_{99} = 2.7\ [mm]$

erence parameters such as: displacement thickness at the step position (δ_h^*), nominal spanwise wavelength for the DRE ($\lambda_{z,D}$), and estimated CF vortices core height y_c [see 129].

LAMINAR BOUNDARY-LAYER SOLUTION

The boundary-layer is solved perpendicular to the leading edge with coordinate system x, y, z (figure 2.3a) and velocity components given by u, v and w. The dynamics of an incompressible three-dimensional (3D) flow are governed by the continuity (equation 2.7a) and the momentum (equation 2.7b-2.7d) equations. A simplified form of these equations is obtained when considering the steady solution of a boundary-layer flow in a swept wing of infinite span [see 30, 170, pp.223-224, pp.342-344]. As an indication, the terms discarded during the simplification of equation 2.7 are color shaded.

$$\frac{\partial u}{\partial x} + \frac{\partial v}{\partial y} + \frac{\partial w}{\partial z} = 0 \tag{2.7a}$$

$$\frac{\partial u}{\partial t} + u\frac{\partial u}{\partial x} + v\frac{\partial u}{\partial y} + w\frac{\partial u}{\partial z} = -\frac{1}{\rho}\frac{\partial p}{\partial x} + \nu\left(\frac{\partial^2 u}{\partial x^2} + \frac{\partial^2 u}{\partial y^2} + \frac{\partial^2 u}{\partial z^2}\right) \tag{2.7b}$$

$$\frac{\partial v}{\partial t} + u\frac{\partial v}{\partial x} + v\frac{\partial v}{\partial y} + w\frac{\partial v}{\partial z} = -\frac{1}{\rho}\frac{\partial p}{\partial y} + \nu\left(\frac{\partial^2 v}{\partial x^2} + \frac{\partial^2 v}{\partial y^2} + \frac{\partial^2 v}{\partial z^2}\right) \tag{2.7c}$$

$$\frac{\partial w}{\partial t} + u\frac{\partial w}{\partial x} + v\frac{\partial w}{\partial y} + w\frac{\partial w}{\partial z} = -\frac{1}{\rho}\frac{\partial p}{\partial z} + \nu\left(\frac{\partial^2 w}{\partial x^2} + \frac{\partial^2 w}{\partial y^2} + \frac{\partial^2 w}{\partial z^2}\right) \tag{2.7d}$$

The assumption of an infinite span leads to a spanwise invariant condition where $\partial/\partial z = 0$ (i.e. terms in $\square$ discarded) and a constant spanwise velocity external to the boundary-layer flow $w_\infty = w_e = \text{cst}$. Moreover, the consideration of a steady solution implies $\partial/\partial t = 0$ (i.e. terms in $\square$ discarded). Lastly, the 2.5D formulation (equation 2.8) is obtained by discarding the remaining terms in $\square$, after an order of magnitude analysis[37] using the boundary-layer assumptions (i.e. $u >> v$, $w >> v$ and $\delta << c_x$). Note that, in the 2.5D formulation, the z-momentum equation (equation 2.8c) is decoupled from the others.

$$\frac{\partial u}{\partial x} + \frac{\partial v}{\partial y} = 0 \tag{2.8a}$$

$$u\frac{\partial u}{\partial x} + v\frac{\partial u}{\partial y} = -\frac{1}{\rho}\frac{\partial p}{\partial x} + \nu\frac{\partial^2 u}{\partial y^2} \tag{2.8b}$$

$$u\frac{\partial w}{\partial x} + v\frac{\partial w}{\partial y} = \nu\frac{\partial^2 w}{\partial y^2} \tag{2.8c}$$

An important implication of the boundary-layer assumptions for experimental measurements is that the pressure variation across (i.e. $\partial p/\partial y \approx 0$) the boundary layer is

[37] Analogous to the process in 2D boundary layers [see 30, pp.145-149]

negligible . Thus, the static pressure measured at the wall can be used to determine the external velocity distribution (u_e) and used as a top boundary condition (i.e. $u|_{y=\infty} = u_e$ and $w|_{y=\infty} = w_e = w_\infty$) for the numerical calculations considering that $\partial p/\partial x = -\rho u_e(du_e/dx)$.

The external velocity distribution $u_e(x)$ is determined from the experiments by first decomposing the wind tunnel free-stream velocity (U_∞) into the respective streamwise ($u_\infty = U_\infty \cos\Lambda$) and spanwise ($w_\infty = U_\infty \sin\Lambda$) components. Then, using the measured pressure coefficient C_p (equation 2.1), the total velocity external to the boundary-layer is calculated using equation 2.9a. Finally, based on the infinite swept wing condition (i.e. $w_\infty = w_e = \text{cst}$) the external velocity of the boundary layer $u_e(x)$ is calculated using equation 2.9b. In addition, the no-slip ($u|_{y=0} = w|_{y=0} = 0$) and non-penetration ($v|_{y=0} = 0$) boundary conditions are specified at the wall when solving the 2.5D boundary-layer equations.

$$U_e(x) = \sqrt{\left(1 - C_p(X)\right) U_\infty^2} \tag{2.9a}$$

$$u_e(x) = \sqrt{U_e(X)^2 - w_\infty^2} \tag{2.9b}$$

Based on the experimental conditions, the in-house TU Delft code solves equations 2.8a-2.8c in an orthogonal grid (airfoil curvature not accounted) through a marching method along a stretched x-coordinate matching the length of the surface coordinate on the airfoil. The marching method is initiated using a Falkner-Skan-Cooke solution [see 171]. The discretization in the stream-wise direction follows a second-order finite difference, while a Chebyshev spectral collocation method is used for the wall-normal direction [see 172, 173, Ch.3].

STABILITY ANALYSIS

The stability analysis concerns the evaluation of the amplification or decay of disturbances in a steady laminar boundary-layer solution known as baseflow. An overview of stability analysis is provided in Schlichting and Gersten [30], Mack [171], and Criminale *et al.* [174]. In particular, the linear stability theory (LST) formulation has been traditionally used in the study of different boundary-layer flows [see 45, 175].

Detailed reviews of different stability methods in swept wing flows can be found in Bippes [34], Arnal and Casalis [70], and Reed *et al.* [175]. An important consideration when studying the stability of boundary-layers dominated by CF instability is that the amplification curves (i.e. N-factors) are highly dependent on the employed stability formulation given possible nonlinear effects developing at late stages of the amplification and transition of CF instability modes [see 176]. Due to its simplicity, the LST formulation has been previously used in the design and analysis of experiments to estimate the spanwise wavelength (λ_z), frequencies (ω), propagation angle ($\Psi = \arctan(\beta_r/\alpha_r)$), and core-height ($y_c$) of the CF vortices [e.g. 34, 71, 108, 129]. Accordingly, in this dissertation, LST is used as an additional tool for the design of the experiments.

The stability of the boundary-layer solution obtained from the 2.5D formulation (equation 2.8) is evaluated only for reference cases without FFS using the Orr-Sommerfeld (OS) equation. Boundary-layer stability analysis aims to estimate the amplification or decay

of small velocity and pressure perturbations. Therefore, the instantaneous components $\mathbf{q} = \langle u, v, w, p \rangle$ are decomposed into a perturbation $\mathbf{q}' = \langle u', v', w', p' \rangle$ and a baseflow $\bar{\mathbf{q}} = \langle \bar{u}, \bar{v}, \bar{w}, \bar{p} \rangle$ the decomposition is given by equation: $\mathbf{q} = \bar{\mathbf{q}} + \mathbf{q}'$

Considering the parallel-flow assumption, which implies that the baseflow is dependent on the (y) coordinate and the wall-normal velocity $\bar{v} \approx 0$, the aforementioned decomposition is substituted into equation 2.7. Thereafter, the nonlinear terms (i.e. the product of perturbations) are discarded by considering that the amplitude of the perturbations is small when compared to the baseflow components. The result is a set of linearized parallel-flow perturbation equations. A detailed description of the aforementioned procedure can be found in Mack [171] and Saric [177].

The LST formulation assumes a wave-like solution[38], as indicated in equation 2.10. In this ansatz, the shape of the vertical perturbation is given by $\phi_q(y)$, the streamwise and spanwise wavenumber are given by α and β, and the frequency by ω.

$$q'(x, y, z, t) = \phi_q(y) e^{i(\alpha x + \beta z - \omega t)} \tag{2.10}$$

When the perturbations amplify in time, the wavenumbers ($\alpha = \alpha_r$ and $\beta = \beta_r$) are considered real numbers[39] (i.e. no amplification in space) and the frequency (ω) complex (i.e. temporal formulation). Instead, when the perturbations amplify in space (i.e. spatial formulation), the frequency is considered real ($\omega = \omega_r$) and the wavenumbers complex (i.e. $\alpha = \alpha_r + \alpha_i$ and $\beta = \beta_r + \beta_i$). In the spatial formulation, the imaginary parts of the wavenumbers (i.e. α_i and β_i) determine the spatial growth[40] and their sign will indicate if the baseflow is stable ($\alpha_i > 0$ or $\beta_i > 0$), neutral ($\alpha_i = 0$ or $\beta_i = 0$) or unstable ($\alpha_i < 0$ or $\beta_i < 0$) to the disturbances under consideration.

The stability of the baseflow is then evaluated using the Orr-Sommerfeld (OS) equation 2.11. The OS equation is obtained by substituting the LST ansatz into the linearized parallel-flow perturbation equations. Then, these equations are recast into a single fourth-order equation in terms of the vertical perturbation eigenfunction ϕ_v given by equation 2.11. A detailed description of the steps involved in obtaining the OS equation can be found in Mack [171] and Saric [177].

$$\left(\frac{d^2}{dy^2} - \alpha^2 - \beta^2\right)^2 \phi_v - Re\left[-i\alpha \frac{d^2\overline{u}}{dy^2} - i\beta \frac{d^2\overline{w}}{dy^2} + (i\alpha\overline{u} + i\beta\overline{w} - i\omega)\left(\frac{d^2}{dy^2} - \alpha^2 - \beta^2\right)\right]\phi_v = 0 \tag{2.11}$$

When analysing cases dominated by CF instability, it is customary to use the spatial stability formulation (i.e. α and β are complex and ω is real). This assumption is based on experimental evidence [see 34], which showed the convective (i.e. spatial, rather than temporal growth) nature of the instability. This implies that in the case of stationary CF disturbances in an infinite swept wing, the frequency is $\omega_r = 0$ and the spanwise growth is $\beta_i = 0$. In addition, the spanwise wavenumber ($\beta_r = 2\pi/\lambda_z$) is specified depending

[38] Considering Eulers' formula: $e^{i\theta} = \cos\theta + i\sin\theta$

[39] Note that the subscript r is used for real numbers while i is used for the imaginary ones.

[40] Substituting the complex form of the wavenumbers into equation 2.10: $e^{-(\alpha_i x + \beta_i z)} e^{i(\alpha_r x + \beta_r z - \omega t)}$

on the spanwise wavelength (λ_z) of the stationary CF instability mode of interest. As a result, the solution of the OS equation (equation 2.11) leads to the determination of $\alpha = \alpha_r + \alpha_i$ given a fixed Re,β_r,ω_r and the baseflow profiles $\overline{u}$ and $\overline{w}$.

An important consideration to solve equation 2.11 is that the perturbations must follow the no-slip and non-penetration boundary conditions at the wall and decay at an infinite distance from it. Thus, the boundary conditions are given by: $\phi_v|_{y=0} = d\phi_v/dy|_{y=0} = 0$ and $\phi_v|_{y=\infty} = d\phi_v/dy|_{y=\infty} = 0$. The stability calculations are performed with an in-house numerical code using Chebyshev spectral collocation and the companion matrix method for the treatment of the eigenvalue problem given by the OS equation [see 172, 178, Ch.3].

Finally, the amplification curve (N-factor) of individual stationary CF instability modes can be estimated by integrating the spatial growth rate (α_i) at a fixed spanwise wavelength ($\lambda_z = 2\pi/\beta_r$) and frequency ($\omega_r = 0$) along the x coordinate following equation 2.12 [see 70].

$$N(x,\lambda_z,\omega) = -\int_{x_0}^{x_L} \alpha_i(x,\lambda_z,\omega)\,dx \tag{2.12}$$

Where x_0 is the first position at which the CF instability mode becomes unstable. The final result of the stability analysis is the envelope ($N_{env}(x,\omega) = \max|_{\lambda_z}\{N(x,\lambda_z,\omega)\}$) of N-curves of unstable spanwise wavelengths of the stationary CF instability modes considered during the analysis.

Part II

Experiments

3

Influence on transition behaviour

This chapter considers the influence of the forward-facing step on the laminar-turbulent transition behaviour under unforced (i.e. smooth leading edge) and forced conditions (i.e. using discrete roughness elements). The results reveal the importance of considering multiple parameters when estimating the critical FFS height. The unforced cases indicate that one-parameter correlations (i.e. based on the crossflow vortex core height or boundary-layer displacement thickness) are not sufficient to universally capture the dynamics of these complex flows. Analysis of the forced cases shows that in addition to local parameters (i.e. step height and vortex core height), the FFS influence on transition depends on the stability characteristics of the incoming instability mode.

Parts of this chapter are published in:

- Rius-Vidales, A.F. & Kotsonis, M. 2020 Influence of a forward facing step surface irregularity on swept wing transition. AIAA Journal **58(12)**, 5243-5253.

3.1. BACKGROUND

As described in §1.3, the quest to find the critical step height at which an FFS will produce an adverse effect on the boundary-layer transition (i.e. transition advancement) of a swept wing flow has motivated a number of investigations. Specifically, Tufts *et al.* [129] performed a detailed numerical investigation and proposed the Tufts-Reed criterion as a method to estimate the critical FFS height that will cause transition advancement. The criterion is based on the observation that due to the inherent spanwise pressure gradient found in swept wings, the local recirculation region upstream and downstream of the FFS edge will take the form of a helical flow travelling from root to tip for a backward-swept wing. The Tufts-Reed criterion suggests that when the step height is higher than the core height of the incoming CF vortices, a constructive interaction occurs between the CF vortices and the downstream helical flow. Thereupon, this interaction leads to a transition advancement and amplification of the stationary CF vortices.

Subsequent experimental investigations by Eppink [136] and Eppink & Casper [135] found no evidence that could support the proposed physical mechanism upon which the criterion is based. Instead, they observed that as the CF vortices approach the FFS, they lift off the surface and do not directly impinge on the step edge. In addition, Eppink [137] observed a spanwise modulation of the local recirculation region (i.e. helical flow) downstream of the FFS edge, which resulted in isolated flow regions and vortex shedding.

Even though Eppink and Casper [135] are in agreement with the observations made by Tufts *et al.* [129], verifying that the interaction of the CF vortices with the FFS leads to their amplificaition, the results from Eppink [136] show that the initial amplitude of the stationary CF instability modes plays an important role in the transition dynamics. More specifically, premature transition for a previously subcritical FFS step height was observed when increasing the height of the DREs used near the leading edge in order to trigger and condition the CF instability mode.

Based on the aforementioned studies, the physical mechanisms which drive the interaction between the FFS and CF vortices remain partially unclear. Consequently, identifying the parameters necessary to adequately describe and scale transition behaviour in cases of FFS-CFI interaction assumes a pivotal role towards enabling LFC on practical aerodynamic surfaces. Up-to-date research mainly focuses on the isolated study of either unforced conditions (i.e. smooth leading edge) or single cases under a forced monochromatic CF instability mode induced by DREs placed near the leading edge. However, the systematic variation of Reynolds number and step height under both forced and unforced conditions is essential towards a better understanding of the salient interrelationship among key parameters.

Therefore, in agreement with the main research *Objective A* (presented in §1.4), local one-parameter correlations (i.e. based on CF vortex core height or boundary-layer displacement thickness) to estimate the critical FFS height are evaluated, and additional parameters which play an important role in the laminar-turbulent transition dynamics in cases of FFS-CFI interaction are identified by conducting a wind tunnel experiment where the FFS local and global influence on the laminar-turbulent transition is systematically varied in both unforced and forced cases for a wide range of conditions.

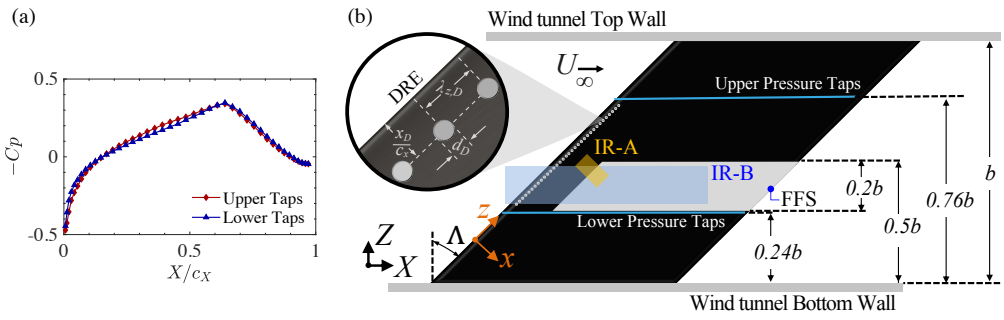

Figure 3.1: Experimental Setup: (a) Streamwise pressure distributions ($\alpha = 3°$, $Re_{c_X} = 3.7 \times 10^6$) measured on the pressure side (max $U_{Cp} = 0.001$). (b) General schematic showing the FFS location, the IR analysis regions (IR-A,IR-B) and details of the DREs. ($\Lambda = 45°$,$c_X = 1.27$ m ,$b = 1.25$ m).

3.2. EXPERIMENTAL SET-UP

3.2.1. INFLOW CONDITIONS AND SURFACE IRREGULARITIES

The experimental study has been carried out on the M3J swept wing model in the Low Turbulence Tunnel (LTT) described in §2.1.1. The measurements are conducted at a fixed angle of attack $\alpha = 3°$ and varying Reynolds number (Re_{cX}) between 2.5 and 4.5 million. The Reynolds number (Re_{cX}) used throughout is based on the reference (see §2.1.1) wind tunnel velocity (U_∞) and the streamwise chord length of the model c_X = 1.27m. As described in §2.1.1 at the operating conditions of interest (i.e. 25 m s^{-1} ≤ U_∞ ≤ 55 m s^{-1}) a low-turbulence intensity level (i.e. $Tu \leq 0.03\%$) has been reported for this wind tunnel facility.

The in-house designed M3J swept wing model described in §2.1.2 was installed in the LTT test section, as illustrated by the cross-sectional view in figure 3.1(b). The wind tunnel model pressure distribution was recorded by streamwise (X) oriented pressure taps connected to the multi-channel pressure scanner described in §2.1.2. From these measurements, the boundary-layer flow on the pressure side of the model was numerically solved following the procedure indicated in §2.3. Moreover, the small variation between the upper and lower pressure measurements ($\alpha = 3°$, $Re_{c_X} = 3.7 \times 10^6$) presented in figure 3.1(a) confirms the validity of the infinite swept wing conditions.

In this study, the laminar-turbulent boundary-layer transition is investigated under both unforced and forced conditions as shown in Table 3.1. In the forced cases, DREs were used to force single-wavelength fundamental CF instability modes. The roughness elements were manufactured in-house by laser cutting an adhesive transfer vinyl film.

As illustrated by figure 3.1(b) and indicated in Table 3.1, in all forced cases the DREs were installed at $x_D/c_x = 0.02$ downstream of the M3J model leading edge. Based on preliminary Linear Stability Theory (LST) estimations, the DREs were chosen to lie just upstream of the neutral point, corresponding to the particular mode.

FFS surface irregularities were designed and manufactured as add-ons for the M3J wind tunnel model, as described in §2.1.3. This work only considers sharp FFS geometries. The FFS step height was measured in-situ by traversing a Micro-Epsilon 2950-25

Table 3.1: Geometrical parameters of tested configurations and nominal DREs settings.

Unforced Cases (without DRE's)							
ID	$\bar{h}$ [µm]	σ_h [µm]	x_h/c_x	$\lambda_{z,D}$ [mm]	d_D [mm]	k_D[µm]	x_D/c_x
Clean-N	-	-	-	-	-	-	-
A-N	350	4	0.2	-	-	-	-
B-N	548	3	0.2	-	-	-	-
C-N	723	2	0.2	-	-	-	-
Forced Cases (with DRE's)							
ID	$\bar{h}$ [µm]	σ_h [µm]	x_h/c_x	$\lambda_{z,D}$ [mm]	d_D [mm]	k_D[µm]	x_D/c_x
Clean-F	-	-	-	4.5/5.5/7.5	2	100	0.02
A-F	350	4	0.2	4.5/5.5/7.5	2	100	0.02
B-F	548	3	0.2	4.5/5.5/7.5	2	100	0.02
C-F	723	2	0.2	4.5/5.5/7.5	2	100	0.02

laser line scanner (reference resolution of 2 µm) along the spanwise extent of the surface irregularity. The average step height ($\bar{h}$), standard deviation (σ_h), and streamwise location (x_h/c_x) of the FFS surface irregularity are presented in Table 3.1 for all cases.

3.2.2. INFRARED THERMOGRAPHY

Surface temperature measurements were acquired on the pressure side of the model using two Optris PI640 IR cameras (640px × 480px, uncooled focal plane array, 7.5-13 µm spectral range, NETID 75 mK). The colored regions in figure 3.1(b) delimit their analysis regions. The first camera (IR-A, zoom-view, $f = 41.5$ mm) covers an area in the vicinity of the FFS (160 mm × 80 mm centered at $X/c_X = 0.2$ and $Z/b = -0.06$), while the second camera (IR-B, wide-view, $f = 10.5$ mm) captures a larger portion of the model (1100 mm × 210 mm centered at $X/c_X = 0.29$ and $Z/b = -0.12$). During the measurements the model was continuously irradiated by seven halogen lamps to increase the thermal contrast on the IR images, as described in detail in §2.2.1.

For every measurement a time-average temperature map is calculated from a series of 55 images acquired at 3.7 Hz. Subsequently, an image perspective correction is performed on each temperature map to account for the airfoil curvature. Then, based on the concept presented by Raffel and Merz [154] and Raffel *et al.* [155] a differential infrared thermography (DIT) technique is applied on consecutive temperature fields with increasing Reynolds number. Next, the transition location is identified by calculating the gradient of the binarized DIT image ($\bar{I}_{DIT}$), and a linear fit of the transition front is calculated for the analysis region as described in detail in §2.2.1.

To analyze the local influence of the FFS, the field of view (FOV) of camera IR-A was rotated 45° (i.e. the sensor height was oriented parallel to the LE direction) as shown in figure 3.1(b) and a spatial power spectral density (PSD) analysis was performed on the thermal intensity profiles along the spanwise (z) component (i.e. height of the IR images) following the procedure described in §2.2.1. The spatial frequency resolution (i.e. smallest resolved wavelength) stemming from the Nyquist limit of the sensor is 0.8 mm.

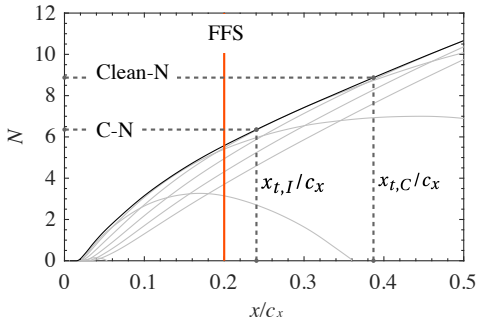

Figure 3.2: Envelope of N-Factors curves (Clean-N) for $\alpha = 3°$ and $Re_{c_X} = 3.7 \times 10^6$. Clean-N ($x_{t,C}/c_x = 0.39$, $N_C = 8.9$) and C-N ($x_{t,I}/c_x = 0.24$, $N_I = 6.4$).

3.2.3. STABILITY ANALYSIS

The stability of the laminar boundary-layer flow solution calculated from the measured pressure distribution from the Clean-N case (i.e. without FFS or DREs) was evaluated by solving the linear Orr-Sommerfeld equation (OS) using the spatial theory formulation [45] as described in detail in §2.3. The final result of the stability analysis is the envelope (N_{env}) of N-curves of unstable spanwise wavelengths of stationary CF instability modes.

As a means of comparison between the Clean-N case and the FFS cases, the change in the N-Factor ($\Delta N_{env} = N_{C,env} - N_{I,env}$) introduced by the FFS is used. This approach has been traditionally employed in the study of surface irregularities for both TS- and CF instability dominated cases [e.g. 115, 118, 119, 121, 179]. It is important to note that in contrast with TS waves dominated flows, the estimated ΔN values in CF instability dominated flows are highly dependent on the employed stability formulation given possible non-linear effects developing at the late stages of amplification and transition of CF instability modes. Therefore, in this work the ΔN approach is used exclusively as an additional metric to study the influence of the FFS and by no means a ΔN model or general conclusion regarding the modification of the stability curves by the FFS can be made.

To illustrate the ΔN methodology, consider the conditions $\alpha = 3°$ and $Re_{c_X} = 3.7 \times 10^6$. From the stability results in figure 3.2, it is possible to determine the N-Factors, based on the transition location for the Clean-N ($N_{C,\text{env}} = 8.9$) and the C-N ($N_{I,\text{env}} = 6.4$), and calculate the change in the N-Factor introduced by the FFS ($\Delta N_{\text{env}} = 2.5$).

Finally, as outlined by Tufts *et al.* [129], the core height (y_c) of the CF vortices can be estimated from a linear stability analysis based on the clean case (i.e. smooth no surface irregularities). This is done by calculating the wall-normal height of 97% of the maximum amplitude of the v-perturbation eigenfunction, corresponding to the most amplified (i.e. maximum N-factor) stationary CF mode at the step location x_h/c_x.

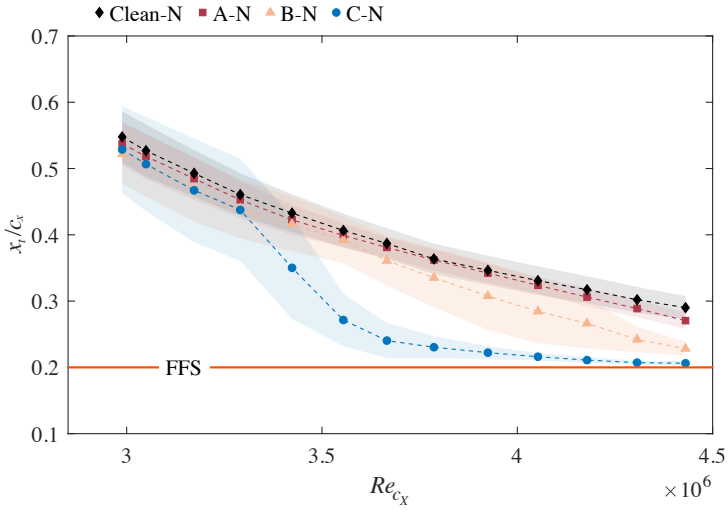

Figure 3.3: Transition location of unforced conditions for a range of Re_{c_X} at fixed $\alpha = 3°$. Shadowed regions indicated the confidence bounds of the transition identification linear fit.

3.3. UNFORCED CONDITIONS

This section presents the influence of an FFS surface irregularity on the unforced laminar-turbulent boundary-layer transition of a swept wing. The transition location and the spatial organization of the CF vortices for different FFS cases are determined based on IR measurements acquired and processed as detailed in §3.2.

3.3.1. GENERAL BEHAVIOR

The location of the transition front was determined for increasing Re_{c_X} at a fixed angle of attack ($\alpha = 3°$) from the "wide-angle" thermal images of camera IR-B by following the procedure outlined in §3.2.2. Figure 3.3 shows the results for the Clean-N and the different FFS cases (A-N, B-N, and C-N).

For the lowest $Re_{c_X} = 3.0 \times 10^6$, transition in the Clean-N case occurs at $x_{t,C}/c_x = 0.55$. From this condition onwards, an increase in Re_{c_X} leads to a gradual upstream movement of the transition front, reaching $x_{t,C}/c_x = 0.29$ at $Re_{c_X} = 4.4 \times 10^6$. When a short FFS (A-N: $\bar{h} = 350$ µm, see Table 3.1) is added, the transition behavior shows little to no difference when compared to the Clean-N case and only a slight deviation is observed for $Re_{c_X} > 3.9 \times 10^6$. As the FFS step height (h) is increased, the deviation from the Clean-N trend becomes increasingly evident. For the B-N ($\bar{h} = 548$ µm, see Table 3.1), this occurs for $Re_{c_X} > 3.5 \times 10^6$, while on the C-N case ($\bar{h} = 723$ µm,see Table 3.1), there is an abrupt deviation for $Re_{c_X} > 3.3 \times 10^6$, where the transition front rapidly reaches a location near the step ($x_{t,I}/c_x = 0.23$ at $Re_{c_X} = 3.8 \times 10^6$). Moreover, when transition does not occur near the FFS, a variation in the uniformity of the transition front is observed with increasing step height. This behavior could possibly be due to an enhancement of the amplitude differences of adjacent CF vortices by the FFS.

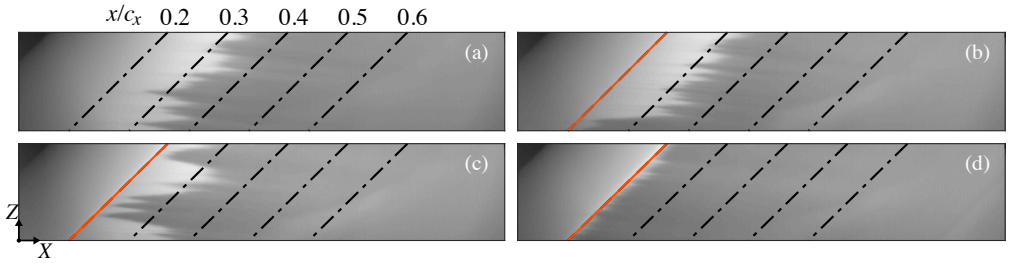

Figure 3.4: IR-B thermal maps (flow from left to right) displaying the effect of FFS (orange line) on the transition front pattern at the unforced condition $\alpha = 3°$ and $Re_{c_X} = 4.1 \times 10^6$: (a) Clean-N, (b) A-N, (c) B-N and (d) C-N.

Table 3.2: Measured to critical step height ratio for $Re_{c_X} = 4.1 \times 10^6$ at $\alpha = 3°$

Criteria	A-N ($\bar{h}/h_c$)	B-N ($\bar{h}/h_c$)	C-N ($\bar{h}/h_c$)
Perraud and Seraudie [118]	0.70	1.10	1.45
Duncan Exp Fit [see 129, 180]	0.62	0.97	1.28
Tufts *et al.* [129]	0.60	0.94	1.25

$\delta^*_h = 332$ µm, $y_c = 580$ µm

Three different regimes are identified for a fixed condition ($Re_{c_X} = 4.1 \times 10^6$ and $\alpha = 3°$). The A-N case is in the *subcritical* regime, since the laminar-turbulent transition process is nearly unaffected by the presence of the step (see figure 3.4b). Conversely, the B-N case (figure 3.4c) lays in the *critical* regime, as the transition location moves upstream towards the step location, departing from the Clean-N case trend (figure 3.4a). Finally, the C-N case is in the *supercritical* (i.e. tripped) regime, as transition occurs near or directly at the step (figure 3.4d).

Eppink [136] and Eppink and Casper [135], have shown in detailed experimental studies, that the process by which the stationary CF mode interacts with the FFS is rather complex as it is dependent on different factors such as: initial amplitude of the CF vortices, strength of the two recirculation regions in the vicinity of the step and its subsequent generation of CF reversal. Thus, further physical understanding of this interaction is required to improve the available critical step height criteria since, to the best of the authors knowledge, no general agreement has been reached regarding the local or global parameters that should be used to estimate the FFS critical step height in a swept boundary-layer.

Perraud and Seraudie [118] observed that the ratio between the step height (h) and the local boundary-layer displacement thickness (δ^*_h) provided an indication for criticality. Duncan [180] performed an empirical fit based on experimental data, and Tufts et al [129] presented the Tufts-Reed criterion based on the ratio of the FFS height (h) to the CF vortex core height (y_c), estimated through a linear stability analysis (§3.2.3) of the boundary-layer flow corresponding to the clean case (i.e. smooth no surface irregularities).

The ratio between the measured ($\bar{h}$) and the critical step height (h_c) predicted by

these different criteria is presented in Table 3.2. The critical ratio ($h/\delta_h^* = 1.5$) observed in Perraud and Seraudie [118] for CF instability dominated flows, leads to a slight under-prediction of the tolerable FFS step height with respect to the criteria proposed by Tufts *et al.* [129] and Duncan [180], as the latter predict a near critical condition for the case B-N.

It is important to note that as described by Tufts *et al.* [129], there is a difference among the definitions of the criteria. The definition presented by Duncan *et al.* [127] and Duncan [180] defines as critical the step height that which cause the movement of the transition location near or at the step. However, the definition presented by Tufts *et al.* [129] is based on the step height that will measurably affect the transition process, leading to a degradation of the laminar flow and amplification of stationary CF modes.

3.3.2. GLOBAL INFLUENCE

To characterize the global influence of the FFS on the laminar-turbulent boundary-layer transition, the reduction in the critical N-factor (i.e. ΔN) induced by the addition of the step was calculated for each case, as described in §3.2.3. The linear stability calculations (LST) were performed on a calculated boundary-layer flow based on the Clean-N pressure distribution. Additionally, the core height (y_c) of the CF vortices was estimated following the procedure described by Tufts *et al.* [129] and outlined in §3.2.3.

For the cases A-N, B-N and C-N, the resulting change in transition location ($\Delta x_t = (x_{t,I} - x_h)/(x_{t,C} - x_h)$) corresponding to different combinations of the ratio $\bar{h}/\delta_h^*$ and $y_c/\bar{h}$ is represented in figure 3.5(a). Note that, when Δx_t is close to unity, the addition of an FFS results in a negligible upstream shift of the transition location ($x_{t,I}$) with respect to the corresponding clean case ($x_{t,C}$). In contrast, when the value is close to zero, the transition location is near the step. Moreover, the change in the amplification factor ΔN-factors (§3.2.3) is presented in figure 3.5(b). When surveying these results, note that an increase in Re_{c_X} results in a decrease in δ_h^* and y_c.

Based on the identified transition location in figure 3.3 and the thermal visualizations of the transition front pattern presented in figure 3.6, it is clear that the B-N case behaves subcritically up until $Re_{c_X} = 3.5 \times 10^6$. An increase in Re_{c_X} ($y_c/\bar{h} = 1.16$, $\bar{h}/\delta_h^* = 1.57$ in figure 3.5a) changes the transition front pattern (see figure 3.6b), and the transition location departs from the trend indicated by Clean-N (see figure 3.3) and approaches the FFS location. Correspondingly, as transition occurs near the step (see figure 3.5a), there is a clear rise in ΔN induced by the step, see figure 3.5(b). A similar behavior at $Re_{c_X} = 3.4 \times 10^6$ occurs for the C-N case ($y_c/\bar{h} = 0.93$, $\bar{h}/\delta_h^* = 2$, in figure 3.5).

Comparing the case A-N to C-N in figure 3.5(b), indicates that when $y_c/\bar{h} >> 1$ the addition of an FFS results in a negligible effect in the laminar-turbulent transition process, which leads to a mild reduction in the N-factors. In contrast, when $y_c/\bar{h} << 1$ the transition process is highly affected by the FFS, resulting in a strong reduction of the N-factors. In this respect, the results are in agreement with the general behaviour observed by Rius-Vidales *et al.* [179]. Nevertheless, the results in figure 3.5 suggest that the $y_c/\bar{h}$ ratio corresponding to the critical regime is not unique since for the C-N case the critical condition occurs at a lower $y_c/\bar{h}$ and higher $\bar{h}/\delta_h^*$ ratio than the one of the B-N case.

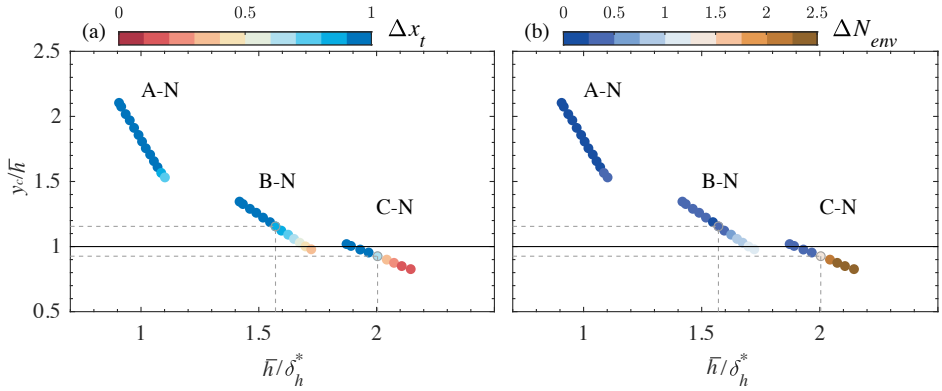

Figure 3.5: Change in (a) transition location (Δx_t) and (b) N-factor (ΔN) with varying estimated core height (y_c) of the CF vortices and boundary-layer displacement thickness (δ_h^*) for the unforced FFS cases (Table 3.1)

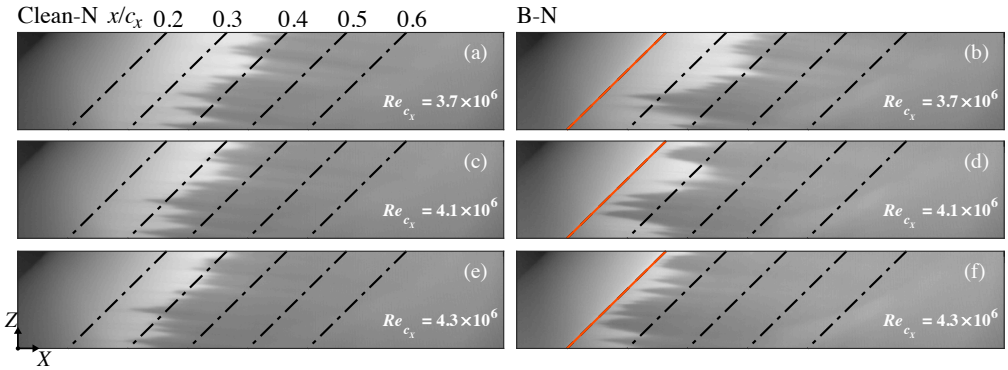

Figure 3.6: IR-B thermal maps (flow from left to right) displaying the FFS (orange line) effect on the transition front pattern at $\alpha = 3°$ and varying Re_{c_X} for the unforced Clean-N (a,c,e) and B-N (b,d,f) cases.

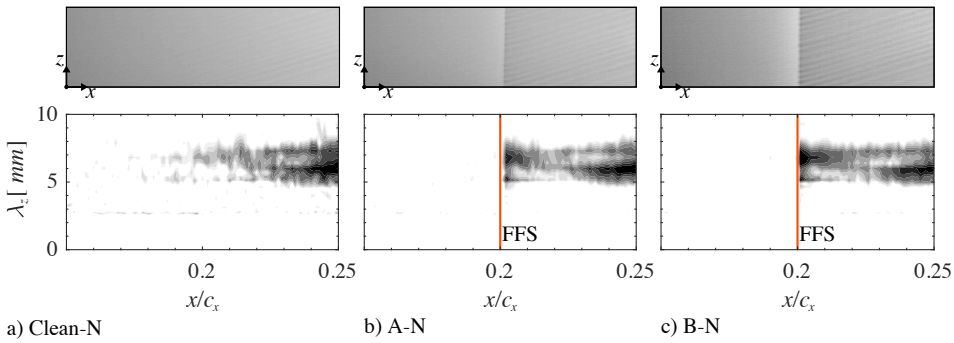

Figure 3.7: Comparison of IR-A thermal maps (top, flow from left to right) and spatial PSD analysis (bottom, ten levels of $\ln(P/\bar{P}_{\max_z})$ from -2.5 to 1) displaying the effect of an FFS (orange line) for the unforced condition $\alpha = 3°$ and $Re_{c_X} = 3.7 \times 10^6$.

3.3.3. LOCAL INFLUENCE

The local influence of the FFS on the laminar-turbulent boundary-layer transition process was studied using the camera IR-A "zoom-view", which images a region encompassing $0.15 \leq x/c_x \leq 0.25$ oriented as described at the end of §3.2.2. From these measurements it is possible to determine the stationary CF instability spatial organization by analyzing the time-average thermal footprint caused by wall shear stress of the CF vortices.

The IR-A thermal measurements and their corresponding spatial PSD analysis at $Re_{c_X} = 3.7 \times 10^6$ and $\alpha = 3°$ are presented in figure 3.7. The Clean-N case spatial PSD (figure 3.7a) suggests no identifiable dominant wavelength (λ_z) of the CF vortices up until $x/c_x = 0.23$, where there is an evident peak at a wavelength of $\lambda_z = 6$ mm.

The addition of a subcritical FFS (A-N: $\bar{h} = 350\,\mu$m) results in two distinct peaks with a clear wavelength and amplitude at the step location ($\lambda_z = 7$ mm and 5 mm at $x/c_x = 0.2$), which are very close to the dominant CF mode wavelength ($\lambda_z = 6$ mm), figure 3.7(b). As the step height is increased towards the critical condition (B-N: $\bar{h} = 548\,\mu$m), figure 3.7(c), there is an evident increase in the amplitude of the identified peaks in the PSD at the FFS.

Finally, it is important to note that when transition occurs downstream of the IR-A measurement region (i.e $x_t/c_x > 0.25$) the addition of the FFS shows no change on the wavelength of the dominant CF instability mode as shown in figure 3.7(b) and (c) where the $\lambda_z = 6$ mm wavelength is still dominant downstream of the step.

3.4. FORCED CONDITIONS

The findings presented in §3.3 suggest that for the tested conditions, there is a non-unique influence of the FFS on the laminar-turbulent transition of the boundary-layer flow on the swept wing model. This is particularly evident when one-parameter correlations are attempted, for example, with h/δ^*_h or y_c/h. These observations highlight the complex interaction between an FFS surface irregularity and the incoming CF vortices. In relation to the observations of Eppink [136] and Eppink and Casper [135], in addition

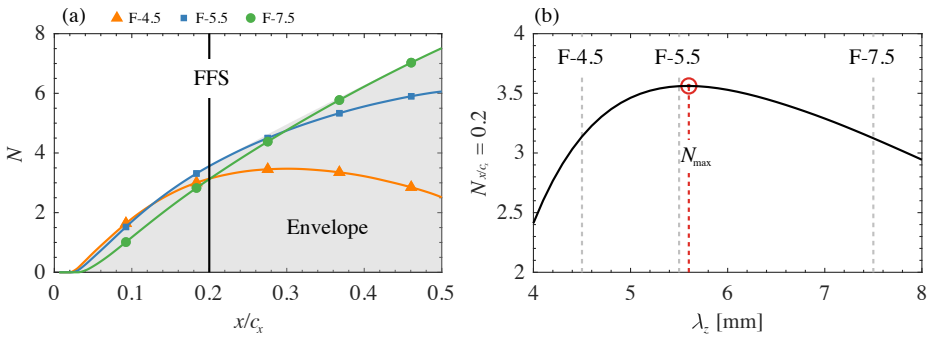

Figure 3.8: Determination of the forcing wavelength of the DREs at $\alpha = 3°$ and $Re_{c_X} = 2.5 \times 10^6$: (a) Envelope of N-Factors curves. (b) N-factors of stationary CF instability modes at the step location ($x_h/c_x = 0.2$).

to the primary variables such as FFS height, boundary-layer thickness and core height of the CF vortices, it appears that the local characteristics of the CF instability such as spanwise wavelength and amplitude potentially play a role in defining the interaction mechanics. Moreover, Tufts *et al.* [129] noticed a dependence between the FFS adverse effect and the spanwise wavelength of the primary CF instability mode, which can possibly be attributed to the change in core height of the CF vortices. To further clarify these effects, this section assesses the influence of an FFS when interacting with conditioned monochromatic stationary CF instability modes.

Prior to the investigation, an LST analysis was conducted for the flow corresponding to the Clean-N case at $Re_{c_X} = 2.5 \times 10^6$ and $\alpha = 3°$, as indicated in §3.2.3. The stability analysis shows that a spanwise wavelength of $\lambda_z = 4.5$ mm will correspond to an early-growth stationary CF instability mode with respect to the most amplified mode (i.e. maximum N-factor) at the step location as shown in figure 3.8. Consequently, a spanwise wavelength of $\lambda_z = 5.5$ mm will correspond to a mid-growth CF instability mode and a $\lambda_z = 7.5$ mm wavelength corresponds to a late-growth mode. To be noted, given the linear assumption in the stability analysis presented in figure 3.8(a), non-linear effects such as possible saturation of the CF instability forced modes are not accounted for. For each of the FFS cases A-F, B-F and C-F (Table 3.1) at $Re_{c_X} = 2.5 \times 10^6$ and $\alpha = 3°$, these CF instability modes were individually forced near the model leading edge ($x_D/c_x = 0.02$, thus upstream of the neutral point) using DREs of equal nominal height and diameter (see table 3.1), so that the initial amplitude of these modes can be assumed to be approximately equal.

The use of DREs narrows the band of modes that de-stabilize the boundary-layer flow by enhancing the stationary CF instability mode corresponding to the DREs spanwise wavelength ($\lambda_{z,D}$). The DREs were manufactured and installed as indicated in §3.2.1. An overview of the forced cases is presented at the bottom of Table 3.1.

Finally, it must be noted that for the results presented in this section, the estimated CF vortex core height (y_c) pertains to the forced CF instability mode ($\lambda_{z,D}$) and not to the most amplified mode at the FFS location.

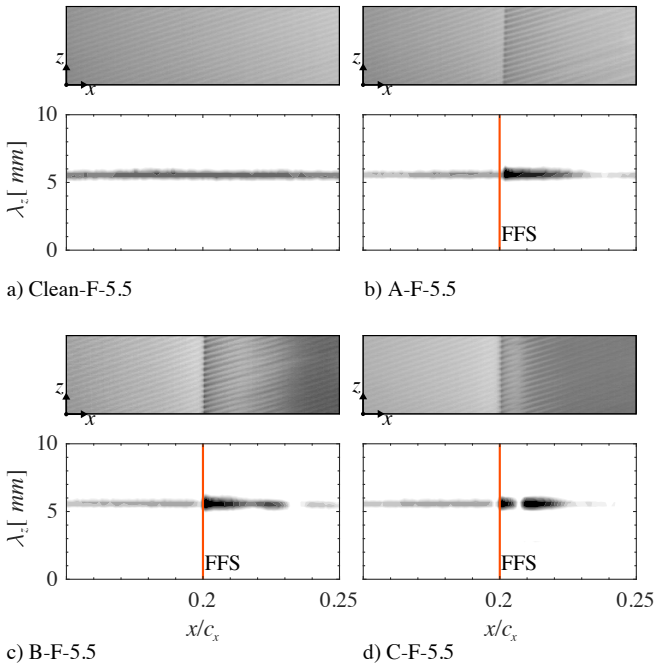

Figure 3.9: Comparison of IR-A thermal maps (top, flow from left to right) and spatial PSD analysis (bottom, ten levels of $\ln(P/\bar{P}_{\max_z})$ from -2.5 to 1) displaying the effect of an FFS (orange line) for the mid-growth CF instability mode forced cases F-5.5 ($\lambda_{z,D} = 5.5$mm) at $\alpha = 3°$ and $Re_{c_X} = 2.5 \times 10^6$.

3.4.1. MID-GROWTH CROSSFLOW INSTABILITY MODE

In the mid-growth case, a stationary CF instability mode corresponding to a spanwise wavelength of $\lambda_{z,D} = 5.5$ mm was forced for each of the FFS cases A-F, B-F, and C-F as indicated in Table 3.1. The LST calculations (curve F-5.5 in figure 3.8a) show that at $Re_{c_X} = 2.5 \times 10^6$ and $\alpha = 3°$, this mode is rigorously growing at the FFS location and continues to be unstable downstream. The strong amplification of this mode in the region $0.15 \leq x/c_x \leq 0.25$ is confirmed by the spatial PSD analysis of the infrared thermographic measurements of camera IR-A (figure 3.9a), indicating distinct and coherent CF vortices evenly spaced at the forcing wavelength. To asses the influence of the FFS on the forced laminar-turbulent boundary-layer transition process, the change of transition location (Δx_t) is represented by the curve F-5.5 in figure 3.10b. Note that for the same Re_{c_X} each forced case will result in a different clean transition location ($x_{t,C}$). Hence, the calculation of Δx_t for each case is referenced to its respective clean (i.e. no FFS) transition location.

The addition of a short FFS (A-F-5.5: $h/\delta^*_h = 0.82$, figure 3.10) results in a subcritical regime FFS behavior, as there is a negligible change in the transition front, figure 3.10. On the other hand, the addition of higher FFS (B-F-5.5: $\bar{h}/\delta^*_h = 1.28$, and C-F-5.5: $\bar{h}/\delta^*_h = 1.69$) leads to a strong upstream shift of the transition front and a super critical regime FFS behavior. Strikingly, the overall behavior of this forced case (F-5.5) differs with that

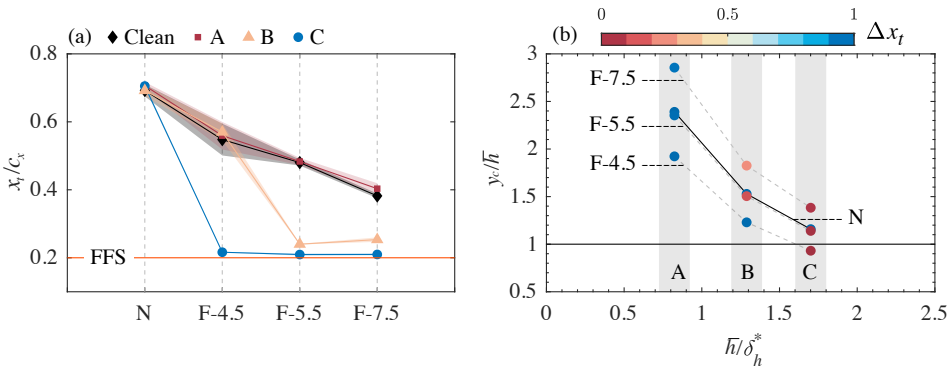

Figure 3.10: Comparison of Clean and FFS cases A,B and C in unforced (N) and forced conditions (F-4.5,F-5.5 and F-7.5) at $Re_{c_X} = 2.5 \times 10^6$ and $\alpha = 3°$: (a) Transition location x_t/c_x. (b) Change in transition location (Δx_{tr}) with estimated core height of the CF vortices (y_c) and boundary-layer displacement thickness (δ_h^*).

observed for the unforced case represented by curve (N) in figure 3.10(b). In the unforced case, a subcritical behavior is observed for all FFS even for less favorable conditions (i.e. decrease in y_c/h and increase in $\bar{h}/\delta_h^*$.). This confirms the hypothesis of a non-unique FFS-CFI interaction which is influenced by particular characteristics of the instability.

The spatial PSD analysis in figure 3.9 indicates that an increase in step height exacerbates the influence of the FFS on the forced CF instability mode, since for all the cases a peak at $\lambda_z = 5.5$ mm is evident. Note that this differs from the unforced case (presented in figure 3.7 on §3.3) where two distinct peaks are located in the proximity of the FFS. The comparison between these cases indicates that the peaks in the unforced case are likely caused by competing CF instability modes at the FFS location, which become evident in the infrared thermography visualizations due to an amplification at the FFS.

Additionally, in figure 3.9 (b) a non-monotonic growth pattern in the IR signal distribution develops downstream of the FFS edge along the x-direction. This pattern resembles the growth-decay-growth behaviour of the primary CF instability mode observed by Eppink and Casper [135]. However, given the nonlinear relation between the temperature signal at the surface of the model and the CF vortices amplitude, the origin of this behaviour cannot be rigorously identified. Future dedicated velocity measurements will aim at such identification.

Finally, when transition occurs near the step, a series of "fork-like" patterns are observed downstream of the FFS (figure 3.9d). In agreement with Eppink [137], these results suggest that there is a strong spanwise modulation of the recirculating flow in the vicinity of the FFS. Thus, an in-depth study of this pattern spatio-temporal organization might further the understanding of the complex interaction between the CF vortices and FFS.

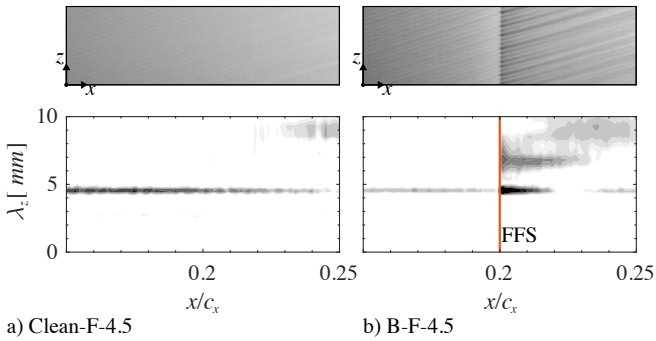

Figure 3.11: Comparison of IR-A thermal maps (top, flow from left to right) and spatial PSD analysis (bottom, ten levels of $\ln(P/\bar{P}_{\max_z})$ from -2.5 to 1) displaying the effect of an FFS (orange line) for the early-growth CF instability mode forced cases F-4.5 ($\lambda_{z,D} = 4.5$mm) at $\alpha = 3°$ and $Re_{c_X} = 2.5 \times 10^6$.

3.4.2. EARLY-GROWTH CROSSFLOW INSTABILITY MODE

For the early-growth case, a stationary CF instability mode corresponding to a spanwise wavelength of $\lambda_{z,D} = 4.5$ mm was forced for each of the FFS cases A-F, B-F and C-F (Table 3.1). The LST calculations (curve F-4.5 in figure 3.8a) show that at $Re_{c_X} = 2.5 \times 10^6$ and $\alpha = 3°$, this mode undergoes a strong amplification upstream of the FFS location and becomes increasingly stable downstream. This reconciles qualitatively with the IR imaging and corresponding PSD analysis for the Clean-F-4.5 case as shown in figure 3.11(a). Furthermore, for the case B-F, the PSD analysis shows an evident amplitude decay of the forced mode and an amplification of a longer spanwise wavelength λ_z mode downstream of the FFS location ($x_h/c_x = 0.2$), as shown in figure 3.11(b).

In this case, the addition of short and medium FFS (A-F-4.5: $\bar{h}/\delta^*_h = 0.82$ and B-F-5.5: $\bar{h}/\delta^*_h = 1.28$) height results in a subcritical FFS regime behavior as there is a negligible shift of the transition front (curve F-4.5 in figure 3.10). A possible explanation for this behavior, which contrasts with the observations pertaining to the mid-growth mode (F-5.5 case), is that although the y_c/h ratio is smaller for the F-4.5 case, the FFS amplifies a forced CF instability mode ($\lambda_{z,D} = 4.5$mm) which will be stable downstream of the FFS and thus the adverse effect on the transition process is minimized. Nevertheless, the addition of a higher FFS (C-F-4.5: $\bar{h}/\delta^*_h = 1.69$) results in a super critical condition similar to the C-F-5.5 case, leading to a transition location near the FFS.

3.4.3. LATE-GROWTH CROSSFLOW INSTABILITY MODE

Finally, when forcing a late-growth mode ($\lambda_{z,D} = 7.5$mm) its dominance is evident in the streamwise range $0.15 \leq x/c_x \leq 0.25$, see figure 3.12(a). This is in agreement with the LST predictions (curve F-7.5 in figure 3.8), suggesting that this mode will monotonically grow upstream and downstream of the step location. Additionally, figure 3.12(b) shows a second spanwise peak, near the FFS, at a wavelength close to the first harmonic of the forced CF instability mode. This behaviour suggests that if the FFS amplifies a broad range of spanwise CF instability modes as suggested by figure 3.7(b) and (c), the addition of the FFS could lead to complex non-linear interactions.

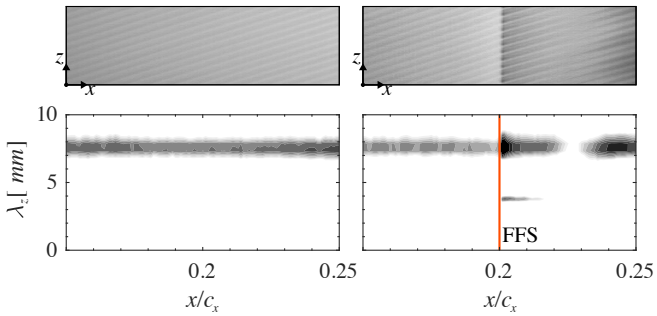

Figure 3.12: Comparison of IR-A thermal maps (top, flow from left to right) and spatial PSD analysis (bottom, ten levels of $\ln(P/\bar{P}_{\max_z})$ from -2.5 to 1) displaying the effect of an FFS (orange line) for the late-growth CF instability mode forced cases F-7.5 ($\lambda_{z,D} = 7.5$mm) at $\alpha = 3°$ and $Re_{c_X} = 2.5 \times 10^6$.

The "wide-view" IR measurements (curve F-7.5 in figure 3.10) indicate that the addition of a short FFS (A-F-7.5: $\bar{h}/\delta^*_h = 0.82$) leads to a negligible change in the transition location. Nevertheless, with increasing FFS height (B-F-7.5: $\bar{h}/\delta^*_h = 1.28$ and C-F-7.5: $\bar{h}/\delta^*_h = 1.69$) the step influence intensifies, as the laminar-turbulent boundary-layer transition occurs near the FFS. This behavior is in agreement with the observations corresponding to the mid-growth case (curve F-5.5 in figure 3.10) and differs from the behavior of the unforced (curve N in figure 3.10) and early-growth (curve F-4.5 in figure 3.10) cases.

The discrepancies between the unforced, early-growth, mid-growth, and late-growth cases for the B-F ($\bar{h}/\delta^*_h = 1.28$) case, suggest that the influence of the FFS on transition is not only determined by the conditions at the step, such as the estimated core height (y_c) of the CF vortices and boundary-layer displacement thickness (δ^*_h). In addition to these parameters, characteristics of the CF instability mode in the vicinity of the step such as wavelength, amplitude and the overall stability of the mode past the irregularity, appear to also have an effect. Therefore, to determine the relation and relative importance of each parameter, future sensitivity studies involving extensive testing are required.

3.5. CONCLUDING REMARKS

The successful application of Laminar Flow Control on swept wings is currently hindered by premature boundary-layer transition due to non-smooth surfaces. Forthwith, an experimental study was carried out at the LTT Wind tunnel facility of TU Delft to determine the local and global influence of FFS on the laminar-turbulent transition of a swept wing boundary-layer.

Previous research into the FFS-CFI interaction has been mainly limited to the isolated study of either unforced conditions (i.e. smooth leading edge) or forced monochromatic modes induced by DREs placed near the leading edge. In this work, important insight into the FFS-CFI laminar-turbulent transition dynamics is obtained by considering cases under both unforced and forced conditions.

Essential to the design of laminar flow components is the estimation of the critical FFS height (i.e. one which causes transition advancement). The results pertaining to the unforced conditions show that the use of local one-parameter correlations (i.e. y_c/h or h/δ_h^*) might not be sufficient to universally capture the laminar-turbulent transition dynamics in cases of FFS-CFI interaction. These findings highlight the need for additional parameters to improve the estimation of the FFS influence on the laminar-turbulent transition of stationary CF instability dominated flows.

Consequently, a non-unique influence of the FFS was observed in the transition process for the cases pertaining to three different forced conditions (i.e. early, mid and late growth CF instability modes). The results reveal that the influence of the FFS on the transition process is highly dependent on the local characteristics of the incoming CF instability mode. In particular, parameters such as mode amplitude and growth rate at the step as well as its nominal stability (i.e. decay or growth) downstream of the FFS appear to significantly determine the response to the surface irregularity. These new insights further confirm the need for multi-parameter correlations for transition prediction in laminar flow components.

4

Influence on development of crossflow vortices

This chapter presents a detailed quantification of the development of crossflow instability under the influence of a forward-facing step. The results reveal that the forced monochromatic stationary crossflow vortices experience an abrupt change in their trajectory as they interact with the step geometry. As the boundary-layer intercepts the step an increase in the vertical velocity component and an amplification of the crossflow vortices is observed. Near the step, the vortices reach maximum amplification, while dampening downstream. The smaller FFS cases show a local stabilising effect on the primary stationary mode and its harmonics, while in the higher step cases transition occurs. The analysis of the temporal velocity fluctuations shows that the velocity fluctuations in the region associated with type I secondary instabilities increase past the FFS edge. Nonetheless, in the shortest FFS cases, these velocity fluctuations eventually decay below the clean configuration (i.e. without an FFS) levels. This behaviour is linked to a novel transition delay effect for the shortest step height investigated.

Parts of this chapter are published in:

- Rius-Vidales, A.F. & Kotsonis, M. 2021 Impact of a forward-facing step on the development of crossflow instability. Journal of Fluid Mechanics **924**, A34.

4.1. BACKGROUND

The main finding of the experiments presented in Chapter 3 (Rius-Vidales and Kotsonis [181]) indicate that local one-parameter correlations based on the estimated CF vortex core-height or relative step height (h/δ^*) might not be sufficient to universally capture the influence of an FFS on the laminar–turbulent transition in cases dominated by stationary CF vortices. Moreover, the discrepancies between the interaction mechanics proposed by Tufts *et al.* [129] and Eppink [130] described in §1.3, highlight numerous unresolved aspects which require further study before the mechanisms of interaction between the FFS and CF vortices can be fully unveiled.

Moreover, except for the recent detailed measurements of Eppink [130], experimental identification of velocity and instability development in the vicinity of the step is mostly unavailable, and reconciliation between local to the FFS effects and global transition location is still absent from the published literature.

Therefore, in agreement with the main research *objective B* (presented in §1.4), a detailed description of the FFS impact on the local development and amplification of the CF instability and its effects on the global transition location is provided by conducting measurements on a swept wing wind tunnel model using Infrared Thermography and Particle Image Velocimetry.

4.2. EXPERIMENTAL SETUP

4.2.1. INFLOW CONDITIONS AND SURFACE IRREGULARITIES

Experiments have been conducted at the atmospheric closed return low-turbulence tunnel (known as LTT) described in §2.1.1. All reported measurements were performed on the pressure side of the wing, for a fixed angle of attack of $\alpha = 3$ deg and a Reynolds number of $Re_{c_X} = 2.3 \times 10^6$. The Reynolds number ($Re_{cX}$) used throughout is based on the reference (see §2.1.1) wind tunnel velocity ($U_\infty = 26.5\ \mathrm{m\,s^{-1}}$) and the streamwise chord length of the model $c_X = 1.27$ m.

The M3J swept wing model described in §2.1.2, was installed in the wind tunnel octagonal test section (2.6m × 1.80m × 1.25m; length × width × height). The static pressure distribution on the model was measured using a multi-channel scanner (described in §2.1.2) connected to two rows of 46 streamwise (X) oriented taps at 24% and 76% of the model span. At the nominal conditions of this study ($Re_{c_X} = 2.3 \times 10^6$,$\alpha = 3$ deg) the streamwise pressure distribution (pressure side of the wing) shows a favorable gradient up to $X/c_X \approx 0.65$ as shown in figure 4.1(a). The nearly invariant pressure along the span, in agreement with Serpieri and Kotsonis [71], confirms the adequacy of the infinite swept wing assumption for the boundary-layer and stability calculations in the measurement region performed following the procedure described in §2.3.

As discussed previously, the objective of the investigation presented in this chapter is to elucidate the interaction between an FFS irregularity and the incoming stationary CF instability. However, the quest for experimentally simulating a representative scenario raises the question regarding which particular mode is more relevant. Several options are available; These entail focusing on the CF instability mode most amplified (i.e. highest N) at the step location [e.g. 129, 181], or the most unstable mode (i.e. highest growth rate) at the step. Another option is to investigate the overall most unstable mode

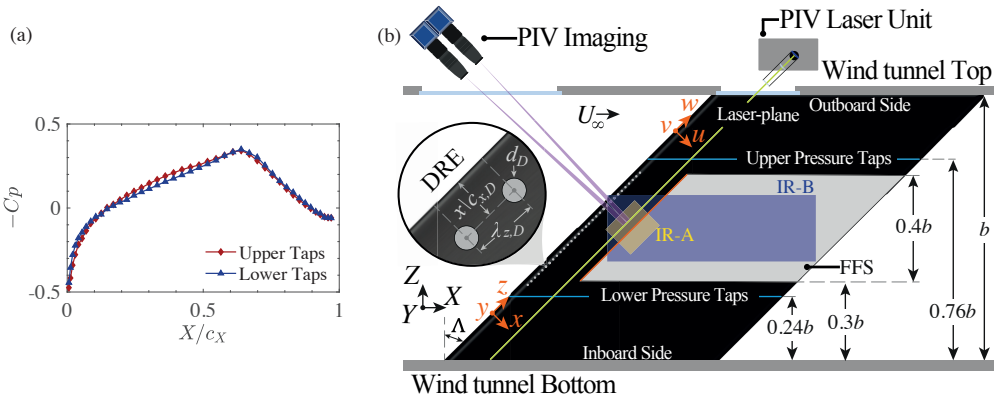

Figure 4.1: Experimental Setup: (a) streamwise pressure coefficient distribution at two spanwise locations at $\alpha = 3$ deg and $Re_{c_X} = 2.3 \times 10^6$ measured on the pressure side (max $U_{Cp} = 0.002$); (b) general schematic (flow direction from left to right, $b = 1.25$ m) showing the FFS location, the IR analysis regions (IR-A,IR-B), planar PIV set-up and details of DREs.

[e.g. 129, 130]. Considering the sensitivity of transition location to step height, the latter option can be further narrowed down to investigating the transition-inducing mode at clean conditions (i.e. no FFS). A preliminary stability analysis reveals that the most amplified stationary CF instability mode prior to transition features a spanwise wavelength close to $\lambda_z = 7.5$ mm and exhibits a monotonic growth upstream and downstream of the step location ($x_h/c_x = 0.2$). Therefore, following the definitions presented in Chapter 3, the experiments in this chapter focus on the study of a late-growth CF instability mode with respect to the most unstable at the step location.

To study the impact of an FFS on this unstable stationary CF instability mode, discrete roughness elements (DREs) are used to force a single fundamental CF instability mode featuring a nominal spanwise wavelength of $\lambda_{z,D} = 7.5$ mm in the vicinity of the leading edge. Motivated by a lack of experimental or numerical evidence pertaining to the interaction of strongly amplified CF instability with steps and in line with the previous experiments presented in Chapter 3 (Rius-Vidales and Kotsonis [181]), DREs with a nominal height of $k_D = 100$ µm and a diameter of $d_D = 2$ mm were manufactured in-house from an adhesive transfer vinyl film using a custom laser cutting system. The DREs were installed at $x_D/c_x = 0.02$ which is just upstream of the forced mode neutral point according to LST calculations.

FFS surface irregularities were designed and manufactured as add-ons for the M3J wind tunnel model, as described in §2.1.3 and illustrated by the gray region in figure 4.1(b). The resulting FFS step height was characterised in-situ by traversing a Micro-Epsilon 2950-25 laser profilometer (reference resolution of 2 µm) along 200 mm of the spanwise extent of the surface irregularity, centred at mid-span. Table 4.1 indicates the resulting average step height ($\bar{h}$), standard deviation (σ_h) and streamwise location (x_h/c_x) of the FFS surface irregularity for all tested configurations. As an indication of the relative size of the FFS inside the boundary-layer flow, the displacement thickness (δ^*_h) is computed based on the aforementioned numerical boundary-layer solution for the streamwise ve-

ID	$\bar{h}$ [µm]	σ_h [µm]	x_h/c_x	δ_h^*[µm]	y_c[µm]
Clean	-	-	-	444	1029
A_{1-4}	368	3	0.150/0.175/0.200/0.225	-	-
B_3	474	3	0.200	-	-
C_3	579	3	0.200	-	-
D_3	759	8	0.200	-	-

Table 4.1: Geometrical parameters of tested configurations. For all cases the nominal DREs settings are: $\lambda_{z,D}$=7.5mm, d_D = 2 mm, k_D = 100 µm, x_D/c_x = 0.02.

locity (u) at the nominal step location ($x_h/c_x = 0.2$) for the clean case (i.e. without FFS). Similarly, from the LST analysis the estimated CF vortex core height (y_c) based on Tufts *et al.* [129] at the step location (indicated in Table.4.1) is extracted from the v-perturbation eigenfunction corresponding to the CF instability mode featuring the spanwise wavelength enforced by the DREs ($\lambda_{z,D} = 7.5$ mm).

Finally, two different coordinate systems are used throughout this study with their origin at the intersection between the leading edge and the wing midspan. As illustrated in figure 4.1(b), the first coordinate system spatial coordinates (X, Y, Z) and velocity components (U, V, W) are referenced according to the X-coordinate being parallel to the wind tunnel floor. In the second coordinate system, the spatial coordinates are given by (x, y, z) and the velocity components (u, v, w). In this case, the x-coordinate is perpendicular to the leading edge.

4.2.2. INFRARED THERMOGRAPHY

Two Optris PI640 IR cameras (640px × 480px, uncooled focal plane array, 7.5-13 µm spectral range, NETID 75 mK), designated as IR-A and IR-B, image the pressure side of the model through small openings on the vertical wall of the test section. Camera IR-A equipped with a telephoto lens (f = 41.5 mm) images a region near the step. Conversely, camera IR-B equipped with a wide-angle lens (f = 10.5 mm) images a larger portion of the model as illustrated in figure 4.1(b). The analysis region by camera IR-A has a dimension of 145 × 200 mm (centred at $X/c_X = 0.2$ and $Z/b = 0$) and for camera IR-B 1000 × 400 mm (centred at $X/c_X = 0.37$ and $Z/b = 0$). During the measurements the model was continuously irradiated by seven halogen lamps to increase the thermal contrast on the IR images, as described in detail on §2.2.1.

The processing and extraction of the transition location from the measurements of camera IR-B were performed using an in-house pattern recognition code and follow the procedure describe in §2.2.1. The camera acquires 78 images at 3.5 Hz. For each measurement series, a time-averaged temperature map is calculated, and a physical space transformation and distortion correction is applied to it. Subsequently, a differential infrared thermography technique (DIT)[154, 155] is applied to consecutive temperature fields with increasing Reynolds numbers following the experiments presented in Chapter 3 (Rius-Vidales and Kotsonis [181]).

Figure 4.1(b) shows that camera IR-A captures, in more detail, the thermal footprint of the flow structures in the vicinity of the FFS. By applying a spatial power spectral den-

sity (PSD) analysis (described in §2.2.1) on the thermal intensity values along the spanwise (z) component of these measurements, the changes in the spatial organisation and direction of the CF vortices induced by the FFS are examined. The spatial frequency resolution (i.e. smallest resolved wavelength) stemming from the Nyquist limit of the sensor is 0.86 mm.

4.2.3. PARTICLE IMAGE VELOCIMETRY

Quantitative measurements of the flow dynamics and instability interacting with the FFS have been enabled using planar PIV (2C-2DPIV), described in §2.2.3. Measurements on a z-y plane normal to the surface and parallel to the leading edge (figure 4.1b) have been conducted at various chordwise locations ($0.17 \leq x/c_x \leq 0.25$). These planes were imaged in streamwise increments of 5 mm ($\approx 0.4\%$ of c_X) for the majority of stations. Additionally, increments of 1 mm were used near the FFS. The translation was enabled using an automated traversing system mounted outside of the wind tunnel test section capable of simultaneously moving the imaging and laser unit with a positioning accuracy of $\pm$ 6.2 μm.

The laser unit comprises a Quantel Evergreen Nd:YAG dual cavity laser (200mJ). Through a set of spherical and cylindrical expansion optics, the laser beam is shaped into a plane, with a thickness of approximately one millimetre. The plane propagates along the z direction (i.e. parallel to the leading edge) as shown in figure 4.1(b).

During the measurements, the wind tunnel is homogeneously seeded with water–glycol droplets using a SAFEX fog generator located in a vent downstream of the test section. The seeding recirculates in the closed circuit of the wind tunnel. Images of seeding particles as they cross through the laser plane are recorded by two LaVision Imager sCMOS camera (sCMOS, 2560 × 2160 pixels, 16-bit , 6.5 µm pixel pitch) positioned outside the test section as shown in figure 4.1(b). Each camera is equipped with a $f = 200$ mm objective operated at $f_\# = 11$ and two 2X teleconverters.

Each measurement consists of 1200 image pairs acquired at 15 Hz per camera. For each image pair, a multistage cross-correlation was performed using LaVision Davis 10 with a final interrogation window of 12 × 12 px^2 and overlap of 75%. Additionally, the results of both cameras are stitched together to capture the development of two full CF vortices in the measurement region. The final analysis at each measurement location has a dimension of 15 × 3 mm (W × H), a vector spacing of 20 µm.

4.2.4. BOUNDARY-LAYER FLOW STABILITY METRICS

The changes in the stability of the CF vortices induced by the FFS are studied by analysing the streamwise evolution of the experimental spanwise steady disturbance profile based on the time-averaged planar PIV velocity measurements described in §4.2.3.

The methodology described by White and Saric [89] and Downs and White [73] indicates that the experimental steady disturbance profile is equivalent to the spanwise root mean square ($\langle\rangle_z$) of the time-averaged perturbation, which for the spanwise component is given by $\langle\hat{w}(y)\rangle_z = [1/n\sum_{j=1}^{n}(w(y,z_j) - \bar{w}(y))^2]^{1/2}$. Subsequently, the streamwise change in the steady disturbance can be determined by calculating the maximum of the profiles along the y-coordinate as $A_M = \max|_y(\langle\hat{w}(y)\rangle_z)$.

It is important to note, that according to perturbation analysis used in stability the-

ory, the velocity perturbation (w') should be calculated by subtracting a basic state or baseflow (W) to the mean velocity component (w). Hence, in this context, $\hat{w} \neq w'$ since the experimentally measured spanwise average $\bar{w}(y)$ corresponds to a mean-flow distorted flow and not to a baseflow. Nevertheless, this approach has been traditionally used as a metric to determine the growth and decay of CF instability modes in experimental conditions and is accordingly followed in the present study as well.

4.3. TRANSITION BEHAVIOUR AND TOPOLOGY

This section presents the influence of an FFS on the laminar–turbulent boundary-layer transition. The determination of the transition location and the topology of the developing CF vortices is based on the IR measurements acquired and processed as indicated in §4.2.2 for the different configurations indicated in table 4.1

4.3.1. INFLUENCE ON TRANSITION LOCATION

The laminar–turbulent boundary-layer transition location was determined for each configuration based on the camera IR-B surface thermal maps. The time-averaged thermal maps presented in figure 4.2(Ia) reveal a jagged transition front pattern which extends along the span of the wing. The nature of this jagged pattern has been traced to the breakdown process typical of stationary CF vortices [e.g. 34, 35, 72, 73]. As the stationary CF vortices saturate, a rapidly growing secondary instability leads to a local breakdown of the CF vortices characterised by contiguous turbulent wedges forming along the span creating the so-called "jagged" or "sawtooth" transition front pattern. Therefore, the appearance of this pattern indicates the dominance of stationary CF instability modes over travelling modes. In contrast, when the latter dominate, a more smooth (i.e. non-wedged) time-averaged transition front is observed due to the movement of CF vortices along the span.

The transition front location and variance along the span is identified from the surface thermal maps of camera IR-B following the DIT technique mentioned in §4.2.2 and employed in Rius-Vidales and Kotsonis [181]. It is particularly noteworthy that the linear fit of the identified transition front locations (white dashed line in figure 4.2Ia) forms an angle with the leading edge, which reduces with increasing step height. This behaviour is related to the non-uniform wind tunnel blockage along the height of the wind tunnel (i.e. along the Z-direction in figure 4.1b) which leads to slightly stronger favourable pressure gradients near the outboard side of the wing. Consequently, to quantify the effect of the FFS height the transition location is extracted from the linear fit at the middle of the measurement domain (• marker in figure 4.2Ia). The results presented in figure 4.3 show that for the Clean configuration (table 4.1) the laminar–turbulent transition occurs at $x_t/c_x = 0.42$ (solid black line in figure 4.3a).

The addition of a moderate FFS (B_3 and C_3 in figure 4.3a) results in a critical regime behaviour, as the boundary-layer transition front shifts upstream of the Clean configuration as illustrated in figure 4.2(IIa-IIb). A further increase in step height (D_3) leads to a supercritical regime behaviour with a substantial reduction in the extent of laminar flow as shown in figure 4.2(IIIa). These results indicate a gradual degradation of the laminar flow with increasing step height analogous to the behaviour observed by Crawford *et al.* [134] and Rius-Vidales and Kotsonis [181] and somewhat different to the one presented

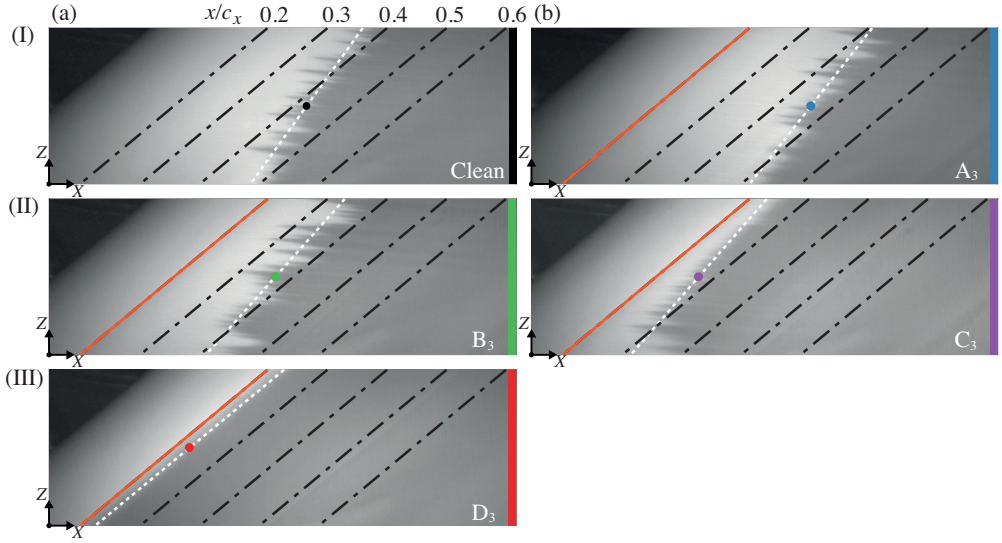

Figure 4.2: The IR-B thermal maps (flow from left to right) displaying the effect of an FFS (orange line) on the transition front pattern, dashed white line indicates transition linear fit and (•) marks its projection to the mid-domain of the measurement : (Ia) Clean, (Ib) A_3; (IIa) B_3; (IIb) C_3; and (IIIa) D_3.

by Duncan *et al.* [127] and Eppink [130] which showed that with increasing step height the transition location more abruptly shifts towards the FFS location.

An important note must be made regarding the use of the terms critical and supercritical, which varies significantly in previous works on roughness effects on transition. Throughout the present study, the term critical is assigned to cases in which the step has an identifiable effect on transition location, while the term supercritical refers to cases in which transition location is very near or at the step location. A supercritical behaviour essentially denotes flow "tripping" due to the step. Therefore, the critical step height definition used in this work is compatible with the one presented by Tufts *et al.* [129].

Notwithstanding the general adverse effects of an increasingly high FFS on transition, it is remarkable to note that a new transition behaviour is revealed when adding a small FFS (A_3 in figure 4.3a-b) at these conditions. Counter-intuitively, the addition of the FFS results in a favourable effect as transition postponement is observed instead of advancement. At first glance, this unexpected result is in disagreement with most of previous experimental or numerical observations on surface irregularities, and common wisdom alike. However, observations recently presented by Ivanov and Mischenko [141] based on the concept presented by Ustinov and Ivanov [142] suggested a transition delay effect under the influence of rectangular (i.e. FFS followed by a BFS) surface reliefs. Nonetheless, regarding surface irregularities in the form of only FFS, the behaviour observed in this work contrasts, with previous studies [e.g. 118, 127, 129, 130, 132, 135–137, 149, 179, 182]. As to the best of the authors' knowledge the present case is the first report of a transition delay in a boundary-layer dominated by CF instability in the presence of an FFS.

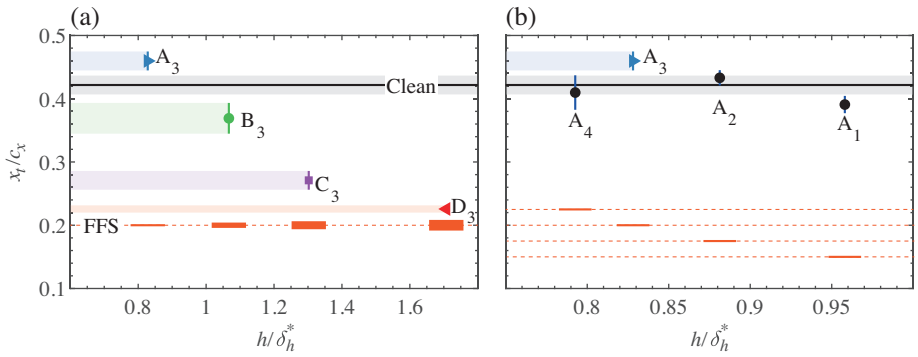

Figure 4.3: Transition location: (a) fixed step ($x_h/c_x = 0.2$) location for different FFS; (b) variation of the step location ($0.15 \leq x_h/c_x \leq 0.225$) for small FFS ($A$).

Given the novelty of this result and the potential such delay behaviour can offer in a LFC strategy, three additional configurations ($A_{1,2,4}$, table 4.1) have been tested. The objective of such variation was to exclude random and systematic measurement errors that might bias the result, as well as to establish a range of governing parameters for which the transition delay effect is observed. Figure 4.3(b), shows the effect of varying the streamwise position of this small FFS (A) on the laminar–turbulent boundary-layer transition. When the FFS is located at the most upstream location, A_1, a slight transition advancement is measured. However, as the FFS is translated downstream the detrimental effect of the step reduces for the case A_2 until a clear transition delay effect is observed for the position of case A_3 ($x_{t,\text{Clean}}/c_x - x_{t,A_3}/c_x = -0.038$). The upstream movement of transition location for the cases A_1 and A_2 further confirms the validity and physicality of the transition delay effect. Nevertheless, the non-monotonic trend and rather narrow range of streamwise FFS locations for which the transition delay effect is observed points to the existence of possibly conflicting mechanisms governing the observed transition location.

Towards further probing the effect, a subtraction of thermal maps pertaining to the A_{1-4} FFS positioned at several streamwise locations from the thermal map of the clean case ($\Delta I_{A_{1-4}} = I_{\text{Clean}} - I_{A_{1-4}}$) for these conditions are shown in figure 4.4. The subtracted thermal maps confirm that the transition delay (dark regions) is not a localised or outlier-dominated effect but occurs over a considerable spanwise extent of the measurement region. Note that the differences in the delay effect on the outboard and inboard section of the wing are again related to the non-uniform blockage along the height of the wind tunnel (i.e. Z-direction figure 4.1b). The global behaviour of transition location with varying FFS height highlights the intricate flow dynamics, which results from the interaction between the FFS and the CF vortices, necessitating high-resolution velocity measurements for further analysis. Notwithstanding the present observations, caution needs to be exercised when interpreting or generalising these results since, in addition to local parameters (i.e. step height, boundary-layer displacement thickness and CF vortex core height) the influence of the FFS also depends on the stability characteristics of the incoming CF instability mode, as shown in Chapter 3 (Rius-Vidales and Kotsonis [181]).

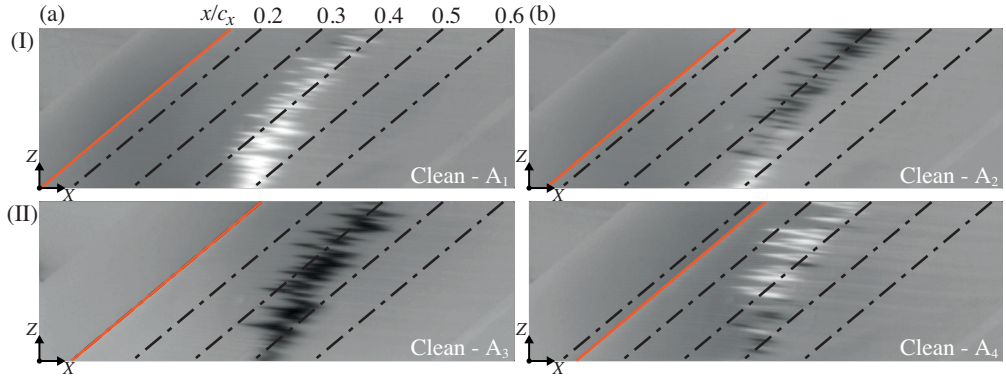

Figure 4.4: The IR-B differential thermal maps (flow from left to right) displaying transition advance and postponement effects by FFS A (orange line): (Ia) ΔI_{A_1}; (Ib) ΔI_{A_2}; (IIa) ΔI_{A_3}; and (IIb) ΔI_{A_4}.

4.3.2. INFLUENCE ON THE ORGANISATION OF THE CROSSFLOW VORTICES

The thermal maps of camera IR-A (figure 4.1b) provide a more detailed visualisation near the step region by showing the thermal footprint of the CF vortices on the surface of the wing model as alternating streaks of high (i.e. lighter) and low (i.e. darker) temperature as presented in figure 4.5(Ia). This particular temperature distribution originates from a variation in the heat transfer of the near-wall fluid due to a change in the magnitude of local skin friction coefficient induced by the high and low shear regions on the baseflow modulated by the CF vortices. Therefore, the local influence of the FFS on the CF vortex thermal footprint is evaluated by calculating the spatial power spectral density (PSD), as indicated in §4.2.2, from a series of spanwise (z-direction) temperature profiles extracted at different streamwise locations.

The results for the Clean configuration in figure 4.5(IIa), identify a series of CF vortices monotonically spaced at the spanwise wavelength of the forcing DREs ($\lambda_z/\lambda_{z,D} = 1$, $\lambda_{z,D} = 7.5$ mm) for the entire measurement region. Upon the addition of a small FFS (A_3, figure 4.5IIb) a clear peak at the forced wavelength is observed at the step location ($x_h/c_x = 0.2$ and $\lambda_z/\lambda_{z,D} = 1$). In addition, a second peak centred at the wavelength of the forced mode first harmonic ($\lambda_z/\lambda_{z,D} = 0.5$) at the step location is also present. This behaviour occurs in all step cases in figures 4.5(IIb-IIc,IVa-IVb) and is in agreement with Eppink [130] where an amplification of the harmonics of the primary CF instability mode has been reported near the FFS.

A close inspection of the thermal maps for the small (A_3) and moderate (B_3) FFS (figures 4.5IIb-IIc), reveal a non-monotonic amplification pattern which develops along the x-direction downstream of the FFS step edge at the wavelength of the primary CF instability mode ($\lambda_z/\lambda_{z,D} = 1$). This non-monotonic pattern corresponds to the observations by Eppink and Casper [135] and Eppink [130] where it was found that as the CF vortices interact with the step they experience a first region of strong amplification, followed by an equally strong reduction and a second region of amplification thus creating a growth–decay–growth pattern of the CF vortices. The first maximum in intensity is located close to the step for all cases, while the first minimum and second maximum move closer to

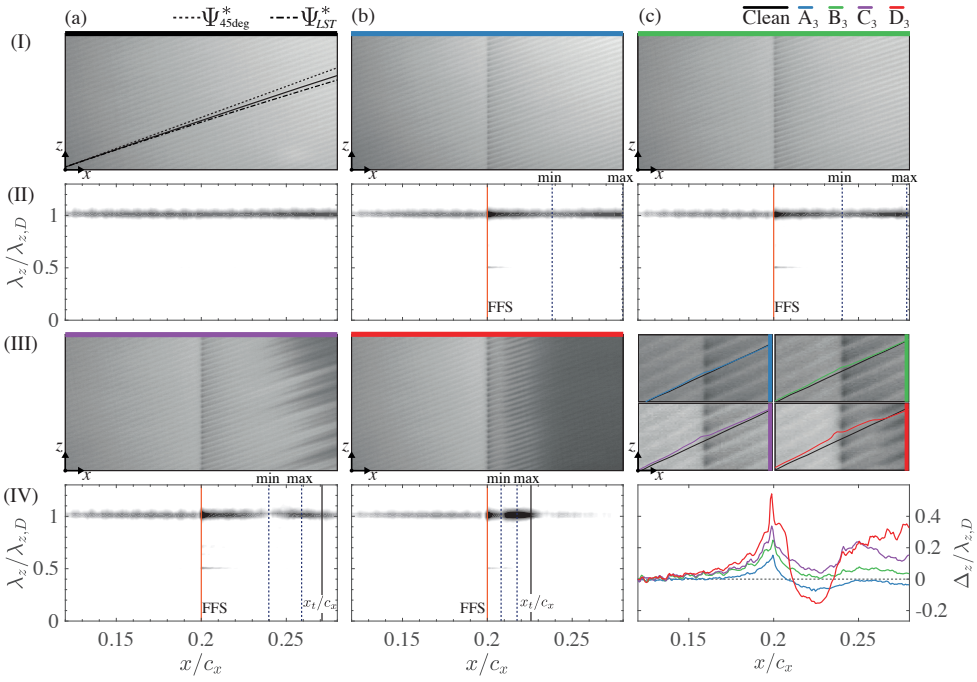

Figure 4.5: Comparison of IR-A thermal maps (I and III, flow from left to right) and spatial PSD analysis (II and IV, 20 levels of $\ln(P/\bar{P}_{\max_z})$ from -3 to 1): (Ia-IIa) Clean; (Ib-IIb) A_3; (Ic-IIc) B_3; (IIIa-IVa) C_3; (IIIb-IVb) D_3; (IIIc) CF vortices trajectories; (IVc) change in CF vortices trajectory due to FFS. ($\lambda_{z,D}$ = 7.5 mm)

the step with increasing step height. Here, it is important to note that for cases C_3 and D_3, a different mechanism is responsible for the appearance of the second maxima. More specifically, in these cases, laminar–turbulent transition occurs within the measurement domain. The pattern of the transition reveals spanwise modulations at the same wavelength as the forced CF vortices. At breakdown, the increased thermal contrast between adjacent laminar and turbulent regions effectively produces the observed second maxima. Therefore, the analysis of the non-monotonic pattern is restricted exclusively to the cases A_3 and B_3 for which the boundary-layer flow remains in a laminar condition for the entire measurement region. In addition, it must be stressed here that although the IR imaging has been performed in radiometric conditions (i.e. surface temperature is measured), the non-uniformity of irradiated energy from the halogen lamps as well as the varying curvature and thermal conductivity of the wing model do not allow for direct extraction of the surface heat transfer coefficient. Nevertheless, the narrow field of view of IR-B largely mitigates these effects, allowing for a qualitative estimation of the amplitude of spanwise modulations in the near-wall shear around the step. In order to draw conclusions on the origin of this behaviour in the thermal maps, quantitative velocity measurements are essential, as described in the following sections.

The spatial spectral analysis employed here can be further exploited to gain insight into the organisation of the incoming CF vortices near the step. As previously discussed,

the thermal maps are representative of the local magnitude of the skin friction coefficient, which in turn is related to the local velocity shear near the wall. In the cases discussed above, the flow near the step is predominantly laminar and is being actively heated. As such, regions of high temperature (i.e. brighter color) represent low shear areas and *vice versa*. The characteristic streaky pattern is then qualitatively correlated with the modulation of the laminar boundary-layer typical of stationary CF instability. Henceforth, the trajectory (d_z) of the coherent structures near the wing surface can be inferred by unwrapping the spectral phase angle (ϕ) of successive (in streamwise direction) temperature profiles.

Figure 4.5(Ia) presents for the Clean configuration a comparison of the trajectory of the CF vortices (solid black line) with a reference line (dashed black line) featuring a streamline angle of $\Psi^* = 45$ deg (i.e. parallel to streamwise $X-$direction). The results indicate that the axis of the CF vortices is slightly tilted towards the inboard side of the wing resulting in a near-wall streamline angle of approximately $\bar{\Psi}^*_w = 42.6$ deg, which closely matches the one predicted by linear stability theory $\bar{\Psi}^*_{LST} = 41.2$ deg (dash–dotted line in figure 4.5Ia). This behaviour is in agreement with previous experiments by Serpieri and Kotsonis [71] which for similar conditions showed that the inclination of the near-wall streamline differs also by a few degrees from the streamwise X-direction in the measurement region.

The collected trajectories for all cases are presented in figure 4.5(IIIc). As a reference for all cases, the Clean configuration is given as a solid black line. Evidently, the interaction with the FFS results in a modification of the trajectory of the CF vortices given by the colour-coded lines. Figure 4.5(IVc), shows the relative trajectory changes ($\Delta_z = d_{z,SI} - d_{z,C}$) between the Clean ($d_{z,C}$) and the FFS ($d_{z,SI}$) cases. For the small FFS case (A_3), as the vortices reach the FFS, their trajectory strongly curves towards the outboard side of the wing (i.e. positive z direction). Shortly downstream of the step edge, the trajectory shows a very sharp turn towards the inboard side of the wing (i.e. negative z direction) before bending outboard again and relaxing to a direction almost parallel to the trajectory pertaining the Clean configuration. Qualitatively, the observed behaviour is similar for all the tested FFS cases, albeit intensifying with increasing step height. A similar behaviour has been reported by Eppink [136] when analysing the inviscid and near wall streamlines. In addition, Eppink [136] showed that near the FFS the bending of the near-wall streamline is more pronounced than the one experienced by the inviscid streamline.

The outboard–inboard–outboard trajectory near the step can be traced to a local modification of the pressure gradient by the FFS. Numerical simulations by Tufts *et al.* [129] and experimental measurements by Duncan *et al.* [127] showed that the addition of an FFS results in strong modification of the pressure gradient near the step. Hence, as the laminar boundary-layer and developing CF vortices approach the step, they will first encounter an adverse pressure gradient upstream of the step, followed by a localised favourable pressure gradient at the step position and a second region of adverse pressure gradient as the flow recovers downstream of the step. The influence of the FFS on the near-step development and the modification to the structure of the CF vortices will be further analysed in §4.4.

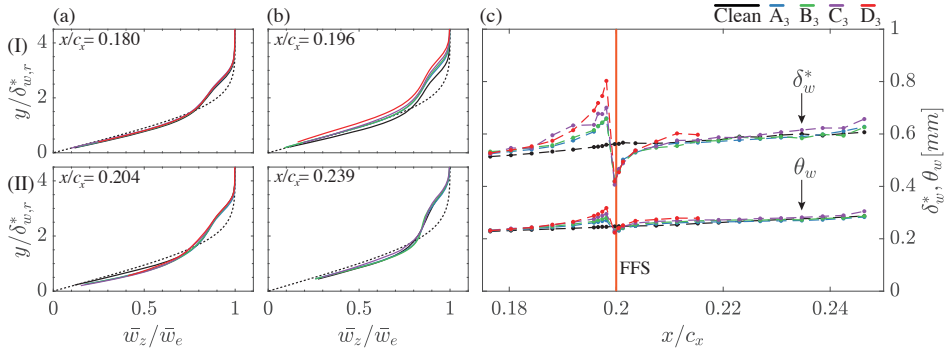

Figure 4.6: Selected profiles of spanwise mean flow velocity $\bar{w}_z$ (a,b) upstream and downstream of the FFS (dashed black line indicated the numerical boundary-layer solution) and (c) boundary-layer properties. ($\delta^*_{w,r}$ = 514µm)

4.4. DEVELOPMENT OF CROSSFLOW INSTABILITY WITH AN FFS

The global and local influence of the FFS on the transition behaviour and topology discussed in §4.3 suggest that complex flow dynamics occur when CF vortices interact with the FFS. This section explores the impact of an FFS on the development of the CF instability by comparing and contrasting the planar-PIV measurements for the Clean baseline configuration and the FFS cases as indicated on table 4.1.

4.4.1. IMPACT ON THE SPANWISE AVERAGED FLOW

As discussed in the previous section, the numerical simulations by Tufts *et al.* [129] and experimental measurements by Duncan *et al.* [127] indicate that the addition of the FFS results in a local modification of the pressure field which results in strong regions of adverse and favourable pressure gradient. In this work, limitations on the experimental set-up (figure 4.1) restrict the static pressure measurements to the Clean configuration. Nevertheless, the effects of the pressure gradient near the step are well captured in the change of the near-wall flow trajectories (figure 4.5IIIc,IVc) and the streamwise evolution of the boundary-layer investigated using PIV measurements of the spanwise (w) and vertical (v) velocity components presented in this section.

The velocity measurements are conducted in z-y planes (i.e. parallel to the leading edge and normal to the wing surface, figure 4.1) at various x/c_x stations. The mean flow $\bar{w}_z$ and $\bar{v}_z$ is calculated by averaging the time-averaged velocity components along the spanwise direction at each x/c_x station. Note, that based on the experimental set-up (see figure 4.1b) a positive $\bar{w}_z$ value indicates an average outboard (i.e. from the root towards the tip of the wing) flow movement. For clarity, the vertical y^*-coordinate is referenced to the clean baseline model surface, while the y-coordinate offsets the step height at its location. In addition, the vertical coordinates are non-dimensionalised with the displacement thickness $\delta^*_{w,r}$ = 514 µm, extracted from the w spanwise velocity PIV measurements at the most upstream plane (x/c_x = 0.176) for the Clean baseline case.

A comparison of the FFS cases with the Clean configuration at selected stations (fig-

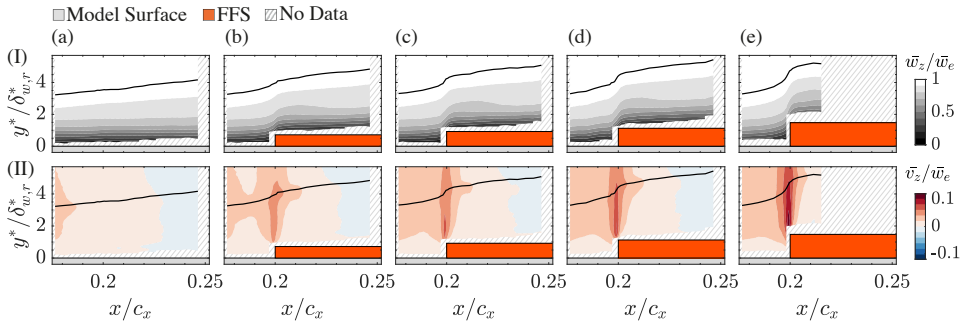

Figure 4.7: Contours of spanwise mean flow velocity (flow direction from left to right) $\bar{w}_z$ (I) and $\bar{v}_z$ (II): (a)Clean; (b) A_3; (c) B_3; (d) C_3; (e) D_3. The solid black line denotes $\delta_{99,w}$ ($\delta^*_{w,r} = 514\mu$m).

ure 4.6) reconciles the existence of an adverse pressure gradient upstream of the step which causes a deceleration in the boundary-layer flow and a reduction in the spanwise $\bar{w}_z$ average velocity component (figure 4.6Ib). This effect intensifies as the step height increases, and results in growth of the boundary-layer displacement (δ^*_w) and momentum (θ_w) thickness upstream of the FFS location, as shown in figure 4.6(c). Conversely, due to the favourable pressure gradient downstream of the FFS edge at $x/c_x = 0.204$ (figure 4.6IIa) there is an acceleration of the boundary-layer flow which leads to a reduction in δ^*_w and θ_w. Farther downstream, at $x/c_x = 0.239$ (figure 4.6IIb), the velocity profiles collapse to the Clean baseline condition except for the case D_3 (i.e. highest FFS), not shown in the figure since it transitions to turbulent flow around $x_t/c_x \approx 0.22$ (figure 4.3a).

Experimental observations by Eppink [130] in the streamline-oriented reference frame, indicate a decrease in the velocity component tangent to the streamline (u_s) and a decrease in the CF component (w_s) upstream of the FFS, which leads to a strong reversal of the CF velocity profile. These observations are in agreement with the near-wall trajectories presented in figure 4.5(IIIc,IVc), which shows that an outboard spanwise motion occurs upstream of the FFS. In the present work, it becomes evident that the face of the FFS forms the equivalent of an attachment line. As expected, due to the sharp FFS geometry near the step location, the incoming boundary-layer experiences a deceleration in $\bar{u}_z$. Although no surface irregularity or pressure gradient can form in the z direction, the modification of $\bar{u}_z$ directly couples to changes of $\bar{w}_z$, through momentum coupling. As such, a strong conversion of wall tangent velocity components (explicitly $\bar{u}_z$ and by consequence $\bar{w}_z$) into a wall normal velocity component ($\bar{v}_z$) is occurring. Evidence of this behaviour is shown in figure 4.7(IIa-IIe) in which all FFS cases lead to a considerable increase in the spanwise-averaged time-averaged vertical velocity $\bar{v}_z$ at the step. For the highest FFS case D_3, the maximum vertical velocity reaches a value of approximately 10 per cent of the external spanwise velocity. These results are in agreement with Eppink [130] where similar levels of amplification are reported. This rigorous upward flow movement by the FFS, which affects the boundary-layer flow will be analysed in more detail on the following sections.

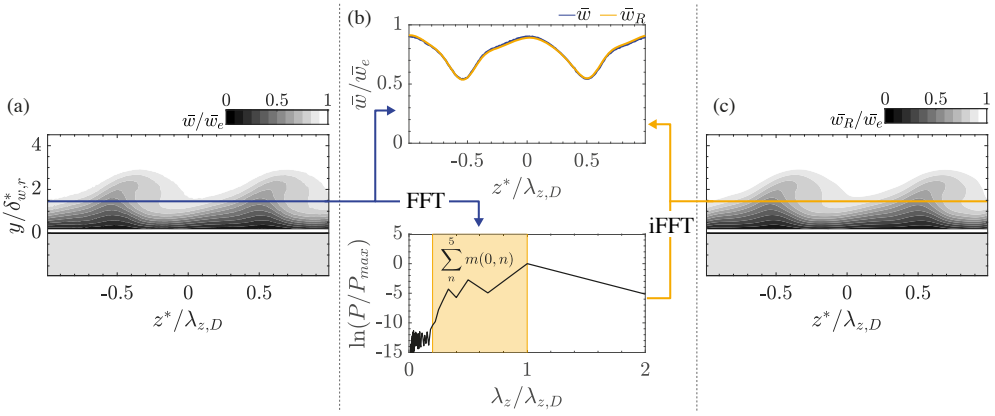

Figure 4.8: Schematic of spatial filtering of time-averaged spanwise velocity w contours (12 levels from 0 to 1, z^* positive direction outboard) for the Clean case: (a) original velocity field; (b) spectral decomposition; (c) reconstructed velocity field.

4.4.2. IMPACT ON THE TIME-AVERAGED FLOW

As elaborated in §4.2.1, the investigation of the influence of an FFS on the development and breakdown of CF instability is facilitated using DREs near the leading edge to condition the wavelength and amplitude of the disturbances. This conditioning allows for a highly periodic and uniform amplitude distribution for the ensuing CF vortices (figure 4.5), which further facilitates the extraction of pertinent information from the velocity fields in terms of spanwise spectral modes.

More specifically, for the analysis of the PIV measurements, the time-average and standard deviation of the velocity components have been spatially filtered using Fourier transformations. As indicated on the diagram in figure 4.8, at each wall-normal position in the measurement plane, a fast Fourier transform (FFT) has been applied on extracted velocity profiles along the z-direction. Subsequently, a pertinent set of Fourier modes are selected to reconstruct the velocity through the inverse fast Fourier transform (IFFT). In addition to enhancing the velocity fields by reducing the measurement noise (which typically appears at small wavelengths), this technique offers the possibility to isolate the effect of the FFS on a particular harmonic of the CF instability mode. Hence, for the remainder of the analysis, the reconstructed velocity fields (subscript R) are used unless otherwise noted. Moreover, the notation $m(0,n)$ [see 34, 94] is used to indicate the Fourier modes used during the reconstruction. Note that the first index in parenthesis corresponds to the frequency of the mode, which for the present study is zero, and indicates a stationary CF instability mode, while the second index (n) denotes multiples of the spanwise wavenumber of the CF vortices forced by the DREs. In addition, when indicated by the summation convention ($\sum_n^5 m(0,n)$), the velocity fields have been partially reconstructed using the wavelengths contained between the primary forced CF instability mode ($\lambda_{z,D} = 7.5$ mm) and its fifth harmonic ($\lambda_{z,D} = 1.5$ mm).

Figures 4.9 and 4.10 show the reconstructed fields for the spanwise ($\bar{w}_R$) and vertical ($\bar{v}_R$) time-averaged velocity, respectively, for the Clean and FFS cases at selected loca-

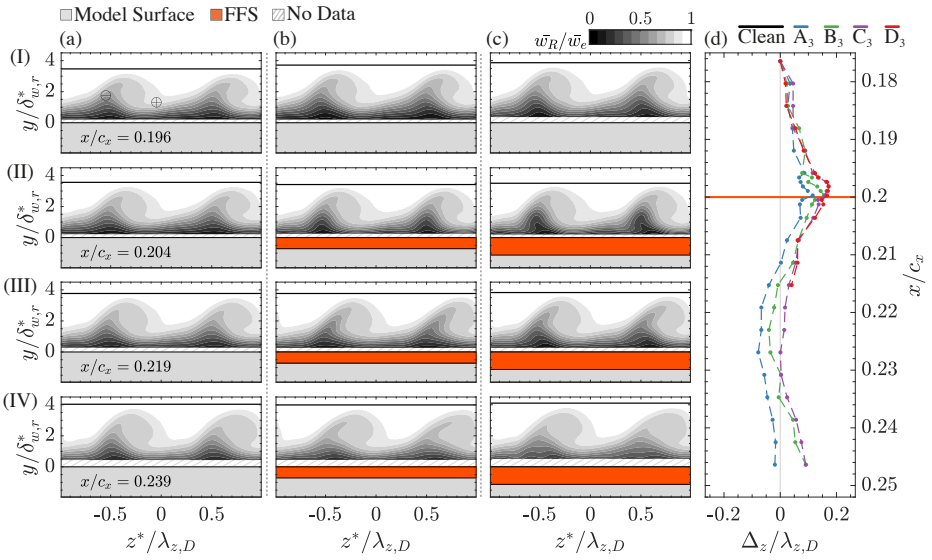

Figure 4.9: Contours of time-averaged spanwise velocity (z^* positive direction outboard), spatially filtered between $\sum_n^5 m(0,n)$: (a)Clean; (b)A_3; (c)C_3; and (d)change in trajectory of the CF vortices due to the FFS. Solid black line denotes $\delta_{99,w}$ ($\delta^*_{w,r}$ = 514µm and $\lambda_{z,D}$ = 7.5mm)

tions upstream and downstream of the step. Note that the z^*-coordinate features a shift with respect to the z-coordinate origin such that the CF vortices align between presented streamwise stations. In the Clean configuration, the spanwise velocity contours $\bar{w}_R$ presented in figure 4.9(Ia), show a pair of stationary corotating vortices. These stationary vortices are evenly spaced at the forced wavelength ($\lambda_{z,D}$ = 7.5 mm) for the entire measurement region as shown by the spatial spectral analysis on the thermal maps presented in figure 4.5(IIa). These CF vortices develop inside the boundary-layer, where they transfer high momentum flow towards the wall (downwelling region, ⊕ in figure 4.9Ia) and low momentum flow away from it (upwelling region, ⊖ in figure 4.9Ia). As these structures evolve downstream, their amplitude and inherent distortion they impart on the mean flow increases [73, 89, 94]. For the condition under study, the initial amplitude provided by the DREs results in a set of nonlinearly amplified vortices when reaching the step location.

The interaction of the stationary CF vortices with the FFS results in topological modifications within the boundary-layer as shown in figure 4.9. As the CF vortices reach the FFS (x/c_x = 0.196, figure 4.9Ib-Ic) there is an evident increase of the transfer of low momentum flow away from the wall (i.e. upwelling region). This corresponds well with the general upward deflection and streamwise deceleration of the incoming flow evident in figure 4.6 and 4.7, as well as the observations of Eppink [130] which indicate an amplification of the vertical velocity component near the FFS. At the same streamwise location, the vertical velocity contours ($\bar{v}_R$) in figure 4.10(Ib-Ic) indicate a strong increase, especially on the inner section of the upwelling region. Henceforth, the overall increase of vertical velocity at the step location is suggestive of the underlying amplification of the

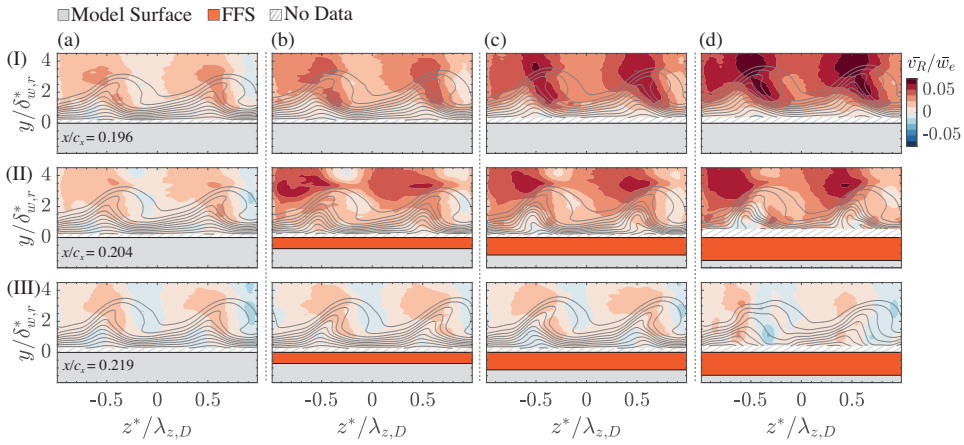

Figure 4.10: Contours of time-averaged vertical velocity and spanwise velocity (grey line 12 levels from 0 to 1 same contours as in figure 4.9) z positive direction outboard, spatially filtered between $\sum_n^5 m(0,n)$: (a)Clean; (b)A_3; (c)C_3; and d) D_3. ($\delta^*_{w,r}$ = 514µm and $\lambda_{z,D}$ = 7.5mm)

instabilities as a result of the flow modifications incurred by the step.

The near-wall structures trajectory identified in §4.3 revealed an outboard–inboard–outboard motion near the wall. In contrast to IR imaging, the PIV measurements facilitate the inspection of this flow deflection away from the wall. Specifically, profiles of spanwise velocity perturbation ($\hat{w}_R$) are extracted along the z-direction at the height of the stationary disturbance profile maxima (calculated as described in §4.2.4) for each measurement plane. Successive spanwise profiles are compared using a vector convolution (i.e. cross-correlation). The result of this analysis is referenced to the most upstream measurement plane and yields the relative location (d_z) along the z-direction assumed by the CF vortices as they evolve downstream. Figure 4.9(d) shows the relative change of trajectory ($\Delta_z = dz_{SI} - dz_C$) between the FFS cases (dz_{SI}) and the Clean configuration (dz_C), confirming that the outboard–inboard–outboard motion described by the near-wall trajectory also occurs away from the wall, in proportional intensity to the FFS height.

Eppink [136] reported an abrupt change of the near-wall streamline angle as the boundary layer flow intercepts the FFS. Henceforth, to evaluate the spanwise motion effect as a function of the distance from the wall, figure 4.11(Ia-IIb) shows a set of wall-parallel $\bar{w}_R$ and $\bar{v}_R$ planes extracted away from the wall (400 µm above the height of the stationary disturbance profile maxima). The dashed lines in figure 4.11(c) indicate the relative shift (Δ_z) along the z direction calculated for each configuration. Additionally, wall-parallel planes extracted at a vertical location closer to the wall (200 µm below the height of the stationary disturbance profile maxima) are presented in figure 4.11(IIIa-IVb) with Δ_z in figure 4.11(d). A comparison of the Δ_z above and below (figure 4.11c and d) the stationary disturbance profile maxima confirm that the outboard–inboard–outboard motion intensifies closer to the wall.

Summarising up to this point, the observed influences of the FFS on the develop-

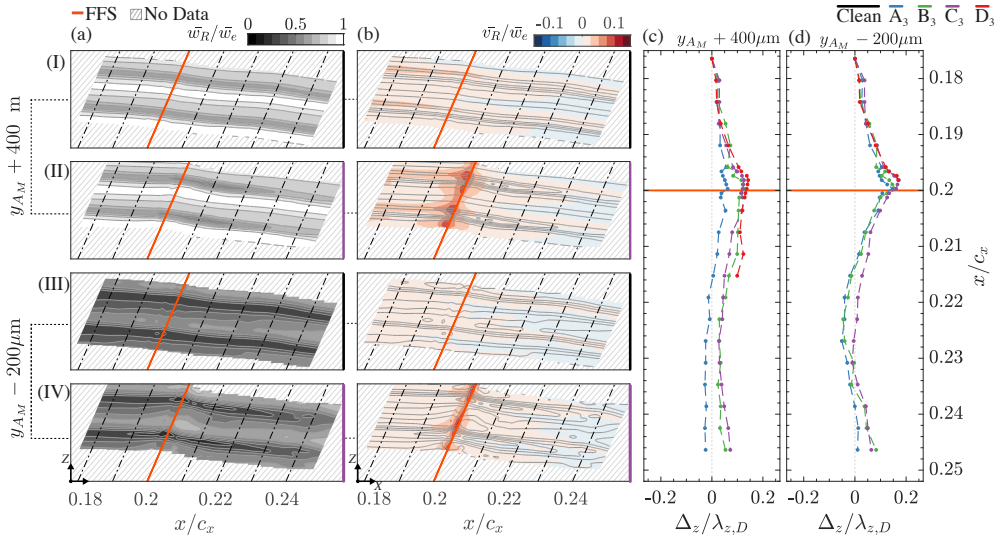

Figure 4.11: Wall-parallel contour maps of time-averaged spanwise and vertical velocity spatially filtered between $\sum_n^5 m(0,n)$. The contours in rows I and II are extracted at 400μm above the height of the steady perturbation maxima (y_{A_M}), while the contours in rows III and IV are extracted closer to the wall at 200μm below y_{A_M} : (I,III) Clean; (II,IV) C_3; and panels (c,d) the corresponding relative change of trajectory ($\Delta_z = dz_{SI} - dz_C$).

ing boundary-layer reveal topological changes in both spanwise averaged flow as well as stationary CF vortices. As the incoming flow approaches the step, a strong outboard–inboard–outboard spanwise motion of the CF vortices is evident. This reflects the non-monotonic changes in pressure imposed by the step shown in Duncan *et al.* [127] and Tufts *et al.* [129]. This effect is stronger near the wall, where the deceleration in the base flow is larger. Consequentially, an intense ejection of vertical velocity is documented at the vicinity of the step in agreement with Eppink [130], resulting from the upward deflection of incoming wall-tangent flow as the latter engages with the step. The role of the spanwise motion on the overall transition scenario cannot be conclusively inferred by the presented measurements. However, potential candidate mechanisms can be proposed. A simple interpretation of this motion can be traced simply on the underlying changes of the base flow, which in turn can lead to modifications of the wavenumber vector of an incoming instability. A different effect could be the potential appearance of non-modal effects, in a mechanism similar to the well known lift-up effect active in regions of strong shear changes [e.g. 51, 183, 184]. Notwithstanding the active mechanism, the relation between the outboard–inboard–outboard motion and the growth of the instability remains a point of interest. To elucidate this, fully three-dimensional velocity measurements or detailed numerical simulations of these flows are deemed necessary.

4.4.3. IMPACT ON PRIMARY CROSSFLOW INSTABILITY AND HARMONICS

As described in §4.2.4, the experimentally measured mode-shape of the stationary disturbance profile is equivalent to the spanwise root mean square ($\langle\rangle_z$) of the time-averaged

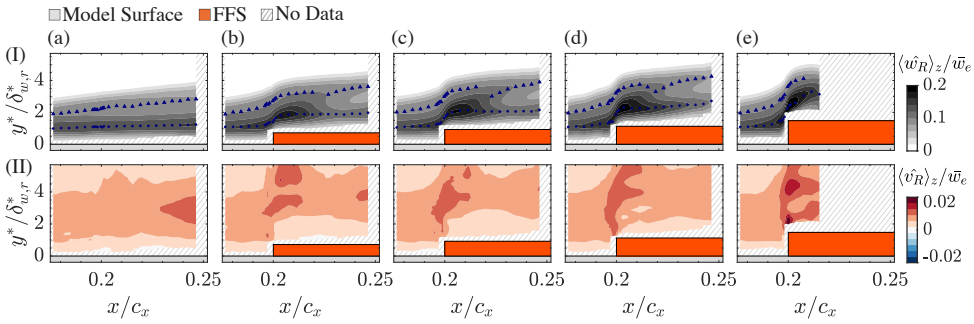

Figure 4.12: Contours of steady disturbances profiles (flow direction from left to right) $\langle \hat{w_R} \rangle_z$ (I) and $\langle \hat{v_R} \rangle_z$ (II) spatially filtered between $\sum_n^5 m(0,n)$. Location of lower (•) and upper lobe (▲) : (a)Clean (b) A_3; (c) B_3; (d) C_3; (e) D_3. ($\delta^*_{w,r}$ = 514µm)

perturbation ($\hat{w}_R$ or $\hat{v}_R$). Previous experimental studies on CF instability [e.g. 71, 73, 89] have used this metric in the analysis of the Euclidean sum of the vertical and streamwise velocity components measured by hot-wire anemometers. By merit of the chosen imaging planes in the present study, the disturbance profiles have been calculated independently for each measured velocity component.

Figure 4.12 presents contour plots of the stationary disturbance profiles $\langle \hat{w}_R \rangle_z$ and $\langle \hat{v}_R \rangle_z$ calculated on the partial reconstructed fields (i.e. $\sum_n^5 m(0,n)$) for all FFS cases. The results for the spanwise disturbance profiles ($\langle \hat{w}_R \rangle_z$) in figure 4.12(Ia-Ie) show a distinguishable lower lobe upstream of the FFS at $x/c_x = 0.18$, situated near the wall at $y/\delta^*_{w,r} \approx 1$, which corresponds to the wall-normal maxima of these profiles (• markers in figure 4.12Ia-Id). In addition, a second upper lobe is also identified (▲ markers in figure 4.12Ia-Id). The appearance of this feature has been linked to the mean flow distortion typical in the nonlinear stages of stationary CF instability development [89, 176]. Near the step location at $x/c_x = 0.2$ there is an evident amplification of the spanwise disturbance profiles ($\langle \hat{w}_R \rangle_z$) followed by a decay ($x/c_x > 0.21$) in all measured cases. Moreover, for $x/c_x > 0.22$ the second upper lobe (▲ markers in figure 4.12Ia-Id) becomes increasingly evident, indicating a strong mean flow distortion as shown in figure 4.9(IVa-IVc).

Previous studies have reported the development of a strong peak near the wall in the disturbance profiles downstream of the step location (see figure 10 in Eppink [130] and figure A5a in Tufts *et al.* [129]). In this work, a second peak near the wall is not evident in the spanwise perturbation profiles $\langle \hat{w}_R \rangle_z$, since as shown in figure 4.12(Ia-Ie) only one lower lobe is present upstream and downstream of the FFS for all the configurations. The lack of the near-wall structure in the present study can be attributed to unresolved regions in the PIV planes, originating from wall reflections. Nevertheless, the vertical perturbation profiles $\langle \hat{v}_R \rangle_z$ (figure 4.12IIa-IId) for the highest step case D_3 do reveal a clear peak near the wall at the location of the FFS in agreement with Eppink [130].

Figure 4.13 presents the spanwise disturbance $\langle \hat{w}_R \rangle_z$ profiles extracted at selected streamwise locations upstream and downstream of the FFS for the partial reconstructed field ($\sum_n^5 m(0,n)$, figure 4.13Ia-IVa), primary forced mode ($m(0,1)$, figure 4.13Ib-IVb) and first harmonic ($m(0,2)$, figure 4.13Ic-IVc). In all FFS cases there is a considerable up-

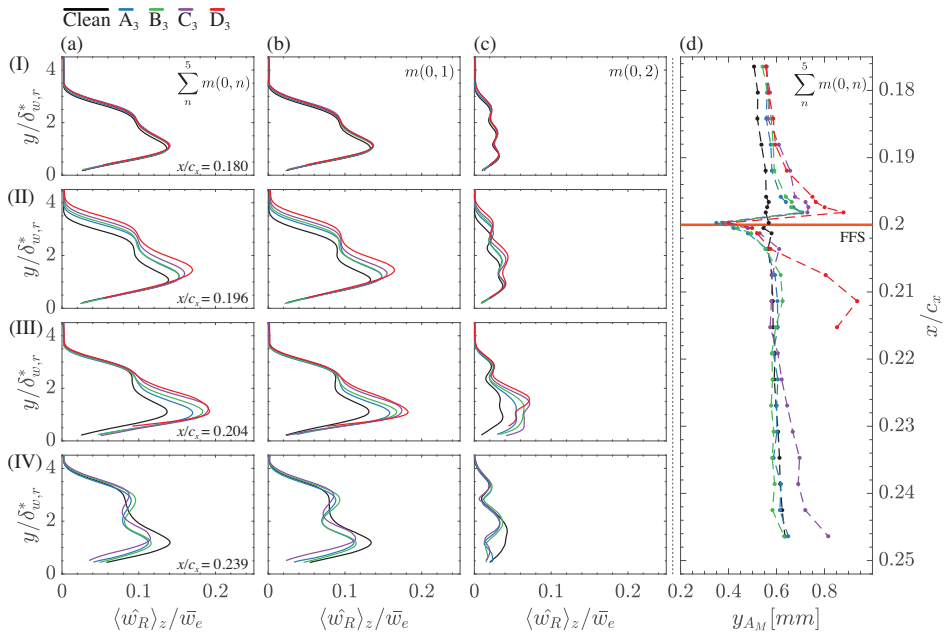

Figure 4.13: Selected profiles (a-c) of the steady disturbance $\langle \hat{w}_R \rangle_z$ upstream and downstream of the FFS for the primary CF instability modes and its first harmonic. (d) Streamwise evolution of the steady disturbance maxima wall-normal height (y_{A_M}). ($\delta^*_{w,r}$ = 514µm)

stream effect which leads to a substantial increase in the profiles maxima ($\max(\langle \hat{w}_R \rangle_z)_y$, figure 4.13IIa). It is noteworthy that the amplitude increase coincides with the localized increase in the vertical velocity component (v), the region of outboard spanwise motion of the CF vortices (figures 4.9d and 4.5IVc) and possible reversal of the CF velocity component (Eppink [130] figures 8 and 9).

Figure 4.13(d), shows the streamwise evolution of the wall-normal location of the lower lobe (i.e. closer to the wall) maxima (y_{A_M}) of the spanwise steady disturbance profiles $\langle \hat{w}_R \rangle_z$ for the partial reconstructed field. Note that the y-coordinate reference is the model surface and therefore it has been offset by the step height. In agreement with Eppink [130, 136] as the CF vortices approach the step they experience an increase in y_{A_M}, essentially lifting off the surface before reaching the FFS edge. Just downstream of the step edge ($x/c_x = 0.204$, figure 4.13IIIa) there is a decrease in y_{A_M} as there is a reduction in the boundary-layer displacement thickness (δ^*_w in figure 4.6c) and a sudden sharp increase in the maximum amplitude of the primary stationary disturbance ($m(0,1)$, figure 4.13IIIb). The highest step height (D_3) is responsible for the maximum amplification. Similarly, the $\langle \hat{w}_R \rangle_z$ profiles corresponding to the reconstructions using only the first harmonic ($m(0,2)$, figure 4.13Ic-IVc) show a considerable amplification at the step location.

In addition to changes in disturbance amplitude, the strong amplification of the primary disturbance mode $m(0,1)$ near the FFS edge results in a significant mean flow dis-

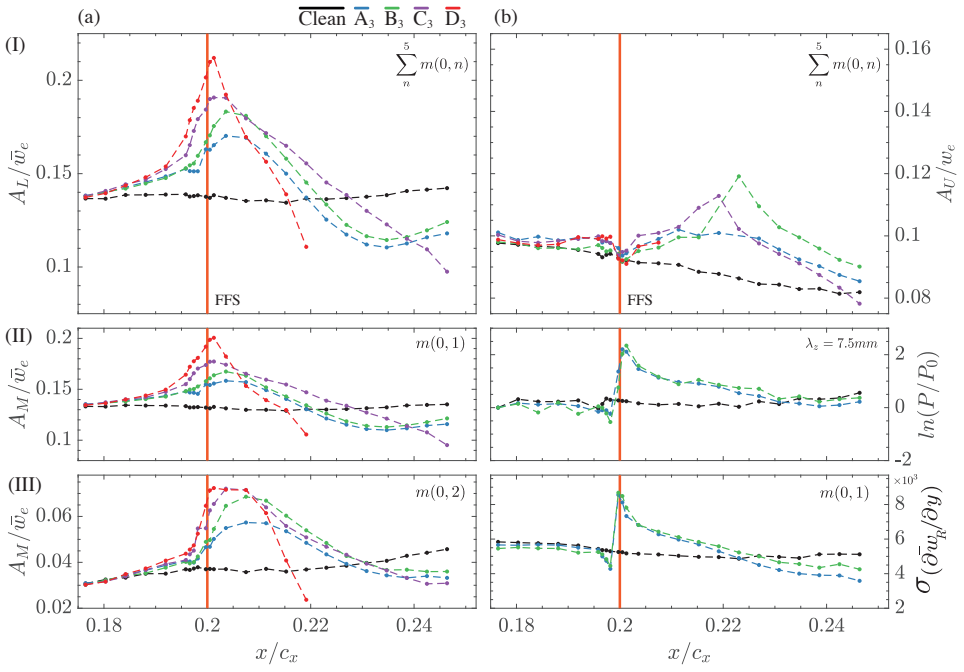

Figure 4.14: Steady disturbance profile amplitudes: (Ia) lower lobe amplitude (A_L); (Ib) upper lobe amplitude (A_U); (IIa) primary CF instability mode ($m(0,1)$) maximum amplitude; (IIa) first harmonic ($m(0,2)$) maximum amplitude; (IIb) IR-B PSD extracted at $\lambda_z = 7.5$mm; (IIIb) primary CF instability mode ($m(0,1)$) standard deviation along the span direction of the wall-normal gradient at $y/\delta^*_{w,r} = 0.68$.

tortion and saturation of the CF vortices. This mean flow distortion is evident in the change of the shape of the mode which leads to the development of two clearly distinguishable local maxima, as shown in figure 4.13(IVb). In a smooth wing CF instability development, the appearance of this second upper lobe signals a typical nonlinear development of stationary CF instability, which results in a strong mean flow distortion and the onset of secondary instability modes [89, 176]. Nevertheless, in this case, breakdown of the CF vortices only occurs for the case C_3 at $x_t/c_x \approx 0.27$ and D_3 at $x_t/c_x \approx 0.22$ as indicated on figure 4.3(a).

Based on the partial reconstruction (i.e. $\sum_n^5 m(0,n)$), the amplitudes of the disturbance profile $\langle \hat{w}_R \rangle_z$ lower (A_L) and upper (A_U) lobes are presented in figure 4.14(Ia-Ib). The results for the FFS cases indicate that the amplitude of the lower lobe (A_L) intensifies rapidly upstream of the step and reaches a maximum value just downstream of the step edge. Hereinafter, as the amplitude of the upper lobe increases (A_U) (i.e. stronger mean flow distortion), there is a steep decay in A_L which leads to values below the Clean baseline case (black line in figure 4.14a). Once this minimum is reached a second region of growth is observed for the cases A_3 and B_3, which do not undergo laminar breakdown in the region $0.18 \leq x/c_x \leq 0.25$ as indicated by the IR thermal maps on figure 4.5(Ib-Ic).

The overall amplification trend is in good agreement with the detailed experimental work presented by Eppink and Casper [135] and [130], where a similar amplification–decay–amplification pattern has been observed on the $\langle \hat{u} \rangle_z$ perturbation peak amplitude. Moreover, the results presented in figure 14 in Eppink [130] indicate that the slope of the second region of growth becomes steeper with increasing step height.

Evidence of this amplification–decay–amplification pattern was previously presented in the spectra of the IR thermal maps (figure 4.5) for the small (A_3) and moderate (B_3) cases. As noted before, for cases C_3 and D_3, the second amplification maxima in the IR maps are instead related to the laminar–turbulent transition front. Therefore, the analysis of this pattern is restricted to the cases A_3 and B_3 for which the boundary-layer flow remains in a laminar condition for the entire measurement region. To further probe the correlation between the growth of the CF vortices and the pattern observed in the spectral analysis of IR-A thermal maps, the power content (P) pertaining to the primary forced mode ($\lambda_z/\lambda_{z,D} = 1$) is shown in figure 4.14(IIb). At each streamwise location P is normalised with the value corresponding to the most upstream ($x/c_x = 0.176$) location (P_0). In addition, figure 4.14(IIIb) presents the standard deviation along the span direction of the wall-normal velocity gradient ($\partial \bar{w}_{R,z}/\partial y$) at $y/\delta^*_{w,r} = 0.68$ above the wall. The results presented in figure 4.14(IIb,IIIb) show a striking correlation, reconciling the amplification–decay–amplification pattern in the spectra of the IR thermal maps to local changes in the surface heat transfer properties due to variations in wall shear (i.e. changes in $\partial \bar{w}_{R,z}/\partial y$) related to the amplification of the CF instability by the step.

Figure 4.14(IIIa) suggests a similar amplification and decay trend for the harmonic ($m(0,2)$) past the step location. These results are in agreement with previous observations [e.g. 130, 181] and support the spatial analysis of the IR measurements in figure 4.5, which showed an amplification of the first harmonic at the step location for all the FFS cases. However, it is striking to note the relatively "delayed" amplification of this first harmonic compared with the primary mode. For each FFS case, the peak of $m(0,2)$ occurs downstream of the corresponding peak of $m(0,1)$. This behaviour further suggests a (partially) indirect influence of the higher harmonics by the FFS. More specifically, the primary CF instability increases in amplitude due to interaction with the FFS, inherently forcing nonlinear amplification of higher harmonics as well as mean flow distortion. In addition, future fully three-dimensional measurements in this region are deemed necessary to characterise a possible deformation of the recirculation region downstream of the FFS location.

Eppink [130] proposed that the first region of growth is linearly caused by a destabilisation of the stationary CF instability modes due to the strong inflectional profiles caused by the adverse pressure gradient near the step. In turn, the second region is attributed to a non-linear development due to the modulation of the recirculation region downstream of the FFS edge, which resulted in streamwise oriented vortices which amplify the harmonics of the primary mode. The behaviours observed by Eppink [130] and the ones explained in this work, highlight the sensitivity and complexity of the FFS-CFI interaction.

Based on the findings presented so far, the steady interaction of the CF vortices with the FFS can be summarised as follows. As the CF vortices travel towards the FFS they experience an adverse pressure gradient which results in an outboard spanwise mo-

tion (figure 4.5IVc and 4.9d), a decrease in the wall-tangent velocity components (figure 4.6Ib) and an increase in the amplitude of the spanwise (w) disturbance profile (figure 4.13IIa) when compared with the clean configuration. In addition, at the step, a portion of the wall-tangent velocity component converts into a strong vertical (v) velocity component due to the upward deflection (figure 4.7IIa-IIe). This vertical component is very localised and appears to reach a maximum on the inner side of the upwelling region of the CF vortices. Downstream of the step, there is a further amplification of the spanwise (w) disturbance profile (figure 4.14Ia at $x/c_x \approx 0.205$) and a sudden inboard spanwise motion (i.e. favourable pressure gradient). This strong amplification drives a further increase of mean flow distortion and rise of non-linear interactions (figure 4.9 and 4.14). This leads to a saturation of the primary CF vortices (figure 4.14Ia at $x/c_x \approx 0.21$), and subsequent increase in harmonic amplitude. Farther downstream, the stationary CF instability decays and the CF vortices experience an outboard spanwise motion (i.e. adverse pressure gradient). Finally, a second region of growth enhanced by the nominal favourable pressure distribution of the wing develops for the smaller FFS cases.

One of the most significant outcomes of the aforementioned observations is revealed when comparing the transition location behaviour evaluated using the IR imaging maps (figure 4.3) and the amplitude growth of the stationary CF instability near the FFS step presented in figure 4.14. For all cases of FFS investigated in this work, the partial reconstructed ($\sum_n^5 m(0,n)$) amplitude at the downstream end of the PIV domain is lower than the Clean case. This is certainly expected for the two highest step cases (C_3 and D_3), as the imminent breakdown of the vortices downstream of the step effectively breaks the spanwise modulation, 'smoothening-out' the apparent amplitude. However, for the two smaller step cases (A_3 and B_3), the laminar boundary-layer survives the passage over the step and emerges apparently stabilised in the downstream vicinity of the step. Naturally this effect is localised, as the CF vortices start growing again, as evident in figure 4.14(Ia) as well as from the appearance of the second maxima in the thermal maps spectra (figure 4.5IIb,IIc). In addition, figure 4.6 confirms the spanwise averaged flow recovery to the Clean case at $x/c_x \approx 0.24$. In combination, it becomes apparent that the drastic effects of the FFS on the transition location cannot be traced solely to the evolution of stationary instabilities, highlighting the importance of temporal fluctuations. Henceforth, the following discussion focuses on the effect of the FFS on the unsteady disturbances.

4.4.4. IMPACT ON THE UNSTEADY DISTURBANCES

As described in detail in §1.2.2, the analysis of temporal velocity fluctuations in specific regions within the CF vortices provides important information regarding steady and unsteady instability development and eventual laminar breakdown. Due to the inherent relation between unsteady secondary instabilities and mean velocity gradients, the latter are first inspected. The interaction of the stationary CF instability with the FFS results in a topological modification of the structure of the CF vortices which further manifests as alterations in the vertical and spanwise velocity gradients presented in figure 4.15. As already shown, downstream of the FFS edge ($x/c_x = 0.204$, figure 4.9IIb-IIc) the sudden and abrupt increase in $\bar{w}_z$ leads to a substantial decrease in the boundary-layer momentum thickness (δ^*_w, figure 4.6c) when compared with the Clean configuration. This transfer of high-momentum fluid towards the wall increases the vertical gradient ($\partial \bar{w}_R/\partial y$)

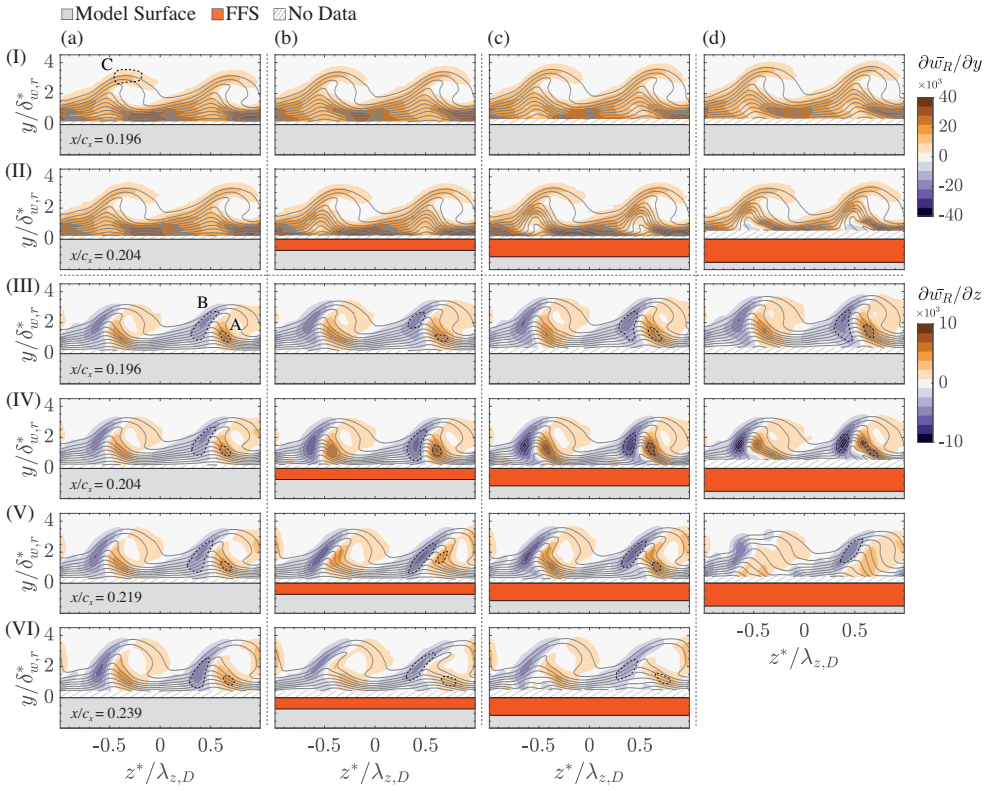

Figure 4.15: Contours of time-averaged velocity gradients and spanwise velocity (grey line 12 levels from 0 to 1 same contours as in figure 4.9) z^* positive direction outboard, spatially filtered between $\sum_n^5 m(0,n)$: (a)Clean; (b)A_3; (c)C_3; (d) D_3. ($\delta^*_{w,r}$ = 514µm and $\lambda_{z,D}$ = 7.5mm). Areas A and B are defined in figure 4.16

near the wall in the downwelling region of the CF vortices as shown in figure 4.15(IIb-IId). In addition, a localised region of negative vertical gradient ($\partial\bar{w}_R/\partial y$) is found at the centre of the upwelling region near the wall for the moderate (C_3) and high (D_3) steps. While the inclusion of the steps produces notable effects on the vertical gradient near the wall, the effect is largely minimal at the cusp of the stationary CF instability (area C), where type II secondary instability is expected to grow. This behaviour reconciles with the observations in §4.4.2, where the major deflection and shearing motion experienced by the stationary CF vortices was identified to be largely oriented in the spanwise direction.

The strong changes in amplitude as well as spanwise shearing motion of the stationary CF vortices past the step edge resulted in noticeable changes in the spanwise velocity gradients, which are predominantly located at the outer and inner sections of the upwelling regions. In contrast to the vertical gradient, changes in the spanwise gradient are global and affect both positive (i.e. inner, area A in figure 4.15IIIa) and negative (i.e. outer, area B in figure 4.15IIIa) gradients. Particularly the outer spanwise gradients have been typically associated with the growth of type I secondary instability. In all monitored

FFS cases, the step induces higher gradient levels than in the Clean configuration near the step (figure 4.15IVa-IVd). This influence is already evident slightly upstream of the step as shown in figure 4.15(IIIa-IIId).

While the intensification of the spanwise gradient is consistently observed for all cases in the vicinity of the step, the downstream development of $\partial \bar{w}_R/\partial z$ is highly dependent on the step height. In the case of the highest FFS (D_3), the interaction of the stationary CF instability with the step leads to an abrupt amplification, saturation and breakdown of the CF vortex structure as shown in figure 4.15(Vd). The interaction of the stationary CF instability with the moderate step case (C_3) follows a similar trend as the CF vortices experience a strong amplification near the step followed by saturation ($x/c_x \approx 0.21$). This leads to a loss in spanwise coherence and decrease in the intensity of the spanwise gradients (figures 4.15IVc-VIc) prior to laminar breakdown, which occurs at $x/c_x \approx 0.27$ (figure 4.3a).

In contrast, for the small FFS cases A_3 and B_3 (not shown in figure 4.15) the CF vortices do not experience breakdown in this streamwise region. Yet, the spanwise gradient experiences a significant decay farther downstream of the step . Particularly for the shallowest case A_3, the spanwise gradient at $x/c_x = 0.239$ (figure 4.15VIb) is in fact rendered lower than the corresponding Clean case at the same streamwise location. This is a direct consequence of the stabilisation and decrease in amplitude of the stationary CF instability, as identified in figure 4.14.

The significant changes in both vertical and spanwise velocity gradients due to the step can further be associated with the development and growth of unsteady shear layer instabilities, widely acknowledged to play an important role in the breakdown of CF instability dominated flows. Figure 4.16 presents a set of contour plots of spanwise temporal velocity fluctuations (σw_R) at selected streamwise locations upstream and downstream of the FFS location. Time-resolved HWA measurements, on the same configuration as the present Clean case and similar flow conditions by Serpieri and Kotsonis [71, 90], identified type I/II instabilities in the frequency range between 3.5 and 8 kHz and type III modes in the range between 350 and 550 Hz, albeit for a lower DRE amplitude. Considering the low repetition-rate of PIV acquisitions employed in the present study (i.e. 15 Hz), spectral analysis and frequency filtering are not applicable. Nevertheless, the long sampling time (i.e. 80 s) ensures that the fluctuating velocity field represents an ensemble of both low- and high-frequency disturbances, which can be considered temporally uncorrelated. Furthermore, these instabilities are strongly localised within the structure of the stationary CF instability, allowing direct evaluation of the development of each type.

The results for the Clean baseline case in figure 4.16(Ia-VIa), show a local maximum of fluctuations at the location corresponding to a type III mode (A in figure 4.16Ia). Monitoring a downstream location (figure 4.16Va) indicates a decaying interaction between weak travelling CF instability modes and the forced stationary CF vortices, as the magnitude of the fluctuations in this region decrease. To better illustrate this decaying behaviour, figure 4.17 presents average values of spanwise velocity gradient and temporal fluctuation amplitude extracted within areas A and B indicated in figures 4.15 and 4.16. The two extraction areas are defined for each plane and step case as isolines of 85% of the local maximum amplitude of unsteady fluctuations on the inner and outer side of

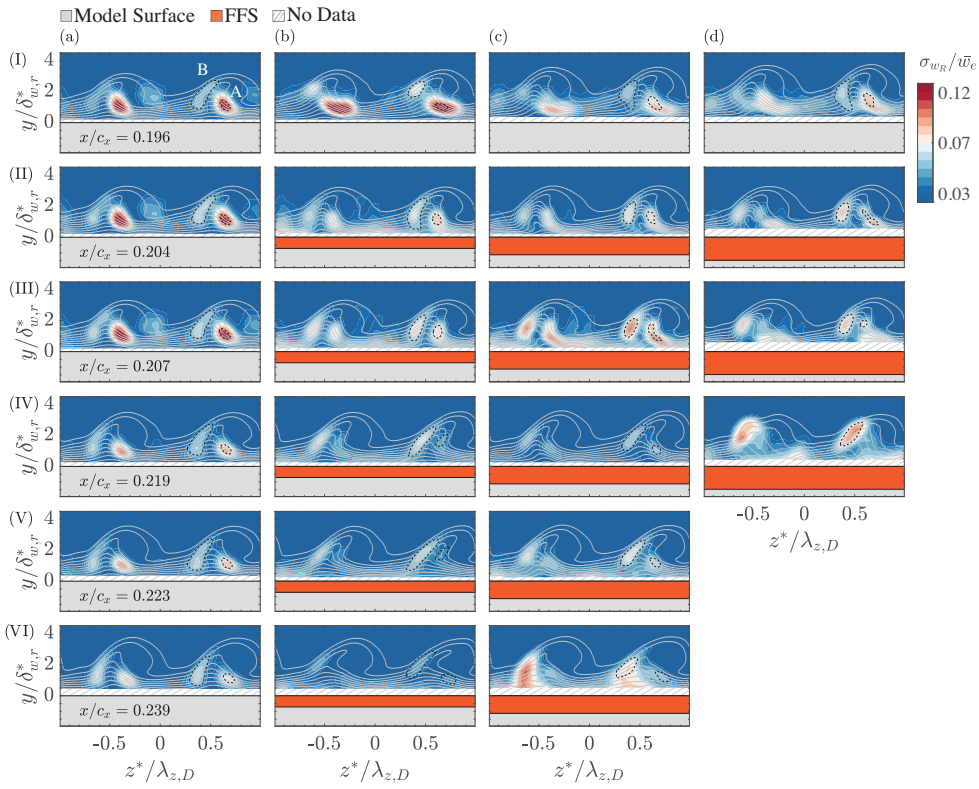

Figure 4.16: Contours of spanwise temporal velocity fluctuations and spanwise velocity (grey line 12 levels from 0 to 1 same contours as in figure 4.9), z^* positive direction outboard spatially filtered between $\sum_n^5 m(0,n)$: (a)Clean; (b)A_3; (c)C_3; (d) D_3. ($\delta^*_{w,r}$ = 514µm and $\lambda_{z,D}$ = 7.5mm.) Extraction areas A and B are defined as isolines of 85% of the local maximum amplitude of unsteady fluctuations on the inner and outer side of the upwelling region.

the upwelling region. Naturally, values corresponding to area A refer to positive spanwise gradients and type-III dominated fluctuations, while values corresponding to area B refer to negative gradients and type-I dominated fluctuations.

Figure 4.17(b) confirms the decay in the temporal velocity fluctuations (σw_R) in region A corresponding to type III instabilities in the Clean baseline case (black line) in the range of $x/c_x > 0.2$. The addition of small (A_3) to moderate (C_3) steps result in a further reduction of velocity fluctuations (σw_R) in this region. Evidently, the addition of the FFS leads to a reduction in the interaction between travelling and stationary CF instability modes. Furthermore, it is striking to note that this stabilising effect is already active upstream of the FFS (compare figures 4.16Ia-Id). This behaviour strongly suggests a change in stability characteristics of the incoming boundary-layer. Considering the findings described in figure 4.14, for the same streamwise range ($0.18 < x/c_x < 0.2$), the primary stationary CF instability appears to destabilise and increase in amplitude. The concurrent dampening of type-III modes can then be associated with a combination of

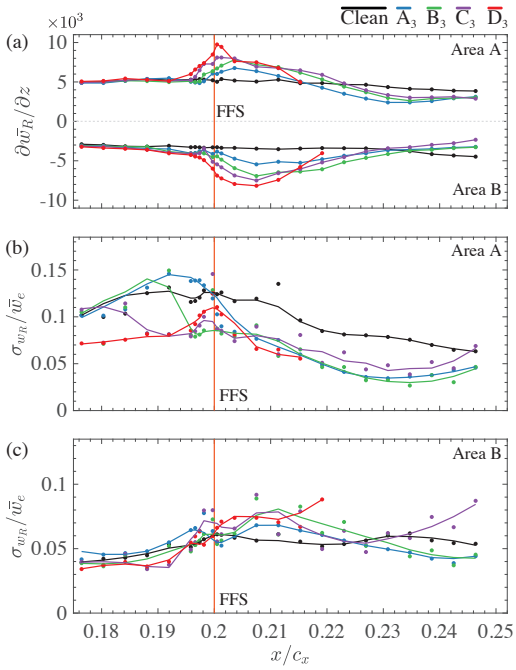

Figure 4.17: Streamwise evolution of averaged extracted values in areas A and B (defined in figure 4.15 and 4.16): (a) positive (area A) and negative (area B) a averaged spanwise velocity gradients; (b) averaged velocity fluctuations in area A; (c) averaged velocity fluctuations in area B.

(possibly conflicting) linear effects (i.e. change of the stability of the mean boundary-layer due to the FFS modification) and nonlinear interaction between stationary and travelling modes. The exact identification of the relative significance of these two effects requires a combination of parameter variations in high-resolution experiments as well as accurate numerical simulations in the near-step region.

Considering the development of secondary instabilities, detailed experimental studies have shown that as the stationary vortices saturate, the strong mean flow distortion results in the development of streamwise and spanwise velocity shears [e.g. 71, 89]. These give rise to high-frequency inviscid instabilities of the Kelvin-Helmholtz type. In the present study, the primary CF instability arrives at the FFS location at a relatively high and constant amplitude of approximately 13% of the local freestream velocity (figure 4.14), signalling saturation levels. Consequently, a noticeable increase in the velocity fluctuations in the region corresponding to the type I mode (area B in figure 4.16) is registered. The Clean baseline case in figure 4.17(c) shows an increase in the velocity fluctuations (σw_R) in this region. Moreover, the addition of an FFS appears to affect the development of these fluctuations considerably. The results in figure 4.17(c) show an increase in velocity fluctuations (σw_R) with respect to the Clean configuration in the region associated with the type I secondary instability. This is consistent for all step cases

in the region directly downstream of the FFS location ($x/c_x \approx 0.21$). For the highest step height (D_3) this increase correlates well with the breakdown of the CF vortices presented in figure 4.16(IVd). For the moderate step height (C_3), the velocity fluctuations (σw_R) in the region associated with the type I mode increase even further for $x/c_x > 0.22$ with respect to the Clean configuration as shown in figure 4.16(Vc and VIc). This amplification of the secondary instability correlates well with the anticipation of the laminar–turbulent transition, presented in figure 4.3 for the respective cases.

In contrast, for the smaller FFS cases (A_3 and B_3) the velocity fluctuations (σw_R) associated with the type-I mode decrease downstream of the FFS location ($x/c_x > 0.22$) to a level lower than the corresponding level in the Clean baseline configuration, compare figure 4.16(VIa-VIb). Moreover, the reduction in σw_R presented in figure 4.17(c) correlates well with a decrease in the spanwise gradients in region B as shown in figure4.17(a). High-resolution and time-resolved measurements are required to identify the spectral content and further confirm the origin of the observed velocity fluctuations. In addition, such future dedicated studies will indicate the connection, if any, to the vortex-shedding mechanisms proposed by Eppink [130]. The unsteady behaviour reconciles sufficiently with the overall delay of transition presented in §4.3.1 for the small FFS (A_3) and provides a first-order insight into the possible transition delay mechanisms pivoting on the reduction of the spanwise gradients and the stabilisation of the type-I secondary instability.

4.5. CONCLUDING REMARKS

The attainment of extended regions of laminar flow in the boundary-layer of high subsonic commercial transport aircraft is highly susceptible to the mechanical smoothness of aerodynamic surfaces. Previous research in CF instability dominated flows revealed a significant influence on the laminar–turbulent transition behaviour by two-dimensional surface irregularities in the form of steps and gaps.

This work focuses exclusively on FFS. Most published studies on this type of surface irregularity have focused on formulating appropriate criteria to determine the critical step height, which do not result in premature transition. Nevertheless, a few recent studies have highlighted unresolved physical aspects governing the FFS-CFI interaction which necessitate detailed flow diagnostics before a universal model or criterion can be used for the design of practical laminar flow components and application of laminar flow control techniques.

In particular, Eppink [130] and the experiments presented in Chapter 3(Rius-Vidales and Kotsonis [181]) associated the impact of the FFS on the development and transition of the CF instability with the amplitude of the incoming CF vortices. Consequently, the present work extends the current investigation of the FFS-CFI interaction to cases where the CF vortices arrive with high amplification to the step location.

The main findings of this work indicate strong topological changes on swept wing flows due to FFS, manifesting in a pronounced outboard–inboard–outboard motion which can be potentially linked to the streamwise development of the CF instability. When comparing with the Clean baseline configuration, as the boundary-layer flow approaches the step there is a clear deceleration in the boundary-layer flow (i.e. adverse pressure gradient) and the stationary CF vortices experience an outboard spanwise motion. Reach-

ing the FFS, the boundary-layer flow is redirected by the FFS resulting in a strong vertical velocity ejection. This behaviour correlates well with the measured amplification of the stationary CF vortices upstream of the FFS location.

Downstream of the FFS edge, the stationary CF vortices experience an abrupt inboard spanwise motion, linked to the localised favourable pressure gradient, reaching their maximum amplification and strong mean flow distortion. Farther downstream, as the flow recovers to nominal pressure conditions, the CF vortices experience a gradual outboard spanwise motion (i.e. adverse pressure gradient) and a substantial amplitude reduction, even below the level pertaining to the Clean configuration. For the smaller step cases, a second region of growth of the CF vortices is observed, enhanced by the nominal favourable pressure distribution of the wing.

In agreement with previous studies by Eppink [130] and the experiments presented in Chapter 3 (Rius-Vidales and Kotsonis [181]), an amplification of higher spanwise harmonics of the stationary CF mode at the step location has been observed. The observed behaviour suggests the dominance of indirect harmonic growth due to nonlinear forcing of the primary mode at the step location. For the smaller FFS cases studied in this work, the step leads to a local stabilization effect after an initial destabilization of the primary stationary mode and its harmonics. For the higher step case, transition occurs shortly downstream of the step location.

The analysis of the unsteady disturbances revealed a reduction in spanwise velocity temporal fluctuations (σw_R) due to the step, in the region associated with type III travelling instabilities. The amplification experienced by the primary CF instability mode due to the step is sufficient to minimise the nonlinear interaction between the stationary and travelling CF vortices. On the other hand, for all the FFS cases, the spanwise velocity temporal fluctuations (σw_R) in the region associated with type I secondary instability, show a substantial increase past the step edge as the primary stationary CF instability mode and its higher harmonics reach their maximum amplification. This is strongly correlated with the modifications imparted on the spanwise gradients of time-averaged velocity, widely acknowledged as the driver for type I secondary instabilities. Downstream of this location, the behaviour strongly differs, depending on the considered step height. For the largest step height, an immediate breakdown of the CF vortices and onset of turbulent flow occurs, likely related to the explosive growth of type I fluctuations. For the moderate FFS case, the σw_R fluctuations slightly decrease before rapidly amplifying, reaching higher levels than the Clean baseline configuration by the end of the measurement domain.

In contrast, for the smallest FFS case, a substantial decrease in the spanwise velocity gradient and σw_R fluctuations in the region associated with type I secondary instability is achieved, reaching levels lower than the Clean baseline configuration by the end of the PIV measurement domain. This behaviour reflects an unprecedented transition delay effect due to a small FFS, holding potential for understanding and facilitating the future design of laminar flow components.

5

Influence on breakdown of crossflow vortices

This chapter presents a detailed analysis of the step-induced unsteady disturbances and ensuing laminar–turbulent transition. The results reveal that the presence of the FFS at the conditions under study leads to either a critical (i.e. moderate transition advancement) or a supercritical transition behaviour (i.e. transition advancing abruptly to the FFS location). Analysis of unsteady flow features for the critical cases indicates temporal velocity fluctuations following closely the development of the baseline configuration (i.e. agreeing with the development of secondary instabilities). Consequently, laminar flow breakdown originates from the outer side of the upwelling region of the CF vortices. In contrast, for the supercritical FFS, the laminar breakdown unexpectedly originates from the inner side of the upwelling region. Evidence points to the existence of an unsteady mechanism possibly supported by locally enhanced spanwise-modulated shears and the recirculation region downstream of the FFS edge. This mechanism appears to govern the abrupt tripping of the flow in supercritical step cases.

Parts of this chapter are published in:

- Rius-Vidales, A.F. & Kotsonis, M. 2022 Unsteady interaction of crossflow instability with a forward-facing step. Journal of Fluid Mechanics, **939**, A19.

5.1. BACKGROUND

As described in detail in §1.2.2, when the stationary CF vortices amplitude saturates a highly modulated boundary–layer results, which gives rise to strong wall-normal and spanwise velocity gradients from which secondary high-frequency instabilities originate. The overall consensus in experimental [e.g. 34, 71, 88–90] and numerical [e.g. 91–93, 95, 97] studies is that the secondary instabilities rapidly amplify leading to the breakdown of the CF vortices and the laminar–turbulent transition.

In cases with FFS, the recent experimental efforts by Eppink [130] and the ones presented in Chapter 4 (Rius-Vidales and Kotsonis [140]) identify a complex dynamic relation governing the interaction between nominally stationary CF vortices and two dimensional FFS. Moreover, the experiments by Eppink [130, 137] revealed the occurrence of high-frequency fluctuations which coincide with the location of the shear layer of the spanwise modulated recirculation region downstream of the step edge. Furthermore, a detailed stability analysis by Groot and Eppink [138] on these experiments revealed the convective nature of these unstable perturbations and identified their development on the top part of the local flow recirculation regions downstream of the supercritical FFS (i.e. tripping at the step position).

The review presented in §1.3, showed that the influence of the step on the amplification of the stationary structure has received significant attention. Nevertheless, the link between the primary stationary CF instability and eventual laminar breakdown is the development of secondary and unsteady instabilities, which in cases with FFS still remains largely unknown.

Henceforth, in agreement with the main research *objective C* (presented in §1.4), this chapter provides a detailed description of the unsteady interaction of the CF vortices with a FFS and the ensuing laminar–turbulent transition by conducting measurements on a swept wing wind tunnel model using IR Thermography and high-resolution time-resolved HWA anemometry.

5.2. EXPERIMENTAL SETUP AND DATA ANALYSIS

5.2.1. INFLOW CONDITIONS AND SURFACE IRREGULARITIES

The experiments are conducted at the Low-Turbulence Tunnel (LTT) of the TU Delft. The wind tunnel features an interchangeable octagonal test section housing the well characterised M3J swept wing model. A detailed description of the facility is provided in §2.1.1. Figure 5.1 presents a cross-sectional view of the wind tunnel test-section. The measurements are conducted at fixed $\alpha = 3°$ and $Re_{c_X} = 2.17 \times 10^6$. The Reynolds number ($Re_{cX}$) used throughout is based on the reference (see §2.1.1) wind tunnel velocity ($U_\infty = 24.8$ m s^{-1}) and the streamwise chord length of the model $c_X = 1.27$ m. Due to the proximity of the hot wire probe to the surface of the model, a protective film was installed on the surface.

The diagram of the experimental setup in figure 5.1(b) shows two distinct coordinate systems. On the first system (X, Y, Z), the streamwise X-coordinate is parallel to the wind tunnel floor and the velocity components are given by U, V and W, respectively. In contrast, on the second system (x, y, z), the streamwise x-coordinate is perpendicular to the leading edge of the swept wing. Note that both systems' origin corresponds

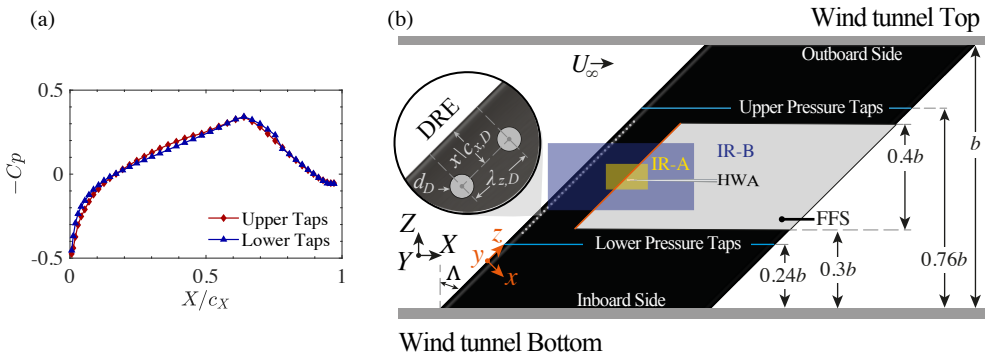

Figure 5.1: Experimental Setup. (a) Streamwise (i.e. along the X coordinate) pressure coefficient distribution at $\alpha = 3°$ and $Re_{c_X} = 2.17 \times 10^6$ on the pressure side of the model (max $U_{CP} = 0.003$). (b) General schematic (flow direction left to right, $b = 1.25$ m $c_X = 1.27$ m) showing the FFS (grey area), the HWA system, IR measurement domains (IR-A,IR-B) and discrete roughness elements (DREs).

5

to the intersection between the leading edge and the wing mid-span. Note that all the measurements are conducted on the "pressure side" of the model.

Figure 5.1(a) shows the static pressure measured by the taps using a multi-channel pressure scanner (described in §2.1.2). The pressure distributions at $Re_{c_X} = 2.17 \times 10^6$ and $\alpha = 3$ deg on the outboard (upper) and inboard (lower) side of the model indicate a predominantly favorable pressure gradient (i.e. pressure minima $X/c_X \approx 0.65$). Moreover, in agreement with Serpieri and Kotsonis [71] the validity of the infinite swept wing assumption used in the boundary–layer and stability calculations described in §2.3 is confirmed due to the nearly identical pressure distributions on the inboard and outboard side of the wing.

FFS surface irregularities were designed and manufactured as add-ons for the M3J wind tunnel model, as described in §2.1.3. This study only considers FFS surface irregularity with a sharp edge (i.e. no ramp or chamfer). During the experiments, the FFS height of each configuration was quantified in-situ by traversing a Micro-Epsilon 2950-25 laser profilometer (reference resolution of 2 µm) along a spanwise segment in the z-direction of 200 mm. Table 5.1 presents the FFS geometrical parameters such as the step height ($\bar{h}$), its standard deviation in the spanwise measurement segment (σ_h), and streamwise location (x_h/c_x). In addition, the displacement thickness (δ^*_h) and the estimated vortex core height (y_c, according to the definition by Tufts *et al.* [129]) for the forcing mode $\lambda_{z,D}$ are extracted at the step location from aforementioned boundary–layer and stability calculations.

Following the experiments presented in Chapter 3 and 4 (Rius-Vidales and Kotsonis [140, 181]) a late-growth (i.e. wrt to the most amplified mode at the step location) is forced to study its interaction with the FFS surface irregularity. This forcing condition is compatible with the one used by Eppink [130] albeit at a significantly higher initial amplitude. At the nominal conditions of this study, the aforementioned linear stability analysis indicates that a stationary CF instability mode with a spanwise wavelength (λ_z) close to 8 mm is highly unstable at and downstream of the step location.

ID	$\bar{h}$ [µm]	σ_h [µm]	x_h/c_x	δ_h^*[µm]	y_c[µm]
Clean	-	-	-	495	1115
A	346	4	0.25	-	-
B	445	3	0.25	-	-
C	708	5	0.25	-	-

Table 5.1: Geometrical parameters of tested configurations. For all cases nominal DREs settings are: $\lambda_{z,D}$ = 8 mm, d_D = 2 mm, k_D = 200 µm, x_D/c_x = 0.02.

Henceforth, for all the configurations presented in Table.5.1, stationary CF modes are conditioned using discrete roughness elements (DREs) spaced at $\lambda_{z,D}$ = 8 mm. DREs are commonly used to narrow the band of stationary CF modes which destabilize the boundary–layer flow in experimental studies [e.g. 36, 71, 86, 89].

It must be noted here that the use of DREs inherently implies the existence of intentional three-dimensional surface irregularities near the leading edge of the model. However, the term "surface irregularity" in this work is strictly reserved for the FFS, as DREs are used only as a conditioning mechanism and are invariantly present in all cases.

In all the cases, the DREs are installed upstream of the neutral point of the forced mode. The amplitude of the DREs was chosen based on the instability regime of interest. More specifically, the experiments in this chapter describe the unsteady interaction of CF vortices and the step geometry. For a stationary CF instability dominated flow without surface irregularities, it is well established that unsteady fluctuations form as secondary instabilities after saturation of the primary stationary CF vortices [e.g. 89]. As such, in the present study, the DREs nominal height was set relatively high (k_D = 200 µm) in order to anticipate the growth and saturation of the primary CF disturbance. This further facilitates the development of the secondary CF instability in both the clean and step cases while allowing for a common HWA traversing range among all tested cases.

5.2.2. INFRARED THERMOGRAPHY

IR Thermography measurements are conducted on the pressure side of the model using two Optris PI640 IR cameras (640px × 480px, un-cooled focal plane array, 7.5-13 µm spectral range, NETID 75 mK). The diagram on figure 5.1(b) shows the cameras' measurement region (IR-A, yellow and IR-B, blue). The first camera IR-A is equipped with a telephoto lens (f = 41.5 mm) to capture the near step region (226 × 175 mm centred at X/c_X = 0.27 and Z/b = 0.02). The second camera IR-B is equipped with a wide-angle lens (f = 10.5 mm) to capture a larger extent of the model surface (760 × 300 mm centred at X/c_X = 0.23 and Z/b = 0.04). During the measurements the model was continuously irradiated by seven halogen lamps to increase the thermal contrast on the IR images, as described in detail on §2.2.1.

The extraction of the transition location from the thermal maps of camera IR-B is performed following the method described in §2.2.1. For each configuration tested (see Table 5.1) a physical space transformation and distortion correction was applied to a time-averaged thermal map calculated from 50 IR images acquired at a sampling rate of 3.5 Hz. Subsequently, a differential infrared thermography technique (DIT) [154] is applied

following the procedure established by Rius-Vidales and Kotsonis [181] and described in §2.2.1, which considers successive measurements at increasing Reynolds numbers.

In addition to the global transition location, the thermal maps of camera IR-A provide a qualitative representation of the CF vortices' thermal footprint, from which the spatial organisation of coherent structures in the boundary–layer as they interact with the FFS can be extracted. To this end, a spatial spectral analysis (described in §2.2.1) is performed on thermal intensity profiles extracted along the spanwise z-direction. Based on the selected camera configuration (i.e. camera location and lens) the smallest wavelength resolved according to the Nyquist limit is 0.84 mm.

5.2.3. HOT-WIRE ANEMOMETRY

The experiments presented in Chapter 4 (Rius-Vidales and Kotsonis [140]) as well as by Eppink [130] utilised several variations of Particle Image Velocimetry (PIV) for a detailed reconstruction and analysis of pertinent CF instability features in the vicinity of surface irregularities. A common outcome in these studies is the importance of the unsteady fluctuations in the incoming boundary–layer and their relation to the surface irregularity's effect on transition. Despite a wealth of spatially-correlated information extracted from optical velocimetry techniques, accurate measurement of amplitude and spectra of minute velocity fluctuations, especially in the vicinity of walls, is at best challenging. Hence, the PIV applicability towards evaluation of unsteady boundary–layer instabilities and their interaction with the FFS is limited by the sampling rate and the random and bias errors stemming from wall reflections, camera noise and laser light illumination. To this goal, the present work uses HWA as a well-established, accurate and time-resolved technique, albeit providing single-point measurements.

The boundary–layer flow measurements are conducted using a Hot-Wire Anemometer (HWA) probe (single wire BL probe, Dantec Dynamics 55P15) operated by a TSI IFA-300 constant temperature bridge. A custom analogue–digital (24bit) acquisition system registers and converts the HWA voltage signal to the corresponding flow velocity based on in-situ calibration and correction for variations in atmospheric pressure and flow temperature [e.g. 159]. Details of the operation and measurement technique are presented in §2.2.2. For the entirety of measurements, the wire of the HWA probe is mounted vertically (i.e. aligned to the Z axis) and orthogonal to the X-coordinate direction as described in §2.2.2 and presented in the diagram in figure 2.9(b).

Wall-normal boundary–layer scans were conducted along the z-direction to form y_t-z measurement planes at different streamwise locations ($0.20 \leq x/c_x \leq 0.28$) to characterise the streamwise development of the CF instability. It must be mentioned here that due to the curvature of the M3J wing, successive planes are not parallel to each other, rather normal (y_t) to the local tangent at the wall. Nonetheless, due to the large chord (c_X=1.27m) and limited measurement domain (< 10% chord), the difference in wall-tangent angle is only 1.2 deg between the most upstream and most downstream measurement planes. Each plane consists of 60 boundary–layer profiles equispaced in the z direction. Each profile is constructed with 40 measurement points along the wall-normal direction y_t. At each measurement point, the hot-wire signal was acquired at a sampling rate of f_s = 51.2 kHz for a total measurement time of two seconds. The final resolution along the z-coordinate is fixed at Δz = 533 µm while the resolution along the

wall-normal direction differs per streamwise location (60µm ≤ Δy_t ≤ 90µm) to account for the growth in the boundary–layer. For each X/c_X station, the measurement plane's starting position along the span (z^*) has been adjusted to track the evolution of three full CF vortices. The starting position for each measurement plane is identified as the wall-normal distance for which the registered velocity reaches around 20% of the local freestream velocity. In addition, a Taylor-Hobson microalignment telescope was used to monitor the position of the wire near the wall. Finally, during post-processing the location of the wall is determined by performing a linear regression on the velocity profiles.

5.2.4. AMPLITUDE GROWTH METRICS

The impact of the FFS on the stability characteristics of the CF vortices is assessed by calculating the steady and unsteady disturbance profiles from the HWA measurements acquired as indicated in §5.2.3. Following White and Saric [89] and Downs and White [73] the experimental steady disturbance profile is calculated for each HWA y_t–z measurement plane as the spanwise root-mean-square of the time-averaged perturbation as given by equation 5.1. In this work the maximum ($A_M = \max|_y(\langle\hat{q}(y_t)\rangle_z)$) of these profiles along the y_t-coordinate is non-dimensionalized with the local external velocity ($\bar{Q}_e$) and used to monitor streamwise changes in the stationary CF vortices;

$$\langle\hat{q}(y_t)\rangle_z = \sqrt{\frac{1}{n}\sum_{j=1}^{n}(\bar{Q}(y_t,z_j)-\bar{Q}_z(y_t))^2} \tag{5.1}$$

In the typical decomposition used in linear stability analysis, the velocity perturbation (u') can be calculated by subtracting a basic state or baseflow from the measured velocity component. In the present experiment, $\hat{q} \neq q'$, since $\bar{Q}_z(y_t)$ (used in equation 5.1) corresponds to the spanwise time-average distorted flow and not to a baseflow. Nonetheless, for the experimental study of CF instability, this metric has been commonly used [e.g. 71, 73, 89].

For the study of the secondary instability, the methodology follows the one employed by Serpieri and Kotsonis [71], Downs and White [73], and White and Saric [89]. For each y_t-z measurement plane, a wall-normal profile is calculated by numerically integrating the temporal standard deviation (σ_Q) along the z-coordinate (i.e. spanwise direction) for every y_t position. Then, the resulting profiles are integrated along the y-coordinate to obtain the amplitude a as indicated in equation 5.2. This metric is used to monitor the streamwise development of unsteady disturbances;

$$a = \frac{1}{\bar{Q}_e}\frac{1}{y_t^m}\frac{1}{z^m}\int_0^{y_t^m}\int_0^{z^m}\sigma_Q(y_t,z)\,dz\,dy_t \tag{5.2}$$

5.3. LAMINAR–TURBULENT TRANSITION BEHAVIOUR

Prior to the analysis of velocity measurements in the vicinity of the FFS, this section presents the overall behaviour of the laminar–turbulent boundary–layer transition identified using IR thermography. Based on the thermal maps obtained from the IR measurements, a detailed characterization of the FFS-induced changes on the transition behaviour and spatial organization of the CF vortices is presented.

5.3.1. INFLUENCE ON THE TRANSITION LOCATION

The laminar–turbulent transition location is determined by monitoring changes in the model surface temperature using an IR thermographic system. For each configuration presented in table 5.1 thermal measurements are conducted on the pressure side of the model following the methodology described in §5.2.2.

Figure 5.2 shows the thermal surface maps captured by the camera IR-B. For the Clean (i.e. no FFS) forced case, the boundary–layer flow remains in a laminar state (i.e. brighter region in figure 5.2Ia) for up to a third of the wing chord. Based on the methodology described in §2.2.1 a linear fit along the span (dashed white lines in figure 5.2Ia-IIb) is calculated and the transition location extracted at the centre of the measurement domain (indicated by • markers). Figure 5.2(III) presents the resulting laminar–turbulent transition location for all tested configurations.

For the Clean forced case the average laminar–turbulent transition location is found at $x_t/c_x \approx 0.32$. In these conditions, the dominance of the stationary CF instability modes over the travelling modes is evident as the transition front pattern is not smooth (i.e. spanwise invariant transition line) but displays a series of contiguous wedges along the span. This pattern is characteristic of the breakdown process of the stationary CF vortices [see 34, 35, 71–73]. The wedged appearance of the transition front pattern is related to the thermal footprint caused by the local breakdown of contiguous stationary CF vortices. Note that the transition front along the span is slightly skewed with respect to the leading edge of the swept wing model. This behaviour is attributed to the non-uniform wind tunnel blockage that the model experiences along the test section's vertical dimension.

Following the observations presented in the experiments in Chapter 3 (Rius-Vidales and Kotsonis [181]) the addition of an FFS leads to different transition behaviours classified into three different regimes. A subcritical regime occurs when the addition of the step results in a negligible effect on the laminar–turbulent transition process as there is nearly no change in the location of the transition front. A critical regime occurs when the addition of an FFS causes an evident and quantifiable upstream movement of the transition front. Finally, a supercritical regime occurs when the addition of an FFS results in an abrupt upstream shift of the transition front near the step location. In the latter case, the flow is said to be tripped.

In this work, the addition of the two moderate FFS (case A and case B in table 5.1) leads to a critical regime transition behaviour, since a quantifiable upstream shift of the transition front occurs as shown in figure 5.2. Consequently, a further increase of the FFS height (case C in table 5.1) leads to a supercritical regime behaviour as the transition front occurs near the FFS, essential tripping the boundary–layer flow at its location.

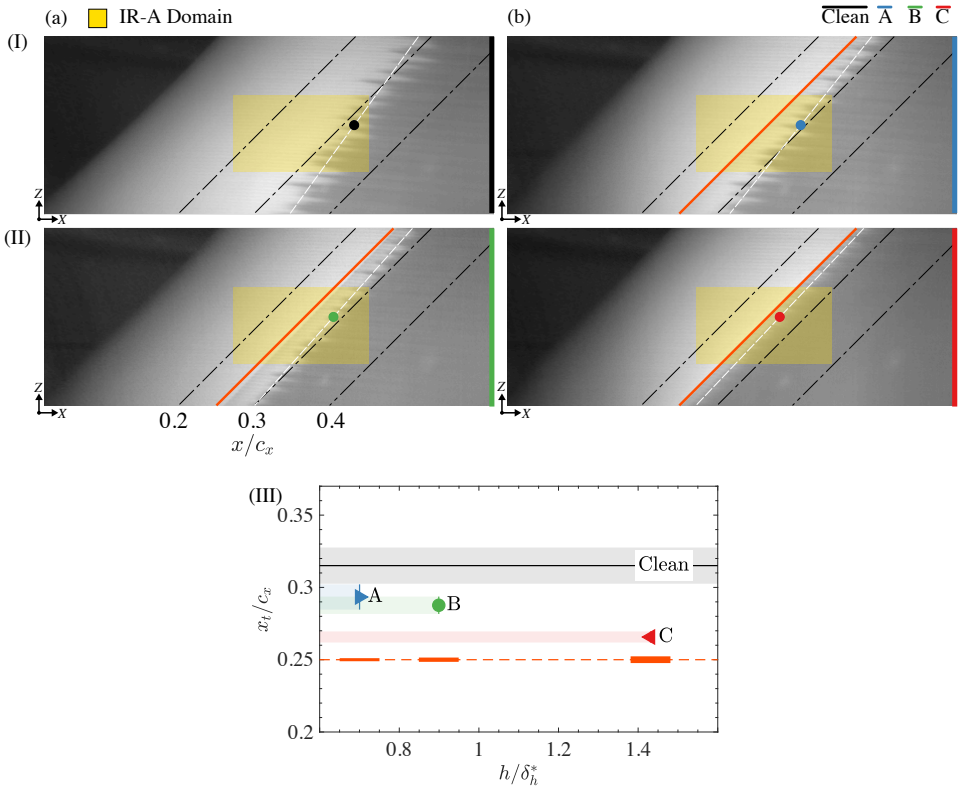

Figure 5.2: Thermal maps from camera IR-B (I and II, flow from left to right) and transition location (III) at $Re_{c_X} = 2.17 \times 10^6$ and $\alpha = 3°$ for three different FFS (A,B and C) at fixed streamwise location (orange line denotes step location, $x_h/c_X = 0.25$). Markers (•) in I and II indicate the projection of the transition linear fit (dashed white line) to centre of the domain: (Ia) Clean; (Ib) A; (IIa) B; and (IIb) C.

5.3.2. INFLUENCE ON THE CROSSFLOW VORTICES SPATIAL ARRANGEMENT

The measurements acquired using camera IR-A (figure 5.1b) provide detailed surface temperature distributions near the FFS location as shown in figure 5.3. A careful inspection of the surface temperature distribution for the Clean case (figure 5.3Ia) reveals the thermal footprint of the CF vortices as a series of streaks nearly parallel to the streamwise X-direction alternating between high- and low-temperature values (i.e. lighter and darker).

A spatial spectral analysis is performed on a series of thermal intensity profiles extracted from the IR thermal maps along the span (i.e. along the z-direction) of the wing model to monitor changes in the spatial organization of the CF vortices. The results for the Clean configuration in figure 5.3(IIIa) verify that the use of DREs effectively narrows down the band of stationary CF instability modes active in the current boundary–layer flow since the spanwise spacing of the CF vortices matches the one forced upstream by the DREs (i.e. $\lambda_z/\lambda_{z,D} = 1$). Furthermore, figure 5.3(IIIa-IVb) indicates the persistence of the introduced wavelength even with the addition of an FFS as the forced mode domi-

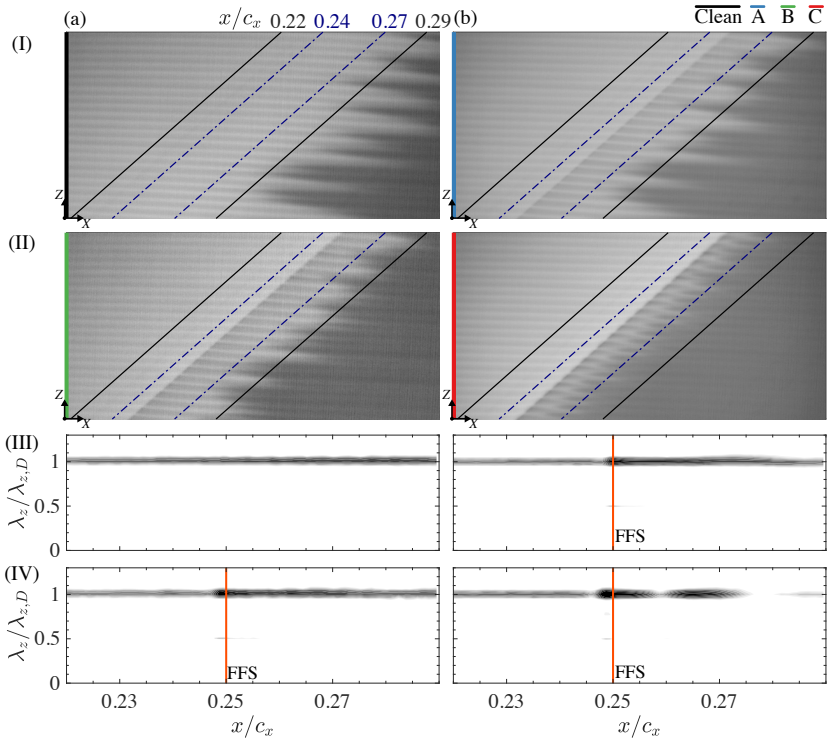

Figure 5.3: Thermal maps from camera IR-A (top, flow from left to right) and spectral analysis (bottom, 10 levels of $\ln(P/\tilde{P}_{\max_z})$ from -3 to 1): (Ia,IIIb) Clean; (Ib-IIIb) A; (IIa,IVa) B; and (IIb,IVb) C. ($\lambda_{z,D} = 8$ mm)

nates upstream and downstream of the step location ($x_h/c_x = 0.25$).

The results presented in Chapter 3 and 4 (Rius-Vidales and Kotsonis [140, 181]) and the experiments by Eppink [130] have shown a pronounced amplification of the primary CF instability mode higher harmonics at the step location. This behaviour is also observed in the experiments presented in this Chapter. For all the FFS cases (figure 5.3IIIa-IVb) there is a clear second peak at the step location ($x_h/c_x = 0.25$) matching the wavelength of the forced mode first higher harmonic (i.e. $\lambda_z/\lambda_{z,D} = 0.5$).

Detailed inspection of the thermal footprint for the highest FFS case (figure 5.3IIa) confirms the "fork-like" pattern previously observed in the experiments presented in Chapter 3 and 4 (Rius-Vidales and Kotsonis [140, 181]) associated with the supercritical regime. To further elucidate the origin of this pattern, three-dimensional flow measurements near the FFS are required. Nevertheless, one has to note the striking similarity of the identified pattern with the vortical structures presented by Eppink [130, figure 20] downstream of the step edge. In the following section, the CF vortices' streamwise development will be studied in more detail based on the HWA measurements.

5.4. INTERACTION OF STATIONARY DISTURBANCES WITH AN FFS

The influence of the FFS on the transition location presented in §5.3, indicates that for the conditions of this study (i.e. initial amplitude, step heights and freestream turbulence) the addition of an FFS leads to a reduction in the extent of the laminar flow. In this section, the HWA measurements are exploited to characterize the stationary flow interaction with the surface irregularity. This analysis covers both the stationary mean flow as well as the stationary CF instability modes.

5.4.1. INFLUENCE ON THE TIME-AVERAGED FLOW

The stationary CF instability development is characterized through detailed measurements of the boundary–layer flow using an automated HWA traversing system. As described in §5.2.2 velocity measurements are conducted in y_t-z planes (i.e parallel to the leading edge and normal to the local model surface) at different streamwise stations in the range $0.20 \leq x/c_x \leq 0.28$. In contrast to the experiments presented in Chapter 4 (Rius-Vidales and Kotsonis [140]) in which PIV was employed, the HWA signal analysed here corresponds to the Euclidean sum, $Q = \sqrt{(u\cos\Lambda + w\sin\Lambda)^2 + v^2}$, based on the HWA probe velocity decomposition presented in §2.2.2.

Figure 5.4 presents a series of boundary–layer profiles ($\bar{Q}_z$) calculated as the spanwise average (i.e. along the z-coordinate) of the entire measurement plane. For clarity, the wall normal y_t-coordinate has been offset by the step height at its location and non-dimensionalized using the displacement thickness at the most upstream station for the Clean configuration ($\delta^*_Q = 620$ µm at $x/c_x = 0.22$). Upstream of the FFS location at $x/c_x = 0.24$ (figure 5.4I) the distortion imparted by the CF vortices on the boundary–layer flow is evident for all cases when comparing them with the numerical BL solution (dashed black line) calculated from the pressure measurements. In addition, at this position a slight deceleration which intensifies with increasing step height is evident on the boundary–layer flow (figure 5.4II).

Downstream of the FFS ($x/c_x \geq 0.256$, figure 5.4I) the interaction with the step leads to a more pronounced mean flow distortion as the profiles do not fully recover to the shape indicated by the Clean configuration within the measurement domain. The upstream deceleration is in agreement with previous numerical and experimental studies which indicate that the addition of an FFS leads to abrupt changes in the nominal pressure distribution in the vicinity of the step [see 127, 129, 139]. Consequently, near the FFS location the boundary–layer first experiences an adverse pressure gradient region. As the flow overcomes the apex of the FFS, it becomes influenced by a very strong favourable pressure gradient region, leading to an acceleration of the flow near the wall (at $x/c_x = 0.256$, figure 5.4I-II). Finally, a second adverse pressure gradient region is formed as the flow and external pressure recovers to the nominal value (i.e. without FFS). This pressure modification plays an important role in determining the trajectory of the CF vortices. In particular, experiments by Eppink [136] and the ones presented in Chapter 4 (Rius-Vidales and Kotsonis [140]) observed that the CF vortices experience a strong spanwise motion as they encounter the FFS. This motion requires further study as it appears to be an important aspect governing the interaction dynamics.

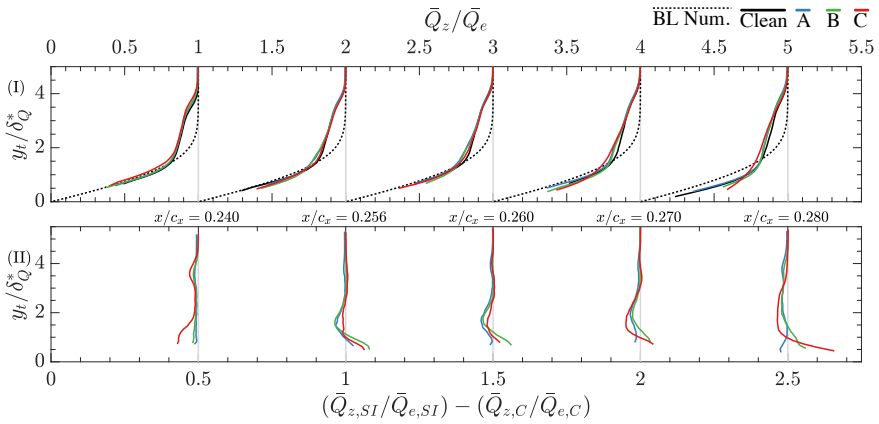

Figure 5.4: Selected boundary–layer profiles (I) of spanwise averaged mean flow velocity $\bar{Q}_z$ and difference (II) between these velocity profiles for the FFS cases ($\bar{Q}_{z,SI}$) and the Clean configuration ($\bar{Q}_{z,C}$) upstream and downstream of the step location. Note that for visualization purposes the profiles magnitude is shifted by 1 in (I) and 0.5 in (II)

5

5.4.2. INFLUENCE ON THE STEADY DISTURBANCE

Figure 5.5 presents the measured time-averaged velocity contours ($\bar{Q}$) at selected locations upstream and downstream of the FFS location. For the Clean configuration (figure 5.5Ia-Va) the velocity distribution corresponding to three stationary CF vortices is evident. The CF vortices manifest as high- and low-velocity regions evenly spaced at the spanwise wavelength forced by the DREs ($\lambda_{z,D} = 8$ mm). This correlates well with the thermal footprint and corresponding spectral analysis presented in figure 5.3(Ia and IIIa).

The primary action of the co-rotating stationary CF vortices is to transport high-momentum fluid towards the wall (downwelling region, $\oplus$ in figure 5.5Va) and low momentum flow away from it (upwelling region, $\ominus$ in figure 5.5Va). As the three-dimensional boundary–layer flow develops, the increase on the amplitude of the stationary CF vortices leads to a more pronounced mean flow distortion [73, 89, 94]. This is particularly evident towards the downstream end of the measurement domain (figure 5.5Va)

Upon the addition of the highest FFS (case C) (figure 5.5Id-Vd) there is a nearly immediate ($x_t/c_x \approx 0.27$) breakdown of the CF vortices leading to an anticipation of the laminar–turbulent boundary–layer transition as indicated in figure 5.2(III). The laminar breakdown strongly impacts the coherency and shape of the modulated boundary–layer due to the increase in diffusion associated with the turbulent motion. Nevertheless, the streamwise persistence of this modulation is remarkable, as the DRE-conditioned wavelength is still visible well into the turbulent flow region (figure 5.3IIb). Furthermore, particular to this FFS case, a distinct region of low-momentum fluid located on the inner side of the upwelling region (A in figure 5.5IId) is evident downstream of the step location.

In contrast, the addition of the smaller FFS cases (A and B in figure 5.5Ib-Vc) do not cause an immediate breakdown of the CF vortices as the laminar–turbulent boundary–

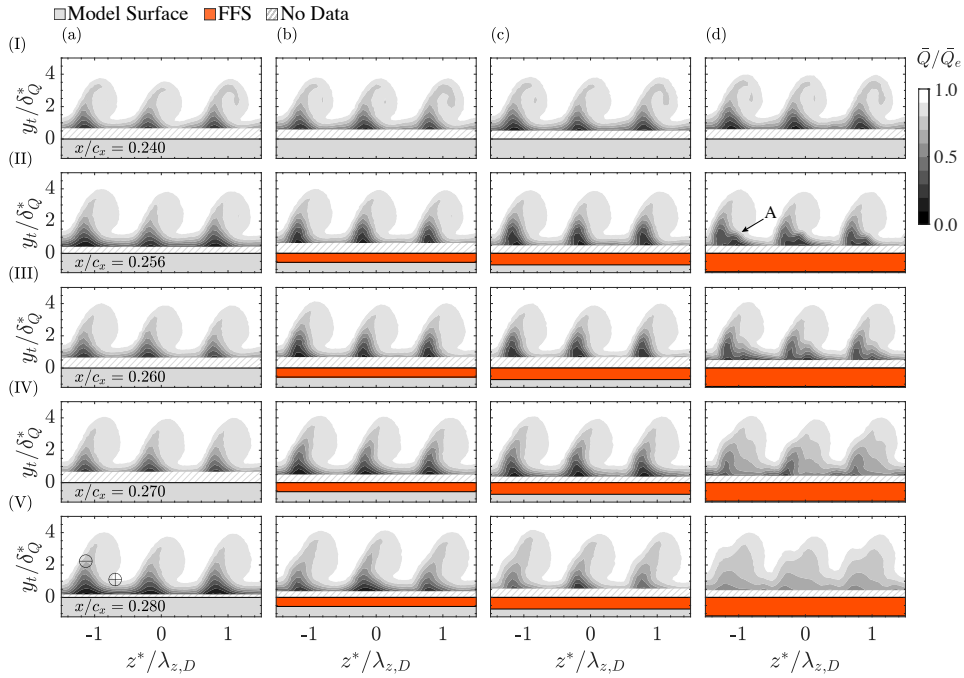

Figure 5.5: Contours of time-averaged velocity (z positive direction outboard): (a) Clean; (b) A; (c) B; (d) C. ($\delta_Q^* = 620\mu$m and $\lambda_{z,D} = 8$ mm)

layer transition occurs at $x_t/c_x \geq 0.28$ (figure 5.2III). Nonetheless, the interaction of the incoming flow with the FFS leads to an increase in the spanwise gradients on the outer side of the upwelling region, where the distance between the isovelocity contours lines reduces. Detailed studies on the development of the stationary CF instability have highlighted the importance of the spanwise gradients in this region on the onset of rapidly amplifying secondary instabilities which eventually lead to the laminar–turbulent transition [e.g. 71, 89, 94]. The effect of these topological changes in the mean velocity gradients and fluctuations will be revisited in more detail in §5.5.

Based on the time-averaged velocity fields ($\bar{Q}$) the steady disturbance profile ($\langle \hat{q} \rangle_z$) is calculated for each measurement plane following the methodology described in §5.2.4. The resulting profiles are presented in figure 5.6 for selected positions upstream and downstream of the step location. Upstream of the FFS at $x/c_x = 0.240$ (figure 5.6Ia) the steady disturbance profiles show two distinguishable local maxima, hereafter referred to as "lobes". The lower lobe (referred to as L) is located closer to the wall at $y_t/\delta_Q^* \approx 1$ and corresponds to the maxima of these profiles. The second lobe (U) is located farther away from the wall at $y_t/\delta_Q^* \approx 3$. Previous studies on smooth surface CF transition (i.e. without surface irregularities) have identified the appearance of the upper lobe as an indication of the nonlinear stages of the CF instability development[e.g. 89, 176]. The present form of perturbation profiles reconciles well with the expectation of nonlinear development

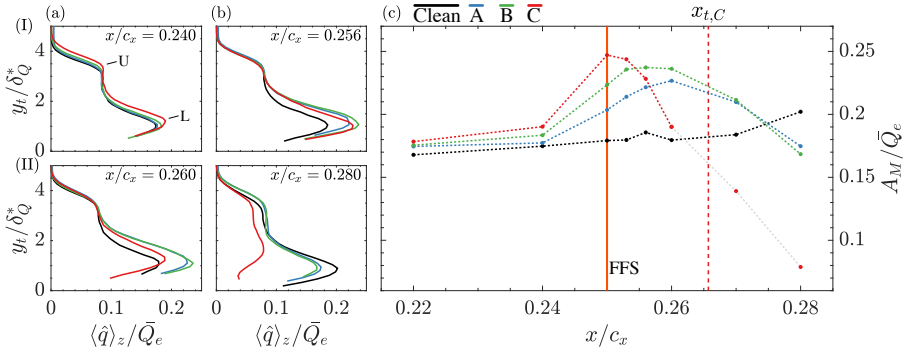

Figure 5.6: Selected steady disturbance $\langle\hat{q}\rangle_z$ profiles upstream and downstream of the FFS location (δ_Q^* = 620 µm). (a,b) Steady disturbance profiles and (c) streamwise evolution of the non-dimensional maximum amplitude (A_M) ($x_{t,C}$ transition location for case C).

5

of the stationary CF instability modes, given the relatively high amplitude used for the upstream forcing by the DREs. Figure 5.6(c) presents the streamwise variation of the maximum amplitude (A_M) obtained from these steady disturbance profiles. In all cases, the maximum amplitude coincides with the L lobe.

In agreement with the results presented in Chapter 4 (Rius-Vidales and Kotsonis [140]) just upstream of the FFS location at $x/c_x = 0.24$ (figure 5.6c), a slight amplification of A_M for all cases is registered, reflecting the changes imparted by the step on the stability of the incoming boundary–layer. Downstream of the step at $x/c_x = 0.256$ (figure 5.6c) there is a sudden increase in the amplitude of the lower lobe, which intensifies with increasing step height. Considering the highest FFS (case C), the maximum amplitude of the disturbance profile reaches a value of around 25% of the local freestream velocity $\bar{Q}_e$ at the step location ($x/c_x = 0.25$). Beyond this streamwise position the amplitude sharply decays due to the aforementioned loss of spanwise coherence prior to the laminar flow breakdown, shown in figures 5.5(IId-IIId). Note that in figure 5.6(c) all the measurements downstream of the identified transition location (figure 5.2III) are connected using a grey dashed line.

For the smaller FFS (cases A and B), the maximum amplitude occurs downstream of the FFS location at $x/c_x \approx 0.256$ and 0.26, respectively. For these cases, there is only a single region of amplification prior to the detected laminar–turbulent transition at $x_t/c_x \approx 0.29$. Henceforth, this behaviour qualitatively agrees with the case C_3 presented in Chapter 4 (Rius-Vidales and Kotsonis [140]) corresponding to a higher FFS ($C_3, h/\delta^* = 1.30$ and $y_c/h = 1.77$) but lower initial amplitude of the CF vortices. In those conditions, the addition of the FFS resulted in anticipation of the laminar–turbulent boundary–layer transition due to an increase in the velocity fluctuations on the upwelling region's outer side. The similar transition and amplification behaviour in this study highlight the importance of the amplitude of the stationary CF vortices when reaching the FFS in determining the criticality of the step.

5.5. INTERACTION OF UNSTEADY DISTURBANCES WITH AN FFS

As the primary stationary CF vortices develop in the boundary–layer, non-linear interactions result in amplitude saturation [34, 35]. This regime typically signals the onset of secondary instabilities due to the strong shears imparted on the flow by the primary CF instability. Previous numerical and experimental studies on stationary CF instability cases without surface irregularities have connected the rapid amplification of these high-frequency secondary instabilities with the vortices breakdown and eventual laminar–turbulent transition of the boundary–layer [e.g. 71, 88, 89, 91, 92, 94, 95]. Despite the wealth of information in smooth surface cases, the interrelation of a surface irregularity such as the present FFS with the development of unsteady disturbances remains largely unknown.

5.5.1. STREAMWISE DEVELOPMENT OF UNSTEADY DISTURBANCES

Previous work on boundary–layers dominated by stationary CF instability without surface irregularities has classified the pertinent unsteady disturbances into three main modes. Figure 5.7 presents the time-averaged velocity gradients for the Clean and FFS cases to assist in their identification within the CF vortex spatial organization. The type I mode [94, 98, 99] or z-mode [93] is commonly located close to the local minimum of the spanwise mean flow gradient on the outer side of the upwelling region (B in figure 5.7IIIa). The type II mode[94, 98, 99] or y-mode [93] is commonly located away from the surface (A in figure 5.7Ia) where the wall-normal gradients reach a local maximum. Finally, the type III mode [94, 95] is commonly located close to the local maxima of the spanwise gradient on the inner side of the upwelling region (C in figure 5.7IIIa). Note that in a stationary CF instability case without surface irregularities, the temporal velocity fluctuations at type I and type II mode locations are attributed to a secondary instability of Kelvin-Helmholtz type [95]. In contrast, the velocity fluctuations corresponding to the type III mode have been traced to the nonlinear interaction between primary travelling and stationary CF instability modes.

For the Clean configuration, laminar–turbulent transition occurs at $x_t/c_x \approx 0.32$ as shown in figure 5.2(III). This behaviour correlates well with the amplitude of the primary CF instability presented in figure 5.6(c), which monotonically increases in the region $x/c_x \geq 0.26$ reaching a level of $A_M/\bar{Q}_e \approx 0.2$ by the end of the measurement domain. This amplitude value closely matches with previous experiments by Serpieri and Kotsonis [71] and is in agreement with typical saturation levels reported for models with 45° sweep in different wind tunnels with similar turbulence intensity levels [e.g. 73, figure 19].

Figure 5.7(IIIa-Vd) shows the time-averaged velocity spanwise gradient (i.e. $\partial\bar{Q}/\partial z^*$) contours at selected positions downstream of the step location. Of particular interest to the development of the secondary instability corresponding to the type I mode is the increase in the negative spanwise gradient (i.e. outer side of the upwelling region, area B in figure 5.7IIIa) as the CF vortices amplify. Figure 5.7(VI) shows the streamwise evolution of the negative spanwise gradients averaged within the dashed-line regions indicated in figure 5.7(IIIa-Vd). The results for the Clean configuration show a slight gradual amplification of the spanwise gradients on the outer side of the upwelling region resulting from the growth of the primary instability and its nonlinear distortion on the mean flow.

In contrast, in all the FFS cases a strong amplification of $\partial\bar{Q}/\partial z^*$ on the outer side of

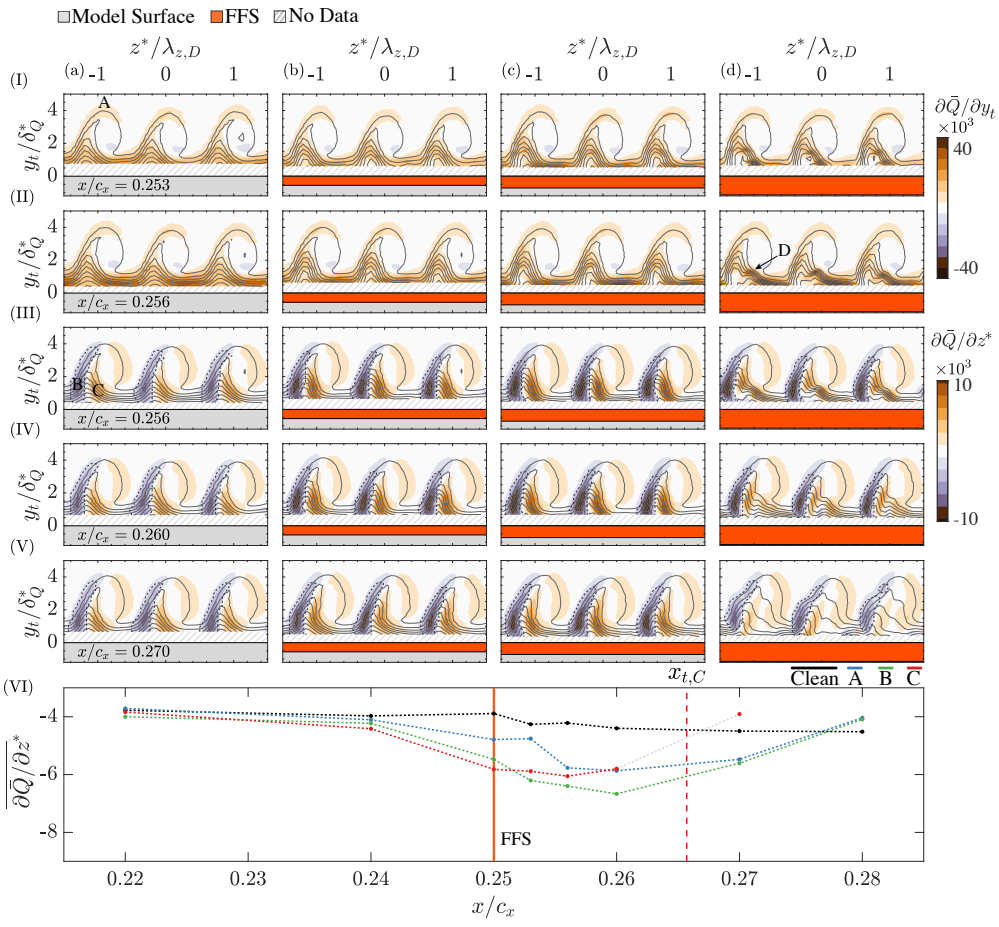

Figure 5.7: Contours of time-average wall-normal (I,II) and spanwise (III-V) velocity gradients and time-average velocity (grey solid lines 10 levels $\bar{Q}/\bar{Q}_e$ from 0 to 1 same contours as in figure 5.5) : (a) Clean; (b) A; (c)B; (d)C; and (VI) streamwise evolution of the average spanwise gradient calculated inside the dashed line regions ($x_{t,C}$ transition location for case C, $\delta_Q^* = 620$ µm and $\lambda_{z,D} = 8$ mm)

the upwelling region occurs near the step location ($x/c_x = 0.25$ in figure 5.7VI). This amplification continues until a position close to where the steady perturbation (figure 5.6c) reaches its maximum value. From this point onwards a strong $\partial\bar{Q}/\partial z^*$ decay occurs due to the loss of coherence by the breakdown of the CF vortices.

On the inner-side of the upwelling region the organization of the spanwise ($\partial\bar{Q}/\partial z^*$) and wall-normal ($\partial\bar{Q}/\partial y_t$) gradients differ considerably between the critical (A and B) and the supercritical (C) FFS cases. In the latter, two positive spanwise gradients maxima manifest near the wall downstream of the FFS at $x/c_x = 0.256$ (figure 5.7IIId). In addition, an increase in the wall-normal gradient is clearly observed (region D figure 5.7IId, local external velocity $\bar{Q}_e = 24.6\ \mathrm{m\,s^{-1}}$) away from the wall.

Eppink [137] also identified a strong positive increase in the wall-normal gradients ($\partial U/\partial y$) at a similar location and attributed it to the shear layer, which develops on the top part of the flow recirculation region downstream of the FFS edge. The results from Eppink [130, 137] showed that the recirculation downstream of the FFS is not continuous along the span but instead is highly modulated at the wavelength of the primary CF instability. Thus, isolated regions of flow reversal form and develop into a complex system of streamwise vortices. Moreover, [130, 137] reports that the formation of this flat and extended (typical height less than 300 µm and length between 7-15 mm) recirculation region downstream of the FFS edge is not only dependent on the step height but also appears to be strongly influenced by the amplitude of the primary CF disturbance.

In this work, it is not possible to conclusively identify the recirculation regions proposed by Eppink [130, 137] since a single wire HWA probe cannot differentiate between velocity components and their direction. Nevertheless, the qualitative agreement of the wall-normal gradients in figure 5.7(Id, IId) with Eppink [137, figure 7] suggests that a similar near-step flow topology occurs for the highest FFS (case C), even though the spatial organization and amplitude of the CF vortices presented in Eppink [137] is distinct from the one in this work.

The spatial organisation of the total temporal velocity fluctuations (σ_Q) and the streamwise change in unsteady disturbance amplitude (a/a_0 with a_0 at $x/c_x = 0.22$) are presented in figure 5.8. For the Clean configuration the slight increase in the unsteady disturbance amplitude (a) for $x/c_x > 0.25$ (figure 5.8VI) is primarily due to fluctuations on the outer side of the upwelling region (figures 5.8IIIa-Va). This behaviour is in agreement with the development of the type I secondary instability acknowledged as the driver in the breakdown of the CF vortices at similar conditions [e.g. 90].

In the moderate FFS cases A and B (figure 5.8VI) a considerable increase in amplitude occurs for $x/c_x \geq 0.26$. This location is slightly downstream from where the primary stationary CF disturbance reach its maximum amplification as shown in figure 5.6(c). Similar to the Clean baseline configuration, the contours of σ_Q in figure 5.8(IVb-Vb) and figure 5.8(IVc-Vc) reveal that the increase in the temporal velocity fluctuations occurs predominantly on the outer side of the upwelling region.

Figure 5.8(VI) indicates that an increase in the FFS height (case C) leads to a strong amplification of the temporal velocity fluctuations downstream of the step. In this case, the interaction of the CF vortices with the FFS leads to a considerable degradation in the extent of laminar flow (i.e. supercritical regime) as the laminar–turbulent transition occurs in the vicinity of the step as shown in figure 5.2(IIb,III). In contrast to the Clean and the smaller FFS cases (A and B), in the higher case C an increase in temporal velocity fluctuations occurs both on the outer and inner side of the upwelling region (figure 5.8IId-IVd). Note that the location of the velocity fluctuations on the inner side in figure 5.8(IId) overlaps with the increase in wall-normal gradients (region D in figure 5.7IId) which Eppink [137] found to be related to the localized flow recirculation region downstream of the FFS edge. The origin of these high-frequency fluctuations (at a comparable frequency to the secondary instability in their Clean case) was traced to a vortex-shedding mechanism of the distorted shear-layer.

Based on the above observations, the addition of an FFS appears to lead to a notable increase in the temporal velocity fluctuations on the outer side of the upwelling region

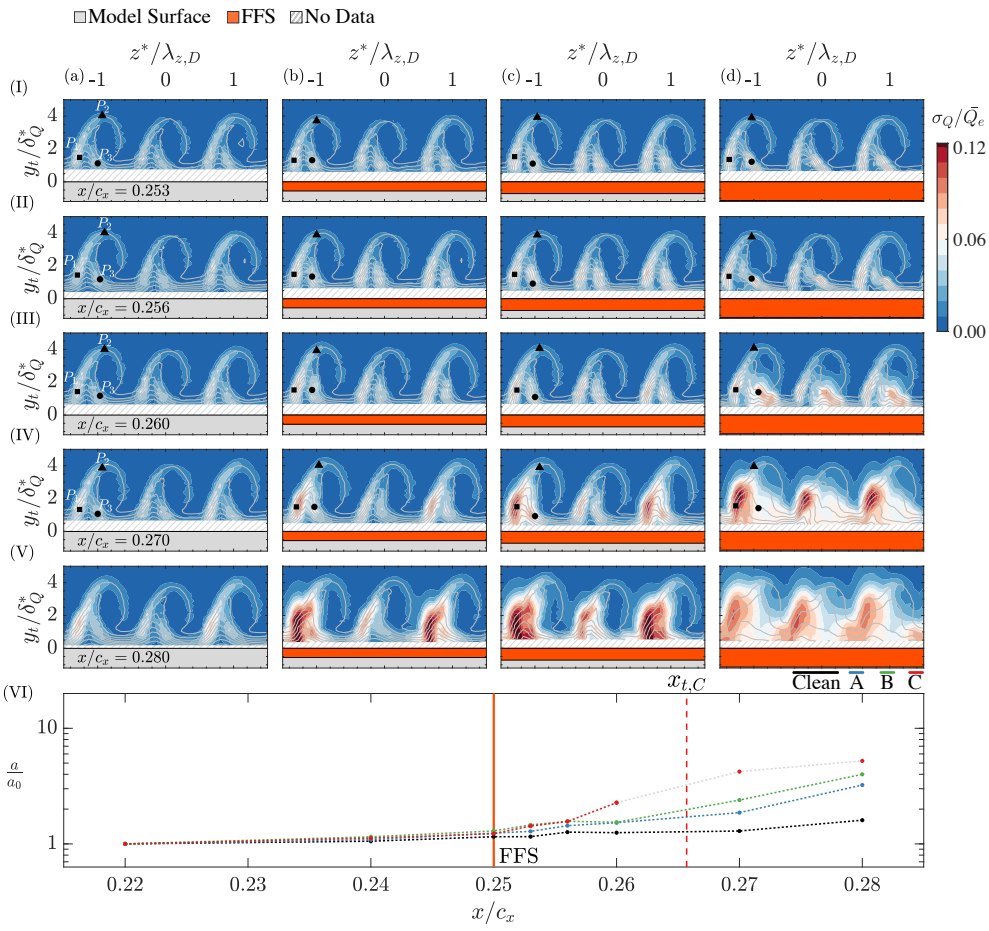

Figure 5.8: Contours of temporal velocity fluctuations (z positive direction outboard) and time-average velocity (grey solid lines 10 levels $\bar{Q}/\bar{Q}_e$ from 0 to 1 same contours as in figure 5.5) : (a) Clean; (b) A; (c) B; (d) C; and (VI) Streamwise evolution of unsteady disturbance amplitude ($x_{t,C}$ transition location for case C, δ_Q^* = 620 µm and $\lambda_{z,D}$ = 8 mm)

of the CF vortices in all the cases considered. The spatial location of these fluctuations suggests a dominance of the type I secondary instability mode over the type II and type III. Nevertheless, in agreement with Eppink [130, 137] for the highest step case (C in table 5.1), a strong increase in the temporal velocity fluctuations also occurs on the inner side of the upwelling region. The following sections explore the development of these unsteady fluctuations to determine their effect on the breakdown of the CF vortices.

5.5.2. SPATIAL ORGANIZATION OF UNSTEADY DISTURBANCES

The analysis presented in §5.5.1 showed that upon the addition of an FFS a considerable increase in the temporal velocity fluctuations (σ_Q) occurs at specific regions within the

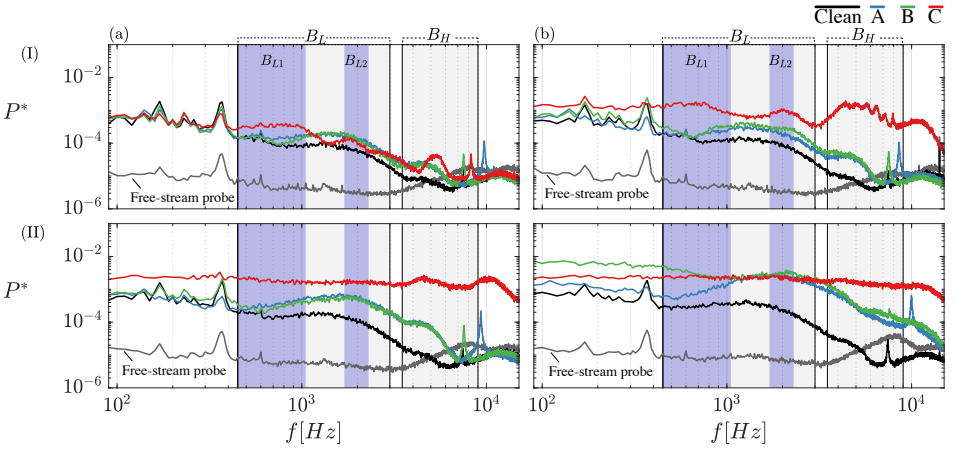

Figure 5.9: Spectral analysis at the inner side of the upwelling region, probe P_3 (• in figure.5.8) at measurement planes downstream of the step location: (Ia) $x/c_x = 0.253$; (Ib) $x/c_x = 0.256$; (IIa) $x/c_x = 0.260$; and (IIb) $x/c_x = 0.270$. Shaded grey and blue regions indicate different frequency bands.

structure of the stationary CF vortices. Henceforth, a spectral analysis on the HWA time-series (i.e. fluctuating velocity $Q' = Q - \bar{Q}$) is conducted at three spatial probe locations (P_1 ■;P_2 ▲; P_3 •) as indicated in figure 5.8(Ia-IVd). The power spectral density (P) is determined for each probe signal following the averaged periodogram method [185] using segments of 5120 samples with an overlap of 50%. The final spectra feature a frequency resolution of $\delta_f = 10$ Hz and are non-dimensionalized following Deyhle and Bippes [77] as $P^* = ((\delta_f P)/U_\infty^2)^{1/2}$.

In addition, the entire velocity fields are bandpass filtered using a zero-phase eighth-order Butterworth filter. Note that the filtered velocity fluctuations (σ_{Q_f}) are referenced to the non-filtered external velocity ($\bar{Q}_e$) at each measurement plane. This filtering technique permits a detailed analysis of the spatial organization of the temporal velocity fluctuations on particular frequency bands as shown in Serpieri and Kotsonis [71, 90].

UNSTEADY DISTURBANCES ON THE INNER SIDE OF THE CROSSFLOW VORTICES

Figure 5.9, shows the spectral analysis of probe P_3 (i.e. • in figure 5.8Ia-IVd on the inner side of the upwelling region) for the measurement planes between $0.253 \leq x/c_x \leq 0.270$. In addition, to monitor the spectral content in the freestream flow, an extra probe is located at the exterior of the boundary–layer for the Clean configuration. As anticipated, the power spectrum in the freestream is relatively flat except for two features of interest. The first one is a pair of low-frequency peaks ($f \approx 170$ and 370 Hz), which correspond to unavoidable mechanical vibrations in the supporting arm of the hot-wire probe appearing at all measurement locations. Similar to Eppink and Wlezien [151], these probe vibrations lead to a qualitative match of the filtered velocity fluctuations (i.e. bandpass filter around the low-frequency peaks) and the topology of the time-averaged wall-normal velocity gradient. The second feature of interest is the high-frequency ($> 10^4$Hz) hump inherent to the HWA bridge.

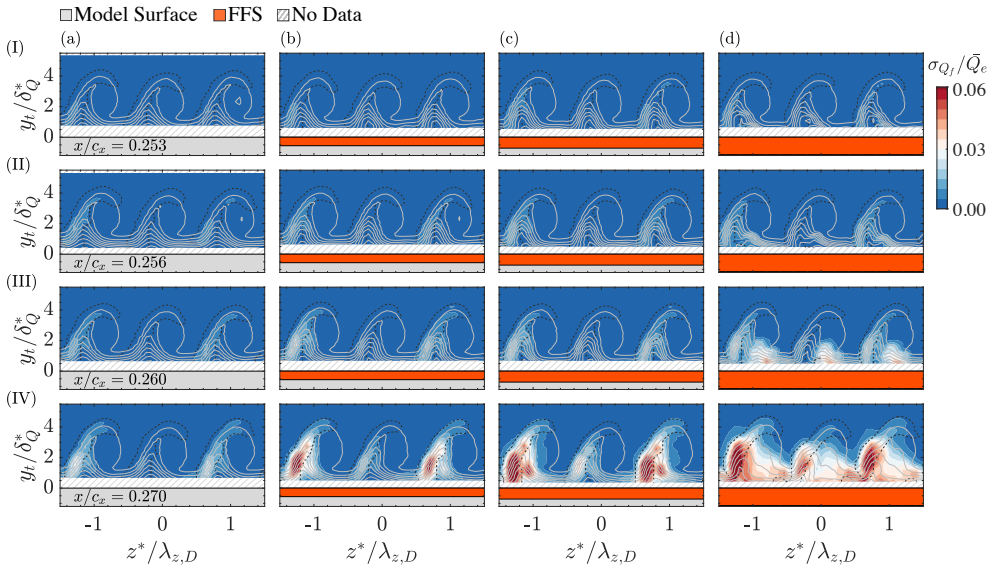

Figure 5.10: Bandpass filtered (B_L,450 Hz ≤ f ≤ 3 kHz) contours of temporal velocity fluctuations (dashed lines indicate the limit between the inner/outer side used for the calculation of a^*) and time-average velocity (grey solid lines 10 levels $\bar{Q}/\bar{Q}_e$ from 0 to 1 same contours as in figure 5.5) : (a) Clean; (b)A; (c)B; (d)C. (δ^*_Q = 620 µm and $\lambda_{z,D}$ = 8 mm)

Instead, inside the boundary–layer at $x/c_x = 0.253$ (figure 5.9Ia) the spectral analysis for the Clean configuration reveals the dominance of low frequency velocity fluctuations between 450 Hz ≤ f ≤ 3kHz, herein this frequency band is referred to as B_L as indicated in figure 5.9. Although the increase of temporal velocity fluctuations at this location is in agreement with Serpieri and Kotsonis [71, 90] and the results presented in Chapter 4 (Rius-Vidales and Kotsonis [140]), contours of the temporal velocity fluctuations filtered at the bandpass B_L (figure 5.10Ia-IVa) show a relatively weaker development of type III modes. This is largely expected since the velocity fluctuations typically associated to the type III mode are in fact the result of the interaction between travelling and stationary CF modes. The latter is considerably stronger in the present study due to the larger amplitude associated with the DREs used at the leading edge.

When considering a critical FFS case (A and B, in table 5.1) an increase in the temporal velocity fluctuations with respect to the Clean configuration occurs mainly inside the low-frequency band B_L as shown in figure 5.9. Even though the shape of the power spectrum remains similar to the Clean configuration, the deviations from it in this frequency band becomes considerable by $x/c_x = 0.270$ (figure 5.9IIb).

In contrast, the shape of the power spectrum for the supercritical FFS case (case C in table 5.1) differs considerably from the Clean baseline. More specifically, downstream of the FFS at $x/c_x = 0.253$ and 0.256 (figure 5.9Ia,Ib) the temporal velocity fluctuations at the low frequency band B_L appear in two distinct regions B_{L1} (450 Hz ≤ f ≤ 1050 Hz) and B_{L2} (1700 Hz ≤ f ≤ 2300 Hz). In addition, high-frequency fluctuations appear (B_H,

3.5 kHz ≤ f ≤ 9 kHz) as a prelude to the flattening of the power spectrum (i.e. turbulent flow) by $x/c_x = 0.260$ as shown in figure 5.9(IIa).

UNSTEADY DISTURBANCES ON OUTER SIDE AND CUSP OF THE CROSSFLOW VORTICES

Figure 5.11 and 5.12, present the spectral analysis for the probes P_1 (i.e. ■ in figure 5.8 on the outer side of the upwelling region) and P_2 (i.e. ▲ in figure 5.8 on the top part of the CF vortices) for the measurement planes between $0.253 \leq x/c_x \leq 0.270$. In the Clean configuration, the power spectrum for probe P_1 and P_2 (figure 5.11 and 5.12, respectively) indicates temporal velocity fluctuations at the high-frequency band B_H. The high-frequency content in the power spectrum at the location of these probes is in agreement with previous studies at similar conditions [e.g. 71, 90], which identified velocity fluctuations corresponding to a type-I secondary instability mode between 3.5–6 kHz, and a type II mode between 7–8 kHz. In addition, the IR measurements in figure 5.2(Ia) confirm that shortly downstream of the last HWA measurement plane, a localized breakdown (i.e. turbulent wedges) of the boundary–layer occurs as expected from the rapid development of these secondary instability modes in this case without FFS.

Consequently, the bandpass filtered contours of σ_{Q_f} at the frequency band B_H (figure 5.13Ia-IVa) show temporal velocity fluctuations spatially located on the outer side of the upwelling region as well as the top part of the CF vortices overlapping with the minimum spanwise gradients and positive wall-normal gradients shown in figure 5.7. This topology of temporal velocity fluctuations is typical of type I and type II modes [71].

Previous numerical and experimental studies in Clean (i.e. without surface irregularities) stationary CF instability cases showed that type I secondary instabilities of the Kelvin-Helmholtz type develop in the shear layer of the CF vortices [e.g. 71, 90, 95]. Therefore, the frequency of these secondary instabilities varies as they convect to higher- and lower-velocity regions in the distorted boundary–layer. This behaviour manifests on the bandpass filtered velocity fluctuations at the frequency band B_L (figure.5.10Ia-IVa), which indicate that temporal velocity fluctuations are also located on the outer side of the upwelling region at a location closer to the wall than the ones observed for the higher frequency band B_H.

For the critical FFS cases (A and B), the spatial organization of the bandpass filtered contours of σ_{Q_f} at the low B_L (figure 5.10Ib-IVc) and high B_H (figure 5.13Ib-IVc) frequency bands closely matches the development of the secondary instabilities (type I and type II modes) observed in the Clean configuration. A mild amplification of these fluctuations is observed as a function of step height, which is attributed to the strengthening of the stationary CF vortices and subsequent intensification of the spanwise and wall-normal shears, which drive these secondary instabilities. In contrast, in the supercritical FFS case C (figure 5.10Id-IVd and 5.13Id-IVd) the spatial distribution of the temporal velocity fluctuations strongly differ from the Clean case. More specifically, downstream of the FFS (i.e. $x/c_x = 0.256$), the maximum temporal velocity fluctuations occur at the upwelling region's inner side coinciding with the location of a possible recirculation region as identified by Eppink [130]. Henceforth, the nature of these fluctuations will be further investigated.

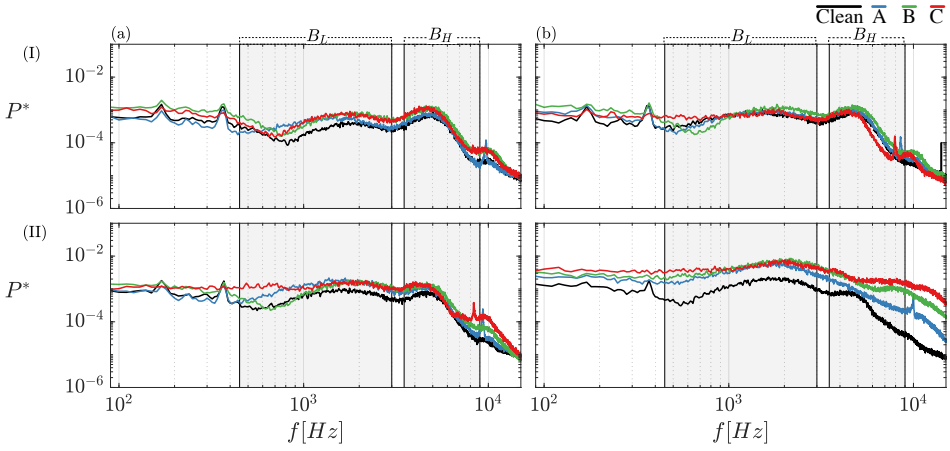

Figure 5.11: Spectral analysis for probe on the outer side of the upwelling region P_1 (■ in figure 5.8) at measurement planes downstream of the step location: (Ia) $x/c_x = 0.253$; (Ib) $x/c_x = 0.256$; (IIa) $x/c_x = 0.260$; and (IIb) $x/c_x = 0.270$. Shaded grey regions indicate different frequency bands.

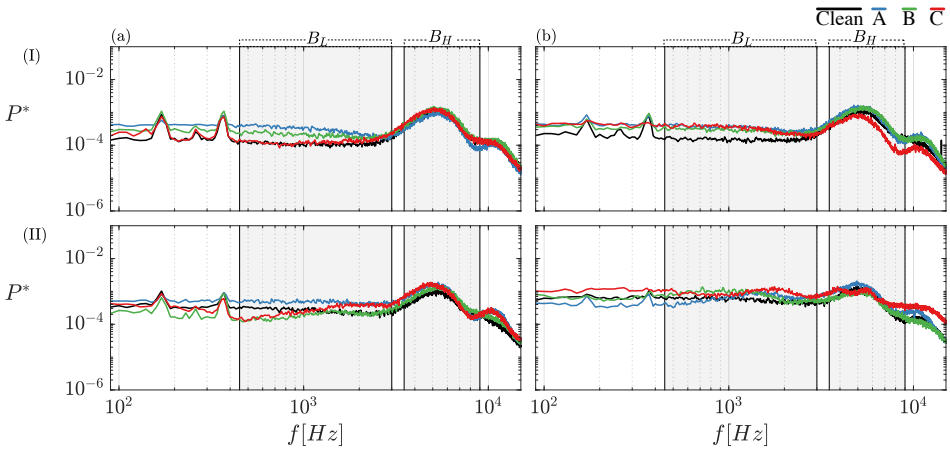

Figure 5.12: Spectral analysis for probe on the cusp of the CF vortex P_2 (▲ in figure.5.8) at measurement planes downstream of the step location: (Ia) $x/c_x = 0.253$; (Ib) $x/c_x = 0.256$; (IIa) $x/c_x = 0.260$; and (IIb) $x/c_x = 0.270$. Shaded grey regions indicate different frequency bands.

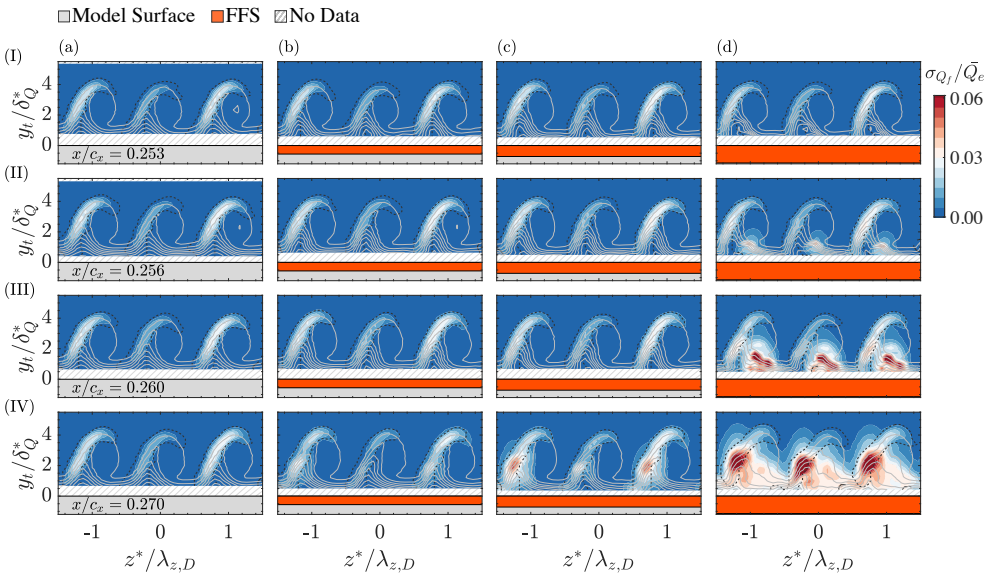

Figure 5.13: Bandpass filtered (B_H,3.5kHz $\leq f \leq$ 9 kHz) contours of temporal velocity fluctuations (dashed-lines indicate the limit between the inner/outer side used for the calculation of a^*) and time-average velocity (gray solid lines 10 levels $\bar{Q}/\bar{Q}_e$ from 0 to 1 same contours as in figure 5.5): (a) Clean; (b) A; (c) B; (d) C. ($\delta_Q^* = 620$ µm and $\lambda_{z,D} = 8$ mm)

UNSTEADY DISTURBANCES IN THE SUPERCRITICAL FFS

The spectral analysis (figure 5.9Ib) at the location of probe P_3 (i.e. • in figure 5.8(Id-IVd) downstream of the FFS ($x/c_x = 0.256$) shows the occurrence of temporal velocity fluctuations at two distinct sub-bands B_{L1} and B_{L2}. To further investigate the origin of these unsteady disturbances, the temporal velocity fluctuations for the Clean and FFS cases at this streamwise position are filtered in these frequency bands and presented in figure 5.14.

The spatial organization of the temporal velocity fluctuations presented in figure 5.14 reveals a striking difference between the supercritical FFS (case C, figure 5.14Id,IId) and the rest of the cases. In particular, for the Clean and critical FFS cases (figure 5.14Ia-IIc), the maximum temporal velocity fluctuations are spatially located on the outer side of the upwelling region. In contrast, for the supercritical FFS the maximum fluctuations are located on the inner side of the upwelling region. More importantly, for the band B_{L1} figure 5.14(Id) the maximum temporal velocity fluctuations in the supercritical FFS coincide with the second positive spanwise gradient maxima near the wall (D_1 in figure 5.14Id) while the one in the frequency band B_{L2} overlaps with the region of strong positive wall-normal gradient (D_2 in figure 5.14IId) identified as region (D) in figure 5.7(IId). As mentioned earlier, Eppink [130] proposes that the strong positive wall-normal gradient in this region is related to the shear layer, which develops on the top of the recirculation region downstream of the FFS. Interestingly, Eppink [130] identified two distinct frequency bands at which the fluctuations in this region occur and reports that

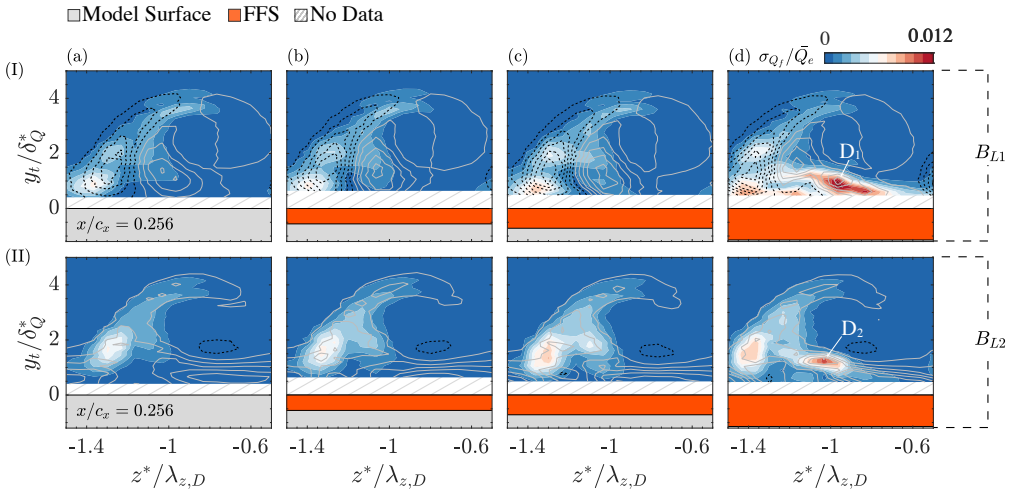

Figure 5.14: Bandpass filtered B_{L1}(I) (450Hz ≤ f ≤ 1050 Hz) and B_{L2}(II) (1700Hz ≤ f ≤ 2300 Hz) contours of temporal velocity fluctuations (gray solid contour lines indicate the positive and dashed ones negative spanwise (I) and wall-normal (II) velocity gradients, the contours corresponds to values in figure 5.7): (a) Clean; (b) A; (c) B; (d) C. (δ^*_Q = 620 µm and $\lambda_{z,D}$ = 8 mm)

5

their range closely matches the one expected from flapping ($0.12U_e/L \leq f_F \leq 0.2U_e/L$, with L being the mean reattachment length) and shedding ($0.6U_e/L \leq f_S \leq 0.7U_e/L$) frequencies of separated shear layers in two-dimensional boundary–layers. The qualitative agreement of the wall-normal gradients (region D on figure 5.7(IId) in this work with the ones reported in Eppink [137, figure 7] indicate the possibility that a strong modulated recirculation region develops downstream of the highest FFS (case C).

Considering that the shedding of the recirculation region may occur at the peak frequency in band B_{L2} (i.e. $f_S \approx 2000$ Hz in figure 5.9Ib), a rough estimation of the mean reattachment length (7.4 mm ≤ L_E ≤ 8.6 mm) and possible flapping frequency range (343 Hz ≤ f_F ≤ 667 Hz) is obtained for the highest FFS case based on the shedding and flapping criteria used by Eppink [130]. Although the assumptions in this method are rather crude, the estimated flapping frequency range falls partially within the low-frequency band (B_{L1}, figure 5.9(Ia-Ib) at which the power spectrum of the supercritical FFS (case C) strongly differs from the Clean baseline one. Moreover, at this low-frequency band B_{L1} (figure 5.14Id) the maximum velocity fluctuations are also located on the inner side of the upwelling region (i.e. where flow recirculation is expected) and extend towards the wall.

Therefore, the evidence in this work points to a possible connection between the flapping/shedding mechanism described by Eppink [130] and the unsteady disturbances on the inner side of the upwelling region for the supercritical FFS (case C). Nevertheless, the origin of the inner side fluctuations remains unclear, and particularly its relation to the mean flow deformation imparted by the step on the flow. As noted by Eppink [130] a possible recirculation region downstream of the FFS edge is not uniquely dependent on the step height but is also influenced by the amplitude of the CF vortices. Similarly,

a second mechanism possibly providing the necessary velocity shears for these fluctuations could be the appearance and development of near-wall Görtler vortices, due to the concave shape of the streamlines as the flow passes the step, similar to the observations presented by Marxen *et al.* [51] in a pressure-induced laminar separation bubble. To conclusively determine the stationary and unsteady flow structure in the vicinity of the FFS, fully three-dimensional velocity measurements or numerical simulations are required.

Finally, when comparing the spectral analysis results on the inner (figure 5.9) and outer (figure 5.11) side of the upwelling region for this supercritical FFS (case C), it is clear that the power spectrum flattens first on the inner side. These results indicate that the laminar–turbulent transition for this case might not initiate on the outer side of the upwelling region as expected from the typical development of the type I secondary CF instability. This behaviour will be further assessed in §5.6.

5.6. LAMINAR FLOW BREAKDOWN DUE TO AN FFS

The analysis of unsteady disturbances presented in §5.5 indicates that the temporal velocity fluctuations for the critical FFS cases (A and B in table 5.1) follow closely the development observed in the Clean baseline configuration. The maximum fluctuations are identified on the outer side of the upwelling region where type I secondary instabilities, widely acknowledged as the driver of the breakdown of the CF vortices, are known to develop. In contrast, when considering a supercritical FFS case (C in table5.1), an entirely different behaviour results. In this case, the first evidence of laminar flow breakdown (i.e. flattening of the power-spectrum in figure 5.9IIa) occurs on the inner side of the upwelling region and does not correspond to the location where the type I secondary instability commonly manifests (i.e. upwelling region's outer side). In this section, the breakdown is further examined to provide insight into the different unsteady behaviours observed in critical and supercritical FFS cases.

White and Saric [89] and Serpieri and Kotsonis [71, 90] have employed the disturbance amplitude (a) (§5.2.4) as a metric to monitor the development of the secondary instability modes. This approach has been particularly successful in typical CF instability cases (i.e. smooth case no FFS) since the bandpass-filtered HWA measurements isolate the different unsteady modes of type I, II and III. The results in §5.5 show that for the highest FFS (case C), the velocity fluctuations simultaneously occur in the outer and inner side of the upwelling region at all examined frequency bands. Thus, calculating the disturbance amplitude (a) on the entire plane without any further processing will undesirably integrate the unsteady fluctuations of secondary instability modes of type I/II with the step-induced shedding/flapping unsteady disturbances, thus losing oversight of their respective contributions.

To avoid this issue, the temporal velocity fluctuations occurring on the outer side and top of the upwelling region are isolated from the ones occurring on the inner side by spatially filtering the bandpass filtered HWA measurements (figures 5.10, 5.13) based on the average velocity spanwise and wall-normal gradients (figure 5.7). Specifically, the boundary between the inner and outer side is defined using the overlap of the minimum spanwise gradient and maximum wall-normal gradient away from the wall for each stationary CF vortex as shown by the black dashed lines in figures 5.10 and 5.13. Subse-

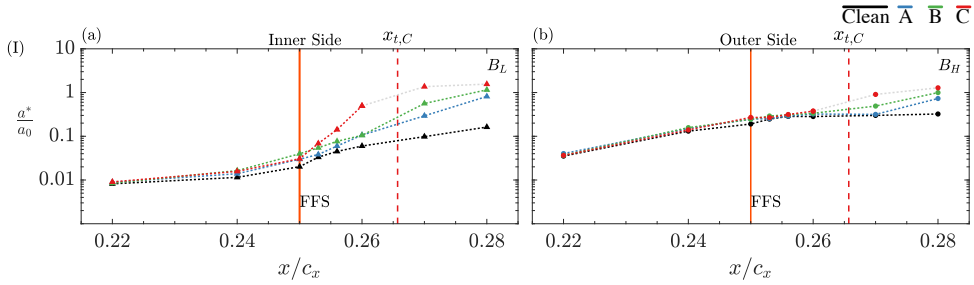

Figure 5.15: Unsteady disturbance amplitude a^* calculated for the inner (a) and outer side (b) of the upwelling region based on regions defined by the dashed lines for different frequency bands in figures 5.10 and 5.13: (Ia) B_L; (Ib) B_H ($x_{t,C}$ transition location for case C).

quently, the unsteady disturbance amplitude a^* is calculated on these spatially filtered measurements. Figure 5.15 presents the streamwise evolution of the unsteady disturbance amplitude (a^*/a_0) with the reference a_0 being taken as the total integral (i.e. no bandpass) at $x/c_x = 0.22$ for each case.

On the inner side of the upwelling region, figure 5.15(a) shows that the addition of a critical FFS case (A or B) leads to a continuous amplification of the unsteady disturbance amplitude (a^*) at the low-frequency band B_L, deviating from the trend indicated by the Clean case (dashed black line). On the other hand, the fluctuations at the higher frequency band B_H on the outer side of the upwelling region (figure 5.15b) follow closely the trend dictated by the Clean configuration until the primary stationary CF instability in these critical FFS cases reaches its maximum amplitude ($x/c_x \approx 0.260$ in figure 5.6c). Farther downstream, an increase in the temporal velocity fluctuations at the frequency B_H corresponding to the development of type-I/II secondary instabilities occurs. Detailed studies of the secondary instability in smooth cases (i.e. without FFS) showed that the development of either type I, II or the interaction of both high-frequency unsteady modes leads to the initiation of the laminar breakdown of the CF vortices [e.g. 71, 89, 94, 186].

To further quantify the origin of breakdown, the HWA measurements are high-pass filtered with a cutoff frequency of $f_c = 12$ kHz. The objective of this filtering is to isolate the increase in velocity fluctuations associated with turbulent flow from the high-frequency ones corresponding to the secondary instability modes captured by the frequency band (B_H). The results for the critical FFS presented in figure 5.16(Ib-IIIc) indicate that by the end of the measurement domain $x/c_x = 0.280$, the HWA measurements on the outer-side of the upwelling region show an increase in temporal velocity fluctuations. This suggests that the origin of laminar–turbulent transition is away from the wall on the outer side of the upwelling region. This behaviour coincides with the development of a type I secondary instability mode. Therefore, the addition of a critical FFS appears to strongly amplify the primary CF instability leading to the premature development of secondary instabilities, which anticipate the laminar–turbulent breakdown.

The analysis in §5.4 and §5.5 showed that in the case of a supercritical FFS (case C), a strong amplification of the stationary CF vortices occurs, as well as an increase in the

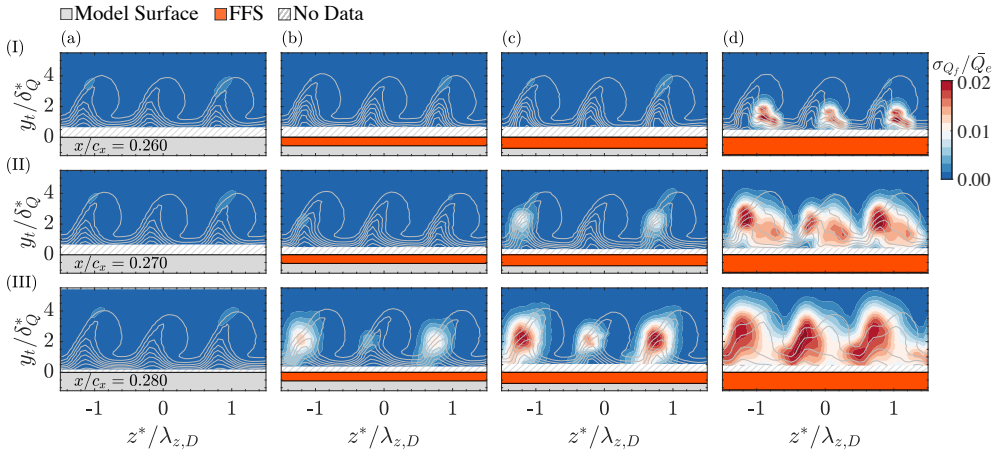

Figure 5.16: High-pass filtered (f_c = 12 kHz) contours of temporal velocity fluctuations and time-average velocity (gray solid lines 10 levels from 0 to 1): (a) Clean; (b) A; (c) B; (d) C (δ_Q^* = 620 µm and $\lambda_{z,D}$ = 8 mm)

5

temporal velocity fluctuations on both the outer and the inner side of the upwelling region, as shown in figure 5.15. Nevertheless, the increase in temporal velocity fluctuations on the inner side appears to play a predominant role in the breakdown of the CF vortices, given that the spectral analysis in figure 5.9 showed the first indications of turbulent flow at this location.

Downstream of this supercritical FFS (case C), a strong increase in the unsteady amplitude at the low frequency bandpass B_L ($x/c_x > 0.253$ in figure 5.15a) is observed. This results are in agreement with the power spectrum shown in figure 5.9(Ib), which indicates the dominance of the temporal velocity fluctuations at this frequency band. Shortly downstream, by $x/c_x = 0.260$ (figure 5.9IIa), the flattening of the power spectrum (i.e. associated with turbulent flow) is observed. Instead, on the outer side of the upwelling region the flattening of the power spectrum occurs farther downstream by $x/c_x = 0.270$ as shown in the spectral analysis in figure 5.11(IIb). At this location, the temporal velocity fluctuations at the higher frequencies B_H (i.e. associated type I and type II) experience a strong amplification as shown in figure 5.15(b). Figure 5.16(Id-IIId), shows the high-pass filtered velocity fluctuations calculated for the supercritical FFS (case C). These results confirm that the laminar–turbulent transition in this case originates first on the inner side of the upwelling region. This location coincides with a possible localized recirculation region based on the qualitative agreement with Eppink [130, 137] described in §5.5.2.

To this point, it is clear that the laminar–turbulent transition for the supercritical FFS does not follow the breakdown scenario of the Clean and critical FFS cases. Henceforth, it is essential to determine the connection, if any, between this behaviour and the increase in temporal velocity fluctuations at the higher frequency band B_H (figure 5.15b) corresponding to secondary instabilities developing on the outer side of the upwelling region.

5.7. CONCLUDING REMARKS

The unsteady interaction of an FFS surface irregularity with the development of CF instability in the boundary–layer of a swept wing model has been experimentally investigated. Decades of research into boundary–layers dominated by stationary CF instability on smooth configurations identified the development of high-frequency secondary instabilities as the unsteady mechanism responsible for driving the laminar–turbulent transition. However, the unsteady mechanisms are still not well understood when considering surface irregularities, given the intricate FFS-CFI interaction and limited published studies.

As the forced stationary CF vortices reach the FFS location, a clear amplification of the primary stationary CF disturbance is observed in all cases. Based on the step height, the ensuing laminar–turbulent transition follows either a critical regime behaviour (i.e. transition upstream of the baseline case) or a supercritical one where a substantial reduction in the extent of the laminar flow is measured as the transition occurs in the vicinity of the step.

A detailed analysis of the spatial organization and development of the temporal velocity fluctuations suggests that the unsteady mechanisms driving the laminar-turbulent transition are strongly influenced by the considered step height (i.e. critical or supercritical). For the critical FFS cases, the location and frequency content of the temporal velocity fluctuations closely follows the development of the secondary instabilities (type I and type II modes) observed in the Clean configuration. The amplification of these fluctuations as a function of step height is attributed to the strengthening of the stationary CF vortices by the FFS and subsequent intensification of the spanwise and wall-normal shears, known to drive the secondary instability. These results confirm the impact of a critical FFS on the development of the secondary instability, previously deduced in Chapter 4 (Rius-Vidales and Kotsonis [140]) from the spatial organization of velocity disturbances at a lower amplitude of the CF vortices.

Instead, for the supercritical FFS case, the spatial and spectral distribution of the velocity fluctuations strongly differs from smaller step cases. In particular, enhanced temporal velocity fluctuations downstream of the step edge are identified in the upwelling region's inner side. These do not correspond to where secondary instability modes of type I/II commonly manifest (i.e. upwelling region's outer side) and appear at higher frequencies than typically observed for a type III mode.

A somewhat similar arrangement in the spatial organization of velocity disturbances was presented in Chapter 4 (Rius-Vidales and Kotsonis [140]) for the supercritical FFS case. Nevertheless, the lack of time-resolved measurements in Chapter 4 (Rius-Vidales and Kotsonis [140]) constrained their analysis to topology-driven inference. Although the exact origin of the unsteady disturbances in supercritical FFS cases is still elusive, evidence in this work points to a possible connection with the unsteady mechanisms related to the distorted shear-layer and/or the localized recirculation region downstream of the step edge, also identified by Eppink [130].

Moreover, the qualitative agreement of velocity fluctuations and wall-normal gradients with the ones reported in Chapter 4 (Rius-Vidales and Kotsonis [140]) and Eppink [137] provides evidence that the unsteady distorted shear-layer is persistent in supercritical

FFS cases at different amplitudes and spatial organization of the CF vortices. The spectral analysis presented in this work suggests that these unsteady disturbances downstream of the supercritical FFS initiate the laminar flow breakdown. Henceforth, this work is a first step towards understanding the unsteady mechanism which triggers laminar–turbulent transition in a supercritical FFS.

6

Conclusions, Recommendations & Outlook

6.1. CONCLUSIONS AND RECOMMENDATIONS

INFLUENCE OF THE FFS ON THE LAMINAR-TURBULENT TRANSITION BEHAVIOUR

The global and local influence of the FFS on the laminar-turbulent transition behaviour has been characterized through a series of wind tunnel experiments under forced and unforced conditions as presented in Chapter 3. In forced conditions, Discrete Roughness Elements (DREs) are used to condition the CF vortices' initial amplitude and spanwise wavelength. In unforced cases, these parameters are influenced by the swept wing model's micro-surface roughness.

Three different transition behaviour regimes due to an FFS are identified through a fine variation of the Reynolds number in the unforced cases. A *subcritical* regime occurs when the laminar-turbulent transition process is nearly unaffected by the presence of the step. Instead, a *critical* regime occurs when the transition location shifts upstream towards the step location, departing from the trend indicated by the baseline case (i.e. without FFS). Finally, a *supercritical* (i.e. tripped) regime occurs when the boundary-layer transition is near or directly at the step. When evaluating local one-parameters (i.e. baseline case boundary-layer displacement thickness δ_h^* or estimated core-height y_c of the CF vortices) to determine the transition behaviour regime, their non-universal applicability is observed.

In the forced conditions, three different stationary CF modes (i.e. variation in y_c) are studied at fixed Reynolds number (i.e. fixed δ_h^*). The forced CF modes are classified based on their nominal stability at the step location. Considering that $\lambda_{z,R}$ and $y_{c,R}$ correspond to the most unstable CF mode at step location (i.e. highest N-factor), an *early-growth* mode ($y_c < y_{c,R}$ and $\lambda_z < \lambda_{z,R}$) undergoes a strong amplification upstream of the FFS location and becomes increasingly stable downstream. Instead, a *mid-growth* mode ($y_c \approx y_{c,R}$ and $\lambda_z \approx \lambda_{z,R}$) rigorously grows at the FFS location and continues to be unstable downstream. Finally, a *late-growth* mode ($y_c > y_{c,R}$ and $\lambda_z > \lambda_{z,R}$) monotonically grows upstream and downstream of the step location. The forcing conditions in the three cases exclude variations in the initial amplitude of the CF vortices. Hence, the CF vortices' amplitude when reaching the FFS is determined by the stability of the forcing mode under consideration.

The results show that, in addition to the relative size of the FFS (i.e. h/δ^* or y_c/h), the influence of the FFS on the global transition behaviour is strongly affected by the local characteristics of the incoming CF vortices (i.e. amplitude and development) dependent on the type of mode being forced (i.e. early, mid or late growth). Under forced conditions, the IR measurements show that the step interacts with the incoming primary stationary CF disturbances and its first harmonic. In contrast, in the unforced cases, the FFS interacts with the vortices generated by competing stationary CF modes at the step location.

The experiments indicate that although one-parameter correlations (i.e. h/δ^* or y_c/h) are very attractive due to their simplicity, they do not account for the complex dynamics which occur when the stationary CF vortices interact with an FFS. Therefore, multi-parameter correlations considering the local characteristics of the incoming CF vortices are recommended instead. Nevertheless, before such correlations can be devised, a fundamental understanding of the steady and unsteady interaction of the CF vortices with an FFS in the identified transition behaviour regimes is required.

INFLUENCE OF THE FFS ON THE DEVELOPMENT OF CROSSFLOW VORTICES

The need for a more in-depth understanding of the interaction dynamics between the FFS and the CF vortices motivated the experiments presented in Chapter 4. Detailed boundary-layer measurements were conducted using PIV. The conditions in the experiments (i.e. Reynolds number and forcing of late-growth CF mode) enabled the characterization of the development of the stationary CF vortices with FFS, which led to a transition behaviour in the critical and supercritical regime.

Furthermore, a novel transition behaviour was observed for the smallest FFS. In this case, the laminar-turbulent transition is delayed, and the transition front is unexpectedly shifted downstream of the baseline case (i.e. without FFS). A fine variation of the relative step height (h/δ_h^*) location reveals that the transition delay is restricted to a very narrow set of conditions. Therefore, further studies are recommended to characterize this behaviour at different conditions of the CF vortices (i.e. amplitude and spanwise wavelength).

The trajectory of the CF vortices is tracked as they approach the step. As the CF vortices interact with the FFS, they experience a tilting motion which correlates well with the expected local pressure gradient imposed by the FFS geometry. Upstream of the FFS location, the CF vortices slightly tilt outboard (i.e. adverse pressure gradient), then over the step strongly tilt inboard (i.e. favourable pressure gradient) and downstream of the FFS again tilt outboard (i.e. adverse pressure gradient) as the flow recovers to the nominal pressure gradient imposed by the swept wing's airfoil. An intensification of this motion is observed closer to the wall and with increasing FFS height. The add-on strategy followed to study FFS in the existing M3J swept wing model restricts the pressure measurement to only the baseline configuration. Given the importance of the pressure gradient imposed by the FFS in the interaction with the CF vortices observed, it is recommended that future models include the capability of measuring the pressure distribution in cases with FFS.

As the CF disturbances reach the FFS, they do not directly impinge on its edge. Therefore, in agreement with Eppink [130], the results in this work do not support the constructive/destructive FFS-CFI interaction model proposed by Tufts *et al.* [129] based on the core height of the CF vortices and their rotation direction. Instead, the local changes in the trajectory of the CF vortices (and thus pressure gradients) correlate well with the observed amplification of the CF disturbances near the FFS location. In addition, the upward deflection of the boundary layer flow at the step location leads to a strong vertical velocity component. The combination of the spanwise motion and the strong vertical velocity appears to play an important role in amplifying the CF vortices near the step region. Consequently, it is recommended to explore this relationship further through detailed three-dimensional numerical and experimental studies.

In all cases near the FFS location, the stationary CF vortices reach maximum amplification and a strong mean flow distortion. The laminar-turbulent transition occurs shortly downstream of the step edge for the largest FFS. In contrast, for all the other steps, the CF vortices amplitude reduces past the baseline configuration level (i.e. without FFS) as they experience a gradual outboard spanwise tilting (i.e. adverse pressure gradient due to nominal pressure recovery). Lastly, for the smallest steps, the CF vortices experience a second amplification enhanced by the baseline favourable pressure

distribution imposed by the swept wing's airfoil.

Downstream of where the primary stationary CF disturbance and its higher harmonics reach their maximum amplification, the spanwise velocity temporal fluctuations increase in the spatial region associated with the development of the secondary CF instability mode of type-I (i.e. upwelling region outer-side). For the FFS in the supercritical regime, the breakdown of the CF vortices occurs just downstream of the step edge. For the moderate FFS case in the critical regime, the velocity fluctuations slightly decrease before rapidly amplifying, reaching higher levels than the Clean baseline configuration by the end of the measurement domain. Conversely, for the other FFS cases, a substantial decrease in the velocity fluctuations occurs by the end of the measurement domain and a transition delay effect with respect to the baseline configuration results for the smallest FFS case.

The experiments conducted show the importance of considering the development of secondary and unsteady instabilities for understanding the FFS-CFI interaction. Of particular relevance are the supercritical FFS cases (i.e. transition at the step) as they display a markedly different spatial organization of the velocity gradients and fluctuations just downstream of the FFS edge.

INFLUENCE OF THE FFS ON THE BREAKDOWN OF CROSSFLOW VORTICES

The connection between the amplification of the primary stationary CF instability by the FFS and the subsequent laminar-turbulent boundary-layer transition is the development of secondary and unsteady instabilities. Therefore, the unsteady interaction of stationary CF vortices with an FFS was characterized through detailed measurements of the boundary-layer flow using hot-wire anemometry as presented in Chapter 5.

In all cases, the forced CF vortices reach a maximum amplification and strong mean flow distortion near the step location. For the highest FFS, the transition behaviour corresponds to the supercritical regime. Instead, for the moderate steps the transition behaviour corresponds to the critical one. For the FFS in the supercritical regime, the spatial organization of the velocity gradients and fluctuations differ considerably from the ones observed for the baseline configuration and the other FFS cases in the critical regime. This behaviour is in agreement with the results presented in Chapter 4. Eppink [137] related this particular spatial arrangement of the wall-normal velocity gradients to the spanwise modulated flow recirculation regions downstream of an FFS.

The analysis of the velocity fluctuations for the baseline configuration and the FFS cases in the critical regime confirm the development of secondary instabilities of type-I/II modes prior to the laminar-turbulent boundary layer transition. In contrast, for the FFS in the supercritical regime, a new region of velocity fluctuations located on the inner side of the upwelling region of the CF vortices emerges downstream of the FFS edge and triggers the laminar-turbulent boundary-layer transition nearby the step location.

The frequency of these velocity fluctuations corresponds well with the ones presented by Eppink [130] indicating a possible relation to the flapping and shedding of the spanwise modulated recirculation region downstream of the FFS. Additionally, the band-pass filtered velocity fluctuations reveal that the maximum velocity fluctuations match the wall-normal and spanwise velocity gradients characteristic of the FFS in the supercritical regime.

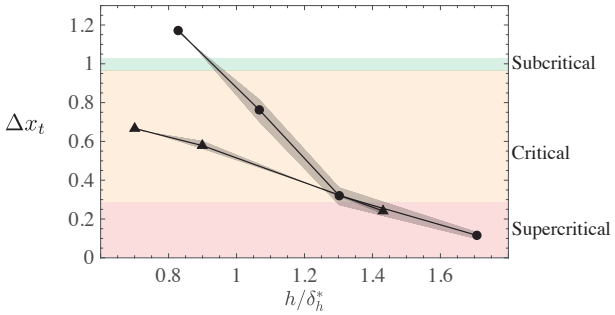

Figure 6.1: Comparison of relative transition location $\Delta x_t = (x_{t,I} - x_h)/(x_{t,C} - x_h)$ for cases presented in chapter 4 and 5 conducted at different Re_{c_X} and forcing conditions which for the Clean configuration result in a lower (•: $A_L/\bar{w}_e = 0.13$) and higher (▲: $A_M/\bar{Q}_e = 0.18$) amplitude of the CF vortices at the step location.

Considering that it is likely that the FFS in the subcritical and critical regime also feature a recirculation region downstream of the FFS edge, it is of great importance that future studies aim at identifying under which conditions the recirculation region leads to the observed alternative laminar-turbulent behaviour and clarify the role that these unsteady disturbances play in the breakdown of the CF vortices, given that recirculation regions are known to support inviscid modes, such as Kelvin-Helmholtz vortices.

In addition to a fine variation in the step height, it is recommended that the identification of the supercritical FFS condition in future investigations include different amplitude of the CF vortices, given that Eppink [130] observed a connection between the extent of the recirculation regions and the amplitude of the incoming CF vortices.

Finally, a comparison of the relative transition location $\Delta x_t = (x_{t,I} - x_h)/(x_{t,C} - x_h)$ for the experiments in Chapters 4 and 5 is presented in figure 6.1. The results clearly show that the FFS influence on the laminar-turbulent transition intensifies as the CF vortices' amplitude increases, given that the critical and supercritical regime transition behaviour shifts to a lower relative step height (i.e. lower h/δ_h^*). These results highlight the important role that the amplitude of the CF vortices play in conditioning the transition behaviour of a given step height (i.e. whether it will follow a subcritical, critical, or supercritical behaviour), and point to the recommendation of characterizing the steady and unsteady interaction of CF vortices with FFS at different amplitude levels.

6.2. OUTLOOK: SWEPT TRANSITION EXPERIMENTAL PLATFORM

This section briefly describes the dedicated Swept Transition Experimental Platform (STEP) for continuing the investigation on the impact of surface irregularities on the development and breakdown of crossflow instability. The new model has been designed following the recommendations presented in this doctoral dissertation, based on the experiments conducted on the M3J swept wing model.

6.2.1. ANECHOIC LOW-TURBULENCE WIND TUNNEL (A-TUNNEL)

The A-tunnel facility is an atmospheric, low-turbulence, closed-circuit, open-jet, and subsonic tunnel. This wind tunnel has been recently re-designed as described in detail by Merino-Martinez *et al.* [187]. The rectangular TUD 25×100 nozzle is used for the STEP model. Under this configuration, the maximum flow speed at the measurement site is 40 m/s or 144 km/h. The main elements of this tunnel presented by Merino-Martinez *et al.* [187] are indicated in figure 6.2(a,b), and described hereinafter. The airflow is driven by two centrifugal fans with ten rotor blades, each connected to a 30 kW DC electric engine installed inside a room (1) external to the anechoic plenum. The airflow is redirected onto the settling chamber (2) on the ground floor of the building. Thereafter, the airflow passes through a honeycomb-shaped flow straightener and four anti-turbulence screens at (3) before entering the cylindrical contraction (4) . Afterwards, the airflow experiences a gradual velocity increase (ratio of 17:1) at the contraction (4) until it reaches the interchangeable TUD 25 × 100 rectangular nozzle (5) on which the STEP model is installed.

The temperature (T_C) of the flow is monitored at the anechoic plenum using a Resistance Temperature Detector (RTD-Pt100)[1] and the atmospheric pressure (P_A) at the same location using a digital barometer[2]. From these measurements the fluid density[3] (ρ) and the reference kinematic viscosity[4] (ν) are calculated. During operation, the reference dynamic pressure at the test-section ($P_{q,5}$) is determined from the total and static pressure difference ($P_{q,5} = P_{t,5} - P_{s,5}$) at the nozzle outlet measured using a pitot tube and a differential pressure transducer [5]. The reference wind tunnel velocity is calculated as: $U_\infty = \sqrt{2P_{q,5}/\rho}$.

As part of the turbulence intensity characterization of the A-tunnel facility, velocity measurements have been conducted in the centre of the rectangular 25 × 100 nozzle using hot-wire anemometry [see 187]. The turbulence intensity[6] (Tu) results for different combinations of free-stream conditions are presented in figure 6.2(c). At the wind tunnel operating conditions in this work (i.e. 15 m/s ≤ U_∞ ≤ 25 m/s, gray region in figure 6.2b), the turbulence intensity is $Tu \leq 0.07\%$. Henceforth, the use of this experimental facility provides suitable flow conditions for the investigation of stationary CF instability, as described in § 1.2.2.

[1] Platinum resistance temperature detector (Pt100), 1/3 DIN (±0.10°C at 20°C)
[2] Barometer by Amphenol (amphenol-sensors.com), model: NPA-201, accuracy: 0.01% of reading
[3] Calculated as $\rho = P_A/(R(273.15 + T_C))$, [kg / m^3] using the specific gas constant $R = 287.05$, [J / kgK]
[4] Calculated as $\nu = \mu/\rho$, [m^2/s] using Sutherlands' equation: $\mu = 1.458 \times 10^{-6}\{T_K^{1.5}/(T_K + 110.4)\}$, [kg/sm]
[5] Pressure sensor by Honeywell (sps.honeywell.com), model: RSC-005ND, range ±1246 pa, accuracy ±13 pa
[6] Turbulence intensity bandpass filtered between 5 and 5000 Hz and calculated as: $Tu{=}1/U_\infty\sqrt{(1/2)(\overline{U'^2}+\overline{V'^2})}$

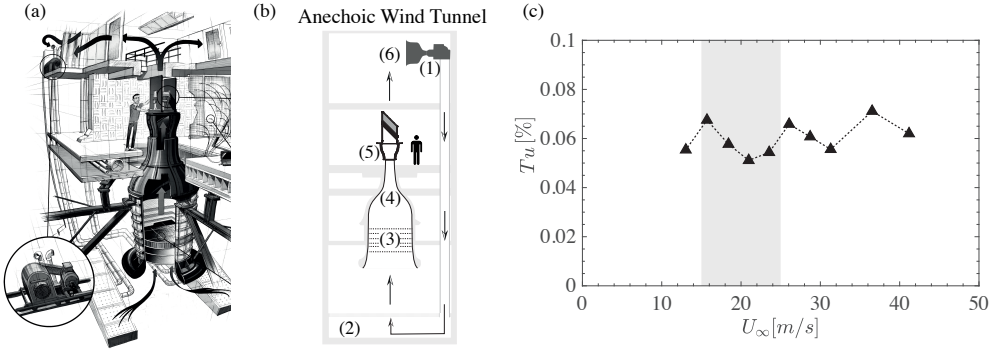

Figure 6.2: Schematic of the Anechoic tunnel (A-tunnel) at the TU Delft Low Speed Laboratory: (a) Artist impression of the wind tunnel facility by Stefan Timmers re-adapted from Merino-Martinez *et al.* [187]. (b) Cut-out diagram of the tunnel showing the different sections of the system. (c) Variation of turbulence intensity (Tu) with free-stream velocity (U_∞). Measurements obtained from Merino-Martinez *et al.* [187] and conducted with the TUD 25 × 100 nozzle installed (bandpass filtered between 5 and 5000 Hz).

6.2.2. THE STEP EXPERIMENT

The Swept Transition Experimental Platform (STEP) is a self-contained test-section designed to be used with the A-tunnel TUD 25×100 cm nozzle. The main element is a 45 degree swept flat-plate, as shown in the photograph in figure 6.3(a). Figure 6.3(b) presents a cross-sectional view of the STEP test-section. The swept flat-plate element is horizontal and spans the entire width of the test-section. Two different spatial coordinate systems are used, and their origin coincides with the intersection between the leading edge and the flat-plate mid-span. In the first coordinate system (X, Y, Z) the X-direction is aligned with the test-section sidewall. In the second coordinate system (x, y, z) the x-direction is perpendicular to the leading edge. The model features a streamwise chord of $c_X = 0.848$m, a thickness of 20 mm, and a modified super-elliptical leading edge (MSE) with an aspect ratio of six based on Schrader *et al.* [188]. The leading edge is polished to a surface roughness[7] of $R_q \approx 0.6\,\mu$m.

The flat-plate element consists of two independent precision machined[8] aluminium sections. The adjustable section (the black region in figure 6.3b) contains the leading-edge portion and is connected to a set of micro-stages [9] allowing its translation with respect to the fixed section (the grey region in figure 6.3b) on which a hinged flap is mounted. Therefore, by adjusting the micro-stage (i.e. relative distance between the sections) a step surface irregularity forms at their intersection (i.e. $x_h/c_x = 0.397$). In contrast to the M3J model, this mechanism allows for a micro-metric adjustment of the step height. On the outboard, inboard and backside, the model is enclosed by polycarbonate walls[10] attached to a custom-made aluminium frame[11]. The use of polycarbonate walls

[7] Measurement with a profilometer manufactured by Mitutoyo (mitutoyo.com), model: SJ-301
[8] CNC manufactured by Dutch Shape (dutch-shape.nl), material: 7075-T6 tooling plate
[9] Precision stage manufactured by MiSUMi (uk.misumi-ec.com), model: XSDG100
[10] Polycarbonate walls manufactured by ITEM (item.de), thickness: 8 mm
[11] Frame manufactured by ITEM (item.de), model: line 8 profiles.

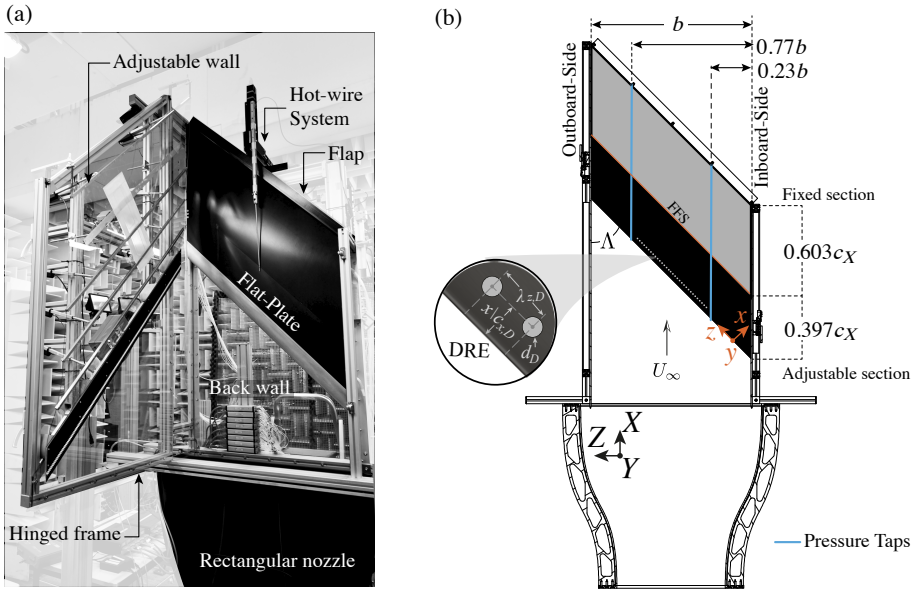

Figure 6.3: Experimental Setup: (a) Photograph of the STEP model installed on the TU Delft A-tunnel. (b) General schematic (flow direction bottom to top, $b = 0.884$ m $c_X = 0.848$ m) showing the movable (black area) and the fixed (grey area) flat-plate elements. The intersection of the flat-plate elements at which the surface irregularity forms is indicated by a solid orange line.

6

ensures adequate access for optical measurement techniques (e.g. PIV).

Access to the measurement region is provided on the front part through a hinged frame which supports an adjustable wall[12] as shown in the photograph on figure.6.3(a). The shape of the wall which conditions the pressure distribution on the flat-plate (i.e. pressure body) is determined by the independent movement of eight linear actuators. To avoid the contamination of the boundary-layer flow at the measurement region, the turbulent boundary-layer from the wind tunnel is bled-out at the walls and pressure body surrounding the flat-plate element.

6.2.3. PRELIMINARY MEASUREMENTS

This section presents a brief overview of a series of preliminary measurements[13] to illustrate the capabilities of the new experimental setup. The pressure imposed by the adjustable front wall onto the flat-plate element is measured at the inboard and outboard side using a total of 126 pressure taps connected to a system of differential pressure transducers[14]. The measured pressure distribution shows a favorable gradient as the static pressure nearly monotonically decreased for the entire extent of the flat plate,

[12] Polyethylene terephthalate glycol film by Vivak®, thickness: 1.5 mm

[13] The measurements where conducted by the author and N.Rajendakumar and used in [189]

[14] Custom-made pressure scanner (NUB-System) with Honeywell HSC series differential pressure transducers with ranges ±160,±600 and ±2488 pa with accuracy ±6,±9 and ±25 pa

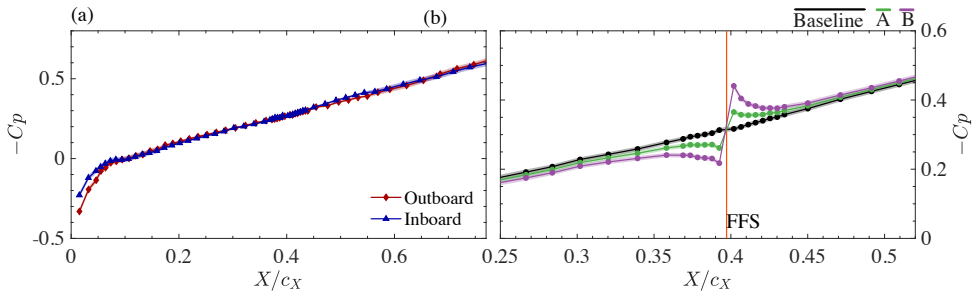

Figure 6.4: Pressure measurements: (a) Streamwise (i.e. along the X coordinate) pressure coefficient distribution on the flat-plate element at $Re_{c_X} = 1.08 \times 10^6$ without FFS, emphasizing the region of interest upstream and downstream of the step position ($x/c_X = 0.397$) . (b) Comparison of the pressure coefficient distribution for the baseline and moderate FFS A($\bar{h} = 591$ µm , $\sigma_h = 2$ µm) and B($\bar{h} = 1292$ µm, $\sigma_h = 2$ µm). The shaded regions indicate the pressure measurement uncertainty.

as shown in figure 6.4(a) for $Re_{c_X} = 1.08 \times 10^6$ ($U_\infty = 19.7\,\mathrm{m\,s^{-1}}$).

Considering the small radius of the modified super-elliptical leading edge, the lack of surface curvature and the streamwise pressure distribution, the boundary-layer flow on the flat-plate is predominantly susceptible to the development of CF instability. In addition, the pressure invariance between the outboard and inboard sides in figure 6.4(a) indicates that the infinite swept condition (discussed in §1.2.2) is a valid assumption in this experimental setup.

Of great importance to the dynamics of the FFS-CFI interaction is the pressure changes imposed by the step, as shown in the experiments presented in Chapter 4. In contrast to the M3J model, in the STEP model the pressure distribution imposed by the FFS is captured in great detail, as shown in figure 6.4(b). The results for the steps of moderate height A($\bar{h} = 591$µm , $\sigma_h = 2$µm) and B($\bar{h} = 1292$µm, $\sigma_h = 2$) confirm that an adverse pressure gradient occurs upstream of the FFS. A favourable pressure gradient follows this at the step location and a second adverse pressure gradient region downstream as the flow recovers to the baseline pressure distribution.

Measurements of the boundary-layer flow have been conducted using a Hot-Wire Anemometer (HWA) probe (single wire BL probe, Dantec Dynamics 55P15) operated by a TSI IFA-300 constant temperature bridge. A description of the HWA measurement technique, in-situ calibration and methodology is provided in §2.2.2. The STEP model is equipped with an automated traversing system (figure 6.3a) capable of translating the HWA probe along the X, Y and Z directions with a position accuracy of ±6.2 µm in each axis. For the entirety of the measurements, the wire of the HWA probe is mounted horizontally (i.e. aligned to the Z axis) and orthogonal to the X-coordinate direction.

A series of wall-normal boundary-layer scans were conducted along the z-direction to form y-z measurement planes at different streamwise locations between $0.35 < x/c_x < 0.65$ to characterize the development of the CF instability. Each profile is constructed of individual measurement points along the wall-normal direction y_t. At each measurement point, the hot-wire signal was acquired at a sampling rate of $f_s = 51200$ Hz for a total measurement time of 2 seconds. The final resolution for the results presented in

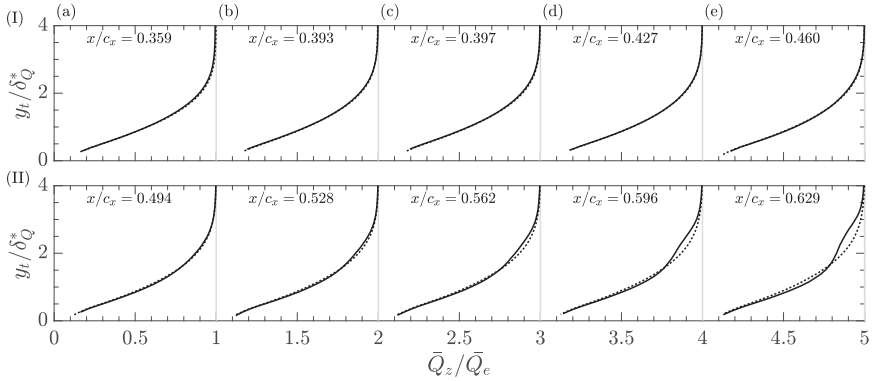

Figure 6.5: Boundary layer profiles of spanwise averaged mean flow velocity $\bar{Q}_z$ for the unforced (dashed line) and forced (solid line) conditions (δ_Q^* = 0.607µm). Note that for visualization purposes the profiles magnitude is shifted by 1

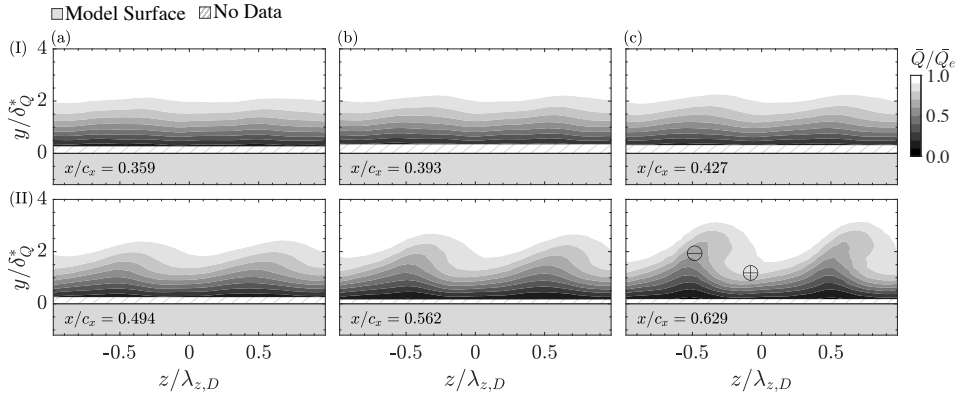

Figure 6.6: Contours of time-average velocity (z positive direction outboard) for the baseline configuration (i.e. without FFS) (δ_Q^* = 0.607µm and $\lambda_{z,D}$ = 9 mm)

figure 6.6 is fixed at Δz = 551 µm and Δy_t = 71 µm.

The measurements were conducted under forced and unforced conditions. In the forced case, DREs were used near the leading edge (i.e. neutral point) to condition the spanwise wavelength ($\lambda_{z,D}$ = 9 mm) and amplitude of the stationary CF vortices corresponding to a late-growth mode. The nominal geometry of the DREs is comparable to the ones used on the experiments presented in Chapter 4 (k_D = 100 µm, d_D = 2mm).

The spanwise-averaged mean flow boundary-layer profiles ($\bar{Q}_z$) for the baseline configuration under unforced (dashed line) and forced (solid line) conditions is shown in figure 6.5. The wall normal y_t coordinate is non-dimensionalized using the displacement thickness at the most upstream station (δ_Q^* = 607 µm at x/c_x = 0.359). At this location (i.e. x/c_x = 0.359, figure 6.5Ia) the distortion of the forced CF vortices on the

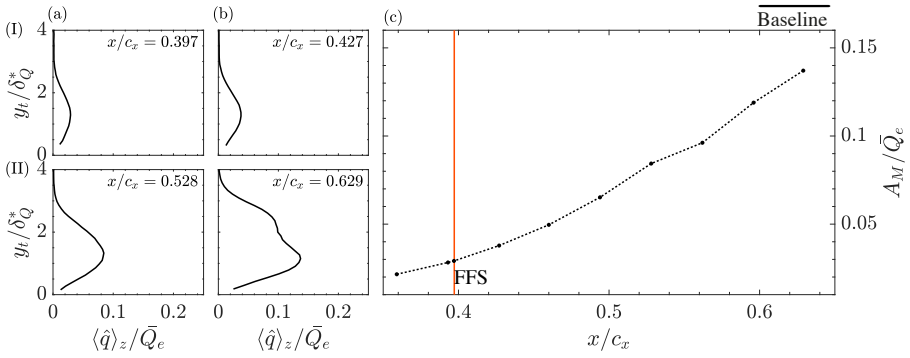

Figure 6.7: Selected steady disturbance $\langle\hat{q}\rangle_z$ profiles (δ^*_Q = 607 µm). (a,b) Steady disturbance profiles and (c) Streamwise evolution of the non-dimensional maximum amplitude (A_M).

boundary-layer is unnoticeable. Conversely, a pronounced distortion is observed for the most downstream measurements at $x/c_x = 0.562$ and 0.629 (figure 6.5IId-IIe).

Figure 6.6 presents the measured time-averaged velocity contours ($\bar{Q}$) at different streamwise locations for the baseline forced case (i.e. without FFS). The velocity distribution shows the direct action of the co-rotating stationary CF vortices, which transport high momentum fluid towards the wall (downwelling region, ⊕ in figure 6.6IIc) and low momentum flow away from it (upwelling region, ⊖ in figure 6.6IIc). The measured stationary CF vortices are spaced at the wavelength forced by the DREs ($\lambda_{z,D}$ = 9 mm).

From the time-averaged velocity fields ($\bar{Q}$), the steady disturbance profile $\langle\hat{q}\rangle_z$ has been calculated for each measurement plane following the methodology described in §5.2.4. The resulting profiles are presented in figure 6.7(a-b) for selected positions. In contrast to the measurements on the M3J model, at the most upstream measurement station $x/c_x = 0.359$ the steady disturbance profile shows only one distinguishable maximum while at the most downstream station $x/c_x = 0.629$ a second lobe appears indicating the nonlinear stages of the CF instability development [see 89, 176]. These results indicate the possibility of studying the linear and nonlinear stages of the CF vortices in more detail. In addition, finer control in the adjustment of the amplitude of the CF vortices interacting with the FFS is possible in this model by increasing the DREs height and varying their position, given the low amplitude ($A_M/\bar{Q}_e \approx 0.03$ at $x/c_x = 0.397$ in figure 6.7c) measured in the baseline configuration at the virtual FFS location using moderately sized DREs.

In conclusion, the STEP model enables the continuation of the research presented in this doctoral dissertation by allowing: i) a finer adjustment of the step height and amplitude of the CF vortices; ii) measurements of the step induced changes in pressure distribution; iii) better physical and optical access for detailed velocity measurements.

Nomenclature

SYMBOLS

A_M	m/s	Steady disturbance profile maximum amplitude.
A_U	m/s	Steady disturbance profile upper lobe amplitude.
A_L	m/s	Steady disturbance profile lower lobe amplitude.
a	- | m/s	Unsteady disturbance amplitude | Speed of sound, Eq. 5.2 | $a=\sqrt{\gamma R T_K}$.
a^*	-	Unsteady disturbance amplitude based on bandpass velocity fields.
B_H	Hz	High-frequency band.
B_L	Hz	Low-frequency band.
b	m	Wing span dimension in the Z-direction.
C_f	-	Skin-friction drag coefficient, $C_f=\tau/(0.5\rho u_e^2)$.
$\bar{C}_f$	-	Total skin-friction drag coefficient, $\bar{C}_f=1/L\int_0^L C_f(x)dx$.
C_d	-	Section drag coefficient, $C_d=d/(0.5\rho u_\infty^2 L)$.
C_p	-	Pressure coefficient, Eq. 2.1
c_x	m	Wing chord in the x-direction.
c_X	m	Wing chord in the X-direction.
d_D	mm	Discrete roughness elements nominal diameter.
d_w	µm	Hot-wire sensor diameter.
d_p	µm	Seeding particle diameter.
f	Hz | mm	Frequency | Camera objective focal length.
f_s	Hz	Sampling frequency.
$f_\#$	-	Camera objective numerical aperture.
h	µm	Forward facing step height.
h_c	µm	Critical forward facing step height.
IW	px^2	Interrogation window.
k_D	µm	Discrete roughness elements nominal height.
L	mm | m	Reattachment length | Characteristic length.
l_{px}	px	Reference length in camera sensor.
L_O	m	Reference length in object.
l_w	mm	Hot-wire sensor length.
M	-	Optical magnification factor, $M=l_{px}\delta_{px}/L_O$
M	-	Mach number, $M=U_\infty/a_\infty$.
M_{cr}	-	Critical Mach number.
M_{dd}	-	Drag divergence Mach number.
N	-	Disturbance amplification factor, Eq. 2.12
N_{env}	-	Envelope of disturbance amplification factor.
N_T	-	Total number of samples.
N_{eff}	-	Effective number of samples.
P	(m/s)^2/Hz	Power spectral density
P^*	-	Non-dimensional PSD $P^*=((\delta_f P)/U_\infty^2)^{1/2}$.

P_A	Pa	Atmospheric pressure, 1 Pa = 1 N/m^2, 1 atm = 101.3kPa.
P_s	Pa	Static pressure, P_s=$P_t - P_q$.
P_t	Pa	Total pressure.
P_q	Pa	Dynamic pressure, P_q=$0.5\rho U^2$.
Q	m/s	Velocity measured by the Hot-wire sensor, Eq. 2.3
Re_{c_X}	-	Reynolds number, Re_{c_X}=$U_\infty c_X/\nu$.
R_q	µm	Root mean square surface roughness.
R	Nm / kgK	Specific gas constant for air R = 287.05.
Tu	-	Turbulence intensity, Tu=$1/U_\infty\sqrt{(1/2)(\overline{U'^2}+\overline{V'^2})}$.
T_I	s	Integral time scale.
T_C	°C	Flow temperature.
t	s	Time.
U, V, W	m/s	Wind tunnel oriented velocity components.
u, v, w	m/s	Leading edge oriented velocity components.
X, Y, Z	m	Wind tunnel oriented reference system.
x, y, z	m	Leading edge oriented reference system.
x_h	m	Surface irregularity location.
x_D	m	Discrete roughness elements streamwise location.
y_c	µm	Estimated core height of the crossflow vortices.
α	deg | rad/m	Angle of attack | Wavenumber along x, α=$2\pi/\lambda_x$
β	rad/m	Wavenumber along z, β=$2\pi/\lambda_z$
δ_{99}	m	Boundary-layer thickness, y distance at which $u(y)$=$0.99u_e$.
δ^*	m	Boundary-layer displacement thickness, δ^*=$\int_0^\infty\left(1-\frac{u}{u_e}\right)dy$.
δ^*_Q	m	Reference displacement thickness based on Q velocity.
δ^*_w	m	Reference displacement thickness based on w velocity.
δ^*_h	m	Reference displacement thickness at the step location.
δ_f	Hz	Spectra resolution.
δ_{px}	µm/px	Camera sensor pixel pitch.
Δt	s	Time delay between PIV image frames.
γ	-	Ratio of specific heat capacities for air γ = 1.4, γ=c_p/c_v
Λ	deg	Sweep angle.
λ_z	m	Wavelength of the crossflow vortices along z coordinate.
$\lambda_{z,D}$	m	Wavelength of the DREs along z coordinate.
λ_L	nm	Laser wavelength.
μ	kg/ms	Dynamic viscosity of air, μ=$1.458\times10^{-6}\{T_K^{1.5}/(T_K+110.4)\}$.
ν	m^2/s	Kinematic viscosity of air, ν=μ/ρ.
ω	rad/s	Angular frequency, ω=$2\pi/T$
ρ	kg/m^3	Density of air, ρ=$P_A/(R(273.15+T_C))$.
ρ_p	kg / m^3	Density of seeding particle.
σ	m / s	Standard deviation.
θ	m	Boundary-layer momentum thickness, θ=$\int_0^\infty\frac{u}{u_e}\left(1-\frac{u}{u_e}\right)dy$.
τ	N / m^2	Wall-shear stress, τ=$\mu(\partial u/\partial y\|_{y=0})$.
τ_p	s	Particle response time.
τ_f	s	Characteristic time of the fluid fluctuations.

ACCENTS AND SUBSCRIPTS

$\bar{a}$	Time-averaged quantity.
$\mathbf{a}$	Vector quantity.
a'	Fluctuating quantity | Perturbation.
$\langle a \rangle_z$	Quantity spanwise root mean square.
a_∞	Quantity related to the free-stream.
a_e	Quantity related to the edge of the boundary-layer.
a_0	Quantity related to an initial reference value.
a_t	Quantity related to the laminar-turbulent transition location.
a_i	Imaginary component.
a_r	Real component | quantity at reference location.
a_z	Quantity evaluated along the z coordinate.
a_R	Spatially reconstructed quantity
a_f	Bandpass frequency filtered quantity

ACRONYMS

BAU	Business as Usual.
CF	Crossflow.
CFI	Crossflow Instability.
CTA	Constant Temperature Anemometer.
COVID-19	Coronavirus disease of 2019.
CO2	Carbon Dioxide emissions.
CORSIA	Carbon Offsetting and Reduction Scheme for International Aviation.
DIT	Differential Infrared Thermography.
DNS	Direct Numerical Simulation.
DRE	Discrete Roughness Element.
EMI	Electromagnetic Interference.
FFS	Forward Facing Step.
FOV	Field of view.
FPA	Focal Plane Array.
GDP	Gross Domestic Product.
HWA	Hot-Wire Anemometry.
IR	Infrared.
ICAO	International Civil Aviation Organization.
KH	Kelvin-Helmholtz.
LFC	Laminar Flow Control.
LTT	Low Turbulence Tunnel.
LST	Linear Stability Theory.
M3J	Swept wing model design at TU Delft.
NLF	Natural Laminar Flow.
NETD	Noise Equivalent Temperature Difference.
NOX	Nitrous Oxide emission.
ONERA	Office National d'Etudes et de Recherches Ae'rospatiales.
OS	Orr-Sommerfeld.

PET	Polyethylene Terephthalate.
PIV	Particle Image Velocimetry.
PSD	Power Spectral Density.
RPK	Revenue Passenger Kilometer.
STEP	Swept Transition Experimental Platform.
SW	Shock wave.
TS	Tollmien-Schlichting.
2D2C	Planar measurement of two velocity components.
2D3C	Stereoscopic measurement of three velocity components.
3D3C	Volumetric measurement of three velocity components.

References

[1] ATAG, "ATAG Aviation Benefits Beyond Borders", Oxford Economics - ATAG, [Online], 2020, Available: edu.nl/wfyut.

[2] P. W. Brooks, "The development of air transport", *Journal of Transport Economics and Policy*, vol. 1, no. 2, pp. 164–183, 1967.

[3] M. Dierikx, "KLM: an Airline Outgrowing its Flag", in *Flying the Flag: European Commercial Air Transport since 1945*, H.-L. Dienel and P. Lyth, Eds. London: Palgrave Macmillan UK, 1998, pp. 126–158. DOI: 10.1007/978-1-349-26951-8_5.

[4] KLM, "First KLM cityhopper Embraer 195-E2 touches down at schiphol", KLM Royal Dutch Airlines, [Online], 2021, Available: edu.nl/7mgdb.

[5] F. Ogier, "KLM First Passenger Aircraft", KLM Royal Dutch Airlines, [Online], 2015, Available: edu.nl/k6h8e.

[6] KLM, "History of KLM 1919-1929", KLM Royal Dutch Airlines, [Online], Available: edu.nl/bf77p.

[7] ——, "Annual report 2019", KLM Royal Dutch Airlines, [Online], 2019, Available: edu.nl/yn46e.

[8] V. Grewe, A. G. Rao, T. Gronstedt, C. Xisto, F. Linke, J. Melkert, J. Middel, B. Ohlenforst, S. Blakey, S. Christie, S. Matthes, and K. Dahlmann, "Evaluating the climate impact of aviation emission scenarios towards the paris agreement including covid-19 effects", *Nature Communications*, vol. 12, p. 3841, 2021. DOI: 10.1038/s41467-021-24091-y.

[9] Airbus, "Global market forecast 2019-2038", Airbus Commercial Aircraft, [Online], 2019, Available: edu.nl/rcej4.

[10] Boeing, "Commercial market outlook 2020–2039", Commercial Marketing The Boeing Company, [Online], 2021, Available: edu.nl/kp9r3.

[11] IATA, "Annual review", International Air Transport Association, [Online], 2020, Available: edu.nl/vb9gh.

[12] ICAO, "Effects of Novel Coronavirus (COVID-19) on Civil Aviation: Economic Impact Analysis", International Civil Aviation Organization, Air transport Bureau [Online], 2020, Available: edu.nl/kda9n.

[13] D. Lee, D. Fahey, A. Skowron, M. Allen, U. Burkhardt, Q. Chen, S. Doherty, S. Freeman, P. Forster, J. Fuglestvedt, A. Gettelman, R. D. Leon, L. Lim, M. Lund, R. Millar, B. Owen, J. Penner, G. Pitari, M. Prather, R. Sausen, and L. Wilcox, "The contribution of global aviation to anthropogenic climate forcing for 2000 to 2018", *Atmospheric Environment*, vol. 244, p. 117 834, 2021. DOI: 10.1016/j.atmosenv.2020.117834.

[14] ICAO, "Consolidated statement of continuing ICAO policies and practices related to environmental protection - Global Market-based Measure (MBM) scheme", International Civil Aviation Organization, Resolution A39-3 [Online], 2016, Available: edu.nl/h3ngc.

[15] E. Torenbeek, *Advance Aircraft Design: conceptual design, analysis and optimization of subsonic civil airplanes*, ser. Aerospace Series. Sussex, England: John Wiley & Sons, 2013.

[16] R. D. Joslin, "Aircraft laminar flow control", *Annual Review of Fluid Mechanics*, vol. 30, no. 1, pp. 1–29, 1998. DOI: 10.1146/annurev.fluid.30.1.1.

[17] G. Schrauf, "Status and perspectives of laminar flow", *The Aeronautical Journal (1968)*, vol. 109, no. 1102, pp. 639–644, 2005. DOI: 10.1017/S000192400000097X.

[18] D. Arnal and J. P. Archambaud, "Laminar-turbulent transition control: NLF,LFC,HLFC", in *Advances in Laminar-Turbulent Transition Modeling AVT-151 RTO AVT/VKI Lecture Series*, Von Karman Institute, Belgium, 2008.

[19] W. Saric, A. Carpenter, and H. Reed, "Passive control of transition in three-dimensional boundary layers, with emphasis on discrete roughness elements", *Philosophical Transactions of the Royal Society A: Mathematical, Physical and Engineering Sciences*, vol. 369, no. 1940, pp. 1352–1364, 2011. DOI: 10.1098/rsta.2010.0368.

[20] M. I. Goldhammer and B. R. Plendl, "Surface Coatings and Drag Reduction", The Boeing Company, Boeing AERO magazine QTR1-13 [Online], 2013, Available: edu.nl/3erej, pp. 15–20.

[21] Boeing, "Airport Compatibility 737-500 Drawings", The Boeing Company, [Online], Available: edu.nl/66ud3.

[22] J. D. Anderson, *Fundamentals of aerodynamics*, 5th ed. New York: McGraw-Hill, 2011.

[23] J. Bertin and R. Cummings, *Aerodynamics for Engineers*, 5th ed. New Jersey: Pearson Prentice-Hall, 2009.

[24] P. G. Hamel, "Birth of Sweepback: Related Research at Luftfahrtforschungsanstalt-Germany", *Journal of Aircraft*, vol. 42, no. 4, pp. 801–813, 2005. DOI: 10.2514/1.9920.

[25] R. Vos and S. Farokhi, *Introduction to Transonic Aerodynamics*, ser. Fluid Mechanics and Its Applications. Dordrecht: Springer, 2015, vol. 110.

[26] A. Rasheed, H. G. Hornung, A. V. Fedorov, and N. D. Malmuth, "Experiments on Passive Hypervelocity Boundary-Layer Control Using an Ultrasonically Absorptive Surface", *AIAA Journal*, vol. 40, no. 3, pp. 481–489, 2002. DOI: 10.2514/2.1671.

[27] L. Prandtl, "Über flüssigkeits bewegung bei kleiner reibung (english translation NACA-TM-452)", *Verh. III, Int. Math.-Kong., Heidelberg, Teubner, Leipzig*, pp. 484–491, 1904.

[28] J. A. D. Ackroyd, B. P. Axcell, and A. I. Ruban, *Early developments of modern aerodynamics*. Oxford: Elsevier Butterworth-Heinemann, 2001, pp. 77–88.

[29] I. Tani, "History of Boundary Layer Theory", *Annual Review of Fluid Mechanics*, vol. 9, no. 1, pp. 87–111, 1977. DOI: 10.1146/annurev.fl.09.010177.000511.

[30] H. Schlichting and K. Gersten, *Boundary-Layer Theory*, 9th ed. Berlin: Springer-Verlag, 2017.

[31] W. S. Saric, H. L. Reed, and E. J. Kerschen, "Boundary-Layer Receptivity to Freestream Disturbances", *Annual Review of Fluid Mechanics*, vol. 34, no. 1, pp. 291–319, 2002. DOI: 10.1146/annurev.fluid.34.082701.161921.

[32] M. Morkovin, "Transition in open flow systems-a reassessment", *Bull. Am. Phys. Soc.*, vol. 39, p. 1882, 1994.

[33] H. L. Reed and W. S. Saric, "Receptivity: The Inspiration of Mark Morkovin (Invited)", in *45th AIAA Fluid Dynamics Conference*, 2015, AIAA Paper 2015–2471. DOI: https://doi.org/10.2514/6.2015-2471.

[34] H. Bippes, "Basic experiments on transition in three-dimensional boundary layers dominated by crossflow instability", *Progress in Aerospace Sciences*, vol. 35, no. 4, pp. 363–412, 1999. DOI: https://doi.org/10.1016/S0376-0421(99)00002-0.

[35] W. S. Saric, H. L. Reed, and E. B. White, "Stability and transition of three-dimensional boundary layers", *Annual Review of Fluid Mechanics*, vol. 35, no. 1, pp. 413–440, 2003. DOI: 10.1146/annurev.fluid.35.101101.161045.

[36] W. Saric, R. Carrillo Jr, and M. Reibert, "Leading-edge roughness as a transition control mechanism", in *36th AIAA Aerospace Sciences Meeting and Exhibit*, 1998, AIAA Paper 1998–781. DOI: 10.2514/6.1998-781.

[37] H. L. Reed and W. S. Saric, "Stability of three-dimensional boundary layers", *Annual Review of Fluid Mechanics*, vol. 21, no. 1, pp. 235–284, 1989. DOI: 10.1146/annurev.fl.21.010189.001315.

[38] W. Pfenninger, "Flow phenomena at the leading edge of swept wings", AGARD, tech.rep AGARDograph 97 Part IV, 1965.

[39] N. A. Cumpsty and M. R. Head, "The Calculation of the Three-Dimensional Turbulent Boundary Layer: Part III. Comparison of Attachment-Line Calculations with Experiment", *The Aeronautical Quarterly*, vol. 20, no. 2, pp. 99–113, 1969. DOI: 10.1017/s0001925900004923.

[40] D. I. A. Poll, "Some observations of the transition process on the windward face of a long yawed cylinder", *Journal of Fluid Mechanics*, vol. 150, pp. 329–356, 1985. DOI: 10.1017/s0022112085000155.

[41] H. L. Reed and W. S. Saric, "Attachment-line heating in a compressible flow", *Journal of Engineering Mathematics*, vol. 84, no. 1, pp. 99–110, 2014. DOI: 10.1007/s10665-013-9662-5.

[42] M. Fiore, O. Vermeersch, M. Forte, G. Casalis, and C. Francois, "Characterization of a highly efficient chevron-shaped anti-contamination device", *Experiments in Fluids*, vol. 57, no. 4, p. 59, 2016. DOI: 10.1007/s00348-016-2149-1.

[43] M. Gaster, "On the Flow Along Swept Leading Edges", *The Aeronautical Quarterly*, vol. 18, no. 2, pp. 165–184, 1967. DOI: 10.1017/s0001925900004170.

[44] ——, "A Simple Device for Preventing Turbulent Contamination on Swept Leading Edges*", *The Aeronautical Journal*, vol. 69, no. 659, pp. 788–789, 1965. DOI: 10.1017/s0368393100081748.

[45] D. Arnal, "Boundary layer transition: Predictions based on linear theory", in *AGARD, Special Course on Progress in Transition Modelling (See N94-33884 10-34)*, 1993.

[46] H. Liepmann, "Investigation of boundary layer transition in concave walls", NACA, Wartime Rep W-87 or ACR 4J28, 1945.

[47] H. Görtler, "Über eine dreidimensionale Instabilität laminarer Grenzschichten an konkaven Wänden (Translation in NACA TM 1375)", *Ges. D. Wiss. Göttingen, Nachr. ad, Math.*, vol. Bd.2, no. Nr.1, 1940.

[48] I. Tani, "Production of longitudinal vortices in the boundary layer along a concave wall", *Journal of Geophysical Research*, vol. 67, no. 8, pp. 3075–3080, 1962. DOI: 10.1029/jz067i008p03075.

[49] J. Floryan, "On the görtler instability of boundary layers", *Progress in Aerospace Sciences*, vol. 28, no. 3, pp. 235–271, 1991. DOI: 10.1016/0376-0421(91)90006-p.

[50] A. V. Boiko, G. R. Grek, A. V. Dovgal, and V. V. Kozlov, *The Origin of Turbulence in Near-Wall Flows*. Berlin Heidelberg: Springer-Verlag, 2002.

[51] O. Marxen, M. Lang, U. Rist, O. Levin, and D. Henningson, "Mechanisms for spatial steady three-dimensional disturbance growth in a non-parallel and separating boundary layer", *Journal of Fluid Mechanics*, vol. 634, p. 165, 2009. DOI: 10.1017/S0022112009007149.

[52] W. Saric, "Görtler Vortices", *Annual Review of Fluid Mechanics*, vol. 26, no. 1, pp. 379–409, 1994. DOI: 10.1146/annurev.fl.26.010194.002115.

[53] J. D. Swearingen and R. F. Blackwelder, "The growth and breakdown of streamwise vortices in the presence of a wall", *Journal of Fluid Mechanics*, vol. 182, no. -1, pp. 255–290, 1987. DOI: 10.1017/s0022112087002337.

[54] F. Li and M. R. Malik, "Fundamental and subharmonic secondary instabilities of Görtler vortices", *Journal of Fluid Mechanics*, vol. 297, pp. 77–100, 1995. DOI: 10.1017/s0022112095003016.

[55] L.-U. Schrader, L. Brandt, and T. A. Zaki, "Receptivity, instability and breakdown of Görtler flow", *Journal of Fluid Mechanics*, vol. 682, pp. 362–396, 2011. DOI: 10.1017/jfm.2011.229.

[56] T. Tandiono, S. H. Winoto, and D. A. Shah, "On the linear and nonlinear development of Görtler vortices", *Physics of Fluids*, vol. 20, no. 9, p. 094 103, 2008. DOI: 10.1063/1.2980349.

[57] W. S. Saric, "Visualization of Different Transition Mechanisms", *Physics of Fluids*, vol. 29, no. 9, pp. 2770–2770, 1986. DOI: 10.1063/1.4738801.

[58] W. Tollmien, "Über die Entstehung der Turbulenz. 1. Mitteilung (Translation NACA TM 609)", *Nachrichten von der Gesellschaft der Wissenschaften zu Göttingen, Mathematisch-Physikalische Klasse*, pp. 21–44, 1929. [Online]. Available: http://eudml.org/doc/59276.

[59] H. Schlichting, "Zur Enstehung der Turbulenz bei der Plattenströmung", *Nachrichten von der Gesellschaft der Wissenschaften zu Göttingen, Mathematisch-Physikalische Klasse*, vol. 1933, pp. 181–208, 1933. [Online]. Available: http://eudml.org/doc/59420.

[60] T. Herbert, "Secondary Instability of Boundary Layers", *Annual Review of Fluid Mechanics*, vol. 20, no. 1, pp. 487–526, 1988. DOI: 10.1146/annurev.fl.20.010188.002415.

[61] Y. Kachanov, "Physical Mechanisms of Laminar-Boundary-Layer Transition", *Annual Review of Fluid Mechanics*, vol. 26, no. 1, pp. 411–482, 1994. DOI: 10.1146/annurev.fl.26.010194.002211.

[62] G. B. Schubauer and H. K. Skramstad, "Laminar boundary-layer oscillations and transition on a flat plate", *Journal of Research of the National Bureau of Standards*, vol. 38, no. 2, p. 251, 1947, (See also NACA TM 909). DOI: 10.6028/jres.038.013.

[63] J. A. Ross, F. H. Barnes, J. G. Burns, and M. A. S. Ross, "The flat plate boundary layer. Part 3. Comparison of theory with experiment", *Journal of Fluid Mechanics*, vol. 43, no. 4, pp. 819–832, 1970. DOI: 10.1017/s002211207000277x.

[64] P. J. Schmid and D. S. Henningson, *Stability and Transition in Shear Flows*, ser. Applied Mathematical Sciences, Volume 142. New York: Springer-Verlag, 2001.

[65] P. S. Klebanoff, K. D. Tidstrom, and L. M. Sargent, "The three-dimensional nature of boundary-layer instability", *Journal of Fluid Mechanics*, vol. 12, no. 1, pp. 1–34, 1962. DOI: 10.1017/s0022112062000014.

[66] P. Wassermann and M. Kloker, "Transition mechanisms in a three-dimensional boundary-layer flow with pressure-gradient changeover", *Journal of Fluid Mechanics*, vol. 530, pp. 265–293, 2005. DOI: 10.1017/s0022112005003708.

[67] W. Gray, "The effect of wing sweep on laminar flow", *Royal Aircraft Establishment (RM TM Aero)*, vol. 255, 1952.

[68] A. Anscombe and N. L. Illingsworth, "Wind-tunnel observations of boundary layer transition on a wing at various angles of sweep back", *Aeronautical Research Council (ARC RM 2968)*, 1952. [Online]. Available: https://reports.aerade.cranfield.ac.uk/handle/1826.2/3531.

[69] Y. Kachanov, "Experimental studies of three-dimensional instability of boundary layers", in *AIAA Fluid Dynamics Conference*, 1996, AIAA Paper 1996–1978. DOI: 10.2514/6.1996-1978.

[70] D. Arnal and G. Casalis, "Laminar-turbulent transition prediction in three-dimensional flows", *Progress in Aerospace Sciences*, vol. 36, no. 2, pp. 173–191, 2000. DOI: 10.1016/S0376-0421(00)00002-6.

[71] J. Serpieri and M. Kotsonis, "Three-dimensional organisation of primary and secondary crossflow instability", *Journal of Fluid Mechanics*, vol. 799, pp. 200–245, 2016. DOI: 10.1017/jfm.2016.379.

[72] J. Dagenhart, J. Stack, W. Saric, and M. Mousseux, "Crossflow-vortex instability and transition on a 45 deg swept wing", in *20th Fluid Dynamics, Plasma Dynamics and Lasers Conference*. 1989, AIAA Paper 1989–1892. DOI: 10.2514/6.1989-1892.

[73] R. S. Downs and E. B. White, "Free-stream turbulence and the development of cross-flow disturbances", *Journal of Fluid Mechanics*, vol. 735, pp. 347–380, 2013. DOI: 10.1017/jfm.2013.484.

[74] W. Saric and H. Reed, "Crossflow Instabilities - Theory & Technology", *AIAA 41st Aerospace Sciences Meeting and Exhibit*, 2003, AIAA Paper 2003-771. DOI: 10.2514/6.2003-771.

[75] J. Serpieri, "Cross-flow instability flow diagnostics and control of swept wing boundary layers.", Ph.D. dissertation, Delft University of Technology, Mar. 2018. DOI: 10.4233/uuid:3dac1e78-fcc3-437f-9579-048b74439f55.

[76] A. F. Rius-Vidales and M. Kotsonis, "Unsteady interaction of crossflow instability with a forward-facing step", *Journal of Fluid Mechanics*, vol. 939, A19, 2022. DOI: 10.1017/jfm.2022.151.

[77] H. Deyhle and H. Bippes, "Disturbance growth in an unstable three-dimensional boundary layer and its dependence on environmental conditions", *Journal of Fluid Mechanics*, vol. 316, pp. 73–113, 1996. DOI: 10.1017/S0022112096000456.

[78] Y. Kachanov, "Three-dimensional receptivity of boundary layers", *European Journal of Mechanics - B/Fluids*, vol. 19, no. 5, pp. 723–744, 2000. DOI: 10.1016/s0997-7546(00)90102-x.

[79] V. R. Gaponenko, A. V. Ivanov, Y. S. Kachanov, and J. D. Crouch, "Swept-wing boundary-layer receptivity to surface non-uniformities", *Journal of Fluid Mechanics*, vol. 461, pp. 93–126, 2002. DOI: 10.1017/s0022112002008297.

[80] L.-U. Schrader, L. Brandt, and D. S. Henningson, "Receptivity mechanisms in three-dimensional boundary-layer flows", *Journal of Fluid Mechanics*, vol. 618, pp. 209–241, 2009. DOI: 10.1017/s0022112008004345.

[81] D. Tempelmann, L.-U. Schrader, A. Hanifi, L. Brandt, and D. S. Henningson, "Swept wing boundary-layer receptivity to localized surface roughness", *Journal of Fluid Mechanics*, vol. 711, pp. 516–544, 2012. DOI: 10.1017/jfm.2012.405.

[82] H. B. E. Kurz and M. J. Kloker, "Receptivity of a swept-wing boundary layer to micron-sized discrete roughness elements", *Journal of Fluid Mechanics*, vol. 755, pp. 62–82, 2014. DOI: 10.1017/jfm.2014.425.

[83] E. White, W. Saric, R. Gladden, and P. Gabet, "Stages of swept-wing transition", in *AIAA 39th Aerospace Sciences Meeting and Exhibit*, 2001, AIAA Paper 2001–271. DOI: 10.2514/6.2001-271.

[84] H. Riedel and M. Sitzmann, "In-flight investigations of atmospheric turbulence", *Aerospace Science and Technology*, vol. 2, no. 5, pp. 301–319, 1998. DOI: 10.1016/S1270-9638(98)80007-2.

[85] B. Müller and H. Bippes, "Experimental study of instability modes in a three-dimensional boundary layer.", in *Proc. AGARD Symp On Fluid Dynamics of Three-Dimensional Turbulent Sheer Flows and Transition*, Cesme, Turkey, 1988, AGARD CP 438, Paper No. 13.

[86] M. Reibert, W. Saric, J. Ruben Carrillo, and K. Chapman, "Experiments in nonlinear saturation of stationary crossflow vortices in a swept-wing boundary layer", in *34th AIAA Aerospace Sciences Meeting and Exhibit*, AIAA Paper 1996-184, 1996. DOI: https://doi.org/10.2514/6.1996-184.

[87] T. Lerche, "Advances in Turbulence VI, Proceedings of the Sixth European Turbulence Conference, held in Lausanne, Switzerland, 2-5 July 1996", *Fluid Mechanics and its Applications*, pp. 357–360, 1996. DOI: 10.1007/978-94-009-0297-8_101.

[88] M. Kawakami, Y. Kohama, and M. Okutsu, "Stability characteristics of stationary crossflow vortices in three-dimensional boundary layer", in *37th AIAA Aerospace Sciences Meeting and Exhibit*, 1999, AIAA Paper A99–16 660. DOI: 10.2514/6.1999-811.

[89] E. B. White and W. S. Saric, "Secondary instability of crossflow vortices", *Journal of Fluid Mechanics*, vol. 525, pp. 275–308, 2005. DOI: 10.1017/S002211200400268X.

[90] J. Serpieri and M. Kotsonis, "Conditioning of unsteady cross-flow instability modes using dielectric barrier discharge plasma actuators", *Experimental Thermal and Fluid Science*, vol. 93, pp. 305–318, 2018. DOI: 10.1016/j.expthermflusci.2018.01.007.

[91] M. Högberg and D. Henningson, "Secondary instability of cross-flow vortices in falkner–skan–cooke boundary layers", *Journal of Fluid Mechanics*, vol. 368, pp. 339–357, 1998. DOI: 10.1017/S0022112098001931.

[92] M. R. Malik, F. Li, and C.-L. Chang, "Crossflow disturbances in three-dimensional boundary layers: Nonlinear development, wave interaction and secondary instability", *Journal of Fluid Mechanics*, vol. 268, pp. 1–36, 1994. DOI: 10.1017/S0022112094001242.

[93] M. R. Malik, F. Li, M. M. Choudhari, and C.-L. Chang, "Secondary instability of crossflow vortices and swept-wing boundary-layer transition", *Journal of Fluid Mechanics*, vol. 399, pp. 85–115, Nov. 1999. DOI: 10.1017/S0022112099006291.

[94] P. Wassermann and M. Kloker, "Mechanisms and passive control of crossflow-vortex-induced transition in a three-dimensional boundary layer", *Journal of Fluid Mechanics*, vol. 456, pp. 49–84, 2002. DOI: https://doi.org/10.1017/S0022112001007418.

[95] G. Bonfigli and M. Kloker, "Secondary instability of crossflow vortices: Validation of the stability theory by direct numerical simulation", *Journal of Fluid Mechanics*, vol. 583, pp. 229–272, 2007. DOI: 10.1017/S0022112007006179.

[96] S. M. Hosseini, D. Tempelmann, A. Hanifi, and D. S. Henningson, "Stabilization of a swept-wing boundary layer by distributed roughness elements", *Journal of Fluid Mechanics*, vol. 718, pp. 1469–7645, 2013. DOI: 10.1017/jfm.2013.33.

[97] K. J. Groot, J. Serpieri, F. Pinna, and M. Kotsonis, "Secondary crossflow instability through global analysis of measured base flows", *Journal of Fluid Mechanics*, vol. 846, pp. 605–653, 2018. DOI: 10.1017/jfm.2018.253.

[98] M. R. Malik, F. Li, and C. Chang, "Nonlinear crossflow disturbances and secondary instabilities in swept-wing boundary layers", in *IUTAM Symposium on Nonlinear Instability and Transition in Three-Dimensional Boundary Layers (ed. P. W. Duck & P. Hall)*, 1996, pp. 257–266. DOI: 10.1007/978-94-009-1700-2_25.

[99] P. Wassermann and M. Kloker, "Transition mechanisms induced by travelling crossflow vortices in a three-dimensional boundary layer", *Journal of Fluid Mechanics*, vol. 483, pp. 67–89, 2003. DOI: 10.1017/S0022112003003884.

[100] R. Messing and M. J. Kloker, "Investigation of suction for laminar flow control of three-dimensional boundary layers", *Journal of Fluid Mechanics*, vol. 658, pp. 117–147, 2010. DOI: 10.1017/S0022112010001576.

[101] J. Serpieri, S. Yadala Venkata, and M. Kotsonis, "Conditioning of cross-flow instability modes using dielectric barrier discharge plasma actuators", *Journal of Fluid Mechanics*, vol. 833, pp. 164–205, 2017. DOI: 10.1017/jfm.2017.707.

[102] W. S. Saric, D. E. West, M. W. Tufts, and H. L. Reed, "Experiments on discrete roughness element technology for swept-wing laminar flow control", *AIAA Journal*, vol. 57, no. 2, pp. 641–654, 2019. DOI: 10.2514/1.J056897.

[103] E. White and W. Saric, "Application of variable leading-edge roughness for transition control on swept wings", in *38th Aerospace Sciences Meeting and Exhibit*. 2000, AIAA Paper 2000–283. DOI: 10.2514/6.2000-283.

[104] J. Lohse, H. P. Barth, and W. Nitsche, "Active control of crossflow-induced transition by means of in-line pneumatic actuator orifices", *Experiments in Fluids*, vol. 57, no. 8, p. 124, 2016. DOI: 10.1007/s00348-016-2213-x.

[105] P. C. Dörr and M. J. Kloker, "Crossflow transition control by upstream flow deformation using plasma actuators", *Journal of Applied Physics*, vol. 121, no. 6, p. 063 303, 2017. DOI: 10.1063/1.4975791.

[106] Z. Guo and M. J. Kloker, "Control of crossflow-vortex-induced transition by unsteady control vortices", *Journal of Fluid Mechanics*, vol. 871, pp. 427–449, 2019. DOI: 10.1017/jfm.2019.288.

[107] P. C. Dörr and M. J. Kloker, "Stabilisation of a three-dimensional boundary layer by base-flow manipulation using plasma actuators", *Journal of Physics D: Applied Physics*, vol. 48, no. 28, p. 285 205, Jun. 2015. DOI: 10.1088/0022-3727/48/28/285205.

[108] S. Yadala, M. T. Hehner, J. Serpieri, N. Benard, P. C. Dörr, M. J. Kloker, and M. Kotsonis, "Experimental control of swept-wing transition through base-flow modification by plasma actuators", *Journal of Fluid Mechanics*, vol. 844, 2018. DOI: 10.1017/jfm.2018.268.

[109] H. Gerhardt, "Section 10: Waviness and Surface Smoothness Criteria", in *Final Report on LFC Aircraft Design Data Laminar Flow Control Demonstration Program*, NORAIR report no NOR-67-136, 1967.

[110] B. Holmes, C. J. Obara, G. L. Martin, and C. S. Domack, "Manufacturing tolerances for natural laminar flow airframe surfaces", SAE Technical Paper 850863, 1985. DOI: 10.4271/850863.

[111] F. A. Zuniga, A. Drake, R. Kenelly Jr, D. Koga, and R. V. Westphal, "Transonic flight test of a laminar flow leading edge with surface excrescences", in *Biennial Flight Test Conference*, 1994, AIAA Paper 1994–2142. DOI: 10.2514/6.1994-2142.

[112] A. Drake, R. V. Westphal, F. A. Zuniga, R. A. Kennelly Jr, and D. J. Koga, "Wing leading edge joint laminar flow test", NASA, Technical Memorandum 4762, 1996.

[113] A. Drake, A. M. Bender, and R. V. Westphal, "Transition due to surface steps in the presence of favorable pressure gradients", in *26th AIAA Applied Aerodynamics Conference*, 2008, AIAA Paper 2008–7334. DOI: 10.2514/6.2008-7334.

[114] A. Drake, A. Bender, A. Korntheuer, R. Westphal, W. Rohe, G. Dale, B. McKeon, and S. Geraschchenko, "Step excrescence effects for manufacturing tolerances on laminar flow wings", in *48th AIAA Aerospace Sciences Meeting Including the New Horizons Forum and Aerospace Exposition*, 2010, AIAA Paper 2010–375. DOI: 10.2514/6.2010-375.

[115] Y. Wang and M. Gaster, "Effect of surface steps on boundary layer transition", *Experiments in Fluids*, vol. 39, no. 4, pp. 679–686, 2005. DOI: 10.1007/s00348-005-1011-7.

[116] M. Costantini, S. Risius, and C. Klein, "Experimental investigation of the effect of forward-facing steps on boundary layer transition", in *Procedia IUTAM Symposium on Laminar-Turbulent Transition (ed. M.A.F. Medeiros & J.R.Meneghini)*, Elsevier, vol. 14, 2015, pp. 152–162. DOI: 10.1016/j.piutam.2015.03.036.

[117] ——, "Non-adiabatic surface effects on step-induced boundary-layer transition", *Flow, Turbulence and Combustion*, vol. 100, no. 4, pp. 1145–1177, 2018. DOI: 10.1007/s10494-018-9913-7.

[118] J. Perraud and A. Seraudie, "Effects of steps and gaps on 2d and 3d transition", in *European Congress on Comp. Methods in Applied Science and Eng., ECCOMAS*, 2000.

[119] J. Perraud, D. Arnal, and W. Kuehn, "Laminar-turbulent transition prediction in the presence of surface imperfections", *International Journal of Engineering Systems Modelling and Simulation 48*, vol. 6, no. 3-4, pp. 162–170, 2014. DOI: 10.1504/IJESMS.2014.063129.

[120] S. Beguet, J. Perraud, M. Forte, and J.-P. Brazier, "Modeling of transverse gaps effects on boundary-layer transition", *AIAA Journal of Aircraft*, vol. 54, no. 2, pp. 794–801, 2017. DOI: 10.2514/1.C033647.

[121] J. Crouch, V. Kosorygin, and L. Ng, "Modeling the effects of steps on boundary-layer transition", in *IUTAM Symposium on Laminar-Turbulent Transition (ed. R.Govindarajan)*, Springer, vol. 78, 2006, pp. 37–44. DOI: 10.1007/1-4020-4159-4_4.

[122] J. D. Crouch and V. S. Kosorygin, "Surface step effects on boundary-layer transition dominated by tollmien–schlichting instability", *AIAA Journal*, vol. 58, no. 7, pp. 2943–2950, 2020. DOI: 10.2514/1.J058518.

[123] J. D. Crouch, V. S. Kosorygin, and M. I. Sutanto, "Modeling gap effects on transition dominated by tollmien-schlichting instability", in *AIAA Aviation 2020 forum*, 2020, AIAA Paper 2020–3075. DOI: 10.2514/6.2020-3075.

[124] C. A. Edelmann and U. Rist, "Impact of forward-facing steps on laminar-turbulent transition in transonic flows", *AIAA Journal*, vol. 53, no. 9, pp. 2504–2511, 2015. DOI: 10.2514/1.J053529.

[125] J. Zahn and U. Rist, "Impact of deep gaps on laminar–turbulent transition in compressible boundary-layer flow", *AIAA Journal*, vol. 54, no. 1, pp. 66–76, 2016. DOI: 10.2514/1.J054112.

[126] D. P. Rizzetta and M. R. Visbal, "Numerical simulation of excrescence generated transition", *AIAA Journal*, vol. 52, no. 2, pp. 385–397, 2014. DOI: 10.2514/1.J052530.

[127] G. T. Duncan, B. K. Crawford, M. W. Tufts, W. S. Saric, and H. L. Reed, "Effects of step excrescences on a swept wing in a low-disturbance wind tunnel", in *52nd Aerospace Sciences Meeting*, 2014, AIAA Paper 2014–0910. DOI: 10.2514/6.2014-0910.

[128] J. L. Eppink, R. W. Wlezien, R. A. King, and M. Choudhari, "Interaction of a backward-facing step and crossflow instabilities in boundary-layer transition", *AIAA Journal*, vol. 56, no. 2, pp. 497–509, 2018. DOI: 10.2514/1.J056267.

[129] M. W. Tufts, H. L. Reed, B. K. Crawford, G. T. Duncan, and W. S. Saric, "Computational investigation of step excrescence sensitivity in a swept-wing boundary layer", *AIAA Journal of Aircraft*, vol. 54, no. 2, pp. 602–626, 2017. DOI: 10.2514/1.C033892.

[130] J. L. Eppink, "Mechanisms of stationary cross-flow instability growth and breakdown induced by forward-facing steps", *Journal of Fluid Mechanics*, vol. 897, A15, 2020. DOI: 10.1017/jfm.2020.367.

[131] E. E. Cooke, M. S. Mughal, S. Sherwin, R. Ashworth, and S. Rolston, "Destabilisation of stationary and travelling crossflow disturbances due to steps over a swept wing", in *AIAA Aviation 2019 Forum*, 2019, AIAA Paper 2019–3533. DOI: 10.2514/6.2019-3533.

[132] T. I. Saeed, M. S. Mughal, and J. Morrison, "The interaction of a swept-wing boundary layer with surface excrescences", in *54th AIAA Aerospace Sciences Meeting*, 2016, AIAA Paper 2016–2065. DOI: 10.2514/6.2016-2065.

[133] G. T. Duncan, B. K. Crawford, M. W. Tufts, W. S. Saric, and H. L. Reed, "Flight experiments on the effects of step excrescences on swept-wing transition", *International Journal of Engineering Systems Modelling and Simulation*, vol. 6, no. 3-4, pp. 171–180, 2014. DOI: 10.1504/IJESMS.2014.063127.

[134] B. K. Crawford, G. T. Duncan, M. W. Tufts, W. S. Saric, and H. L. Reed, "Effects of step-excrescence location on swept-wing transition", in *53rd AIAA Aerospace Sciences Meeting*, 2015, AIAA Paper 2015–1233. DOI: 10.2514/6.2015-1233.

[135] J. L. Eppink and C. Casper, "Effects of forward-facing step shape on stationary crossflow instability growth and breakdown", in *AIAA Aviation 2019 Forum*, 2019, AIAA Paper 2019–3532. DOI: 10.2514/6.2019-3532.

[136] J. L. Eppink, "The effect of forward-facing steps on stationary crossflow instability growth and breakdown", in *2018 AIAA Aerospace Sciences Meeting*, 2018, AIAA Paper 2018–0817. DOI: 10.2514/6.2018-0817.

[137] ——, "High-frequency secondary instabilities downstream of a forward-facing step", in *AIAA Scitech 2020 Forum*, 2020, AIAA Paper 2020–2243. DOI: 10.2514/6.2020-2243.

[138] K. J. Groot and J. L. Eppink, "Stability analysis of the flow over a swept forward-facing step using piv base flows in a nonorthogonal coordinate system", in *AIAA Aviation 2021 Forum*, 2021, AIAA Paper 2021–2908. DOI: 10.2514/6.2021-2908.

[139] J. Casacuberta, S. Hickel, and M. Kotsonis, "Mechanisms of interaction between stationary crossflow instabilities and forward-facing steps", in *AIAA Scitech 2021 Forum*, 2021, AIAA Paper 2021–0854. DOI: 10.2514/6.2021-0854.

[140] A. F. Rius-Vidales and M. Kotsonis, "Impact of a forward-facing step on the development of crossflow instability", *Journal of Fluid Mechanics*, vol. 924, A34, 2021. DOI: 10.1017/jfm.2021.497.

[141] A. V. Ivanov and D. A. Mischenko, "Delay of laminar-turbulent transition on swept-wing with help of sweeping surface relief", *AIP Conference Proceedings*, vol. 2125, no. 1, p. 030 041, 2019. DOI: 10.1063/1.5117423.

[142] M. Ustinov and A. Ivanov, "Cross-flow dominated transition control by surface micro-relief", *AIP Conference Proceedings*, vol. 2027, no. 1, p. 020 013, 2018. DOI: 10.1063/1.5065091.

[143] E. Dobbinga and J. A. Van Ghesel Grothe, "De lage snelheids windtunnel van de sub-afdeling vliegtuigbouwkunde der technische hogeschool", *De Ingenieur, Algemeen gedeelte, No. 38*, A461–A476, 1955.

[144] J. Serpieri and M. Kotsonis, "Design of a swept wing wind tunnel model for study of crossflow instability", in *33rd AIAA Applied Aerodynamics Conference*, 2015, AIAA Paper 2015–2576. DOI: 10.2514/6.2015-2576.

[145] G. Zoppini, S. Westerbeek, D. Ragni, and M. Kotsonis, "Receptivity of crossflow instability to discrete roughness amplitude and location", *Journal of Fluid Mechanics*, vol. 939, A33, 2022. DOI: 10.1017/jfm.2022.220.

[146] T. Astarita and G. M. Carlomagno, *Infrared Thermography for Thermo-Fluid-Dynamics*, D. Rockwell, C. Tropea, and W. Merzkirch, Eds., ser. Experimental Fluid Mechanics. Berlin Heidelberg: Springer-Verlag, 2013, vol. 11.

[147] C. C. Wolf, A. D. Gardner, and M. Raffel, "Infrared thermography for boundary layer transition measurements", *Measurement Science and Technology*, vol. 31, no. 11, p. 112 002, 2020. DOI: 10.1088/1361-6501/aba070.

[148] S. Zuccher and W. S. Saric, "Infrared thermography investigations in transitional supersonic boundary layers", *Experiments in Fluids*, vol. 44, no. 1, pp. 145–157, 2008. DOI: 10.1007/s00348-007-0384-1.

[149] B. K. Crawford, G. T. Duncan, and W. S. West D. E.and Saric, "Robust, automated processing of ir thermography for quantitative boundary-layer transition measurements", *Experiments in Fluids*, vol. 56, no. 7, p. 149, Jul. 2015. DOI: 10.1007/s00348-015-2011-x.

[150] A. Boiko, A. Ivanov, V. Borodulin, and D. Mischenko, "Quantification technique of transition to turbulence in boundary layers using infrared thermography", *International Journal of Heat and Mass Transfer*, vol. 183, p. 122 065, 2022. DOI: 10.1016/j.ijheatmasstransfer.2021.122065.

[151] J. L. Eppink and R. Wlezien, "Data analysis for the nasa/boeing hybrid laminar flow control crossflow experiment", in *41st AIAA Fluid Dynamics Conference and Exhibit*, 2011, AIAA Paper 2011–3879. DOI: 10.2514/6.2011-3879.

[152] J. Lemarechal, M. Costantini, C. Klein, M. Kloker, W. Würz, H. Kurz, T. Streit, and S. Schaber, "Investigation of stationary-crossflow-instability induced transition with the temperature-sensitive paint method", *Experimental Thermal and Fluid Science*, vol. 109, p. 109 848, 2019. DOI: 10.1016/j.expthermflusci.2019.109848.

[153] R. C. Gonzalez and R. E. Woods, *Digital Image Processing*, 4th ed. Essex, England: Pearson Education Limited, 2018.

[154] M. Raffel and C. Merz, "Differential infrared thermography for unsteady boundary-layer transition measurements", *AIAA Journal*, vol. 52, no. 9, pp. 2090–2093, 2014. DOI: 10.2514/1.J053235.

[155] M. Raffel, C. B. Merz, T. Schwermer, and K. Richter, "Differential infrared thermography for boundary layer transition detection on pitching rotor blade models", *Experiments in Fluids*, vol. 56, no. 2, p. 30, 2015. DOI: {10.1007/s00348-015-1905-y}.

[156] N. Otsu, "A threshold selection method from gray-level histograms", *IEEE Transactions on Systems, Man, and Cybernetics*, vol. 9, no. 1, pp. 62–66, 1979. DOI: 10.1109/TSMC.1979.4310076.

[157] C. G. Lomas, *Fundamentals of Hot Wire Anemometry*. New York, USA: Cambridge University Press, 1986.

[158] H. Bruun, *Hot-Wire Anemometry: Principles and Signal Analysis*. New York, USA: Oxford University Press, 1995.

[159] M. Hultmark and A. Smits, "Temperature corrections for constant temperature and constant current hot-wire anemometers", *Measurement Science and Technology*, vol. 21, no. 10, p. 105 404, 2010. DOI: 10.1088/0957-0233/21/10/105404.

[160] F. Jørgensen, "Directional Sensitivity of wire and fibre-film probes.", *DISA Info*, vol. 11, pp. 31–37, 1971.

[161] W. S. Saric, "Boundary-layer stability and transition", in *Springer Handbook of Experimental Fluid Mechanics*, C. Tropea, A. Yarin, and J. F. Foss, Eds. Springer, 2007, ch. 12.3, pp. 886–896.

[162] R. Adrian and J. Westerweel, *Particle Image Velocimetry*. New York, USA: Cambridge University Press, 2011.

[163] M. Raffel, C. E. Willert, F. Scarano, C. J. Kähler, S. T. Wereley, and J. Kompenhans, *Particle Image Velocimetry, A Practical Guide*, 3rd ed. Cham, Switzerland: Springer International Publishing, 2018.

[164] H. Coleman and W. Steele, *Experimentation and Uncertainty Analysis for Engineers*, 4th ed. Hoboken, USA: John Wiley and Sons, 2018.

[165] A. Sciacchitano, "Uncertainty quantification in particle image velocimetry", *Measurement Science and Technology*, vol. 30, no. 9, p. 092 001, 2019. DOI: 10.1088/1361-6501/ab1db8.

[166] A. Sciacchitano and B. Wieneke, "PIV uncertainty propagation", *Measurement Science and Technology*, vol. 27, no. 8, p. 084 006, 2016. DOI: 10.1088/0957-0233/27/8/084006.

[167] B. L. Smith, D. R. Neal, M. A. Feero, and G. Richards, "Assessing the limitations of effective number of samples for finding the uncertainty of the mean of correlated data", *Measurement Science and Technology*, vol. 29, no. 12, p. 125 304, 2018. DOI: 10.1088/1361-6501/aae91d.

[168] H. Tennekes and J. L. Lumley, *A First Course in Turbulence*. The MIT Press, 1972. DOI: 10.7551/mitpress/3014.001.0001.

[169] S. Yadala, M. T. Hehner, J. Serpieri, N. Benard, and M. Kotsonis, "Plasma-based forcing strategies for control of crossflow instabilities", *AIAA Journal*, vol. 59, no. 9, pp. 3406–3416, 2021. DOI: 10.2514/1.J060101.

[170] F. M. White and J. Majdalani, *Viscous Fluid Flow*, 4th ed. New York, USA: McGraw Hill, 2021.

[171] L. Mack, "Boundary layer linear stability theory", in *Special Course on Stability and Transition of Laminar Flows*, 1984, AGARD–R-709.

[172] K. Groot, "Biglobal stability of shear flows: Spanwise & streamwise analyses", Ph.D. dissertation, Delft University of Technology, Dec. 2018. DOI: 10.4233/uuid:60ef07b2-00db-418b-9495-5a9baf6105df.

[173] J. A. Weideman and S. C. Reddy, "A MATLAB differentiation matrix suite", *ACM Transactions on Mathematical Software (TOMS)*, vol. 26, no. 4, pp. 465–519, 2000. DOI: 10.1145/365723.365727.

[174] W. Criminale, T. Jackson, and R. Joslin, *Theory and Computation of Hydrodynamic Stability*, 2nd ed., ser. Cambridge Monographs on Mechanics. Cambridge: Cambridge University Press, 2019.

[175] H. L. Reed, W. S. Saric, and D. Arnal, "Linear Stability Theory Applied to Boundary Layers", *Annual Review of Fluid Mechanics*, vol. 28, no. 1, pp. 389–428, 1996. DOI: 10.1146/annurev.fl.28.010196.002133.

[176] T. S. Haynes and H. L. Reed, "Simulation of swept-wing vortices using nonlinear parabolized stability equations", *Journal of Fluid Mechanics*, vol. 405, pp. 325–349, 2000. DOI: 10.1017/S0022112099007260.

[177] W. Saric, "Introduction to Linear Stability", in *Advances in Laminar-Turbulent Transition Modeling*, AVT-151 RTO AVT/VKI, Lecture Series, VKI Inst, Belgium, 2008.

[178] G. Danabasoglu and S. Biringen, "A Chebyshev matrix method for the spatial modes of the Orr-Sommerfeld equation", *International Journal for Numerical Methods in Fluids*, vol. 11, no. 7, pp. 1033–1037, 1990. DOI: 10.1002/fld.1650110709.

[179] A. F. Rius-Vidales, M. Kotsonis, A. P. Antunes, and R. Cosin, "Effect of two-dimensional surface irregularities on swept wing transition: Forward facing steps", in *2018 Fluid Dynamics Conference*, 2018, AIAA Paper 2018–3075. DOI: 10.2514/6.2018-3075.

[180] G. T. Duncan, "The effects of step excrescences on swept-wing boundary-layer transition", Ph.D. dissertation, Texas A and M Univ., College Station, TX, Aug. 2014. DOI: 1969.1/153665.

[181] A. F. Rius-Vidales and M. Kotsonis, "Influence of a forward facing step surface irregularity on swept wing transition", *AIAA Journal*, vol. 58, no. 12, pp. 5243–5253, 2020. DOI: 10.2514/1.J059566.

[182] J. L. Eppink, "Stereo particle image velocimetry measurements of transition downstream of a foward-facing step in a swept-wing boundary layer", in *55th AIAA Aerospace Sciences Meeting*, 2017, AIAA Paper 2017–0306. DOI: 10.2514/6.2017-0306.

[183] M. Landahl, "A note on an algebraic instability of inviscid parallel shear flows", *Journal of Fluid Mechanics*, vol. 98, no. 2, pp. 243–251, 1980. DOI: 10.1017/S0022112080000122.

[184] L. Brandt, "The lift-up effect: The linear mechanism behind transition and turbulence in shear flows", *European Journal of Mechanics-B/Fluids*, vol. 47, pp. 80–96, 2014. DOI: 10.1016/j.euromechflu.2014.03.005.

[185] P. Welch, "The use of fast fourier transform for the estimation of power spectra: A method based on time averaging over short, modified periodograms", *IEEE Transactions on audio and electroacoustics*, vol. 15, no. 2, pp. 70–73, 1967.

[186] F. Li, M. Choudhari, and L. Dua, "Stationary crossflow breakdown due to interaction between secondary instabilities", in *47th AIAA Fluid Dynamics Conference*, 2017, AIAA Paper 2017–4302. DOI: 10.2514/6.2017-4302.

[187] R. Merino-Martinez, A. R. Carpio, L. T. L. Pereira, S. v. Herk, F. Avallone, D. Ragni, and M. Kotsonis, "Aeroacoustic design and characterization of the 3D-printed, open-jet, anechoic wind tunnel of Delft University of Technology", *Applied Acoustics*, vol. 170, p. 107 504, 2020. DOI: 10.1016/j.apacoust.2020.107504.

[188] L.-U. Schrader, L. Brandt, C. Mavriplis, and D. S. Henningson, "Receptivity to free-stream vorticity of flow past a flat plate with elliptic leading edge", *Journal of Fluid Mechanics*, vol. 653, pp. 245–271, 2010. DOI: 10.1017/s0022112010000376.

[189] N. Rajendakumar, "An experimental investigation of interaction of crossflow instability with forward facing steps", MSc Dissertation Delft University of Technology, Sep. 2021.

[190] Boeing Commercial Airplane Group, "High reynolds number hybrid laminar flow control (HLFC) flight experiment II. aerodynamic design", NASA, NASA/CR-1999-209324, 1999.

[191] ——, "High reynolds number hybrid laminar flow control (HLFC) flight experiment III. leading edge design, fabrication, and installation", NASA, NASA/CR-1999-209325, 1999.

[192] P. G. Parikh, H. J. Koppelman, T. M. Harris, and F. M. Swanstrom, "Skin panel joint for improved airflow", Unites Stated Patent 8,282,042 B2, Oct. 2012.

[193] A. Kundu, J. Watterson, S. Raghunathan, and R. MacFadden, "Parametric optimization of manufacturing tolerances at the aircraft surface", *Journal of aircraft*, vol. 39, no. 2, pp. 271–279, 2002. DOI: 10.2514/2.2924.

A

Appendix: 66018M3J geometry

A

As described in §2.1.2, the M3J swept wing model used throughout this dissertation features the 66018M3J airfoil, a modified version of a NACA-66018. The main difference between the airfoils is the location of the maximum thickness, as shown in figure.A.1. A complete overview of the selection and the design of the airfoil and the M3J swept wing model is provided by Serpieri [75, Chapter.3]. For completeness, the non-dimensional (i.e. using c_x) coordinates of the 66018M3J airfoil geometry are presented in Table.A.1

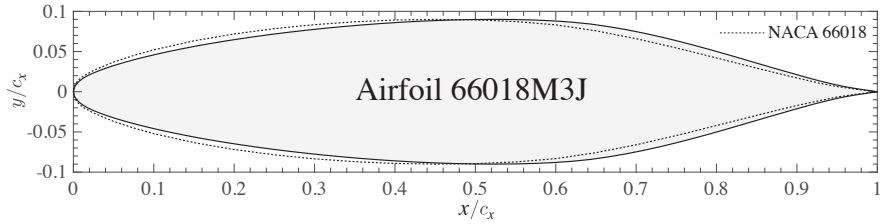

Figure A.1: Comparison of the shape of the 66018M3J and NACA-66018 airfoils. The coordinates are non-dimensionalized with the chord orthogonal to the leading edge c_x = 900mm

ID	x/c_x	y/c_x	ID	x/c_x	y/c_x	ID	x/c_x	y/c_x	ID	x/c_x	y/c_x
1	1.000000	0.000000	34	0.475840	0.089378	67	0.003646	-0.009305	100	0.572240	-0.089230
2	0.998690	0.000194	35	0.451740	0.088594	68	0.007137	-0.013007	101	0.596060	-0.088209
3	0.996350	0.000540	36	0.427760	0.087554	69	0.011779	-0.016561	102	0.619660	-0.086598
4	0.992860	0.001056	37	0.403940	0.086235	70	0.017562	-0.019935	103	0.642970	-0.084245
5	0.988220	0.001744	38	0.380340	0.084694	71	0.024472	-0.023174	104	0.665950	-0.080977
6	0.982440	0.002599	39	0.357030	0.082919	72	0.032492	-0.026436	105	0.688550	-0.077081
7	0.975530	0.003622	40	0.334050	0.080952	73	0.041604	-0.029709	106	0.710700	-0.072630
8	0.967510	0.004917	41	0.311450	0.078799	74	0.051787	-0.033033	107	0.732360	-0.067808
9	0.958400	0.006551	42	0.289300	0.076469	75	0.063016	-0.036384	108	0.753480	-0.062635
10	0.948210	0.008680	43	0.267640	0.073995	76	0.075266	-0.039752	109	0.774010	-0.057286
11	0.936980	0.011285	44	0.246520	0.071357	77	0.088508	-0.043132	110	0.793890	-0.051831
12	0.924730	0.014393	45	0.225990	0.068591	78	0.102710	-0.046513	111	0.813090	-0.046364
13	0.911490	0.017969	46	0.206110	0.065716	79	0.117840	-0.049875	112	0.831560	-0.040993
14	0.897290	0.021944	47	0.186910	0.062735	80	0.133870	-0.053194	113	0.849260	-0.035807
15	0.882160	0.026254	48	0.168440	0.059635	81	0.150740	-0.056452	114	0.866130	-0.030880
16	0.866130	0.030880	49	0.150740	0.056452	82	0.168440	-0.059635	115	0.882160	-0.026254
17	0.849260	0.035807	50	0.133870	0.053194	83	0.186910	-0.062735	116	0.897290	-0.021944
18	0.831560	0.040993	51	0.117840	0.049875	84	0.206110	-0.065716	117	0.911490	-0.017969
19	0.813090	0.046364	52	0.102710	0.046513	85	0.225990	-0.068591	118	0.924730	-0.014393
20	0.793890	0.051831	53	0.088508	0.043132	86	0.246520	-0.071357	119	0.936980	-0.011285
21	0.774010	0.057286	54	0.075266	0.039752	87	0.267640	-0.073995	120	0.948210	-0.008680
22	0.753480	0.062635	55	0.063016	0.036384	88	0.289300	-0.076469	121	0.958400	-0.006551
23	0.732360	0.067808	56	0.051787	0.033033	89	0.311450	-0.078799	122	0.967510	-0.004917
24	0.710700	0.072630	57	0.041604	0.029709	90	0.334050	-0.080952	123	0.975530	-0.003622
25	0.688550	0.077081	58	0.032492	0.026436	91	0.357030	-0.082919	124	0.982440	-0.002599
26	0.665950	0.080977	59	0.024472	0.023174	92	0.380340	-0.084694	125	0.988220	-0.001744
27	0.642970	0.084245	60	0.017562	0.019935	93	0.403940	-0.086235	126	0.992860	-0.001056
28	0.619660	0.086598	61	0.011779	0.016561	94	0.427760	-0.087554	127	0.996350	-0.000540
29	0.596060	0.088209	62	0.007137	0.013007	95	0.451740	-0.088594	128	0.998690	-0.000194
30	0.572240	0.089230	63	0.003646	0.009305	96	0.475840	-0.089378	129	1.000000	0.000000
31	0.548260	0.089814	64	0.001313	0.005524	97	0.500000	-0.089851			
32	0.524160	0.090020	65	0.000000	0.000000	98	0.524160	-0.090020			
33	0.500000	0.089851	66	0.001313	-0.005524	99	0.548260	-0.089814			

Table A.1: Coordinates of the 66018M3J airfoil geometry non-dimensionalized with the chord orthogonal to the leading edge c_x = 900mm

B

Appendix: a note on manufacturing tolerances

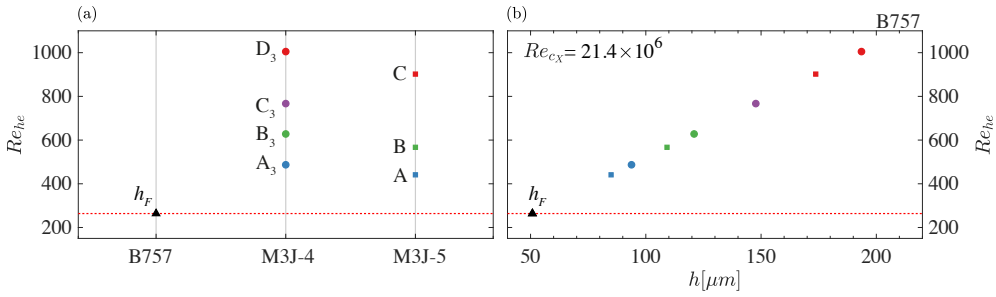

Figure B.1: Relation of FFS height in Chapter 4 (◯ cases $A_3 - D_3$ at $Re_{c_X} = 2.3 \times 10^6$) and Chapter 5 (□ cases $A - C$ at $Re_{c_X} = 2.17 \times 10^6$) to the FFS tolerance specified for a practical HLFC component (△, $h_F = 51\mu$m at $Re_{c_X} = 21.4 \times 10^6$). (a) Comparison of $Re_{he} = u_e h/\nu$ based on conditions at flight B757 ($Re_{c_X} = 21.4 \times 10^6$) and wind tunnel swept wing model M3J-4 ($Re_{c_X} = 2.3 \times 10^6$) and M3J-5 ($Re_{c_X} = 2.17 \times 10^6$) conditions. (b) Calculation of corresponding step height (h) to match each Re_{he} at the design conditions of the HLFC boeing 757-200 ($M = 0.8$, $C_L = 0.5$ at 11,887 m, $Re_{c_X} = 21.4 \times 10^6$) obtained from [190].

In this appendix, the FFS cases presented in Chapter 4 and 5 are compared to manufacturing tolerances used in laminar-flow components on a high-subsonic transport aircraft. This exercise aims to give the reader a rough idea of current manufacturing limits and their relation to the FFS under study in this dissertation. A valuable source of information regarding the practical implementation of laminar flow technologies is the technical reports of the joint NASA-Boeing test program [190, 191], where part of the wing of a Boeing 757-200 was retrofitted for Hybrid Laminar Flow Control (HLFC). More specifically, the outboard leading edge panels were replaced with a boundary-layer suction system.

Relevant to this dissertation is the specified FFS surface irregularity tolerance at the junction of the system with the front spar. The tolerance given for an FFS in this region is $h_F = 51$ µm (0.002 in) (see [190, pg.11-13] and [191, pg.6-7]). Such tight tolerance requires aircraft manufacturers to devise special procedures and unconventional panel joint arrangements. An example can be found in a recent patent of The Boeing Company for a "Skin panel joint for improved airflow" [192]. It has to be noted that although there are procedures to achieve tight tolerances, determining the optimum tolerance is ultimately a multidisciplinary problem. Given that the rise in manufacturing cost to comply with a tolerance compatible with the aerodynamic requirements can lead to an increase in the aircraft's direct operation cost (DOC), as discussed by Kundu *et al.* [193] in the case study of an isolated nacelle.

Figure B.1(a) shows a comparison of $Re_{he} = u_e h/\nu$ at the wind tunnel conditions ($Re_{c_X} = 2.3 \times 10^6$ and 2.17×10^6) for the FFS cases in tables 4.1 and 5.1 with the one based on the tolerance $h_F = 51$ µm at the design conditions of the HLFC Boeing 757-200 ($M = 0.8$, $C_L = 0.5$ at 11,887 m, $Re_{c_X} = 21.4 \times 10^6$)[1] reported in [190]. Note that Re_{he} has been used for practical reasons in this exercise. However, as described in Chapter 3, the

[1] The calculations are based on approximate conditions for wing section WBL-290 extracted from [190].

interaction between FFS-CFI is a complex flow problem which requires further investigation into multi-parameter correlations to be able to adequately determine the impact of a given FFS height on the laminar-turbulent transition behaviour. Finally, figure B.1(b) shows the step height (h) required to match the wind tunnel $Re_{h,e}$ at flight conditions. The results of this exercise suggest that the step heights studied in this dissertation could be achievable in a practical laminar flow component.

Biographical Note

Alberto was born on the 13 of September 1990 in Mexico City. He is a dedicated, social and enthusiastic person, who enjoys working with others to find innovative solutions to complicated problems. With the support of his mother and the teachings of his father, at an early age he developed the necessary mechanical skills to take part in the family's hobby of antique car restoration (see figure B.2). Little did Alberto's parents know that those basic lessons in engineering would cultivate and forge his passion for engineering and equip him with a lifetime toolbox.

Alberto decided to study a bachelor's degree in Mechanical and Electrical engineering in Mexico. He graduated with honours from Universidad Iberoamericana in 2013. During this period, he initiated different research projects and was involved in many extracurricular activities since he was elected president of his university's student body. Soon after graduation, Alberto worked in Mexico as a design and analysis engineer.

In 2014, he travelled to the Netherlands to fulfill his life aspiration of becoming an aerospace engineer. He pursued a master degree in this field at the Delft University of Technology from 2014 to 2016. Due to his technical background, Alberto was instantly attracted to experimental aerodynamics the more he explored this field, the more he became intrigued by it. Thus, he decided to pursue a doctoral education just after graduating with honours "Cum Laude" from his MSc studies. Alberto is convinced that having respect for each other and our environment is essential to improve our present and shape a better future for our society and world.

Figure B.2: The author of this disseration in 1992 (two years old), learning how to restore a 1926 Ford model T wheel from the best engineering teacher he ever had.

CURRICULUM VITÆ

Alberto Felipe RIUS VIDALES

13-09-1990 Born in Mexico City, Mexico.

EDUCATION

2017–2022 PhD in Aerospace Engineering
Delft University of Technology, The Netherlands
Thesis: Influence of a Forward-Facing Step on Crossflow Instability and Transition
Promotor: Dr. M. Kotsonis and Prof. dr. F. Scarano

2014–2016 MSc in Aerospace Engineering
Delft University of Technology, The Netherlands
Thesis: Airwake Flow Dynamics on a Simplified Frigate Shape
Supervisors: Prof. dr. F. Scarano and Dr. A. Sciacchitano

2009–2013 BSc in Mechanical and Electrical Engineering
Universidad Iberoamericana, Mexico

ACADEMIC DISTINCTIONS

2016 Master of Science Cum Laude, Delft University of Technology, The Netherlands

2014 Excelencia Académica, Universidad Iberoamericana, Mexico

2014 Mención Honorífica, Universidad Iberoamericana, Mexico

PROFESSIONAL EXPERIENCE

2022-2024	Post-doctoral Researcher Delft University of Technology, The Netherlands
2014	Design and Analysis Engineer Eberspächer, Mexico
2012-2013	Operations Manager Ferrari & Maserati, Mexico
2009–2013	Research Assistant Universidad Iberoamericana, Mexico

SCIENTIFIC CONTRIBUTIONS

IN THIS DISSERTATION

A.F. Rius-Vidales & M. Kotsonis, *Unsteady interaction of crossflow instability with a forward-facing step*, Journal of Fluid Mechanics **939**, A19. (2022).

A.F. Rius-Vidales & M. Kotsonis, *Impact of a forward-facing step on the development of cross-flow instability*, Journal of Fluid Mechanics **942**, A34 (2021).

A.F. Rius-Vidales & M. Kotsonis, *Influence of a forward facing step surface irregularity on swept wing transition*, AIAA Journal **58(12)**, 5243-5253 (2020).

NOT IN THIS DISSERTATION

F. Tocci, G. Chauvat, **A.F. Rius-Vidales**, M. Kotsonis, S. Hein & A. Hanifi, *Direct numerical simulations of the effects of a forward-facing step on the instability of crossflow vortices*, **[Article in preparation]**.

M. Barahona, **A.F. Rius-Vidales**, F. Tocci, P. Ziegler, S. Hein & M. Kotsonis, *Tollmien-Schlichting Waves over Forward-Facing Steps: An Experimental and Numerical Study*, 12^{th} International Symposium on Turbulence and Shear Flow Phenomena **[Submitted Article]**.

A.F. Rius-Vidales, M. Kotsonis, *Impact of a Two-Dimensional Forward Facing Step Surface Irregularity on Swept-Wing Transition*, IUTAM Symposium on Laminar-Turbulent Transition, Poster C9 (2019).

A.F. Rius Vidales, M. Kotsonis, A.P. Antunes & R. Cosin, *Effect of Two-Dimensional Surface Irregularities on Swept Wing Transition: Forward Facing Steps*, AIAA Fluid Dynamics Conference , AIAA Paper 2018-3075 (2018).

A.F. Rius Vidales, *Air-Wake Flow Dynamics on a Simplifed Frigate Shape - An Experimental Study by Large-Scale Tomographic PTV*, Master Thesis, Delft University of Technology, (2016).

A.F. Rius Vidales, G.C.A. Caridi, J.F.G. Schneiders, A. Sciacchitano, F. Scarano & K. Knepper, *A large-scale Tomographic PTV study of Wake Flow Dynamics on the Landing Deck of a Ship Frigate*, In Proceedings of 11th International Conference on Flow-Induced Vibration and Noise (eds. Gonzalez Diez, S.Belfroid & J.Golliard), pp.137-146, (2016).

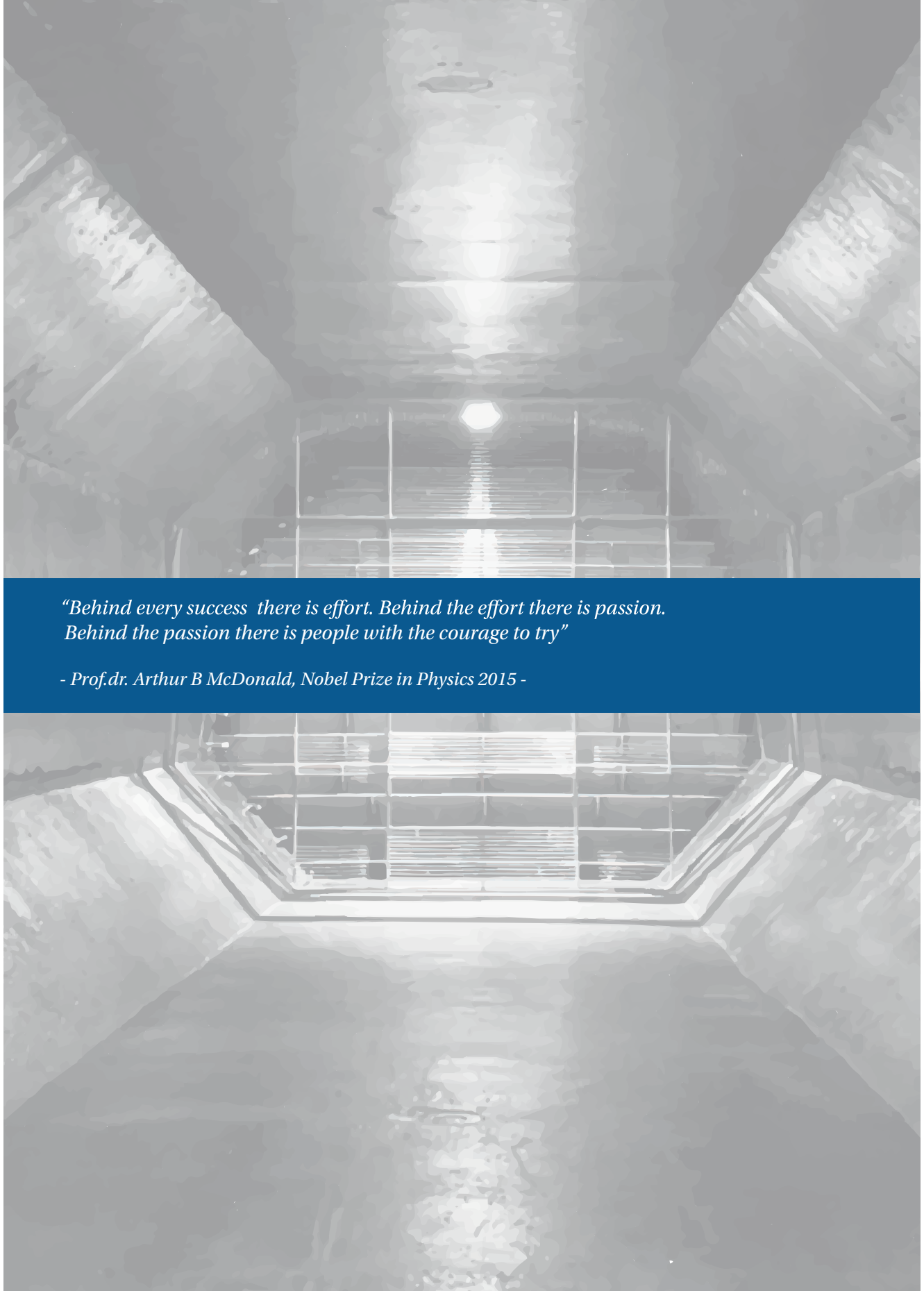

"Behind every success there is effort. Behind the effort there is passion. Behind the passion there is people with the courage to try"

- Prof.dr. Arthur B McDonald, Nobel Prize in Physics 2015 -

ISBN - 978-94-6366-544-5